Photodissociation Spectroscopy of Gaseous Bio-ions in a Commercial Quadrupole Ion Trap Mass Spectrometer

Edward Matthews

Doctor of Philosophy

University of York

Chemistry

August 2018

Abstract

This thesis presents the results of photodissociation spectroscopy experiments performed on biologically interesting molecular and cluster ions within a commercial quadrupole ion trap mass spectrometer. The experimental apparatus uses an excitation laser which is tuneable between the visible and mid-UV. Both cationic and anionic species have been studied using this instrument.

Electronic photodissociation spectroscopy has been used to distinguish between the gaseous protonation isomers of nicotinamide and para-aminobenzoic acid. Similar "protomers" have previously been identified using other gaseous techniques, but these studies are the first to use electronic photodissociation within a commercial mass spectrometer. It is shown that the electronic absorption spectra of individual "protomers" can be resolved by monitoring the production of photofragments as the laser is scanned.

The gaseous electronic absorption spectra of deprotonated alloxazine and lumichrome are recorded using photodissociation; these molecules are the simplest flavin chromophores which form the basis for much cellular chemistry. It is found that both molecules undergo resonant transitions near their calculated electron affinities, which are assigned as dipole-bound excited states. By monitoring the production of a photofragment, it is shown that this excited state is sufficiently long lived to undergo relaxation for alloxazine but not for lumichrome. This subtle difference is explained through the structural differences between these molecules.

Finally, photodissociation spectroscopy is used to study the clusters formed between hexachloroplatinate and the nucleobases. These clusters represent model systems for identifying photochemical reactions that occur between a photoactivatable pharmaceutical and DNA. The electronic absorption spectra of these clusters are broadly similar and are dominated by ligand-to-metal charge transfer transitions within the hexachloroplatinate moiety. It is shown through an analysis of the photofragments across the spectral range that the excitation wavelength controls the distribution of photofragments and that the nucleobase influences the available fragmentation pathways.

Contents

Chapter 5: Evidence for the Impact of Methyl Group Free Rotors on the Stability of Dipole-Bound Excited States in the Flavin Chromophore Anions of Alloxazine and Lumichrome

Chapter 6: UV laser photoactivation of hexachloroplatinate bound to individual nucleobases in vacuo as molecular level probes of a model photopharmaceutical

List of Figures

List of Tables

List of Schemes

Acknowledgements

I would like to thank my supervisor, Dr Caroline Dessent, for her encouragement and guidance throughout my thesis. I would also like to thank Dr Ananya Sen for patiently training me to use lasers and mass spectrometers, as well as always taking time out of her day to collect data with me. I would like to thank Rosaria Cercola and Mathew Hawkridge for always bringing a smile to my face and providing invaluable advice, both scientific and personal. I would like to thank Kelechi Uleanya for challenging my beliefs and perspectives. I would finally like to thank the remaining members of the Dessent group as well as the physical chemistry office at York for providing an enjoyable and stimulating environment over the course of my PhD.

Author's Declaration

I declare that the research presented in this thesis is my own and is original. This thesis has not previously been submitted for award at this or any other institution. All sources are acknowledged as References.

Chapter 3 has been published:

"Locating the Proton in Nicotinamide Protomers via Low-Resolution UV Action Spectroscopy of Electrosprayed Solutions"
E. Matthews and C. E. H. Dessent, J. *Phys. Chem. A*, 2016, **120**, 9209–9216.
http://dx.doi.org/10.1021/acs.jpca.6b10433

Chapter 4 has been published:

"Experiment and theory confirm that UV laser photodissociation spectroscopy can distinguish protomers formed via electrospray"
E. Matthews and C. E. H. Dessent, *Phys. Chem. Chem. Phys.*, 2017, **19**, 17434–17440.
http://dx.doi.org/10.1039/c7cp02817b

Chapter 6 has been published:

"UV laser photoactivation of hexachloroplatinate bound to individual nucleobases in vacuo as molecular level probes of a model photopharmaceutical"
E. Matthews, A. Sen, N. Yoshikawa, E. Bergström and C. E. H. Dessent, *Phys. Chem. Chem. Phys.*, 2016, **18**, 15143–15152.
http://dx.doi.org/10.1039/C6CP01676F

Additional papers where I am the primary author have also been written across the course of my PhD and can be found online:
"Protomer-Dependent Electronic Spectroscopy and Photochemistry of the Model Flavin Chromophore Alloxazine"
E. Matthews, R. Cercola and C. E. H, Dessent, *Molecules*, 2018, **23**, 2036.
https://doi.org/10.3390/molecules23082036

Chapter 1

Introduction to Photodissociation Spectroscopy on Gaseous Bio-ions

1.1 Spectroscopic Studies of Biomolecules in the Gas Phase

Biological systems exploit photochemical processes in many life functions, such as the photoisomerism of retinal in photoreceptor cells which is responsible for sight,[1] or the absorption of chlorophyll in plants which enables photosynthesis to occur. Conversely, light can also be harmful to an organism's life functions; such as the absorption of ultraviolet (UV) light by the DNA nucleobases which can cause genetic mutations to occur.[2] Additionally, light-activated drugs are being designed to improve treatments for diseases, such as cancer, by improving the selectivity for diseased cells, thereby decreasing the complications associated with drug treatments.[3] The gas phase offers an excellent environment for understanding the fundamental photochemistry of these biologically important chromophores which is not influenced by intermolecular interactions or solvent effects. Individual gaseous molecules can be isolated from a complex mixture experimentally, enabling the photochemistry of a single species in a single charge state to be analysed, where a mixture may exist in solution.[4]

Biological chromophores vary in size, charge state and atomic composition, which means that there is not a single technique that can study all chromophores. Instruments which perform spectroscopy on gaseous molecules can generally only be used for either neutral or charged species. Ion photodissociation (PD) spectroscopy can be used to record electronic absorption spectra and determine the photochemistry of gaseous cations and anions;[5] while ionisation techniques such as resonance-enhanced multiphoton ionisation (REMPI) spectroscopy and zero kinetic energy (ZEKE) spectroscopy can be used to determine the electronic absorption spectra of neutral molecules and clusters.[6, 7] With each of these techniques, the electronic absorption spectra are not determined by measuring the decrease in the intensity of a laser as it passes through the gaseous molecules, but as a function of

the fragmentation of the gaseous species (i.e. the intensity of a photofragment or a photoelectron) that occurs following electronic excitation. Photoelectron spectroscopy (PES) is a related gas-phase technique which can determine the electronic structure of gaseous anions.[8]

A large quantity of photochemical information can be obtained in the gas phase; however, biological chromophores are naturally found in the condensed phase. This discrepancy means that the relevance of gaseous photochemistry must be questioned when using this information to discuss solution-phase behaviour. Indeed, molecules exists where the most stable protonation (or deprotonation) site changes between the solution and gas phases,[9] e.g. para-hydroxybenzoic acid (PHBA); studies on gaseous PHBA have shown that the distribution of gaseous protonated structures changes with the solvent used for electrospray ionisation.[10] Gaseous spectroscopy experiments generally rely on quantum chemical calculations to verify the gaseous structure by optimising structures and simulating electronic absorption spectra. The simplicity of the gaseous environment makes such calculations faster than if solvents and local environments were considered, enabling the use of complex computational methods.

This thesis will attempt to determine the structure and photochemistry of several biologically relevant molecules and clusters by conducting gas-phase PD spectroscopy experiments in a commercial quadrupole ion trap (QIT) mass spectrometer. This information will be used to evaluate the applicability of performing PD spectroscopy in a commercial instrument and for determining photochemical fragmentation processes. As such, this introduction will describe PD spectroscopy, and will review existing experiments based around commercial and home-made mass spectrometers.

1.2 Electronic Photodissociation Spectroscopy Overview

Laser PD spectroscopy has been used as a tool for determining the physical properties of gaseous ions since the late 1960s, when Brauman and Smyth recorded the electron detachment cross section of hydroxide anions at six different wavelengths.[11] Since then, laser PD has become a powerful spectroscopic technique

for recording gaseous spectroscopy.[5] PD experiments can be used to determine: geometric structures;[9] vibrational modes;[12] electronic absorption spectra;[13] photofragmentation mechanisms;[14] and excited-state dynamics of gaseous ions.[15] PD spectroscopy experiments use tuneable lasers to fragment gaseous ions via resonant excitation (or electron detachment). The fragmentation patterns reveal information about the photochemistry and thermochemistry of the ions.[16, 17] The versatility of PD as a spectroscopic technique is shown by its application to species varying from diatomic ions to intact proteins.[11, 18-20] PD spectroscopy can also be performed on a diverse group of gaseous ionic species, including: organic molecular ions (M^+ or M^-);[21] protonated or deprotonated organic molecules ($[M+H]^+$ or $[M-H]^-$);[22] charged metal complexes ($[ML_x]^{n-}$ or $[ML_x]^{n+}$);[23] and charged clusters ($X \cdot Y^+$ or $X \cdot Y^-$).[14]

In an ion PD experiment, molecular or cluster ions are introduced to a mass spectrometer through an ion source. Gaseous ions are guided through the vacuum and are collected in an ion trap or a storage ring. Quadrupole mass filters and resonant ejection techniques are used to selectively isolate ions with a desired mass-to-charge ratio, ensuring spectral purity. Once collected, an ion packet is irradiated with one or multiple monochromatic lasers which resonantly induces fragmentation in some of the gaseous population. Mass spectra are recorded for the gaseous ions both with and without irradiation. Ions peaks which are only observed in the mass spectrum with irradiation are the photofragments; the identities of the photofragments can be determined from their mass-to-charge ratios. The mechanisms by which photofragments can be produced follow two broad categories: ionic fragmentation (Equation 1.1) and electron detachment (Equation 1.2). These mechanisms will be discussed further in Chapter 2.

$$M^{+(-)} + h\nu \rightarrow A^{+(-)} + B$$

Equation 1.1

$$M^{n-} + h\nu \rightarrow M^{(n-1)-} + e^-$$
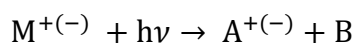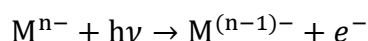
Equation 1.2

As mentioned above, absorption coefficients are calculated from the intensities of ions in the photofragment mass spectra. This can either be done by measuring the production of one or several photofragments or by calculating the depletion in signal

of the parent ion.[11, 24] If the output wavelength of the laser is scanned, absorption coefficients of the ions can be calculated at each wavelength and compiled into an absorption spectrum.

This thesis is primarily concerned with electronic PD spectroscopy performed using UV and visible light sources; however, it is important to mention that gaseous ions can also be fragmented by vibrational PD.[25] Figure 1.1 is a schematic potential energy curve which shows the differences in the way that fragmentation is induced with vibrational and electronic photodissociation. For UVPD, electronic excitation generally provides the ion with sufficient internal energy, such that if the molecule relaxes non-radiatively then the electronic ground state will be vibrationally excited above the threshold for fragmentation to occur. This means that UVPD experiments
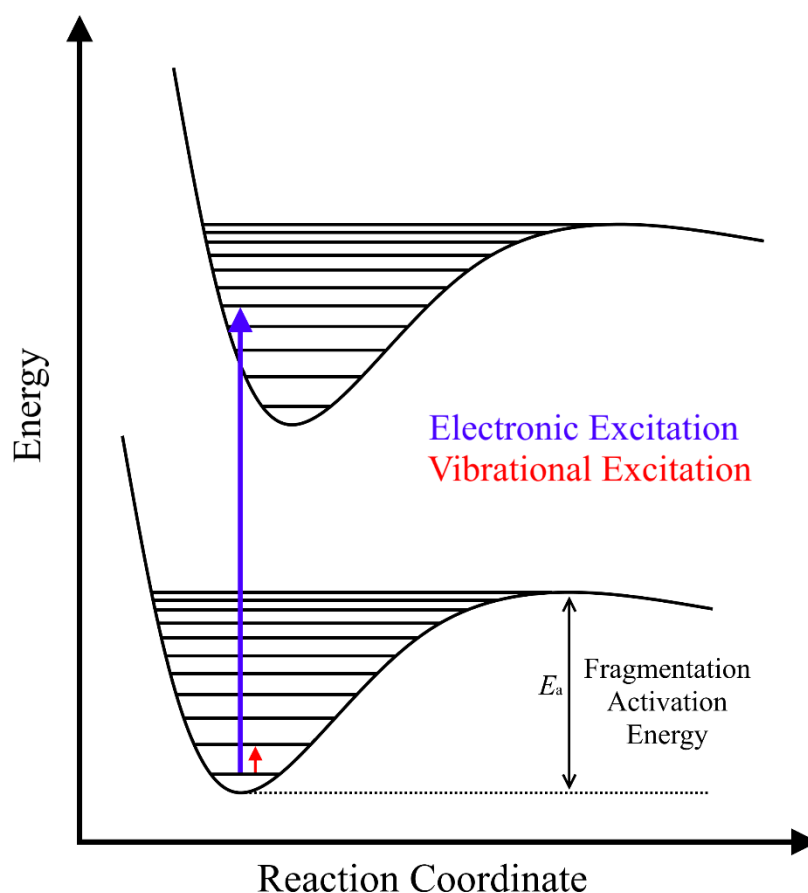
Figure 1.1 Schematic potential energy surfaces of a gaseous molecule showing different methods of gaseous photodissociation. The size of the arrow is representative of the energy transfer to the gaseous molecule for electronic or vibrational absorption.

which are performed in conditions where only one-photon absorption occurs produce true absorption spectra, so long as radiative electronic relaxation does not occur. (UVPD fragmentation processes are discussed further in Chapter 2).

Vibrational PD spectroscopy is now routinely performed on gaseous ions. The general experimental methods for performing vibrational PD spectroscopy are similar to those for electronic PD spectroscopy, except that tuneable infrared (IR) lasers are used to dissociate the ions. The energy of IR photons is lower than that of UV photons (shown schematically in Figure 1.1), this means that stable gaseous ions often require several IR absorption events to induce fragmentation; this is referred to as infrared multi-photon dissociation (IRMPD). However, the anharmonicity of molecular vibrations means that the energy separation between vibrational levels decreases as the vibrational level is increased (shown in Figure 1.1). This means that an IR laser with a narrow linewidth will only excite a single transition in vibrational energy level of a given vibrational mode (i.e. $v = n \rightarrow v = n + 1$). To achieve dissociation in an IRMPD experiment, gaseous molecules must be irradiated for a sufficiently long time to allow the internal energy gained from an IR excitation to be dissipated amongst other degrees of freedom, thereby allowing subsequent vibrational excitations to occur. IRMPD has been used to study the structures of biologically important ions and clusters including nucleotides, peptide residues, and glycans.[26-28] Vibrational spectroscopy is well-suited for distinguishing between structural and conformational isomers, which means that IRMPD experiments can lead to the assignment of an unambiguous gaseous structure. This is important when the structure of the ion in the solution phase is unknown.

Gaseous PD experiments can complement solution-phase spectroscopic experiments by providing information that is unavailable in the solution phase. A major advantage of working with gaseous ions is the spectral purity provided by mass isolation. This feature was used in a liquid chromatography (LC) – ultraviolet photodissociation (UVPD) mass spectrometric characterisation of intact proteins, where 46 unique sequences were identified following the isolation and fragmentation of gaseous proteins produced from a single ion source.[4] Mass isolation also allows the photophysics of specifically sized ionic clusters (i.e. $[M^+]_n[A^-]_m$) to be determined, whereas a distribution of cluster sizes may exist in solution which will produce broad

absorption spectra that have contributions from many ionic species.[29] An additional advantage of gaseous experiments is that the absence of a solvation shell simplifies the photochemistry of isolated ions when compared to the solution phase, since the stabilisation of ground- or excited-state orbitals does not occur in the gas phase. Gaseous experiments can therefore be used comparatively to examine the effects of solvation on the photochemistry of a molecule or ion.

1.3 Photodissociation Spectroscopy – Ion and Cluster Sources

The types of ionic species which can be studied using PD spectroscopy are limited by the ionisation sources that are used to introduce ions into the experimental apparatus. Since PD is performed in mass spectrometers, the advancements in ion source technology which have been used in mass spectrometry have also been used for PD. Early PD experiments, such as those by Brauman or Dunbar, used electron ionisation (EI) to gaseous produce ions.[11, 18, 30] Electron ionisation is a hard ionisation technique which promotes extensive fragmentation of the ion, making the source unsuitable for introducing large biomolecules or weak clusters to the gas phase.

In order to study more fragile gaseous species using PD, ions must be prepared using soft ionisation sources, such as electrospray ionisation (ESI). ESI was developed in the 1980s by Fenn, who found that injecting a solution through a charged needle into a bath of nitrogen gas produced gaseous ions which could be guided into a mass spectrometer and analysed.[31, 32] The main requirement for observing ionic species in ESI mass spectrometry is that the molecule is soluble in an ESI compatible solvent such as water; this makes ESI an ideal technique for producing gaseous biomolecule ions. Additionally, ESI produces gaseous ions which have minimal fragmentation, which allows mass spectra of unstable molecules to be recorded; ESI is used in analytical mass spectrometry when characterising large polymeric biomolecules.[33, 34] Furthermore, the minimal fragmentation provided by ESI can allow for non-covalent bonds which exist in solution to be retained in the gas phase, thus making ESI ideal for producing gaseous ionic clusters.[29, 35] Ions can also be clustered with solvent molecules during ESI by seeding the nebulising gas with a solvent.[36] ESI is ubiquitous as the ion source in modern PD experiments, owing to the diversity of charged species which can be introduced to the gas phase via ESI.[37-42]

1.4 Commercial UV Photodissociation Mass Spectrometers

Within the scientific literature of PD experiments, a distinction can be found between experiments which are designed around commercial and home-made mass spectrometers. Commercially available mass spectrometers benefit from having reliable, compact designs with minimal user input required in daily maintenance, and engineer assistance is also available for technical issues. However, the compact design of commercial mass spectrometers limits the space available to modify the experiment. Home-built mass spectrometers can theoretically be any size, which enables research groups to tailor the PD experiment for a desired purpose by allowing more control over the selection and spacing of all components. This also enables research groups to continually update the set-ups for new developments in ion trapping or detection technology.

Several physical chemistry groups have adapted commercially available mass spectrometers to be used for electronic spectroscopy. Amongst the first to use these machines was the Weinkauf group, whose experiment used a modified ESI quadrupole ion trap (QIT) mass spectrometer (Esquire 3000, Bruker Daltonics).[15, 43-45] The experiment was initially used to study the effects of protonation on the electronic absorption spectrum of the amino acid tryptophan,[43] and the interpretation of the experimental data relied on electronic structure calculations to determine the most stable gaseous protonation site and simulate electronic spectra using the DFT/MRCI method.[46] The Weinkauf experiment was later modified to record time-resolved absorption spectra using an ultrafast Ti:Sapphire laser and used to determine the excited-state lifetimes of biologically relevant ions, including protonated adenine and a protonated tryptophan-leucine dipeptide.[15, 44] Using a commercial mass spectrometer to record the excited-state dynamics of gaseous ions is an impressive historic scientific accomplishment, since time-resolved ion absorption experiments are still rare even amongst home-made PD experiments.[47-50]

Another research group that has embraced commercial mass spectrometers for PD is the Dugourd group. Their experimental set-up has also used an ESI QIT mass spectrometer (LCQ Duo, ThermoElectron) instrument for both analytical and

spectroscopic PD.[50-55] This experimental apparatus has been used to study the effect of electron detachment on large gaseous polyanionic biomolecules like DNA oligomers and protein ions.[51-53] Electron detachment from a DNA polyanion to create a radical DNA anion was shown to destabilise the DNA molecule, such that CID following electron detachment yields enhanced fragmentation compared to CID without electron detachment. This is desirable when using mass spectrometry to sequence polymeric molecules because it gives additional information about the sequence of monomers.[51, 52] Dugourd has also used this experiment to study the electronic spectra of smaller biomolecules, including deprotonated tryptophan and protonated flavin mononucleotide.[50, 55] Recording the absorption spectra of the charged biomolecules is important because charged molecules are ubiquitous in biological environments.

Another innovation in electronic PD spectroscopy using commercial mass spectrometers was made by the Jockusch group. Their experiment used an ESI-QIT mass spectrometer (Esquire 3000+, Bruker Daltonics) which was modified to record both the absorption and emission spectra of gaseous ions.[56-61] This experiment has been used to study the photochemistry of gaseous xanthene, rhodamine and fluorescein dyes; the absorption and fluorescence spectra of the rhodamine dyes show clear blue shifts from the solution to the gas phase.[56-59] The experiments by Jockusch and co-workers revealed the convenience of using commercial mass spectrometers when determining the relationship between experimental conditions on the photochemistry, since parameters such as the accumulation time, ion trap pressure and q_z value could be controlled using the commercial software. The fluorescence spectrometer used within this spectrometer has a nanosecond time resolution which enabled the emission lifetimes of the gaseous ions to be recorded.

Commercial mass spectrometers have been shown to be well suited for studying the physical properties of gaseous ions, with proven success in recording the photochemistry of biological ions as well as other gaseous species. An advantage of commercial mass spectrometers is the abundance of photofragmentation data which can be used to determine the photochemical reactions which ions undergo; fragment data are easily collected and processed using the commercial software which is provided by the manufacturer of the mass spectrometer. Commercial PD instruments

are most commonly used in one-colour PD experiments; however, the Riehn group has recently used a QIT-MS (Amazon Speed, Bruker Daltonics) to record pump-probe spectroscopy in several gaseous organometallic complexes.[49, 62, 63] This experiment has been used to study the ultrafast dynamics of a photocatalyst which showed that an initially formed metal-to-ligand charge transfer excited state migrated from one metal centre to another. The lifetimes of these excited states, as well as two intermediate states, were calculated from pump-probe measurements.[49]

In addition to UVPD, IRMPD is also performed within commercial mass spectrometers.[27, 64, 65] The requirement of multi-photon absorption to induce fragmentation in IRMPD means that the lasers used in IRMPD experiments are generally higher power than the lasers used in UVPD experiments. Indeed, an IRMPD study of para-aminobenzoic acid (PABA) by Kass, which used a table-top laser (Nd:YAG pumped OPO/OPA), was unable to fragment a structural isomer of PABA because the laser power was too low.[9] Several research groups have instead used a tuneable free electron laser (FEL) as a high-energy light source to induce fragmentation, such as the research groups based in the FELIX laboritories.[26, 66, 67] One such IRMPD experiment at the FELIX laboratories uses a commercial mass spectrometer (AmaZon Speed ETD, Bruker Daltonik) to perform gaseous spectroscopy. This instrument has been used to study structural motifs and reaction mechanisms in biologically relevant ions, and has recently included deamidation and dehydration reactions in dipeptides.[26, 68] These degradation reactions occur in the solution phase and are believed to contribute to some diseases. Computational chemistry was used in these studies to identify the reactive gaseous conformers by simulating vibrational spectra, reaction transition states and activation energies were also calculated.

1.5 Home-built UV Photodissociation Mass Spectrometers

Home-made PD experiments are purposely built to perform spectroscopy, so are generally more suited to study high-resolution spectroscopy when compared with instruments that use commercial mass spectrometers. A common method for improving resolution in PD spectroscopy is cooling the gaseous ions in cryogenically cooled ion traps. Lowering the internal temperature of ions improves the resolution

of absorption spectra because Doppler broadening within the absorption bands is reduced. Conducting PD experiments at cryogenic temperatures is relevant to the field of astrophysics because complex organic molecules are known to exist in the interstellar medium and these molecules are subjected to high-energy radiation.[69]

High-resolution spectroscopy was shown in a UVPD experiment on hydroxide ions within a cooled linear ion trap (LIT), an experimental absorption spectrum resolved the onset of electron detachment from the rotational states $J = 2$, 1 and 0 as the photon energy increased, the internal temperature of the ions was calculated from the populations of the J states.[70] Cold gaseous ion spectroscopy has also been performed by the Jouvet group, who have used electronic spectroscopy to determine the gaseous structures of organic and organometallic molecules.[71-73] The high-resolution absorption spectra are used to obtain accurate vertical transition energies which can be used to benchmark quantum chemistry calculations.

The control over space which is offered by home-built instruments has enabled experiments to be designed to use multiple lasers to fragment gaseous ions. The groups of Rizzo and Zwier have PD experiments which use cooled LITs to store ions, these experiments have been used to record high-resolution UV-IR double resonance absorption spectra of several biologically important molecules.[38, 74-77] Rizzo recently used the experiment to record the UVPD absorption spectrum of a helical oligopeptide.[77] Increasing the ion-cooling duration improved the resolution of the absorption spectrum to the point where absorption bands from four separate conformational isomers were resolved. UV-IR double resonance spectroscopy was used to record the vibrational spectra of each of these conformers as well as to vibrationally heat a specific conformer to change the gaseous populations, in so-called hole-filling spectroscopy.

Custom-built experiments which do not include ion cooling are also found within the UVPD literature, such as those by Weber and Nielsen. These experiments have been used to measure the gaseous electronic absorption spectra of organic and inorganic ions.[23, 42, 78, 79] Specifically, Nielsen has studied the effect of partial solvation by a single water molecule on the electronic absorption spectrum of ortho- and para-nitrophenolates, the spectra showed that partial solvation red-shifted the charge

transfer transition in the ions.[78] Nielsen's group also has a home-built ion luminescence spectroscopy instrument which has been used to study spectral shifts between the solution and gas phase for a series of highly fluorescent charged dyes.[80]

1.6 Alternative Gaseous Experiments

UVPD spectroscopy is the only gaseous technique that can measure the electronic absorption spectra of gaseous ions. However, alternative techniques exist which are used to determine gaseous structures or spectroscopically interrogate gaseous ions or molecules. Structural techniques include collision induced dissociation (CID), ion mobility spectrometry (IMS) and analytical photodissociation methods (either UV or IR). Alternative gaseous spectroscopy techniques include IRMPD, resonance enhanced multiphoton ionisation (REMPI) spectroscopy and photoelectron spectroscopy (PES).

Collision induced dissociation (CID) mass spectrometry has been widely used for decades to determine the thermal fragments of gaseous ions, with ions studied ranging from small organic ions to polypeptides.[81, 82] Gaseous fragmentation mechanisms of organic molecules are well known from the interpretation of electron impact mass spectra by researchers such as McLafferty.[83] In a CID experiment, gaseous ions are heated through collisions with a buffer gas, this heating leads to rearrangements or fragmentation. A distinction can be made in CID experiments between low- and higher-energy collisional dissociation (HCD). In low-energy CID, ions are gently heated through multiple collisions with the buffer gas, which generally leads to fragmentation via the mechanism with the lowest activation energy. HCD can instead accelerate ions to have translational energies of several keV; colliding these ions with a buffer gas results in extensive fragmentation. Indeed, scanning the translational energy in HCD experiments has been used to determine the relative activation energies of different fragmentation pathways.[84]

Ion mobility spectrometry (IMS) is a method of separating gaseous ions based on their gaseous mobilities when passing through a buffer gas under the influence of an electric field.[85] Whilst many different IMS instruments exist, ions are separated by their collision cross-section which is determined by the shape and size of the ion.

IMS is commonly used in conjunction with mass spectrometry (IMS-MS), where IMS is used as a pre-filter for the mass spectrometer analysis.[86] IMS has been used as a method to separate gaseous isomers in IRMPD and UVPD experiments,[38, 87-89] such as to separate the structural isomers of protonated para-aminobenzoic acid produced via ESI before recording gaseous spectroscopy. As with PD experiments, IMS instruments can either be commercially obtained or home-built.

Analytical ion PD is also commonly used as a mass spectrometry technique to determine the sequences or structures of large biomolecules.[90] These experiments generally use fixed output lasers, such as a 12.6 μm CO_2 laser or a 193 nm ArF excimer laser, as tools to fragment the gaseous ions. The degree of fragmentation can be controlled with the irradiation period and power of the laser,[24, 91] and extensive fragmentation can provide a complete description of the secondary structures of large polymeric biomolecules.[92-94] Laser fragmentation can compete with other analytical techniques, such as CID, whilst avoiding the low mass cut-off associated with performing experiments in ion traps.[95]

As has been discussed, IRMPD is a type of PD experiment where photofragmentation is induced by resonantly exciting vibrational modes in the gaseous ions. The IR spectroscopy of gaseous ions has been studied extensively in the gas phase, and much recent work relates to biological ions and charged clusters.[96-99] In a gaseous study of metallated lumiflavin clusters, IRMPD was used to record the vibrational absorption spectra of the clusters in order to determine the most-preferable metal binding sites for the differently sized metals.[97] Assignment of the gaseous structures relied on quantum chemical calculations to simulate vibrational absorption spectra for many structures of the conformational isomers of metallated lumiflavin. IR experiments are also conducted at cryogenic temperatures in custom-built instruments by dissociating weakly bound clusters that are formed between the gaseous ions and a cold buffer gas. Johnson has recorded the vibrational absorption spectra of a cryogenically cooled 12-carbon dicarboxylate via the predissociation of carboxylate-$(H_2)_n$ clusters.[100] The absorption spectra are highly resolved and show that only a single conformer exists in the cold environment.

REMPI is a method used to detect and perform spectroscopy on neutral molecules and clusters in the gas phase.[101-103] In a REMPI experiment, one or several lasers are overlapped with a supersonically-expanded molecular beam in a vacuum chamber to produce photoelectrons and cations; these ionic species can then be detected. Supersonic expansion cools the molecules and clusters to the point where high-resolution spectroscopy can be performed. All molecular beam experiments are home-built, and the design of each experiment controls the type of spectroscopy which can be studied. De Vries and co-workers used REMPI spectroscopy to record the vibronic absorption spectra of the isolated nucleobases and base pairs.[104] The study used hole-burning spectroscopy to separate absorption spectra from different tautomeric gaseous species. The cold nature of molecular beam techniques allowed for the hydrogen-bonded nucleobase pairs to be found in the gas phase. However, introducing molecules into the gas phase within molecular beam techniques (e.g. heating or laser-desorption) requires the molecule to have a high vapour pressure. This means that a smaller selection of biomolecules can be studied in the gas phase when compared with gaseous methods which use ESI.

The final gaseous technique that will be discussed is photoelectron spectroscopy (PES), which is used to determine the electronic structure of gaseous anions.[105-107] Since the technique is used to study anions, many experimental features (i.e. ion sources, ion guides and ion traps) are shared with PD spectroscopy. PES was used to study the effect of hydrogen-bonded clustering on the electronic stability of deprotonated acids.[108] While clustering should stabilise the anion, the study found that the adiabatic detachment energy (ADE) of the anion was decreased upon clustering; this surprising result was attributed to rearrangement mechanisms (e.g. hydrogen-atom transfers) which can occur on the neutral potential energy surface. As with other forms of gaseous spectroscopy, PES can be used to determine dynamical information. This has been shown in a frequency-, angle- and time-resolved PES study of a π-stacked anionic dimer by Verlet, which was achieved using a combination of tuneable lasers, ultrafast lasers and photoelectron imaging.[109] The study found that a number of the valence-bound excited states, which occurred above the detachment threshold of the dimer, underwent efficient internal conversion to a dipole-bound state on an ultrafast timescale. These dipole-bound states underwent autodetachment on a much longer timescale.

1.7 Thesis Overview

In this thesis, a laser interfaced commercial mass spectrometer will be applied to perform the first UVPD studies of a selection of gaseous ions and complexes of biological interest. The experiments employ a highly scannable, broad-range laser system which has been operated between 220 and 600 nm, which has enabled absorption spectra to be obtained for these gaseous ions. Whilst the instrument employed is technically similar to those of Dugourd and Jockush,[50, 56] we focus for the first time on exploiting the instrument for photochemical investigations and demonstrate the instrument's potential as a photochemical tool.

Chapter 2 describes the instrumental design and experimental protocol which has been used to undertake PD experiments, as well as the computational methods which have been employed to aid the interpretation of the data obtained within the different experiments.

Chapter 3 presents a study of protonated nicotinamide ($NA \cdot H^+$) which is introduced into the gas phase via ESI. PD spectroscopy is used to record the gaseous electronic absorption spectrum of mass-isolated $NA \cdot H^+$, to determine whether protonation isomers (protomers) can be detected. We find that two isomers are present and identify their protomer-dependent photochemistry. In Chapter 4, we extend these measurements to the PABA system and show how photofragments can be used to identify protomers. The role of protic and aprotic solvents during the during the ESI process is also discussed.

Chapter 5 is an electronic PD study of deprotonated alloxazine and lumichrome. The electronic absorption spectra of these deprotonated flavin ions are used to determine the gaseous structures and are compared with the solution-phase absorption spectra. It is shown that a single structure exists in the gas phase for both molecules and that the electron detachment onset for these molecules is resolved in the absorption spectrum. The differing photochemical behaviour shown by these anions around the electron detachment threshold is discussed.

Chapter 6 uses PD spectroscopy to study the photochemistry of nucleobase – hexachloroplatinate clusters, where the nucleobases being studied are adenine, cytosine, thymine and uracil. PD is used as a tool to identify photoproducts that may form between platinum-based photo-pharmaceuticals and DNA. We find that the excitation wavelength strongly influences the distribution of photoproducts in these clusters and that the choice of nucleobase influences the types of photofragments which are produced.

Chapter 2

Photodissociation Methods and Theory

2.1   Photodissociation - Mass Spectrometry Instrument Overview

The instrument which is used to obtain the data presented in thesis is a laser-coupled electrospray ionisation – quadrupole ion trap (ESI-QIT) mass spectrometer (AmaZon, Bruker Daltonik). A block diagram of the experimental hardware is given in Figure 2.1. The mass spectrometer has been modified to enable laser-coupling, allowing the pulsed laser to pass through the ion trap, thereby allowing the laser to dissociate the ions. The photons which are used to fragment the gaseous ions are produced by a 10 Hz Nd:YAG (Surelite, Continuum) pumped OPO (Horizon 1, Continuum) which can selectively produce wavelengths ranging between 193 and 2700 nm (6.42 – 0.46 eV). The laser beam is optically guided towards an interface with the mass spectrometer and is focused through the ion trap with a 200 mm plano-convex lens. A beam shutter (Model SH05, Thorlabs Inc.) is used to control the transmission of the laser beam into the mass spectrometer. A prism is mounted on a motorised flip mount (Model MFF001, Thorlabs Inc.) which is used selectively to
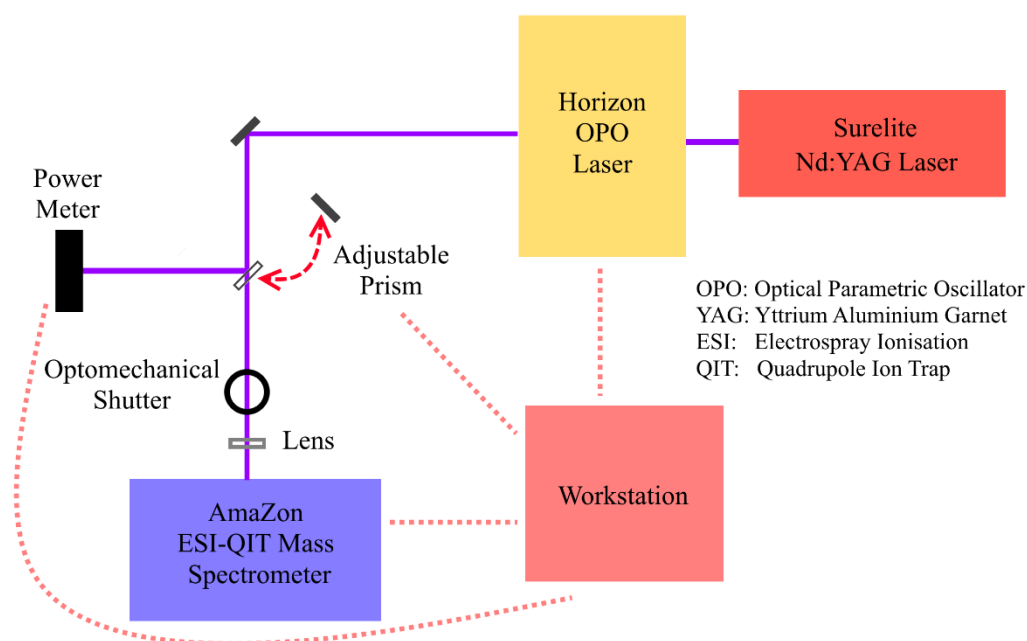
Figure 2.1 Block diagram of the laser-mass spectrometry experimental set-up.

direct the laser beam to a laser power meter (Power Detector UP19K-15S-VR, Monitor is a Gentec-EO Tuner). The individual components of the experiment are monitored and controlled with a workstation. A detailed description of these components will be given in the following sections.

2.2   The Laser-Coupled Mass Spectrometer

2.2.1   *The Bruker AmaZon Mass Spectrometer*

Figure 2.2 is a diagram of the AmaZon (Bruker Daltonik) mass spectrometer, showing the route of ions through the mass spectrometer. The AmaZon mass spectrometer is a quadrupole ion trap (QIT) mass spectrometer with an electrospray ionisation (ESI) source. The ESI source operates under atmospheric conditions, whereas the QIT region of the mass spectrometer has an operational pressure in the region of 10^{-6} mbar. To achieve the $\sim 10^9$ decrease in pressure, four differentially pumped vacuum stages are used in the mass spectrometer.

Nebuliser-assisted ESI is the exclusive source of gaseous ions within the experiments conducted throughout this thesis. The gaseous ions produced from ESI travel from the spray chamber to the vacuum system through an inlet capillary, which is heated
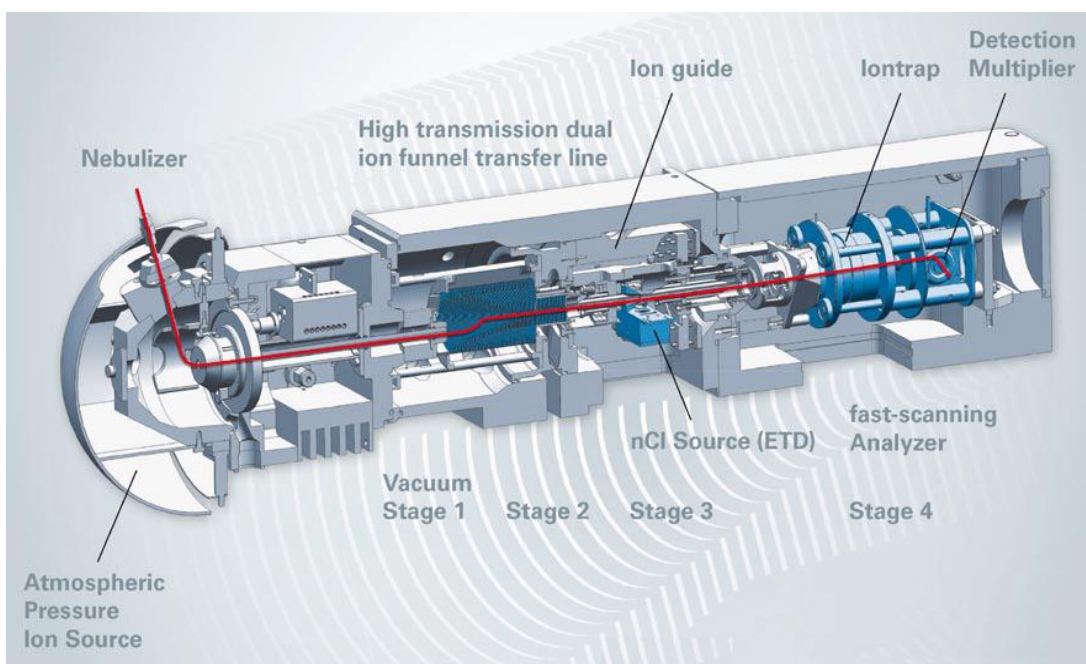
Figure 2.2 Diagram of the AmaZon (Bruker Daltonik) mass spectrometer. Image taken from the AmaZon user manual.[110]

to aid the desolvation process. A heated drying gas also flows around the entrance of the inlet capillary to further assist desolvation. Once inside the vacuum chamber, ions are guided towards the QIT through a double-stage ion funnel, two multipole ion guides and two ion lenses. The QIT is used to collect, store, mass isolate, fragment and mass-analyse gaseous ions; and laser PD is performed on ions stored in the QIT. After ions have been sufficiently interrogated (i.e. photodissociated, collisionally dissociated) in the QIT, the ions are sequentially ejected according to their mass-to-charge (m/z) ratio and are detected by a Daly conversion dynode detector.[111]

The AmaZon mass spectrometer is controlled from a workstation using commercial software (TrapControl Version 7.2, Bruker Daltonik). TrapControl is used to control the source conditions (e.g. voltage applied to the ESI needle; nebulising gas pressure; drying-gas flow rate; and drying-gas temperature) as well as the voltages applied to the ion optics within the mass spectrometer (e.g. ion funnel, multipole and lens voltages). These conditions can be automatically tuned to maximise the number of ions of a particular m/z ratio. TrapControl is also used to control the timings and operations of the QIT, including: ion accumulation time, mass isolation and ion fragmentation using collision induced dissociation (CID). As will be explained in Section 2.5, the ion fragmentation capabilities of the QIT are employed to facilitate laser PD within this experiment. Once an appropriate mass spectrometry method has been chosen for a laser PD experiment, TrapControl is used to record and store mass spectra for a controllable period of time.

More detailed explanations of the theory behind the use of ESI as an ion source and QITs for storing and fragmenting ions will be given in following sections. Additionally, the modifications made to the mass spectrometer to enable laser coupling will also be described. Furthermore, the mass spectrometry methods which allow laser PD data to be collected and processed will also be discussed.

2.2.2 *Electrospray Ionisation (ESI) Source*

The ion source used within the laser-coupled mass spectrometer is electrospray ionisation (ESI).[31, 32, 112] The use of ESI to produce gaseous ions is well established across the scientific literature and detailed explanations of the processes involved in ESI can be found in review articles and textbooks on ESI mass spectrometry.[113-116] Figure 2.3 is a diagram of an ESI source showing the main features of ESI, this process can be divided into the production of charged droplets and the desolvation of analyte ions.

To produce charged droplets, a solution containing an analyte is injected through a needle. A potential difference of between 2 and 6 kV is maintained between this needle and a spray cap located near the entrance to the vacuum system, creating an electrostatic field in the electrospray chamber. As solution passes through the needle, the charged needle attracts ions of a particular polarity and repels ions of the opposite polarity. Ions repelled from the needle become increasingly charge-concentrated in the solution as the solution passes through the needle. As the charge-concentrated solution is ejected from the needle, the shape of the solution distorts under the
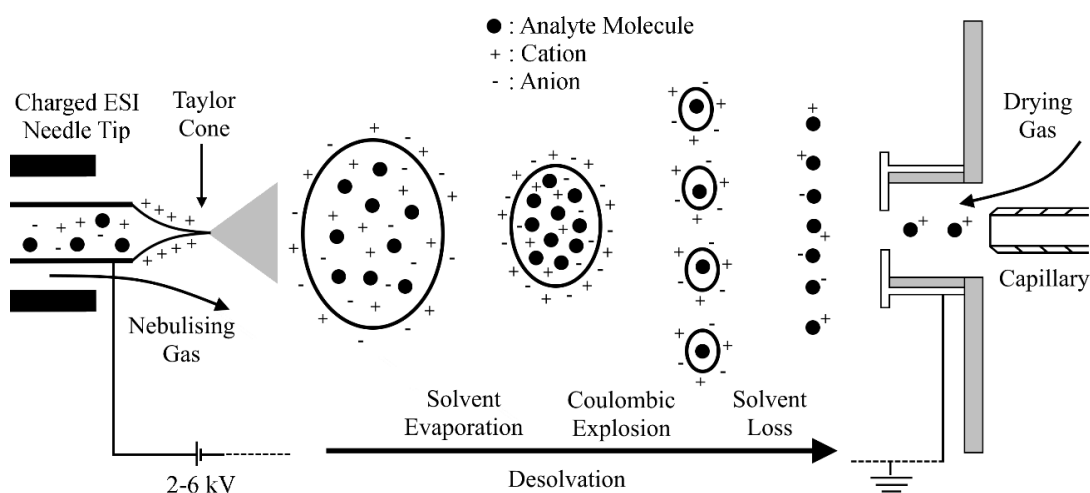
Figure 2.3 Diagram of an electrospray ionisation (ESI) source. Positive and negative charges are included in the droplets to show that ESI can be used to produce gaseous cations or anions.

influence of the electrostatic field into a so-called Taylor cone.[117] The Coulombic repulsion between ions of the same polarity causes the ejected solution to break apart into highly-charged microscopic droplets. The solution is sprayed alongside a nebulising gas (nitrogen) which assists the formation of small droplets. Analyte ions which will be detected by the mass spectrometer are introduced into the gas phase from these charged droplets.

Once in the gas phase, the highly charged droplets are heated using a drying gas (nitrogen) which is flowing in the opposite direction of the droplets. Solvent molecules evaporate from the droplets, decreasing the average distance between ions of the same polarity, increasing the Coulombic stress within the droplets. The point at which the total Coulombic repulsion is the same as the surface tension of the droplets is known as the Rayleigh limit, and when this point is reached the droplets explode into smaller droplets.[118] This process continues until the droplets are small enough for analyte ion desolvation to occur; this is thought to occur from highly charged droplets with nanometre diameters.[115, 119]

It is understood that the mechanism by which analyte ion desolvation occurs is dependent on the analyte ion. Low-mass analyte ions are thought to be transferred to the gas phase according to the ion evaporation model (IEM).[120, 121] Heavy globular species (e.g. folded proteins) are thought to enter the gas phase via the charged residue model (CRM).[112, 122] The mechanisms by which these models lead to the production of isolated ions are again well discussed within the scientific literature and can be found in review articles and books on the electrospray process.[113-116] The molecular and cluster ions studied within this thesis are all low-mass ions and clusters so are likely to be isolated by the IEM.

2.2.3   *Quadrupole Ion Trap (QIT) Mass Spectrometry*

The original quadrupole ion trap (QIT) was designed by Paul and Steinwedel.[123] Figure 2.4 shows a schematic diagram of the trap, which consists of two end-cap electrodes (**1** and **3**) on either side of a ring electrode (**2**). Ions enter the ion trap through one of the end cap electrodes and are stored between the electrodes (**4**). Helium gas is constantly leaked into the ion trap to act as a buffer to ions entering
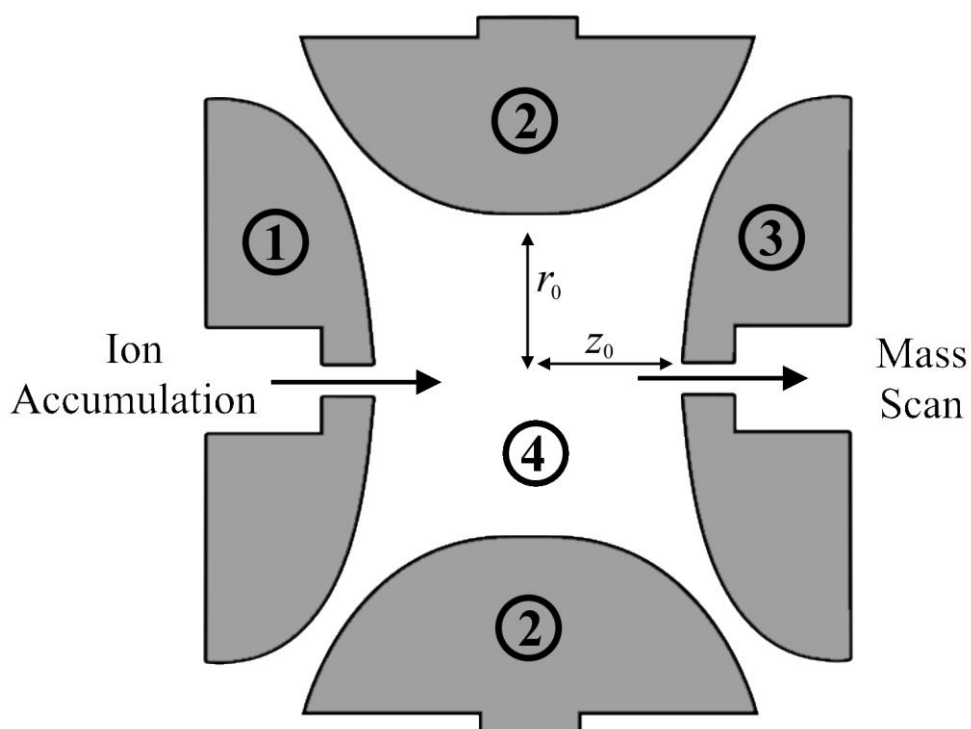
Figure 2.4 Diagram of a quadrupole ion trap (QIT) mass spectrometer, adapted from the AmaZon Manual.[110] **1** is the entrance end cap, **2** is the ring electrode, **3** is the exit end cap, and **4** is the ion cloud and buffer gas.

the trap, the collisions with helium atoms reduces the kinetic energy of the incoming ions which increases the likelihood that the ions will become trapped.

A trapping potential (Φ_0) is applied to the ring electrode, comprising a constant direct potential (U) and an alternating (RF) potential (V). The opposite potential (i.e. -Φ_0) is applied to the two end cap electrodes. Ions which enter the QIT are subjected to the electric field created by these potentials. The equations of motion (EOM) which describe the motion of the ions within the ion trap are dependent on U and V as well as the mass-to-charge ratio of the ions.[124] Ion trajectories can be calculated by integrating the EOMs, this is done by converting the EOMs to the form of the Mathieu equation which has a known integral.[125, 126]
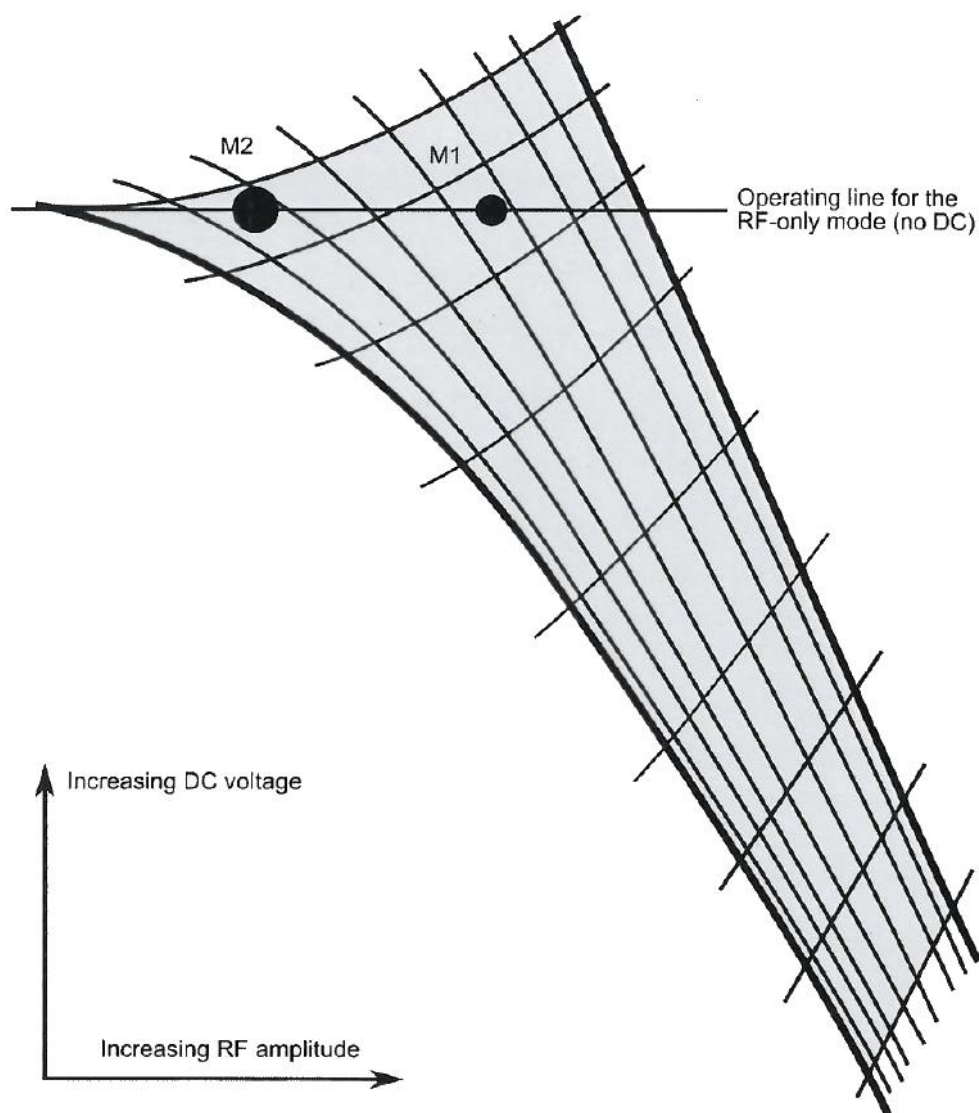
Figure 2.5 Stability diagram for ions in a quadrupole ion trap. Image taken from the AmaZon Manual.[110]

Calculated ion trajectories have been used to determine the range of voltages (U and V) which result in a stable trajectory for an ion with a particular m/z.[127] Stability is defined as a trajectory where the location of an ion does not axially or radially exceed the distance between the centre of the ion trap and the electrodes (r_0 and z_0 for the ring and end-cap electrodes, respectively), an example stability diagram for ions in a QIT is given in Figure 2.5. For a trapped ion with a specific m/z, values of U and V which lie within the shaded area of the curve will result in a stable trajectory. The QIT in the AmaZon mass spectrometer is operated using only an RF voltage (i.e. $U = 0$), so the stability area becomes a line of acceptable RF voltages, which is shown by the horizontal line in Figure 2.5. The values of V which produce stable ion trajectories change with the m/z of the ion, with the maximum voltage resulting in a

stable trajectory being inversely proportional to the m/z of the ion. In practical terms, this feature of the QIT means that there is a maximum m/z range that the QIT can stably trap; this is known more generally as the low-mass cut-off.

The process of recording mass spectra in a QIT follows a repeatable cycle; i.e clear trap, accumulate, isolate, fragment, and mass analyse. The experimental conditions within each of these steps are controlled using the TrapControl software. "Clear trap" is the initial segment which follows a previous mass spectrum acquisition, and this designation means that no ions should be present within the trap. In the accumulation step, ions travelling through the mass spectrometer from the ESI source are allowed through a gate lens and pass into the QIT. The accumulation time can be varied using the TrapControl software to control the number of ions which enter the ion trap.

During isolation, an intense broadband RF field is applied to the QIT, exciting the secular frequencies of all ions in the QIT and causing their trajectories to become unstable. This broadband RF field has a narrow window, such that the secular frequency of an analyte ion with a particular m/z ratio is not excited and remains in the QIT. The m/z ratio and the width of the isolation window are controlled using TrapControl.

During fragmentation, the secular frequency of the isolated ion is gently excited by a narrowband RF field, inductively increasing the kinetic energy of the ions whilst keeping the trajectories stable in the QIT. These ions collide with the helium buffer gas present in the QIT, converting the kinetic energy into internal energy of the ions. Fragmentation and rearrangement can occur if the ions receive enough internal energy to overcome the activation energy for these reactions; this process is commonly referred to as collision induced dissociation (CID).[82, 128] The fragmentation duration, as well as the amplitude of the RF voltage inducing fragmentation, can be controlled using the TrapControl software. Following CID on a parent ion, fragment ions can be isolated and fragmented further; the TrapControl software allows up to ten cycles of isolation and fragmentation. Following fragmentation, ions which are present in the ion trap are sequentially ejected according to their m/z ratio by gradually increasing the RF amplitude (V) of the ion trap.

2.2.4   Modifications made to the AmaZon Mass Spectrometer

The AmaZon mass spectrometer that was used in this thesis has been modified for laser-coupling, to allow gaseous PD experiments to be performed. Figure 2.6 is a labelled diagram of the laser-coupled QIT of the mass spectrometer, showing the modifications made to the mass spectrometer.
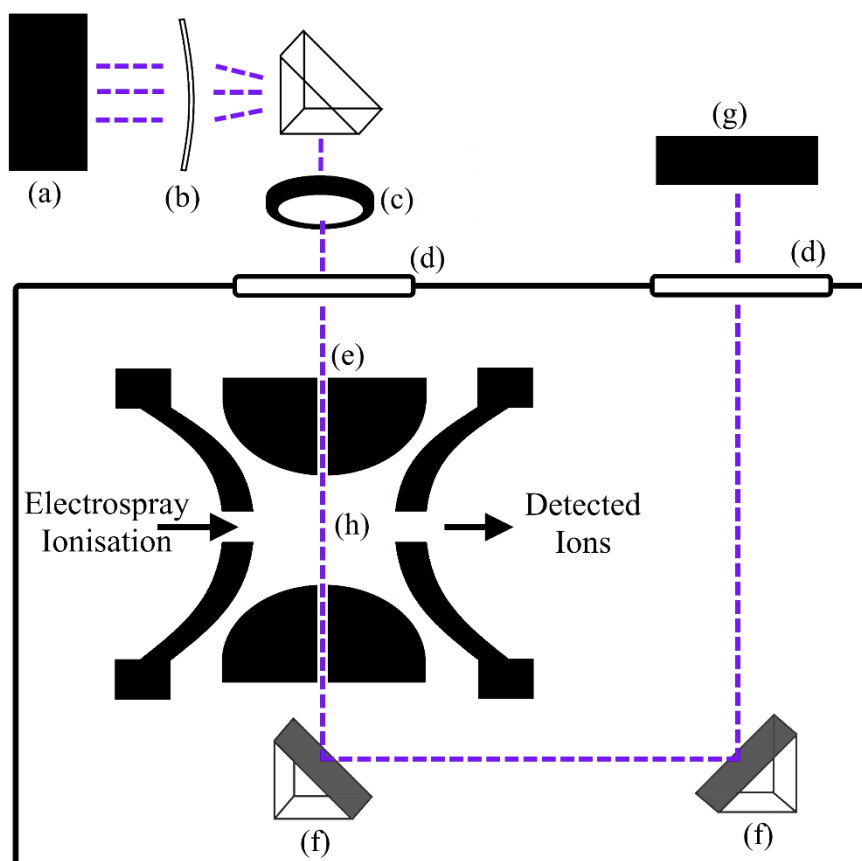
Figure 2.6 Diagram of the modifications made to the QIT mass spectrometer to allow photodissociation spectra to be recorded. Where (a) is a Nd:YAG pumped OPO tuneable laser source; (b) is a 200 mm focal length UVFS lens (LE4467-UV, Thorlabs Inc.); (c) is an optical shutter (Model SH05, Thorlabs Inc.); (d) is a pair of flange mounted uncoated UVFS windows (WG41050, Thorlabs Inc.); (e) is a 2 mm hole drilled through the ring electrode of the ion trap to allow the passage of laser light; (f) is a pair of aluminium mirrors (PF05-03-F01, Thorlabs Inc.); (g) is a UV-Vis spectrometer (USB2000+ UV-VIS, Ocean Optics Inc); and (h) is the centre of the ion trap where photodissociation occurs. Image adapted from Reference 14.

Figure 2.6 shows that two uncoated UV fused silica (UVFS) windows (d) are present in the upper flange of mass spectrometer. The windows are transparent to UV and visible light which allows the laser beam to pass in and out of the vacuum chamber. To accommodate these windows, two holes were machined into the upper vacuum flange of the mass spectrometer which fit a KF-16 centring ring. A stainless steel centring ring (with an attached O-ring) is placed on top of each hole, the centring rings only extend downwards which allows the UVFS windows to be placed directly on top of the O-ring. The seal made between the UVFS window, the O-ring and the vacuum flange prevents air from leaking into the high-vacuum chamber of the mass spectrometer.

The location of the first window is directly above the QIT. A hole has been drilled through the ring electrode of the QIT (e), to allow the laser to pass through the ion trap. The holes are tapered, with a diameter of 6 mm at the edge of the ring electrode which reduces to 2 mm towards the centre of the QIT. The tapered hole minimises the flow of the helium buffer gas out of the QIT, thus maintaining optimum trap performance.

The QIT is located above an aluminium mirror (f) which is highly reflective across the range 220 nm – 20 µm. This first mirror reflects the laser beam towards a second aluminium mirror (f) which reflects the laser beam out of the vacuum chamber through the second UVFS window (d). The pair of mirrors are used to facilitate the alignment of the laser through the trap.

In addition to the modifications made within the mass spectrometer, several threaded holes have been inserted in the structural housing that contains the mass spectrometer. The threaded holes have been used to secure an optical breadboard on top of the mass spectrometer, enabling the placement of optical mounts and the manipulation of the laser beam between the OPO laser and the mass spectrometer. The optical components shown in Figure 2.6 include a lens (b) which is positioned such that the focal point of the lens is within the centre of the ion trap (h). Additionally, a mechanical shutter (c) is used selectively to block or transmit the laser light from the OPO laser (a) into the ion trap. A spectrometer (g; USB2000+ UV-VIS, Ocean Optics Inc) is used to verify the wavelength which is produced from the OPO laser.

The optical route between the laser and the mass spectrometer is described in Section 2.3.3.

2.3   Nd:YAG pumped OPO used to produce photons in the photodissociation spectroscopy experiment

2.3.1   The Nd:YAG Pump Laser

A neodymium-doped yttrium aluminium garnet (Nd:YAG, $Nd:Y_3Al_5O_{12}$) laser (Surelite, Continuum) was used in the PD mass spectrometry experiment to pump an OPO laser. Nd is present in the YAG rod as trivalent Nd^{3+} and this ion is responsible for the lasing properties of the YAG rod. Figure 2.7 is a four-level energy scheme that shows the important transitions involved in the laser activity of Nd^{3+}. In this scheme, Nd^{3+} ions that are present in the electronic ground state ($^4I_{9/2}$) can absorb light to become electronically excited ($^4F_{3/2}$); the light that excites this transition is supplied by flashlamps which surround the YAG rod. This excited state relaxes, without emission, into another excited state ($^4F_{3/2}$) which can decay by emitting a 1064 nm photon to another electronic state ($^4I_{11/2}$). This state can then decay to the electronic ground state without emitting radiation.
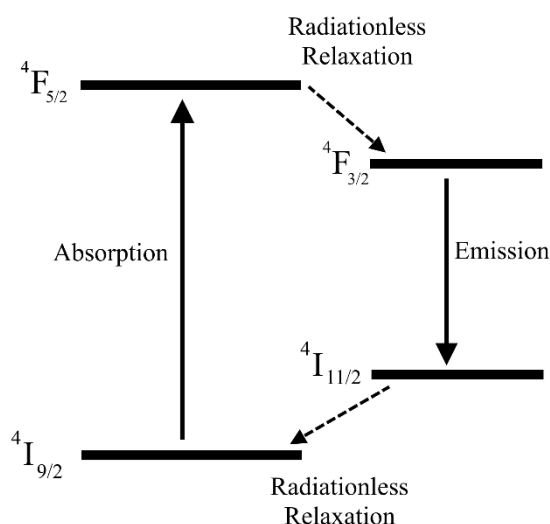
Figure 2.7 Simplified diagram of the energy levels involved in the emission of 1064 nm light by a Nd^{3+}:YAG laser.

For the trivalent Nd^{3+} ions, the excited electronic state with the longest lifetime is $^4F_{3/2}$. This means that a population inversion is created between the $^4F_{3/2}$ and $^4I_{11/2}$ electronic states in the YAG rod. The radiative decay of this excited state can be stimulated by a photon with the same energy as this transition, and this is the origin of the lasing properties of the Nd:YAG rods. The flashlamps irradiate the YAG rod with a repetition rate of 10 Hz, meaning that the population inversion of the Nd^{3+} ions and subsequent lasing of the YAG also occurs with a repetition rate of 10 Hz.

The YAG rod and flashlamps are held in a Q-switch which stops the laser from releasing a laser pulse unless a voltage is applied to a Pockels cell. A diagram showing the activity of a Q-switch either to prevent or enable the output of laser light from the laser chamber is given in Figure 2.8. The second and third harmonics (532 and 355 nm, respectively) of the fundamental laser output (1064 nm) are generated by frequency doubling and sum frequency mixing the fundamental and second harmonics of the laser. The efficiency of these processes is controlled manually using an adjustable knob which changes the orientation of the crystals which produce the laser harmonic frequencies. 1.8 mJ of the third harmonic (355 nm) is required to efficiently pump the OPO laser.
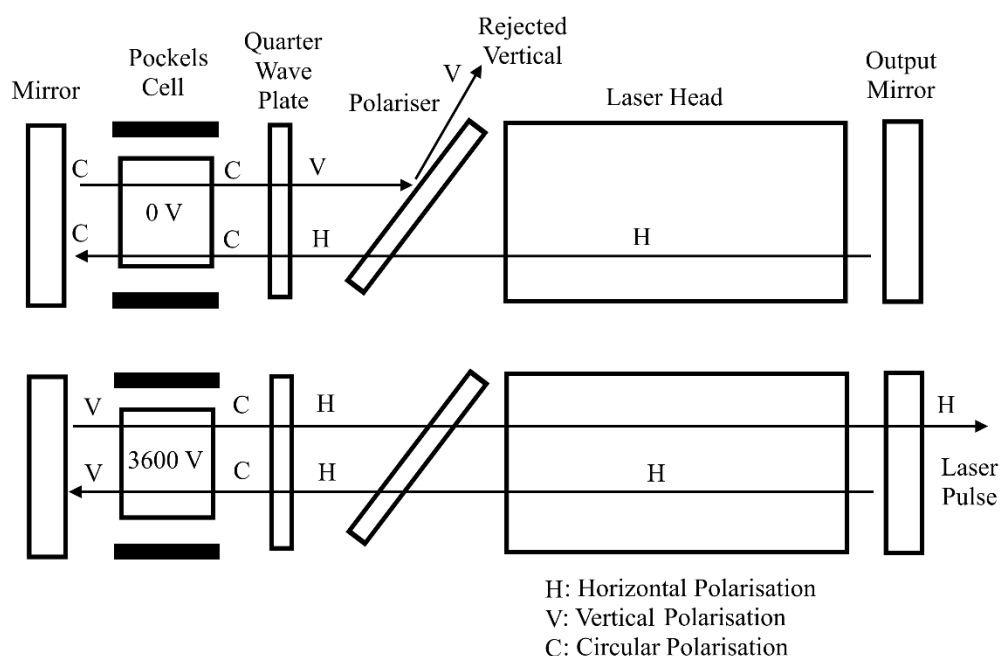
Figure 2.8 Diagram of the Q-switch used to produce laser pulses in the Surelite Nd:YAG laser. Image adapted from the Surelite manual.

2.3.2   Horizon Optical Parametric Oscillator (OPO) Laser

The laser that has been used in this thesis to produce an adjustable and tuneable supply of photons is an Nd:YAG pumped optical parametric oscillator (OPO) laser (Horizon, Continuum). An optical parametric process is a three-photon interaction, where a single photon (the pump) is split into two low-energy photons, where the higher-energy photon is called the signal and the lower-energy photon is called the idler. For this process to occur, the energy and momentum of the initial photon must be conserved in the two photons that are produced, as shown in Equations 2.1 and 2.2:

$$E_{\text{pump}} = E_{\text{signal}} + E_{\text{idler}}$$

Equation 2.1

$$\mathbf{k}_{\text{pump}} = \mathbf{k}_{\text{signal}} + \mathbf{k}_{\text{idler}}$$

Equation 2.2

where E is the energy of the photon and $\mathbf{k}$ is the photon's momentum vector. The OPO process can occur in non-linear optics, and β-barium borate (BBO, BaB_2O_4) crystals are used within the Horizon OPO laser. The angle the pump beam makes with respect to the optical axis of the crystal determines the frequencies of the signal and idler that are possible for momentum to be conserved. Accurately controlling the rotation of the BBO crystals therefore allows the Horizon OPO laser to be used as a tuneable laser source.

The routes that the photons take through the OPO laser to produce different wavelengths are given in Figure 2.9, and a legend for the numbered components is given in Table 2.1. The OPO process occurs within the box housing BBO crystals 10 and 11, and these crystals are used to split the third harmonic of the pumping Nd:YAG (355 nm). The signal and idler are directly emitted from the laser through
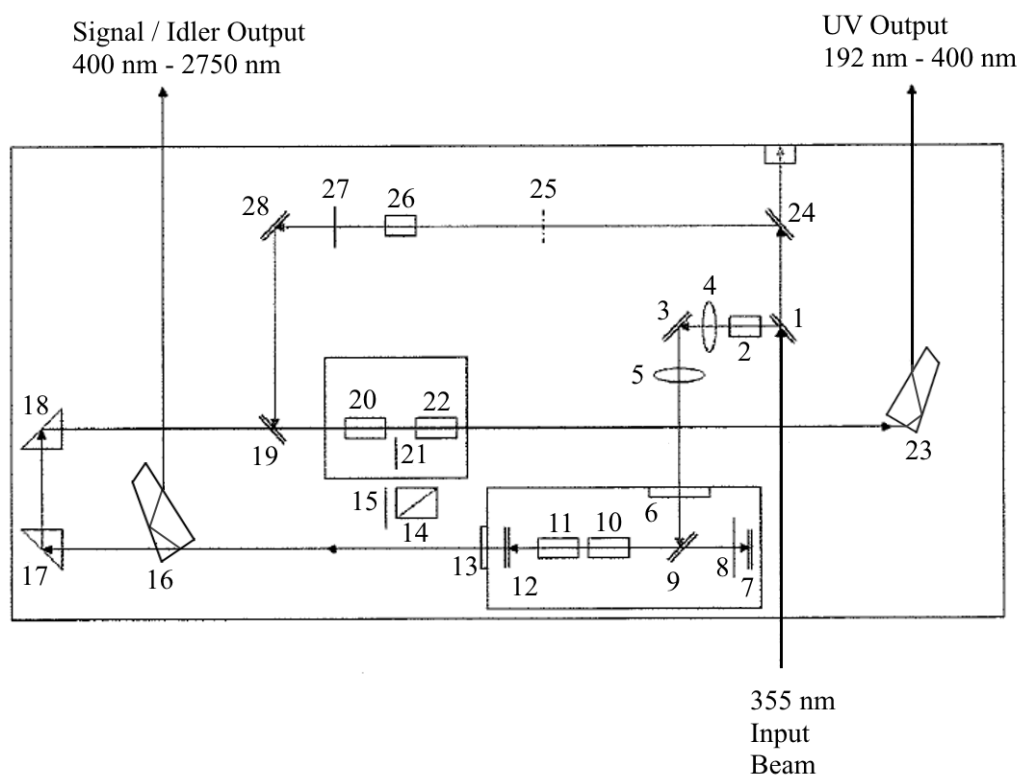
Figure 2.9 Horizon OPO optical layout. Image adapted from Horizon manual. A legend to the optical elements is given in Table 2.1. Components 14 and 26 are optional optics which are not present in the Horizon laser used in this thesis.

---

the left exit port, when scanning the laser between 400 and 2750 nm. A Pelin Broca prism on a rotating stage is used to ensure that the different wavelengths which can be produced by the OPO process exit the laser with exactly 90° of reflection.

UV photons are prepared by processing the signal/idler in the BBO crystals labelled 20 and 22. This is done by frequency doubling the signal/idler photons, or by sum-frequency generation between the signal/idler and the Nd:YAG fundamental wavelength (1064 nm). The fundamental is overlapped with the pathway of the signal/idler by reflecting the fundamental on optics 24, 28 and 19. The UV photons are emitted from the laser through the right exit port of the OPO laser, a Pelin Broca prism is used to ensure the UV photons are reflected by exactly 90°. The OPO laser can produce UV photons ranging between 192 and 400 nm.

Table 2.1 Legend to the Horizon OPO components used in Figure 2.9. Data taken from the Horizon manual.

Legend to Horizon OPO Layout			
Description	**Item Number**	**Description**	**Item Number**
355 nm Dichroic Mirror	1, 3	BBO Crystal	10, 11, 20, 22
Half Wave Plate	2a, 8, 15, 27	Mirror	12, 19, 24, 28
Polariser	2b, 14, 26	Pelin Broca Prism	16, 23
Lens	4, 5	90 Degree Prism	17, 18
Window	6, 13	Waveplate	21
Porro Prism	7	Beam Dump Assay	25
Injection Pump Mirror	9		

The OPO laser is connected to a workstation via USB and is controlled through commercial software. This software is used to control the output wavelength of the laser and to attune the laser power at each wavelength. Step-motors controlling the orientations of the BBO crystals (optics 10, 11, 20 and 22) and the Pelin Broca prisms (optics 16 and 23) are used to control the alignment and power of the laser, the OPO has been calibrated to produce an average pulse energy of ~1 mJ at each wavelength between 650 – 220 nm. When recording laser scans in different wavelength regions of the OPO laser, it is necessary to adjust the position of three optical elements, labelled optic 15, 21 and 25.

2.3.3   *The optical route between the OPO laser and the mass spectrometer*

A labelled picture of the experimental apparatus is given in Figure 2.10. The optical routes taken by the UV and visible/near-IR (NIR) photons are given in the upper and lower images, respectively. UV photons enter the optical bench from the OPO laser
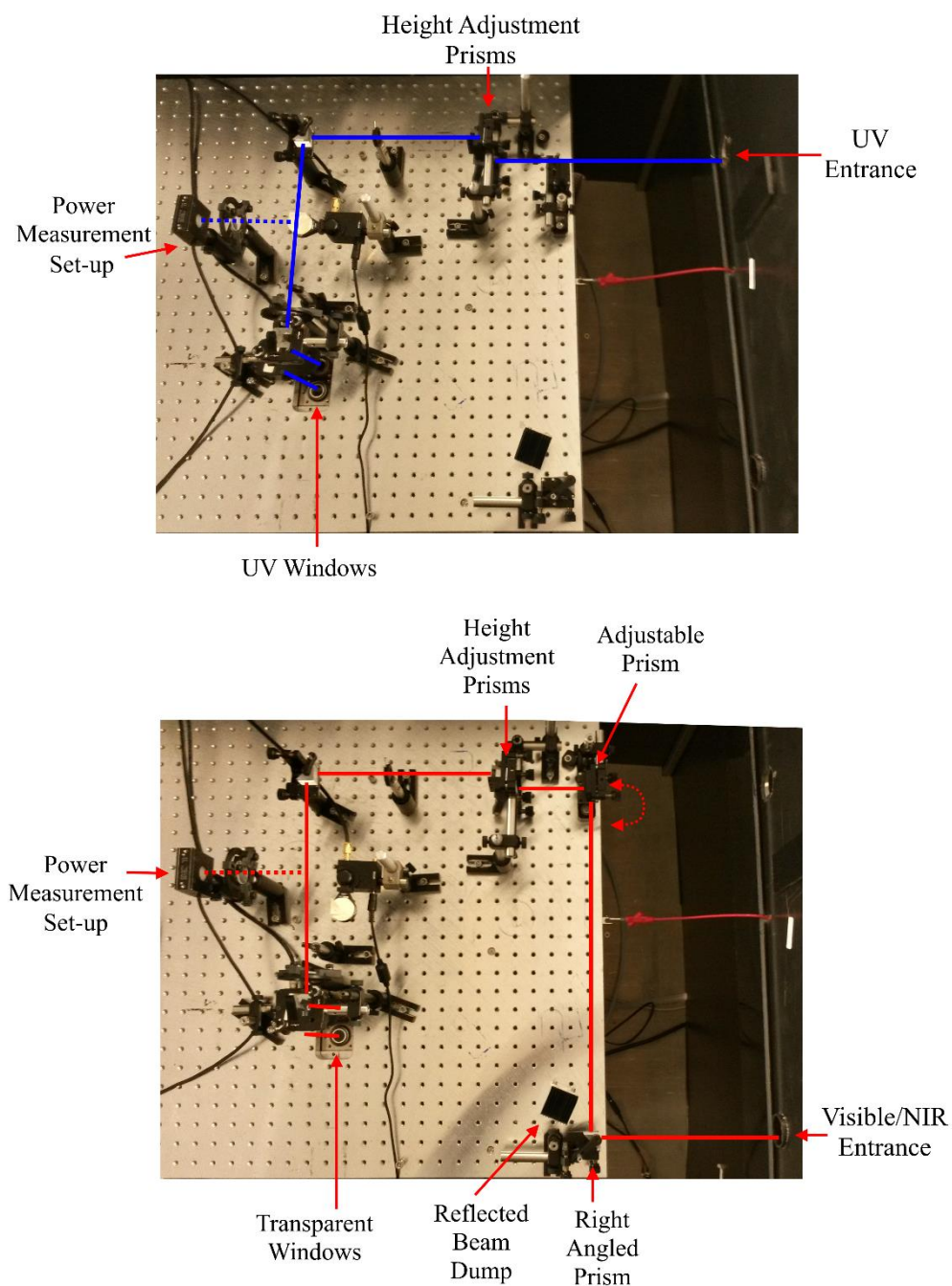
Figure 2.10 Labelled pictures of the optical bench housed above the AmaZon mass spectrometer, showing the path of the (top) UV (193 - 400 nm) and (bottom) visible/NIR (400 - 2700 nm) light between the OPO laser and the optical interface of the mass spectrometer.

through a tube. The height of the incoming laser beam is adjusted using a pair of right-angled UV fused silica prisms which act as a periscope. The height of the laser beam is adjusted from ~4 cm to ~12 cm above the optical table, which makes the future manipulation of the beam easier. The height-adjusted laser beam hits a right-angled prism and is reflected by 90° towards the mass spectrometer. A more detailed view of the route between this right-angled prism and the mass spectrometer is given in Figure 2.11.

The pathway of the visible/NIR light in the optical bench is given in the lower part of Figure 2.10. Light enters the optical bench through a tube connected to the OPO laser. The incoming laser beam is manipulated to overlap with the route taken by the UV laser using a pair of right angled prims. The second right-angled prism can be moved in and out of place, either to enable the transmission of UV or visible/NIR light. After passing through the adjustable right-angled prism, the visible/NIR laser beam follows the same path through the optical bench as the UV laser.

Figure 2.11 is a zoomed picture of the optical elements which follow the height adjustment prisms on the optical bench. Laser pulses (UV, visible or NIR) enter this region through an iris (a) and are reflected 90° by the first right-angled prism (j). If the adjustable prism (b) is in the pathway of the laser (as shown in Figure 2.11) then the laser will be reflected towards the power meter (h), passing through a lens (i) on the route. If the adjustable prism does not block the laser beam exiting the right-angled prism then the laser will be directed to a right-angled prism (d) positioned directly above the QIT of the AmaZon mass spectrometer. On this route, the laser passes through an iris (c) and lens (g). The right-angled prism (d) reflects the laser beam straight down towards the mass spectrometer (e). The laser passes through an optomechanical shutter (f) and a transparent window (see Section 2.2.4) to enter the mass spectrometer (e), and light is reflected out of the mass spectrometer through a second transparent window (see Section 2.2.4 for details).
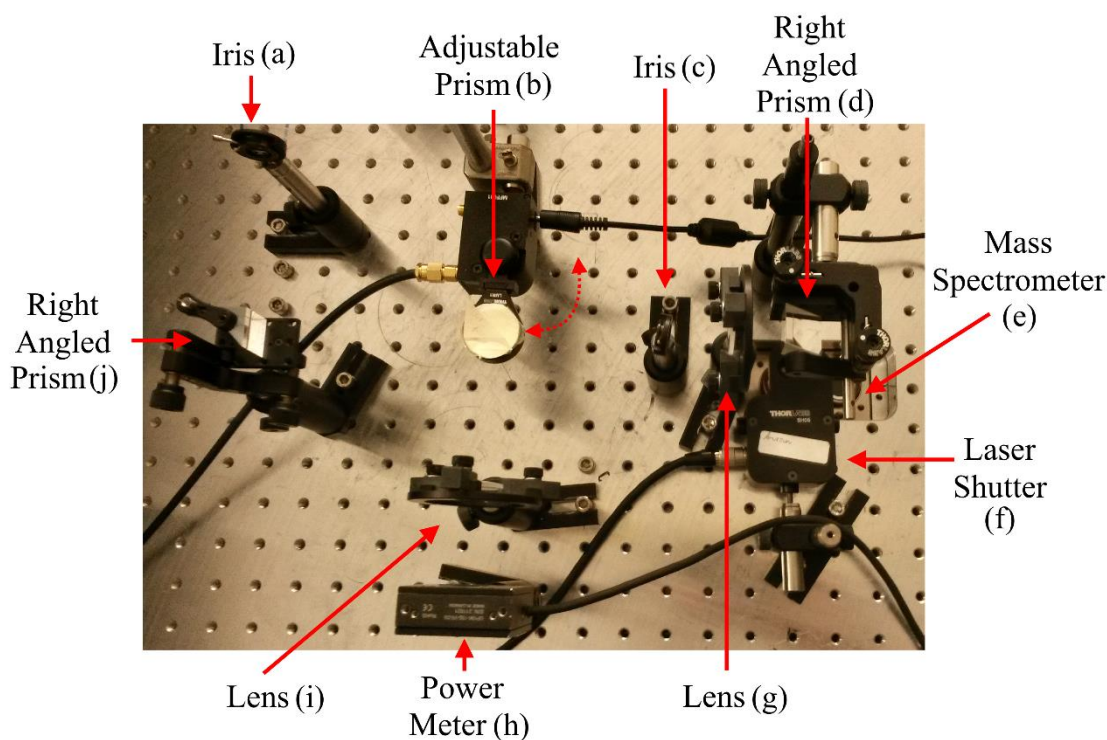
Figure 2.11 Labelled picture of the optical bench on top of the AmaZon mass spectrometer, showing the region of the table containing the power measurement set-up as well as the optical interface of the mass spectrometer.

The adjustable prism (b) is attached to a motorised flip mount (Model MFF001, Thorlabs Inc) which has two possible orientations which differ by 90º (i.e. one position reflecting the beam towards the power meter and one position out of the path of the beam). The flip mount switches between these two orientations when it receives a 5V TTL (transistor-transistor logic) signal. A home-written LabVIEW virtual instrument (VI) is used to command a data acquisition (DAQ) device (Model USB-6211, National Instruments) to output a 5V TTL signal to the motorised flip mount, thereby allowing the position of the adjustable prism (b) to be controlled from a workstation.

The head of the power meter is connected to a controller which monitors the average power of the laser. The power meter has an analogue output port which outputs between 0 and 1 V depending on the ratio between the power of the laser and the maximum power that can be recorded on the power meter. This output port is connected to an analogue input pin of the DAQ which samples the incoming voltage

at a rate of 1000 Hz. A home-written LabVIEW VI is used to average the voltages over three seconds and convert the voltage to the average power of the laser (by multiplying the voltage by the maximum power the power meter can record) and then to the average energy within each laser pulse (by dividing by the repetition rate of the laser). The VI can also export the most recent value of the pulse energy, providing a digital record of the laser power when performing laser PD experiments.

The laser shutter (Model SH05, Thorlabs Inc.), used to control the transmission of light through the QIT, is triggered by an external TTL signal. When the TTL voltage is 0 V the shutter closes and when the TTL voltage is 5 V the shutter opens. The shutter is connected via a BNC cable to a benchtop shutter controller (Model SC10, Thorlabs Inc.) which supplies this TTL signal. For mass spectrometry PD experiments, the shutter controller is operated in its external gate (X Gate) mode, where the shutter controller receives a TTL signal from the AmaZon mass spectrometer. This signal leads to the opening and closing of the shutter. Details of the timing of this signal will be given in Section 2.5.

2.4   UV Photodissociation Spectroscopy

2.4.1   Gaseous Absorption in Photodissociation Experiments

In solution-phase electronic absorption spectroscopy, absorption (A) is measured in a spectrophotometer by recording the depletion in light intensity that a molecule or ion in solution causes when passing a laser through that solution, according to the Beer-Lambert law (Equation 2.3):

$$A(\lambda) = \ln\left(\frac{I_0}{I}\right) = \varepsilon(\lambda) \cdot c \cdot l$$

Equation 2.3

where I and I_0 are the intensities of monochromatic light, with and without passing through a solution sample, respectively, $\varepsilon(\lambda)$ is the molar absorption coefficient at wavelength λ, c is the solution concentration and l is the path length.

The Beer-Lambert law is useful for measuring the absorption of molecules in solution, however, in gaseous photodissociation experiments, electronic absorption cannot be measured directly from changes in the intensity of the excitation laser. This is because the number of ions that can be stored in ion traps is sufficiently low ($<10^8$ cm^{-3}) that directly measuring the depletion in the laser intensity is technically not possible.[25] Absorption cross sections are instead quantified using action spectroscopy, where absorption is approximated by measuring a photochemical change in the gaseous ions following interaction with light. The photochemical reaction that occurs upon UV absorption must result in the depletion of the gaseous species, either by fragmentation or electron detachment, or the population of ions will not change upon absorption.

A formalism for determining an absorption cross section (σ) in photodissociation experiments, derived from the Beer-Lambert law, was first established by Brauman and Smyth whilst studying the photodetachment of the hydroxide anion (Equation 2.4):[11]

$$I(t) = I_0 \exp\left(-\, tf \int \sigma(\lambda)\rho(\lambda)\, d\lambda\right)$$

Equation 2.4

Where I_0 and $I(t)$ are the intensity of an ion without irradiation and after being irradiated for duration t, respectively, f is the geometrical overlap factor between the light beam and the ions, $\sigma(\lambda)$ is the absorption cross section at wavelength λ, and $\rho(\lambda)$ is the photon flux. The integral is over the wavelength range that is used to dissociate the ions. The experiment by Brauman and Smyth used a continuous-wave (cw) laser with a broad spectral output, whereas the Nd:YAG pumped OPO laser used in this thesis is a 10 Hz pulsed laser which is tuneable and has a narrow linewidth. Using pulsed lasers also ensures that the gaseous ions can be irradiated by a set number of laser pulses, which provides a large degree of control over the irradiation time of the ions. If the overlap between the ion packet and the laser pulse is assumed to be constant at every wavelength and the ions are irradiated by a single laser pulse then Equation 2 can be simplified and rearranged to give the absorption coefficient (Equation 2.5):

$$\sigma(\lambda) = \ln\left(\frac{I_0}{I}\right)\Big/\rho(\lambda)$$

<div align="right">Equation 2.5</div>

where I_0 and I are the intensities of a gaseous ion without and with irradiation, respectively, and these values can be determined by recording mass spectra of the precursor ion with and without irradiation. If the profile and duration of each laser pulse is assumed to be the same, then the photon flux, $\rho(\lambda)$, can be approximated by the average number of photons per pulse. The number of photons per pulse is proportional to the product of the average laser pulse energy and the wavelength of the laser (λ). The average laser pulse energy is calculated from the laser power measurements, described in Section 2.3.3. Using Equation 2.5, the approximate gaseous absorption coefficient (otherwise known as the photodepletion) of an isolated ion can be recorded at every wavelength accessible to the OPO laser and compiled into a gaseous absorption spectrum. Photodepletion is equivalent to gaseous absorbance when the laser power is sufficiently low that only one-photon absorption occurs and that every absorption event results in the depletion of that ion.

2.4.2   Gaseous Photofragmentation Mechanisms

Gaseous fragmentation reactions are well known in the field of mass spectrometry.[128, 129] The fragmentation patterns of ions which are ionised by electron ionisation (EI) or fragmented in the gas phase using techniques such as collision-induced dissociation (CID) are routinely used to determine gaseous ion structures.[130] In a PD experiment, the total absorbance of an ion is recorded by measuring a depletion in ion intensity that is caused by laser irradiation, with the mechanisms by which depletion occurs being ionic fragmentation (Equation 2.6) and electron detachment (Equation 2.7). If these fragmentation pathways produce an ionic species, then the ionic fragment will be observed in the photofragment mass spectrum. (The AmaZon mass spectrometer can only detect ions with m/z greater than 50, therefore ionic fragments with m/z less than 50 will not appear in photofragment mass spectra.)

$$M^{+(-)} + h\nu \rightarrow A^{+(-)} + B$$

<div align="right">Equation 2.6</div>

$$M^{n-} + h\nu \rightarrow M^{(n-1)-} + e^{-}$$
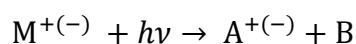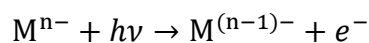
<div align="right">Equation 2.7</div>

Ionic fragmentation can occur following electronic excitation via two general mechanisms: fragmentation in a weakly-bound or dissociative excited state; or fragmentation in a vibrationally excited electronic ground state, these two processes are summarised in Figure 2.12. Upon electronic excitation, the potential energy surface of the initially accessed excited state, or a subsequently accessed excited state, may be repulsive with respect to a bond coordinate. If the excited-state lifetime of the dissociative excited state is longer than, or comparable to, the time taken for unimolecular dissociation to occur along the repulsive surface then excited-state fragmentation will occur.[131]
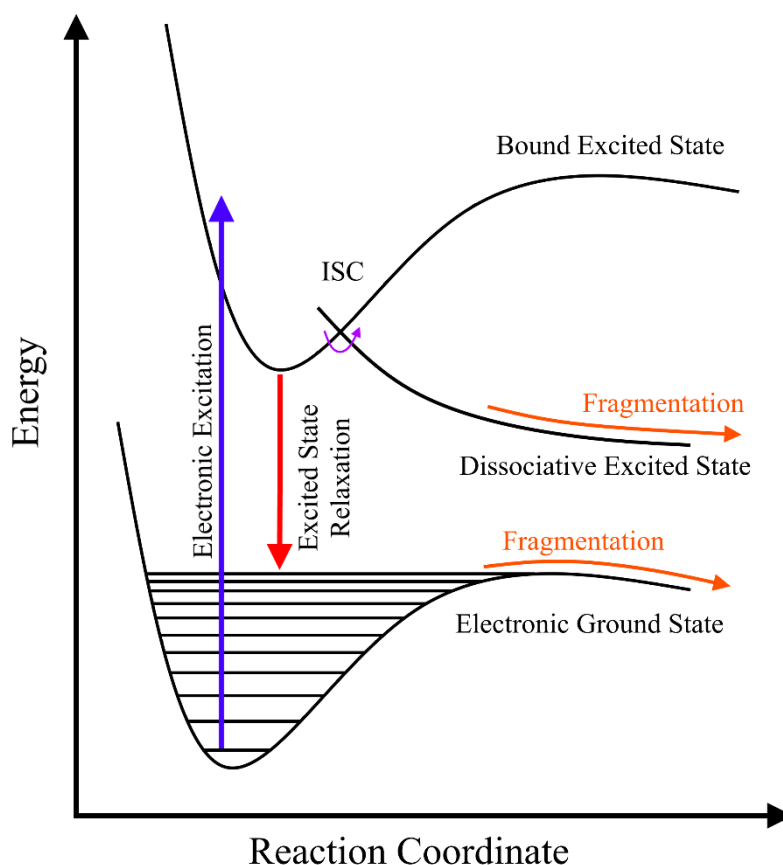
Figure 2.12 Schematic potential energy surfaces of a gaseous molecule showing fragmentation mechanisms in the excited state and the electronic ground state. ISC: intersystem crossing.

If instead the fastest excited-state deactivation pathway is non-radiative relaxation to the electronic ground state, then the ionic fragmentation will occur in a vibrationally excited electronic ground state.[45]   In the solution phase, such states undergo vibrational relaxation via collisions with solvent molecules. Vibrational relaxation is not possible in the gas phase (aside from collisions with the helium buffer gas) and so the vibrationally hot molecules dissipate the excess internal energy via fragmentation. UV-Vis PD resulting in fragmentation in the electronic ground state is often comparable to other ground-state fragmentation experiments such as CID or infrared multiphoton dissociation (IRMPD).

Electron detachment is an important mechanism by which the population of gaseous anions can be depleted in PD experiments. This can occur if anions are irradiated with photons that possess more energy than the binding energy of the excess electron. For monoanions, photo-induced electron detachment produces a neutral molecule and electron. The neutral molecule cannot be detected by mass spectrometric methods and so electron detachment cross-sections can only be measured from the photodepletion.[55] Electron detachment from multiply-charged anions (MCAs), however, produces an anionic species that can be detected through mass spectrometry. MCA electron detachment is more complicated than monoanionic detachment because a photon must have enough energy to overcome the electron binding energy and a repulsive-Coulomb barrier (RCB) associated with the two excess charges.[8, 23, 132, 133]

The intensities of ionic photofragments (and ionic electron detached fragments) are recorded alongside the intensities of the parent ions in the PD mass spectra which are used to calculate photodepletion. This means that the intensities of all of the photofragments can be tracked as the output wavelength of the laser is scanned. These intensities can be used to calculate the photofragment production intensities (PF) according to Equation 2.8:

$$\text{PF} = \left(\frac{I_{\text{Frag}}}{I_0}\right)\bigg/\rho(\lambda)$$

Equation 2.8

38

where I_{Frag} is the intensity of a fragment ion. I_0 and $\rho(\lambda)$ are the parent ion intensity without irradiation and the photon flux, respectively. The photofragment production intensities of a fragment are collated and presented as production spectra, which show the change in production with the changing wavelength of the laser. PF spectra can resolve different absorption spectra (i.e. for different m/z fragments) if multiple chromophores are present, this can be different from PD spectra which are a sum of every absorption process which leads to fragmentation or electron detachment. Differences between PD and PF spectra arise when fragments are only produced following specific excitations, or when a distribution of structural isomers are present in the gas phase.

2.4.3   Multiphoton Processes in Photodissociation Experiments

As was stated earlier, PD best approximates gaseous absorption coefficients when gaseous absorption and fragmentation arises from one-photon absorption. This is because absorption features that result from non-resonant multi-photon absorption will appear in absorption (PD) spectra with transition energies n times lower than the true excitation energy, where n is the number of photons involved in the excitation; the probability of n-photon absorption occurring is proportional to the photon flux to the power of n.[134] The total depletion of a gaseous ion at any wavelength can therefore be written as a power series of PD that result results from single- and multi-photon processes according to Equation 2.9:

$$\ln \frac{I_0}{I} = \sigma(1\text{PA}, \lambda) \times \rho(\lambda) + \sigma(2\text{PA}, \lambda) \times \rho(\lambda)^2 + \sigma(3\text{PA}, \lambda) \times \rho(\lambda)^3 \dots$$

<div align="right">Equation 2.9</div>

where $\sigma(n\text{PA})$ are the gaseous absorption cross sections of n-photon absorption at wavelength λ and ρ is the photon flux at wavelength λ. The relationship between power and the probability of multiphoton absorption occurring means that multiphoton effects can be probed by performing power studies. In a power study, the depletion of ions, i.e. $\ln(I_0/I)$, is recorded at a single wavelength as the power of the laser is changed. A plot of depletion against laser power can fitted to a polynomial

function, with the coefficients of the different powers showing the relative contributions of the different *n*-photon absorption processes. If the power plot is linear, then photodepletion occurs under one-photon conditions. If multiphoton absorption occurs, then the contribution of the absorption can be determined from the gradient of a log-log plot of power against PD.[134]

Multiphoton effects can also affect the intensities of fragment ions because these initially formed fragments may be chromophores in the same absorption regions as the parent ion. Fragment absorption (referred to as secondary absorption) will result in the fragmentation of the primary fragment ions into secondary fragments. Secondary absorption can be probed using laser power studies, since the probability of fragments absorbing will increase as the power of the laser is increased. Fragment ions which do not absorb photons and then fragment will follow the same relationship as PD since more depletion results in more fragmentation. Fragments which do absorb photons will decrease in intensity (or barely change intensity) as the power of the laser is increased.

2.5 Laser photodissociation mass spectrometry methods and experimental protocol

The previous sections of this methods and theory chapter have described the various pieces of hardware that are used to collect photodissociation – mass spectrometry data and the theory behind recording ion absorption spectra in the gas phase. This section will describe the methods and protocols used within the experiment to collect, extract and process mass spectrometry data. The mass spectrometry data include: total ion mass spectra; CID mass spectra; scanning-wavelength PD mass spectra; and fixed-wavelength laser power PD mass spectra.

2.5.1   General Mass Spectrometry Methods

The isolated ions and clusters that have been studied in this thesis have all been introduced to the gas phase via ESI (Section 2.2.2). Solutions for ESI were prepared by dissolving the specific molecules and complexes in an ESI compatible solvent (water, methanol, acetonitrile) with a concentration between 10^{-4} and 10^{-6} mol dm^{-3} (details for the individual systems will be given in the relevant results sections). Solutions were injected into the AmaZon mass spectrometer, through the inbuilt ESI apparatus, using a 1 cm^3 syringe connected to the ESI needle by PEEK tubing. For the light-sensitive solutions, aluminium foil was wrapped around the volumetric flasks used to store the solutions as well as the syringe used for ESI. ESI source conditions (e.g. solution flow rates, voltage applied to the needle, nebulising gas pressure, dry-gas flow rate, and dry-gas temperature) were adjusted using the TrapControl software for each system to provide an intense and stable flow of analyte ions to the ion trap, details for each ion studied in this thesis will be in the relevant methods sections of each results chapter. The voltages applied to the ion optics leading to the QIT were optimised to provide the largest number of analyte ions for each species that was studied. This was achieved using the automated tuning capabilities of the TrapControl software.

Total ion spectra (TIS) of the ions produced by electrospray have been collected to determine the nature of the species that are produced via ESI. The ions studied in Chapters 3-5 were either protonated or deprotonated, so these species appear with a

m/z offset by 1 mass unit when compared with the molecular weight of the respective neutral molecule. In Chapter 6, dianionic clusters of $PtCl_6^{2-}$ and a nucleobase were studied, and these appear with an m/z of half of the combined molecular weight of the components. The identities of analyte ions and clusters were verified by comparing the isotopic distribution patterns in the TIS with simulated isotope patterns.

Once verified, ions on interest were isolated and fragmented using CID. The isolation conditions varied with the ionic species being studied, however, ions were generally isolated twice before performing fragmentation experiments. To do this, the QIT was first set to isolate ~1 m/z less than the m/z of the analyte with a mass width of ~2 m/z, and then following this, the QIT isolated ~1 m/z above the m/z of the analyte with a mass width of ~2 m/z. This procedure was used to provide molecular and isotope purity within a CID or photodissociation experiment. This procedure could not isolate a single isotope of the dianionic $PtCl_6^{2-}$ clusters which have an m/z difference of 0.5 between isotopes. Deviations from this approach will be specified in the relevant results sections when they occur.

CID mass spectra were recorded on ions isolated in the ion trap by exciting the secular frequencies of the ions of interest with a RF voltage which has an amplitude ranging between 0 and 2.5 V; CID voltages were controlled using the TrapControl software. The identities of CID fragments have been assigned by determining the neutral losses which are required to produce a fragment. For the $PtCl_6^{2-}$ nucleobase clusters, the CID voltages have been scanned to produce CID fragmentation spectra which are used to compare the relative binding energies of the different clusters.

The AmaZon's QIT can be operated in three different scan modes: ultrascan has a mass range of 70 – 2200 m/z with a scan rate of 32500 m/z s^{-1}; enhanced resolution has a mass range of 50 – 2200 m/z with a scan rate of 8100 m/z s^{-1}; and extended mass range has a mass range of 200 – 4000 m/z with a scan rate of 27000 m/z s^{-1}. The scan rate is inversely proportional to the mass resolution of the mass spectrometer, and the enhanced resolution scan mode was used within all mass spectrometry experiments to provide the most accurate data.

2.5.2   Photodissociation Mass Spectrometry Methods

The absorption cross sections (photodepletion) of the gaseous ions studied in this thesis were calculated by comparing the intensities of the gaseous ions with and without irradiation, according to Equation 2.5. These intensities were taken from PD mass spectra.

As was shown in Section 2.2.4, the AmaZon mass spectrometer has been adapted to perform laser photodissociation experiments by having an optical route through the QIT. For the purpose of calculating gaseous absorption coefficients, it is necessary to only allow the laser to pass through the QIT when the analyte ions have been mass isolated, such that the ensuing photofragmentation relates to the analyte ion. Additionally, mass spectra must be recorded on the isolated analyte ions without irradiation. A mechanical shutter is used to control the transmission of the laser through the ion trap (described in Section 2.3.3); when open, the pulsed laser can pass through the QIT and fragment ions, but when closed, the laser is dumped onto the shutter and the ions in the QIT are not fragmented.

The AmaZon mass spectrometer can output a TTL signal from the front external interface of the mass spectrometer, which can be set to trigger at any stage of the QIT cycle: (e.g. clear trap, accumulation, isolation, fragmentation). The mass spectrometer selectively outputs a TTL signal only within the fragmentation stage of the QIT cycle, and this is set to occur for single isolation (MS) and multiple isolations (MS/MS and MS^n). The laser is therefore only allowed to pass through the QIT when an analyte ion has been isolated and is being stored for fragmentation, with the fragmentation voltage set to 0 V. The absence of a CID voltage means that any fragmentation or parent ion depletion that occurs during the fragmentation period is solely attributable to laser photodissociation. In general, the fragmentation period is set to 100 ms, to ensure that an average of one laser shot from the 10 Hz Nd:YAG pumped OPO laser is used to dissociate the ions. To record a mass spectrum without irradiation, the analyte ion of interest is simply mass isolated without enabling fragmentation, providing the same conditions for isolation without allowing the shutter to open.

Since both "Laser ON" and "Laser OFF" mass spectra are required to calculate photodepletion (Equation 2.5), a method or routine must be able to collect both sets of data. The PD data collected in Chapters 3, 4 and 6 of this thesis recorded "Laser ON" and "Laser OFF" data in separate data files, which were collected in consecutive mass spectrometry acquisitions. The acquisition period was usually set to 60 seconds for both the "Laser ON" and "Laser OFF" data, the mass spectra recorded in each datafile were averaged to produce a single "Laser ON" or "Laser OFF" mass spectrum at a particular wavelength. Details of the routines used in laser scans, data extraction and data processing will be given later.

The PD experiments in Chapter 5 of this thesis collected "Laser ON" and "Laser OFF" data within the same data file by utilising the "Multiple Reaction Monitoring" (MRM) functionality of the AmaZon mass spectrometer. MRM is a mass spectrometry technique, used in analytical liquid chromatography (LC-) and gas chromatography (GC-) mass spectrometry, which can be used to record the CID fragmentation of several mass-selected precursor ions. In MRM mode, the QIT can
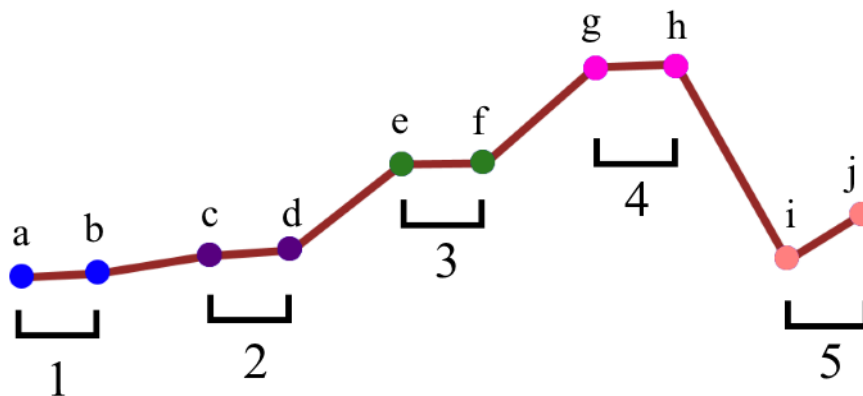
Figure 2.13 Ion intensity chromatogram produced from the first ten spectra taken in a multiple-reaction monitoring photodissociation experiment on five different ions (1-5). The labels a, c, e, g, and i are for mass spectra recorded with irradiation, whilst the labels b, d, f, h, and j are for mass spectra recorded without irradiation.
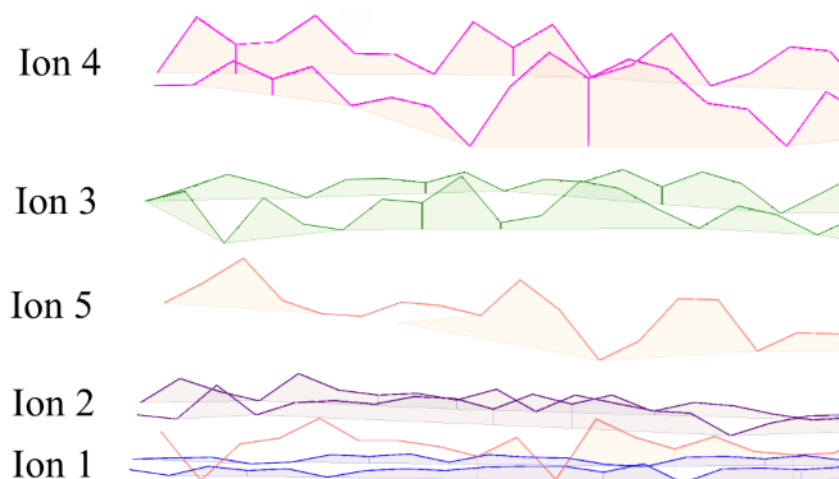
Figure 2.14 Separated ion intensity chromatograms of a five ion MRM PD experiment recorded over one minute.

be used to isolate and fragment up to ten different ions within a single acquisition, mass spectra of the different ions are recorded consecutively and are stored within the same mass spectra chromatogram. In the context of PD spectroscopy, this means that "Laser ON" and "Laser OFF" data can be collected for up to five different ions within the same data file, increasing the efficiency of data collection. The main restriction on using MRM to collect PD data is that the different analyte ions must all be efficiently ionised by ESI and transported to the QIT using the same source conditions and the same voltages on the ion guides; this restriction limits MRM to species that are similar (i.e. it is unlikely that it would be possible to study a small protonated organic molecule and an organometallic cluster using a single MRM method).

Figure 2.13 is an ion chromatogram of the first ten mass spectra collected in a PD experiment, studying five ions using the MRM functionality of the AmaZon mass spectrometer. For each ion (1-5), a mass spectrum is recorded with "Laser ON" (labelled a, c, e, g and i) and "Laser OFF" (labelled b, d, f, h and j). After the ten mass spectra of the different species have been recorded, a mass spectrum of the first species (a) is recorded and the cycle repeats. The cycling mass spectra are collected until the acquisition period (generally 30 seconds per ion) is over. The MRM method results in a single chromatogram of mass spectra which can be deconvoluted into

chromatograms of the individual species using DataAnalysis (Version 4.2, Bruker Daltonik). DataAnalysis is a program provided by Bruker Daltonik which is used process data collected in Bruker instruments. An example of the ten deconvoluted chromatograms in a five-ion experiment is given in Figure 2.14, each vertex in each
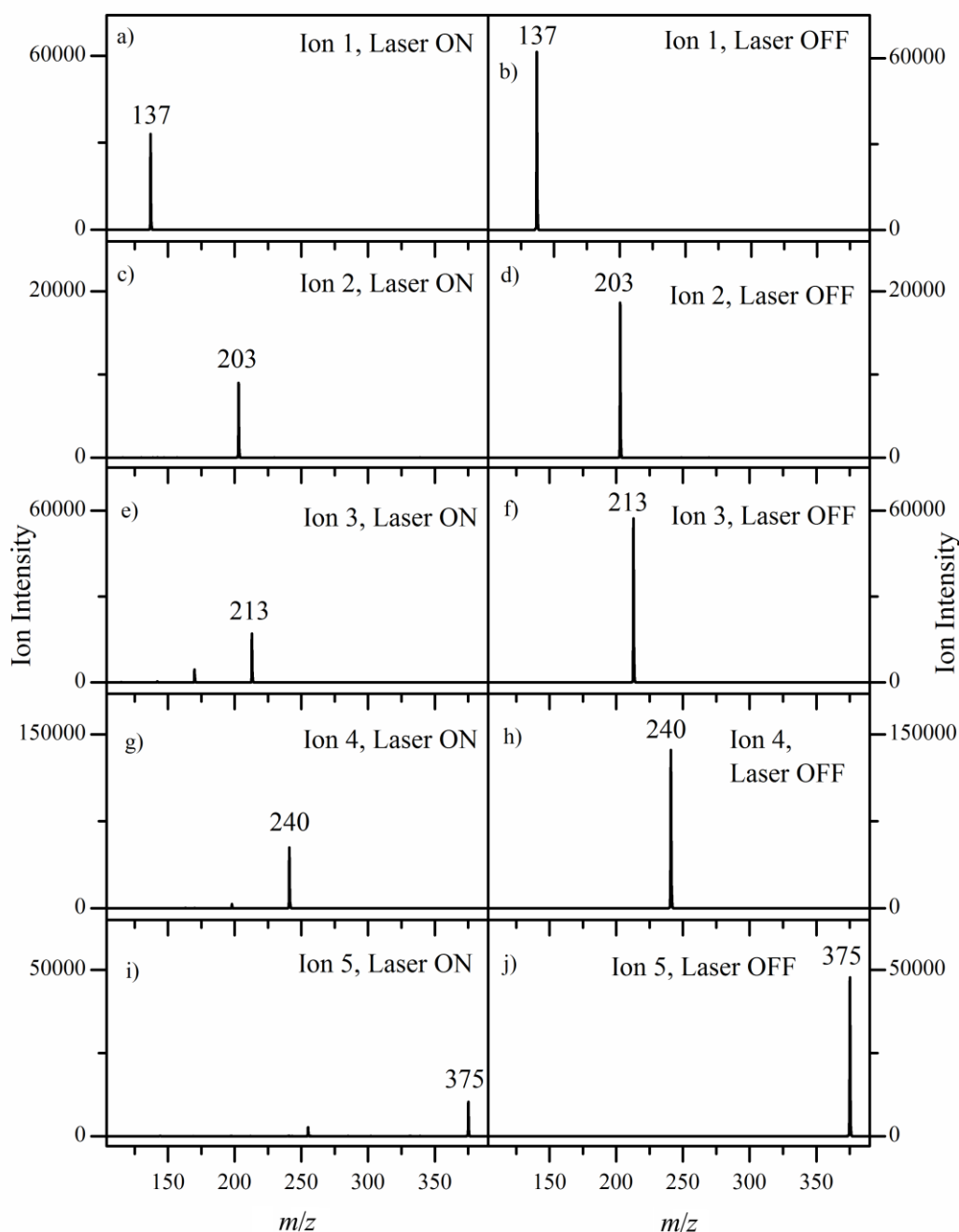
Figure 2.15 Averaged mass spectra of the laser-MS chromatograms shown in Figure 2.14, where ions 1-5 are: deprotonated hydroxybenzoic acid; deprotonated tryptophan; deprotonated alloxazine; deprotonated lumichrome; and deprotonated riboflavin, respectively. Mass spectra a, c, e, g, and i are with irradiation and spectra b, d, f, h, and j are without irradiation.

chromatogram corresponds to a mass spectrum of the ion. The mass spectra in the individual chromatograms are averaged to produce a single mass spectrum that is representative of the ion intensities for a particular ion, either with or without irradiation by photons with a particular wavelength.

Averaged mass spectra from the chromatograms presented in Figure 2.14 are given in Figure 2.15, where ions 1-5 are: deprotonated hydroxybenzoic acid; deprotonated tryptophan; deprotonated alloxazine; deprotonated lumichrome; and deprotonated riboflavin, respectively. For all ions, the parent ion intensities are noticeably lower with "Laser ON", showing that each gaseous ion is a chromophore at the irradiation wavelength. The absolute intensities of the parent ions can be used to calculate absorption coefficients of the different ions according to Equation 2.5.

2.5.3   Methods for recording gaseous absorption spectra

As was shown in the above section, the AmaZon mass spectrometer can be used to collect the "Laser ON" and "Laser OFF" data which is required to calculate gaseous absorption coefficients. However, the majority of absorption coefficients that have been calculated in this thesis are presented in absorption spectra, where mass spectrometric data must be collected whilst varying the output wavelength of the OPO laser. Additionally, the laser power must be recorded at every wavelength to compensate the depletion in ion intensity for photon flux within the ion trap.

Figure 2.16 is a simple flowchart which shows the steps involved in collecting mass spectrometric data while scanning wavelengths. For a scan across a wavelength range, the starting wavelength ($WL_{Initial}$) is set by the software controlling the OPO laser. At the beginning of a scan, the adjustable prism must intercept the laser (Section 2.3.3) and reflect the laser onto the power meter. Unless otherwise specified, the power of the laser is attuned to give ~10 mW (~1 mJ) of power, which is done by changing the relative orientations of the BBO crystals in the OPO laser using the Horizon laser control software. The BBO crystals which is adjusted changes with the wavelength region of the laser; optics 10 (Figure 2.9) is used to attune the laser power at wavelengths longer than 400 nm, and optic 20 (Figure 2.9) is used to alter the laser
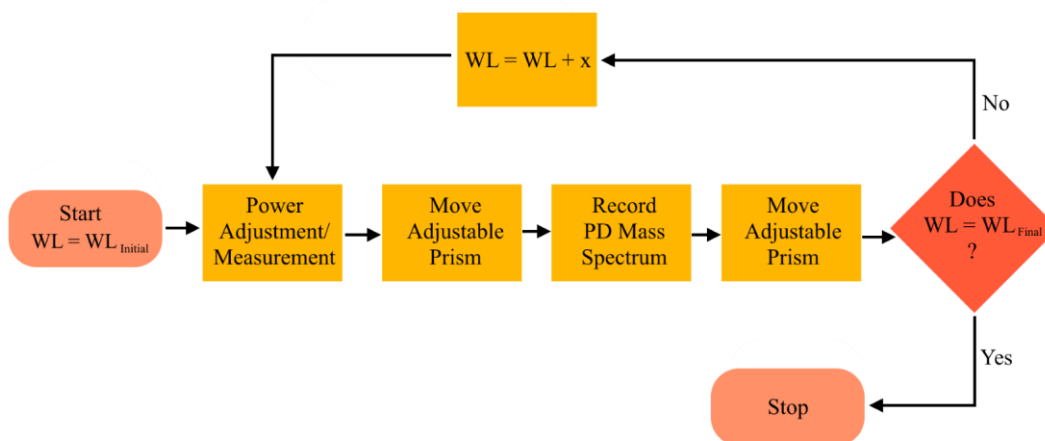
Figure 2.16 Flow chart of the experimental protocol used to collect mass spectra using the AmaZon mass spectrometer as the output wavelength of the OPO laser is scanned.

power for wavelengths shorter than 400 nm. Laser power is displayed on the workstation as was explained in Section 2.3.3. When the laser power is acceptable (between 8 – 12 mW, 0.8 – 1.2 mJ), the power is copied into an Excel spreadsheet along with the laser wavelength and the exact positions of the step motors which produce the recorded laser power.

Following power tuning, the adjustable prism is moved out of the way of the laser, allowing the laser to pass through the optics leading to the ion trap. For the first measurement, the alignment of the laser must be checked; the bench optics on top of the mass spectrometer have been arranged such that if the laser passes through the centre of an iris (iris a, Figure 2.11), then the laser will pass through the centre of a lens (lens g, Figure 2.11) and will be focused through the centre of the ion trap without clipping on any surface in the mass spectrometer. The position of the beam is centred by changing the orientation of a Pelin-Broca prism in the OPO laser (optic 16 or 23, Figure 2.9) using the Horizon laser control software, the alignment of the beam is monitored by holding translucent paper behind the iris. When the alignment of the laser has been corrected, laser-PD mass spectrometry data is collected using a mass spectral acquisition method described in the above section.

Following the completion of the mass spectrometry acquisition, the adjustable prism is moved to again reflect the laser onto the power meter. At this point, the wavelength

of the laser is checked to see if the final wavelength (WL_{Final}) of the scan has been reached; if yes then the scan stops, if no then the wavelength of the laser is changed using the Horizon control software and the cycle repeats. When recording laser scans, mass spectrometry data collected at different wavelengths are stored in data files with the same name but with an increasing counter, i.e. each data file has a suffix of XXXX which begins at 0000. Using this file naming system assists the processing routine which will be described later.

The wavelength ranges of laser scans are controlled by the OPO laser's hardware and control software. In this thesis, the scan regions used are: 220 – 234 nm, 234 – 292 nm, 292 – 400 nm, 400 – 500 nm, and 500 – 700 nm. These scan ranges are software-locked under the conditions which laser scans are conducted. This is because the positions of the crystals change significantly between the scan regions, meaning that the pump laser must be blocked when converting between scan regions to avoid damaging the components in the OPO laser. Additionally, the route through the OPO to produce wavelengths shorter and longer than 400 nm is different, the process to convert the laser to produce <400 nm or >400 nm light requires a half wave plate to be inserted/removed from the OPO laser and adjustable elements of the optical table to be moved (Figure 2.10).

2.5.3   Automation of Laser Scans

The systematic and repetitive nature of the data collection procedure when scanning the output wavelength of the OPO laser means that it is possible to automate the collection of scan data. Macro software (Pullover's Macro Creator, version 5.0.5) is used to click, type and copy/paste data for this purpose. The steps involved in data collection (Figure 2.16) can all be activated by clicking in very specific locations which do not change as the scan progresses. Thus, building a useable macro involves knowing where to click and how long the pauses between actions need to be to allow the procedures (e.g. moving then adjustable prism or recording the mass spectrometric data) to complete.

Additionally, the macro can compare the clipboard (stored by copying a string) to a definable variable. This is used within the power adjustment/measurement stage of

the procedure to check if the laser power falls within the acceptable range (8 – 12 mW). If the power is outside of the range then the position of an adjustable BBO crystal is adjusted to normalise the laser power. This procedure repeats until the power of the laser is acceptable, and the values of the step motors that produce a useable power are stored along with the laser power which are used as a calibration in future scans.

Within any laser scan, the mass spectrometer is set up to collect data in prefix/counter mode, where the prefix of all data files is the same and the suffix is a counter beginning with 0000 which ticks up by one for each subsequent file. The prefix contains information on the date, ion names, the starting wavelength, the direction of the scan, the scan step, and the power of the laser which is desired (e.g. Date_Molecule_1.0mJ_320st_2nm_up). The number in the data file is cross-referenced to the wavelength in the power measurement Excel spreadsheet, which contains information on the wavelength and the positions of the step-motors.

2.5.4   *Laser Scan Data Extraction and Processing*

The data collected within laser scans must be extracted to provide ion intensities of parent ions and fragments which are used to calculate the photodepletion intensities of the ions as well as the photofragment productions at every wavelength. Laser data extraction relies on the use of the programs DataAnalysis and AutomationEngine (Bruker Daltonics). DataAnalysis is a commercial program provided by Bruker to extract data collected using Bruker instruments and AutomationEngine is an auxiliary program which allows the tasks performed by DataAnalysis to be automated using Visual Basic (VB) scripting.

The VB script makes use of the constant prefix and sequential, numeric suffix given to the data files when recording a laser scan. The automation script calls each data file to be extracted by DataAnalysis sequentially, DataAnalysis processes the chromatograms stored in the data files into averaged mass spectra and exports a tab-separated-value (TSV). For ions studied using MRM, a TSV document is exported for every ion studied, including "Laser ON" and "Laser OFF". These documents are numbered according to the number in the suffix of the data file. The exported

document contains a mass list and the intensity of every ion in a particular averaged mass spectrum.

Once an entire dataset is extracted, the data files are transferred from a Windows operating system to the University of York's Linux-based research service (research0.york.ac.uk). Once on the remote Linux drive, the data within the TSV documents are extracted using a series of scripts written using Bash-Shell language. These scripts comprise of a file manipulation script, an extraction script and a wrapper script. The file manipulation script extracts the TSV documents from the data files and processes the file names to correspond to the exact laser wavelength which was used to collect the data and includes "ON" or "OFF" to refer to whether the mass spectrum is "Laser ON" or "Laser OFF". The extraction script operates by extracting the intensities of ions in the data files which have the same m/z as ion in a pre-made reference file, this can currently be used to extract the intensities of up to twenty ions. The ion intensities are merged into a single TSV document which is sorted by wavelength. The wrapper script is used to provide the information on the starting wavelength and scan step-size used to manipulate the data files, as well as to direct the extraction script to the correct reference file for the ion being extracted. This script also creates directories to store the extracted scan data.

The extracted and sorted scan data is copied from the Linux terminal into an Excel spreadsheet where it is matched to the laser power data which was collected for the dataset. Once in the spreadsheet, the photodepletion of the parent ions and the photofragment production of every extracted fragment are calculated using Equations 2.5 and 2.8, respectively. Laser scans across the spectral range relevant to an individual ion are repeated over several days until at least three sets of data have been collected at each wavelength. These photodepletion and photofragment data is averaged at every wavelength studied within Excel using the AverageIF function.

Photodepletion and photofragment intensities are plotted against photon energy within Origin 8.5 (OriginLab Corporation), the absorption spectra presented in this thesis are given with a smoothing line which is an adjacent-average of the data points.

2.5.5   Laser Power Studies

Laser power studies are performed to determine the role of multiphoton effects in the photodepletion spectra (see Section 2.4.3). To do this, laser-mass spectrometry data must be collected at one or more wavelengths as the power of the laser is changed, the wavelengths which are selected for power studies are the absorption maxima of bands present in the photodepletion spectra.

In a power study, the power of the laser is tuned to a set value by adjusting the positions of BBO crystals in the OPO laser, the power is recorded and a PD-mass spectrum is acquired. After the mass spectrum has been acquired, the laser power is changed and the process continues. Since it is important to know the role of multiphoton effects at the laser power which laser scans are recorded (~10 mW), PD data are recorded above and below the scan laser power in power studies (generally between 3 – 18 mW). PD data are collected multiple times over a power range so that the extracted data can be averaged. The PD data are acquired using the same methods as laser scans and is processed using the same software and routines as data collected in laser scans. Once extracted, the logarithmic depletion of the ion signal, $\ln(I_0/I)$, is plotted against the power of the laser and is fitted to a linear or polynomial function within Origin 8.5, to be compared with Equation 2.9.

2.6   Computational Methods

Computational chemistry has been used in this thesis to support and explain the experimental photodepletion spectra as well as to identify photofragments, this has included: conformer/isomer searching to determine the lowest energy structure of parent ions; structure optimisations; calculating the electron detachment energies (both vertical and adiabatic) of anionic parent molecules; predicting the electronic absorption spectra of parent ions and clusters; determining the nature of photofragments; and estimating the total enthalpy change that associates fragmentation. When appropriate, calculations on isolated ions are repeated using an implicit solvent model to approximate the solution phase properties of the ions and clusters.

In this thesis, all quantum chemical calculations on molecules and ions in their electronic ground state have been calculated using density functional theory (DFT), within the program Gaussian 09 (revision D.01, Gaussian, Inc.).[135] Simulated electronic excitation spectra in Chapters 3, 4, 5 and 6 have been calculated using time-dependent density functional theory (TDDFT) using Gaussian 09. Simulated excitation spectra in Chapter 4 were also calculated using the multireference configuration interaction (MRCI) and spectroscopy-oriented configuration interaction (SORCI) methods, using the program ORCA (Version 3.0.3).[136, 137]

2.6.1   General Quantum Mechanics

The aim of quantum chemical calculations is to use the well-established quantum mechanical theories and equations to predict the physical properties of ions and molecules, the energy of a quantum mechanical system is calculated using the Schrödinger equation (Equation 2.10).[138]

$$\hat{H}\Psi \; = \; E\Psi$$

<div align="right">Equation 2.10</div>

The Schrödinger equation calculates the energy (E) of a molecular system that is described using a many-body wavefunction (Ψ), as the eigenvalue of a Hamiltonian operator ($\hat{H}$) and the wavefunction (Ψ).

In principle, if all the information about a system is known, then the energy of the system can be calculated. However, the Schrödinger equation cannot be solved exactly for molecules more complex than the hydrogen atom; this is because the motions of the electrons and nuclei are correlated, from their Coulombic interactions, which means that there are no analytical solutions to the motions of the nuclei or electrons. Therefore, quantum chemical approaches to predict the properties of polyatomic molecules must make suitable approximations to enable the calculation of numerical solutions to the Schrödinger equation.

One such approximation is the Born-Oppenheimer approximation,[139] this approximation assumes that the wavefunction (Ψ) which describes motions of the

nuclei and electrons can be separated into its constituent parts (i.e. $\Psi_{Total} = \psi_{electronic} \otimes \psi_{nuclear}$). This approximation is justified because electrons are about 1836 times lighter than protons or neutrons and thus travel much faster than the nuclei. After making this approximation, the electrons can be described as moving in a static external potential, V_{ext}, produced by the fixed nuclei. The Born-Oppenheimer approximation significantly reduces the complexity of the quantum mechanical system and allows for the calculation of the electronic energy using an electronic Hamiltonian operator ($\hat{H}_e$).

Several computational methods exist for evaluating the electronic energy of a given molecule or ion, including: the Hartree-Fock (HF) method; density functional theory (DFT); and post-HF methods (e.g. Configuration Interaction, Møller–Plesset perturbation theory, etc.). Using these methods, the electronic energy of the ground electronic state (or excited electronic states) can be calculated, so long as the wavefunction which is used to calculate the energy is representative of the electronic structure of the molecule.

2.6.2   Density Functional Theory (DFT)

One of the guiding philosophies behind DFT is that the electronic structure of a molecule controls its physical properties; thus, if the electron density of a molecule is exactly known, then its physical properties can be calculated. The origins of DFT lie in the Thomas-Fermi model (and later Thomas-Fermi-Dirac model) which calculates the total energy of a system from its electron density (ρ), shown in Equation 2.11:[140-142]

$$E[\rho] = T[\rho] + V_{ext}[\rho] + V_{ee}[\rho]$$

<div align="right">Equation 2.11</div>

where $T[\rho]$ is the kinetic energy, $V_{ext}[\rho]$ is the external potential (nuclear) interaction energy and $V_{ee}[\rho]$ electron-electron interaction energy.

Modern DFT methods utilise the Hohenberg-Kohn and Kohn-Sham theories;[143, 144] these theories addressed the main issue with the Thomas-Fermi-Dirac method,

namely that the electrons were treated as non-interacting particles. Within the Kohn-Sham equations, the kinetic energy is calculated for a set of non-interacting electrons in an auxiliary system, the external potential of the auxiliary system (the Kohn-Sham potential) is optimised in such a way that the electron density of the real system behaves as though the electrons do interact. Using this method, the kinetic energy of the interacting electrons, represented by one electron orbitals (Kohn-Sham orbitals), can be calculated using a single Slater determinant. Additionally, the Kohn-Sham energy functional contains an exchange-correlation energy which corrects the energy functional for errors in the electron-electron repulsion and electron kinetic energies. However, the exact method of calculating the exchange-correlation energy is generally unknown; therefore, the exchange-correlation energy must be approximated.

2.6.3 Density Functionals used Within this Thesis

Many functionals are available in modern quantum chemistry packages which have methods of estimating the exchange and correlation energies, the functionals are often parametrised and calibrated by comparing calculated energies with experimental data. The density functionals that have been used in this thesis are the hybrid functionals: B3LYP (Chapter 4),[145] PBE0 (Chapter 5),[146] M06-2X (Chapter 6),[147] and MN12-SX (Chapter 3).[148]

The B3LYP functional uses Becke's three parameter (B3) exchange functional as well as the Lee-Yang-Parr (LYP) and Vosko-Wilk-Nusair (VWN) correlation functionals, the B3 functional contains 20% exact (HF) exchange.[145, 149, 150] The Becke exchange functional is parametrised for the rare gases and is widely used in computational chemistry.

PBE0 is a hybrid functional, exchange energy is calculated using 75% of the exchange functional of Perdew, Burke and Ernzerhof (PBE) and 25% exact exchange, correlation is calculated using the Perdew-Wang functional.[146, 151] The PBE0 functional contains no experimental parametrisation, the models for calculating exchange and correlation are derived from fundamental constants. The absence of empirical parametrisation means that the PBE0 model is widely applicable for

quantum chemistry, including small organic molecules which it is used with in this thesis.

The M06-2X and MN12-SX functionals are two of the "Minnesota" functionals developed by Truhlar and coworkers.[147, 148] The M06-2X is a hybrid functional which calculates the exchange energy using 54% exact exchange, the remainder of the exchange energy is calculated using an earlier exchange functional (M05); correlation energy of the M06-2X functional is calculated using the M05 correlation functional.[152] M06-2X is parametrised for non-metals and is ideal for studying main group thermochemistry. The MN12-SX is a screened exchange energy functional which uses 25% exact exchange at short ranges and 0% exact exchange at long ranges.[148] The MN12-SX functional has been parametrised using a mixture of chemistry and physics data, making the functional widely applicable in quantum chemistry.

Chapter 3

Locating the Proton in Nicotinamide Protomers via Low-Resolution UV Action Spectroscopy of Electrosprayed Solutions

3.1 Preamble

The following work has been published in the *Journal of Physical Chemistry A*. All data, including experimental and computational, have been collected by me. Data processing routines and the interpretation of the results have also been performed by me. The initial draft of the manuscript was written by me and revised by Caroline Dessent.

Electronic supplementary information (ESI) which was included with the publication is appended to this Chapter as Section 3.7. This includes computational results; collision-induced dissociation mass spectra; photofragment mass spectra; and photofragment production spectra of some low-intensity photofragments.

Full Reference to the publication:

"Locating the Proton in Nicotinamide Protomers via Low-Resolution UV Action Spectroscopy of Electrosprayed Solutions"

E. Matthews and C. E. H. Dessent, *J. Phys. Chem. A*, 2016, **120**, 9209–9216.

http://dx.doi.org/10.1021/acs.jpca.6b10433

3.2 Abstract

Even in relatively simple molecules, the sites of protonation or deprotonation formed upon electrospray ionisation can be controversial. This situation means that it is important to develop new approaches for identifying "protomers" and "deprotomers". In this study, we demonstrate that routine, low-resolution UV laser photodissociation

spectroscopy can be applied to identify the gaseous protomers of nicotinamide formed upon electrospray. Nicotinamide is an important biological molecule that possesses multiple protonation sites associated with its pyridine and amide groups. We obtain a gas-phase absorption spectrum for protonated nicotinamide that closely resembles the solution-phase spectrum. However, photoexcitation of protonated nicotinamide produces numerous ionic photofragments, and the spectral profiles for production of these photofragments from protonated nicotinamide reveal the existence of two distinctive chromophores, which can be traced to the existence of pyridine and amide protomers. We observe that these protomers are associated with absorption bands centred at 4.96 and 4.73 eV, respectively, with the protomers appearing in an approximate ratio of ~2:1. The fact that the considerably less favourable amide protomer is observed in substantial quantities in the gas phase is surprising given that the pyridine protomer is the lower-energy species in both solution and gas phase. The high amounts of amide protomers observed here can be explained as arising from asymmetric pyridine protomer–amide bound dimers, present in solution or in the electrosprayed droplets, which lead to enhanced formation of the unexpected amide-protonated isomers.

3.3 Introduction

There has been a keen debate over recent years relating to the influence of electrospray ionisation on the location of protonation and deprotonation sites of electrosprayed ions.[9, 10, 98, 153-158] This debate is important, as electrospray mass spectrometry is now being used increasingly to probe solution-phase reactions.[159-161] Following on from work by Kass and Oomens on para-hydroxybenzoic acid,[9, 10, 153-155] Roithova and co-workers performed a seminal investigation of how the electrospray process affects the gas-phase ratios of deprotonated isomers of this molecule.[156] NMR was used to probe the solution-phase structures and ion-mobility mass spectrometry (IM-MS) to identify the gas-phase isomers. They were able to show that, while the carboxylate isomer is preferred in solution irrespective of the solvent, the opposite is true for the gas-phase isomers. However, the exact ratio of isomers formed in the gas phase depended strongly on the ESI solvent, pH, and solution concentration.[98, 156-158, 162] These results led Roithova and co-workers to conclude that the gas-phase populations do not exactly match the solution-phase

populations but are a reflection of the situation in solution. More generally, this means that it is very important to have tools available to accurately determine the identity of "protomers" and "deprotomers",[163-166] and also to have a full understanding of how gaseous populations relate to solution-phase populations as a function of experimental conditions.

Toward this end, recent studies have investigated the general applicability of IM-MS for correctly identifying protomers or deprotomers.[98, 158, 162, 165, 166] This is of critical importance given how broadly IM-MS is being applied to determine the structures of protonated peptides, as well as other proton-labile biological and pharmaceutical ions.[167] Von Helden and co-workers very recently tested the applicability of IM-MS for detecting protomers by combining it with midrange IR spectroscopy using a free-electron laser to spectroscopically identify the protomers of benzocaine.[98] This work was important, as it showed the advantages of using an IR spectroscopic approach to definitively identify protomers, avoiding the most significant difficulty associated with IM-MS analyses of these systems, that of correlating the experimental and calculated collision cross sections.[158]

In this work, we report the first UV laser photodissociation spectroscopy study of gaseous protonated nicotinamide, produced from aqueous solution using electrospray ionisation. Nicotinamide can be protonated at either the pyridine nitrogen or on the amide side chain (Figure 3.1),[168] and may therefore exist as protomers following electrospray. Our goal in this study is to establish whether relatively low-resolution UV spectroscopy of ambient temperature, electrosprayed ions can be used to distinguish between different protonation sites within a small aromatic molecule. We focus here on both characterising the protonation of nicotinamide and, more importantly, in testing the utility of our straightforward laser spectroscopic approach,[14, 169] as a suitable methodology for identifying small protomeric ions generated via electrospray.

The nicotinamide (NA) moiety is a constituent of the important biological coenzyme nicotinamide adenine dinucleotide (NAD).[170] NA is a known UV absorber with an absorption profile that varies with pH.[168] Molecular extinction coefficient
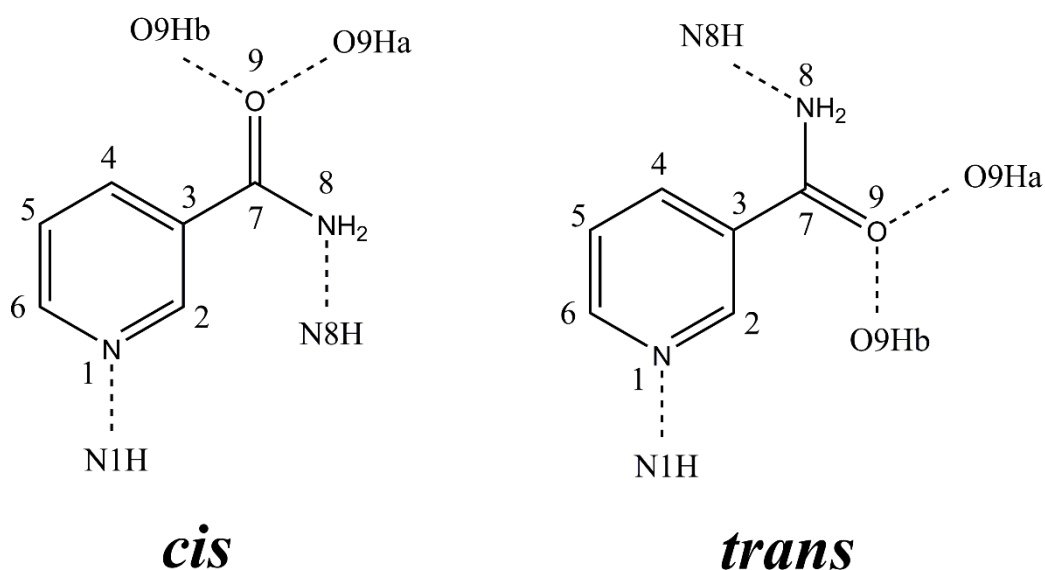
Figure 3.1 Schematic diagram of the structures of *cis*- and *trans*-nicotinamide, illustrating the possible protonation sites (**N1H**, **N8H**, **O9Ha**, and **O9Hb**).

measurements as a function of pH have indicated that the two isosbestic points observed are associated with protonation of the amide and pyridine sites of NA, hence there is considerable interest in gaining a definitive understanding of the effect of NA protonation sites on the UV absorption spectrum. An additional motivation for the current study is the fact that NA has received significant recent media attention as a possible oral and topical sunscreen.[171-173] The UV spectroscopy conducted in this work allows us to assess the intrinsic suitability of NA as a photoprotector.

3.4 Methods

Gas-phase UV photodissociation experiments were conducted in an AmaZon ion-trap mass spectrometer, which was modified for the laser experiments as described in detail elsewhere.[14] This instrument has all the advantages of a commercial mass spectrometer (flexible ion sources, mass selection and isolation of primary and secondary ions and fragments via MS[n] schemes, etc.), coupled with the ability to record UV absorption and photodissociation spectra in a routine manner. The UV photons in these experiments were produced by an Nd:YAG (10 Hz, Surelite) pumped OPO (Horizon) laser, giving ~1 mJ across the range 215-345 nm. The laser step size was 1 nm. Photofragmentation experiments were run with an ion

accumulation time of 100 ms. A fragmentation time of 300 ms was employed, so that each mass selected ion packet interacted with three laser pulses. However, due to the fact that the ions are continually circulating within the ion cloud, the probability of multiphoton excitation of an ion is very low. This was verified by conducting a laser-power study at the gaseous photodepletion maximum (a figure showing this is given in Section 3.7.1), which showed that ion photodepletion was linear with respect to laser power, consistent with no multiphoton dissociation of the ions studied here. The photodepletion intensity of the clusters and the photofragment production have been calculated using equations 3.1 and 3.2 and are presented as a function of the photon energy:

$$\text{Photodepletion Intensity} = \frac{\ln\left(\frac{I_{\text{OFF}}}{I_{\text{ON}}}\right)}{\lambda \times P}$$

Equation 3.1

$$\text{Photofragmentation Production} = \frac{\left(\frac{I_{\text{Frag}}}{I_{\text{OFF}}}\right)}{\lambda \times P}$$

Equation 3.2

Where I_{ON} and I_{OFF} are the peak intensities with laser on and off, I_{Frag} is the fragment intensity with laser on, λ is the excitation wavelength (nm) and P is the laser pulse energy (mJ). Solution-phase UV absorption spectra (aqueous solution, 3×10^{-5} mol dm^{-3}, acidified with HCl) were recorded using a Shimadzu 1800 UV spectrophotometer with a 1 cm UV cuvette, using distilled water as a baseline.

Solutions of NA (1×10^{-5} mol dm^{-3}) in deionised water were introduced to the mass spectrometer through electrospray ionisation using a nebulising gas pressure of 10.0 psi, an injection rate of 300 µL hr^{-1}, a drying gas flow rate of 8.0 L min^{-1}, and a capillary temperature of 140 °C. NA was purchased from Sigma Aldrich and used without purification. The voltages applied to the ion optics were tuned to maximise the ion signal of protonated NA ($m/z = 123$) using the automated tuning capabilities of the TrapControl (Bruker) software. A small number of additional experiments were conducted of NA in pure acetonitrile solution (1×10^{-4} mol dm^{-3}). Full laser spectral scans were not conducted for the protonated NA produced from acetonitrile

solutions, but photodissociation mass spectra were recorded at selected photon energies, including 250 and 263 nm (4.73 and 4.96 eV).

Calculations were performed using density functional theory at the MN12-SX/6-311+G** level as implemented in Gaussian 09.[135, 148, 174, 175] All reported structures (including fragments) correspond to true minima as confirmed by frequency calculations. All protomers of NA were reoptimised using the polarised continuum model to approximate solvation effects. Time dependent-density functional theory (TDDFT) was used to calculate vertical excitation energies for protonated NA.

3.5 Results and Discussion

3.5.1 UV absorption spectra of NA·H$^+$: Gas phase and solution phase

Protonated nicotinamide, NA·H$^+$, is readily produced upon electrospray ionisation of solutions of NA. Figure 3.2a displays the gas-phase absorption spectrum (recorded
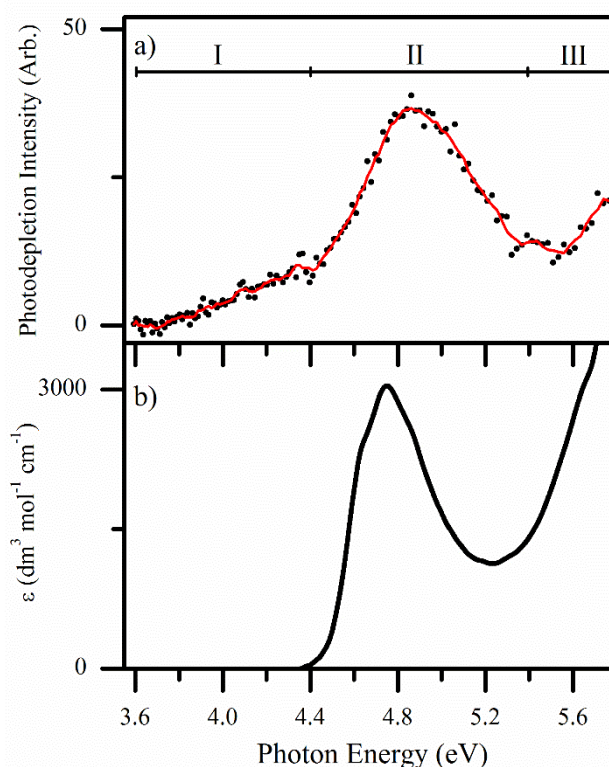
Figure 3.2 (a) Gas-phase photodepletion spectrum (absorption spectrum) of NA·H$^+$ across the range 3.6 – 5.8 eV (345 – 215 nm). The solid line is a five-point adjacent average of the data points. (b) Aqueous absorption spectrum (3 × 10^{-5} mol dm^{-3}) of nicotinamide at pH 1.

via photodepletion)[14, 169, 176] of mass-selected NA·H$^+$ across the 3.6−5.8 eV range. Mass-selection is a key feature of our experimental approach since it means that the gas-phase photodepletion spectra we record are unambiguously associated with the *m/z* selected ion. This situation is quite distinct from solution-phase UV spectroscopy, where spectra can be polluted by the presence of aggregates or chemical species formed via various decay process of the initial chemical species. We find that NA·H$^+$ displays strong photodepletion in the UV, with a photodepletion onset around 3.7 eV. The spectrum can be described in terms of three regions: a weak, broad region at the low-energy range of the spectrum associated with a shallow increase in photodepletion between 3.7 – 4.45 eV (**I**); a strong, well-resolved band peaking at 4.85 eV (**II**); and another strong photodepletion region that peaks above 5.8 eV (**III**), causing an increasing photodepletion cross-section at the high-energy end of the spectrum.

For comparison, the aqueous (mildly acidic) absorption spectrum of NA is displayed in Figure 3.2b. The spectrum agrees well with a previously published one.[168, 177] The aqueous NA·H$^+$ absorption spectrum has two main bands: a broad peak centred around 4.75 eV and a band associated with the increasing absorption above 5.7 eV. The 4.75 eV feature has been attributed to a $\pi \rightarrow \pi^*$ transition, with the absorption coefficient increasing with increasing acidity.[168] Fine structure is just visible at 4.64 and 4.87 eV in the absorption spectrum. These features are also seen in the absorption spectrum of the related molecule, pyridine, and have been assigned as vibrational fine structure.[178, 179] Comparing the gas-phase photodepletion spectrum to the solution-phase absorption spectrum, the main absorption band is blue shifted by 0.1 eV on moving from solution to the gas-phase, while the band peaking above 5.8 eV (**III**) is unresolved in both spectra. It is interesting to note that the weak, region **I**-feature evident in the gas-phase photodepletion spectrum is quenched in the solution-phase spectrum.

To gain further insight into the nature of the excited state (or excited states) being accessed across the gaseous absorption spectrum, we now turn to analysing the cationic photofragments produced following photoexcitation across the 3.6-5.8 eV range.

3.5.2 Photofragmentation of NA·H$^+$

Figure 3.3 displays the difference (laser on - laser off) photofragment mass spectrum of NA·H$^+$, irradiated at the photodepletion maximum of 256 nm (4.84 eV). The *m/z* = 80, 96 and 106 photofragments appear prominently, and are also the major fragment ions produced upon low-energy collision-induced dissociation (CID) of the ground-state NA·H$^+$. The CID results for NA·H$^+$ are presented and discussed in Sections 3.7.3 and 3.7.4. The *m/z* = 124 photofragment is also prominent, but is thought to be a secondary photofragment formed upon addition of water to the *m/z* = 106 fragment in the ion trap.[180] Additional photofragments with significant intensity are observed at *m/z* = 50-53, 78, 79 and 107. The low-mass fragments (*m/z* = 50-53) are seen in the electron impact (EI) mass spectra of NA and pyridine and are masses associated with fragments of the pyridine ring.[181, 182] Specifically, the EI spectrum of nicotinamide shows the 49-52 cluster of peaks in a similar ratio to the 50-53 cluster in the photodissociation spectrum, consistent with these fragments originating from NA and NA·H$^+$, respectively. (Further data for the *m/z* = 50-53, 78, 79, 107 and 124 photofragments is presented in Section 3.7.5, along with a full discussion of the production pathways of these minor photofragments.)

Photofragment action spectra are acquired simultaneously with the photodepletion spectrum in our instrument, providing a complete picture of the wavelength
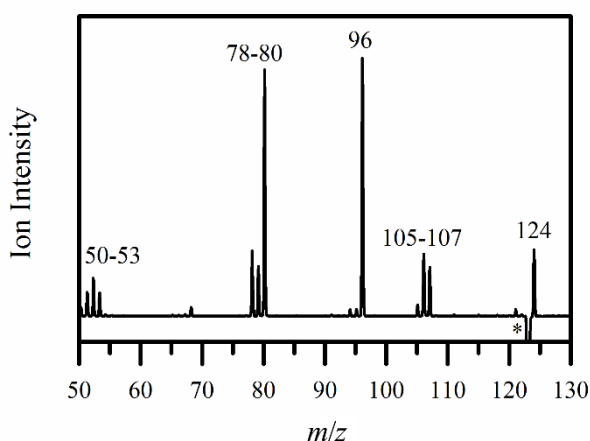
Figure 3.3 Photofragment difference (laser on – laser off) mass spectrum of NA·H$^+$, excited at the photodepletion maximum of 256 nm (4.84 eV). * indicates the depleted NA·H$^+$ ion signal.
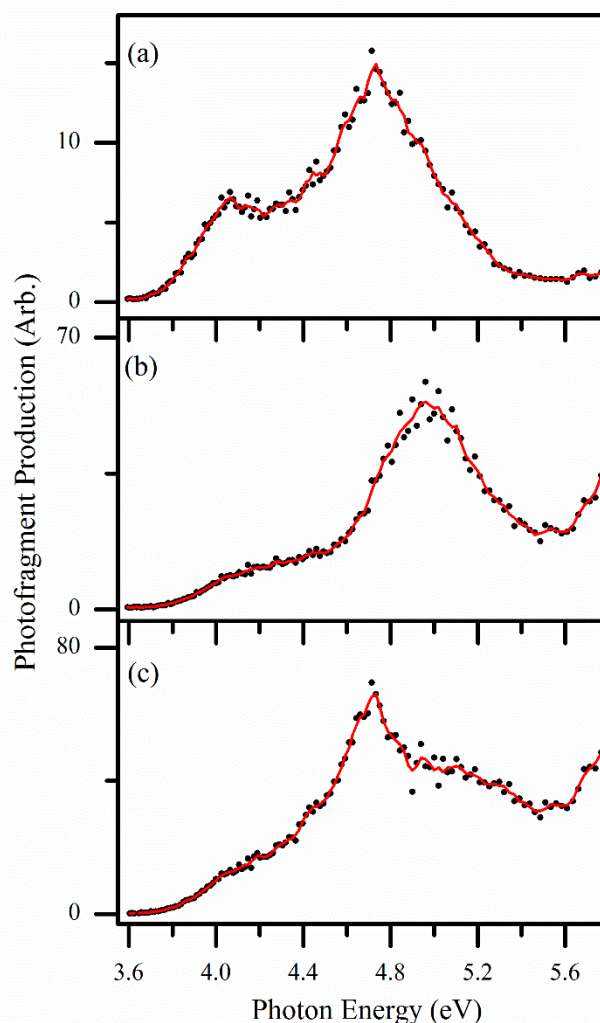
Figure 3.4 Photofragment action spectra of the fragments with *m/z* = (a) 106, (b) 96, and (c) 80 produced following photoexcitation of mass-selected NA·H$^+$ ions, across the range 3.56 – 5.8 eV. The solid line is a three-point adjacent average of the data points.

dependent fragmentation products. Figure 3.4 displays the action spectra of the prominent *m/z* = 106, 96 and 80 photofragments. The action spectrum of the *m/z* = 106 fragment (Figure 3.4a) shows a strong band centred at 4.73 eV and a weaker band centred at 4.06 eV. The strong band is red shifted by ~0.12 eV relative to the absorption maximum, **II** (Figure 3.2a), while the weaker band is far more prominent than the weak absorption band in region **I** of the total absorption spectrum. Additionally, the fragment with *m/z* = 106 shows a steep decline in production above 4.7 eV to a low baseline at ~5.8 eV, despite the fact that the NA·H$^+$ absorption profile is increasing between 5.6 - 5.8 eV. It is likely that this drop-off in the *m/z* = 106

Chapter 3

fragment at high-energies arises as a result of the $m/z = 106$ photoion fragmenting due to high internal energy above ~5.0 eV (Section 3.7.3).

The photoproduction spectrum of the fragment with $m/z = 96$ (Figure 3.4b) is notably different from that of fragment $m/z = 106$ (Figure 3.4a), with a production onset at ~3.7 eV, an unresolved weak band between 4.0 – 4.4 eV and a resolved strong band peaking at 4.96 eV to higher energy than the dominant feature in the $m/z = 106$ spectrum. In further contrast to the $m/z = 106$ fragment spectrum, the $m/z = 96$ ion displays an increasing profile to the higher-energy range of the spectrum.

Figure 3.4c shows the action spectrum of the $m/z = 80$ fragment. This spectrum is again distinctive from the spectra of the $m/z = 106$ and 96 fragments, and displays a weak band between 4.0 – 4.4 eV, a sharp peak at 4.73 eV, and a broad absorption shoulder centred around 4.94 eV. Like the $m/z = 96$ fragment, the $m/z = 80$ ion fragment also increases in intensity towards the high-energy region of the spectrum. Comparison of the $m/z = 80$ spectrum with the $m/z = 106$ and 96 spectra indicates that the $m/z = 80$ spectrum contains features that are present in each of the $m/z = 106$ and 96 spectra. For example, the $m/z = 80$ spectrum could be deconvoluted so that it contains bands centred at 4.73 (common with the $m/z = 106$ fragment) and 4.96 eV (common with the $m/z = 96$ fragment). This indicates that the $m/z = 80$ photofragment can be produced via two distinctive pathways, one which is also associated with the $m/z = 106$ fragment and the other associated with the $m/z = 96$ fragment. The structural identities of the $m/z = 106$, 96 and 80 fragments will be examined in Section 3.4.

Analysis of the photofragment action spectra reveals that two distinctive chromophores of the NA·H$^+$ moiety are present; one chromophore is associated with the spectrum that includes the sharp band centred at ~4.7 eV, while the second is associated with the spectrum that includes the broader absorption band centred around 4.9 eV. All three fragment spectra display absorption between 4.0-4.4 eV (region **I** of the NA·H$^+$ absorption spectrum), although absorption in this region is stronger in the $m/z = 106$ fragment spectrum. A straightforward explanation for the existence of two chromophores associated with NA·H$^+$ would be the presence of two distinct gaseous protomers. In the next section, we present quantum chemical

calculations of the NA·H$^+$ moiety to investigate the properties of the protomers of NA.

3.5.3 Quantum Chemical Calculations of the Protomers of Nicotinamide

Structures of NA·H$^+$ were optimised with the additional proton bonded to each carbon, nitrogen and oxygen atom of NA (Full results are given in Section 3.7.2). As expected, the lowest-energy protonation locations were found to be the heteroatom, namely the pyridine nitrogen **N1H**, the amide nitrogen **N8H** and the amide oxygen **O9H** (Figure 3.5). For each of these protonation sites, two conformers exist, associated with either a *cis* or *trans* orientation of the amide nitrogen with respect to the pyridine nitrogen.[183, 184] In addition to these *cis*/*trans* isomers, two distinct oxygen-protonated structures of NA are possible, where the excess proton points into open space (**O9Ha**) or is aligned towards the molecule (**O9Hb**).

The relative electronic energies of the low-energy NA·H$^+$ isomers as well as the calculated amide rotational barrier heights are listed in Table 3.1. This data shows that protonation at the pyridine nitrogen produces the lowest-energy protomer, followed by protonation at the amide oxygen, and then the amide nitrogen. These calculations indicate that the **N1H** protomer should dominate in the gas phase; a Boltzmann distribution of the protomers, calculated at T = 413 K, predicts an **N1H**:**O9Hb** ratio of ~4 × 10^5:1. Additional calculations to assess the solution-phase

Table 3.1 Relative computational energies of the optimised conformers of gas-phase NA·H$^+$ and the computed rotational barrier height for rotation, calculated using the MN12-SX functional with the 6-311+G** basis set.

	Relative Energy (cis) / kJ mol^{-1}	Relative Energy (trans) / kJ mol^{-1}	Rotational Barrier Height / kJ mol^{-1}
N1H	6.71	0.0	17.43
N8H	111.72	117.44	37.92
O9Ha	53.02	55.52	31.85
O9Hb	44.85	45.37	19.04

energies of the protomers revealed that the **N1H** protomer is also the lowest-energy protomer in aqueous solution (this is presented in Section 3.7.2). (For simplicity, **O9Hb** will be referred to as **O9H** from this point since **O9Hb** was found to be substantially lower in energy than **O9Ha**.) We note that the *cis* and *trans* isomers display similar relative energies for all of the protomers, and it is therefore likely that both *cis* and *trans* forms of a particular protomer will be produced in the gas phase given the size of the barrier heights. Mixtures of *cis* and *trans* isomers of analogous aromatic amides have indeed been spectroscopically observed in the gas phase previously.[185-188]
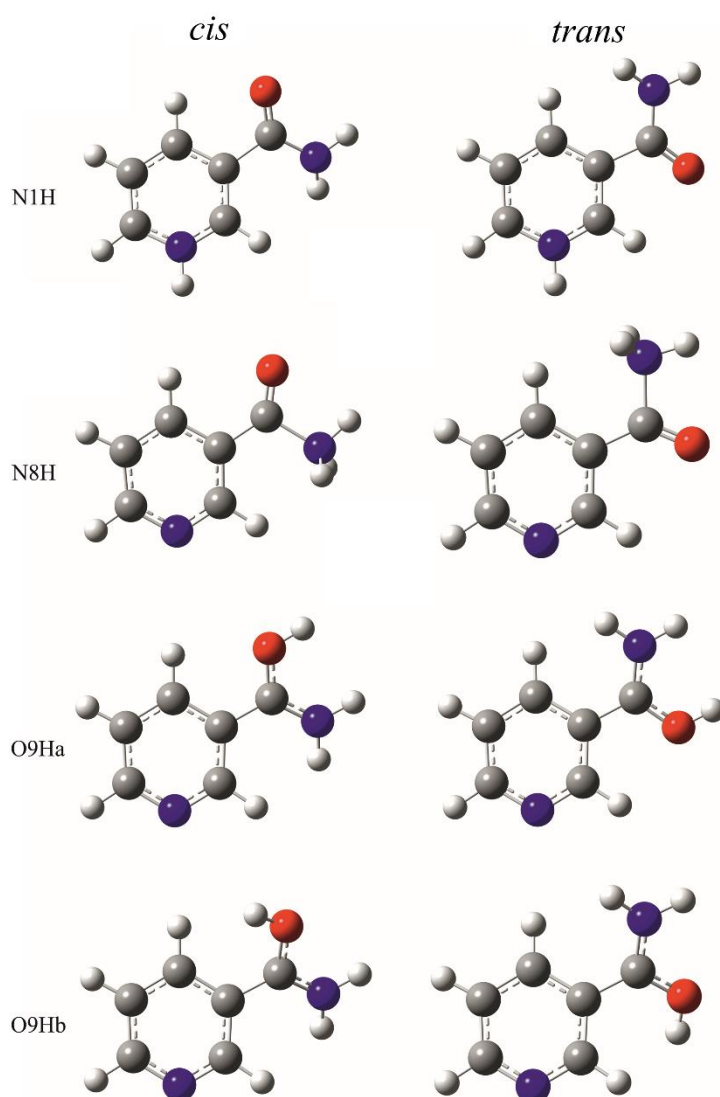
Figure 3.5 Optimised structures of nicotinamide protonated at the pyridine nitrogen (**N1H**), amide nitrogen (**N8H**), amide oxygen with H pointing away from the molecule (**O9Ha**) and amide oxygen with H pointing towards the molecule (**O9Hb**). Given in both *cis* and *trans* orientations.
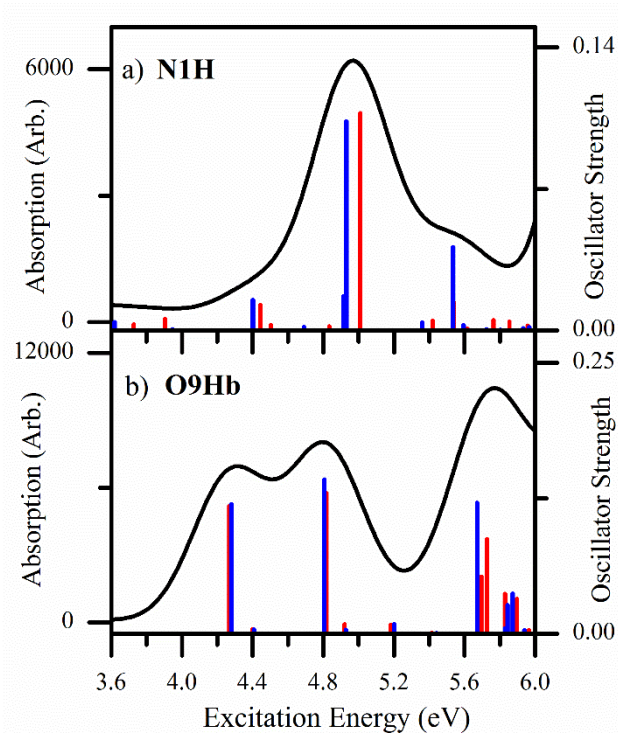
Figure 3.6 Calculated TDDFT excitation energies of (a) the **N1H** and (b) **O9Hb** protomers of NA·H$^+$. The oscillator strengths of the individual transitions (red for the *cis* isomers and blue for the *trans* isomers) are given by the vertical bars, while the full line spectrum is a convolution of the calculated transitions with Gaussian functions (0.25 eV HWHM). The excitation energies in the figure have been red-shifted by 0.5 eV to allow for the known tendency of TDDFT to overestimate the excitation energy.[189]

TDDFT calculations were performed to obtain theoretical excited-state spectra for the lowest-energy pyridine **N1H** and amide **O9H** protomers. These spectra are presented in Figure 3.6 and show that the absorption spectra associated with these two protomers are dramatically different. Further TDDFT calculations on the other isomers of NA·H$^+$ are included in Section 3.7.6, along with a discussion of the orbitals involved in the electronic excitations.

Comparison of the calculated spectra with the photofragment spectra reveals that the profile of the calculated pyridine **N1H** protomer spectrum (Figure 3.6a) is very similar to the experimental spectrum for the *m/z* = 96 photofragment (Figure 3.4b).

There is also good general agreement between the shapes of the calculated amide **O9H** protomer spectrum (Figure 3.6b) and the $m/z = 106$ photofragment spectrum (Figure 3.4a). For the amide protomer, the prominent band calculated to appear at ~4.25 eV appears to correspond well to the experimental feature seen at ~4.1 eV in the $m/z = 106$ channel. In addition, the calculated spectrum of the pyridine protomer displays a main absorption band over the scanned region at ~5 eV, while the amide isomer main band peaks at a lower energy ~4.8 eV. The difference in band maxima predicted by the TDDFT calculations (0.18 eV) is therefore in good agreement with the difference in the observed experimental band maxima (0.23 eV). The very good agreement between the spectral profiles and shift in the band maxima between the individual photofragment spectra and the calculated protomer spectra gives strong support to our assignment of the different photofragment spectra as originating due to the presence of two distinctive chromophores of NA·H$^+$ associated with two protomers. This leads us to assign the $m/z = 106$ photofragment spectrum as arising from the amide protomer (which displays the lower-energy band maximum) and the $m/z = 96$ photofragment spectrum as arising from the pyridine protomer.

3.5.4 Further discussion of the photofragmentation pathways following assignment of the pyridine and amide protomer spectra

The assignment of the photofragmentation spectra to two distinct protomers of NA·H$^+$ given above is further supported by considering the possible identities of the photofragments with $m/z = 106$ and $m/z = 96$. With reference to the possible structures given in Scheme 3.1, the $m/z = 106$ fragment seems certain to be structure **106a** which could readily originate from an amide protonated parent ion via loss of a neutral NH$_3$ molecule. Such loss of small neutral molecules from "even electron" organic ions via heterolytic rearrangement reactions is well known.[190, 191] In contrast, a pyridine protomer that produced a $m/z = 106$ fragment would likely result in the exotic structure **106b**. The tailing off in the $m/z = 106$ photofragment ion signal at high energies (Figure 3.4a) is entirely consistent with the presence of the **106a** structure, since this ion can readily lose CO at high internal energy to produce an $m/z = 78$ ion (This is shown via CID measurements in Section 3.7.3).

Scheme 3.1 Potential structures for the observed ionic fragments of protonated NA and computed energies of production (in eV).

Designation	Fragment Mass		
	106	96	80
a	2.04	3.30	2.79
b	4.07	1.57	0.67
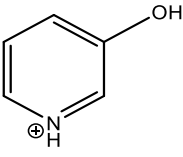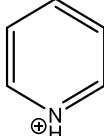
Similarly, the $m/z = 96$ fragment ion seems very likely to correspond to the **96b** structure, which can be readily formed from the pyridine protomer by loss of a neutral HCN unit.   Section 3.7.3 includes a quantitative discussion of the fragmentation pathways which supports these fragment assignments. Pathways for production of the $m/z = 80$ fragment via loss of neutral HNCO from both the pyridine **N1H** and amide **O9H** protomers are also discussed in Section 3.7.3.

3.5.5 Relation of electrospray generated protomers of NA·H⁺ to solution-phase

properties

The relative populations of the pyridine and amide protomers can be estimated by comparing the photofragment ion intensities uniquely associated with fragmentation of each protomer. This can either be done by simply comparing the observed experimental photo-ion intensities, or through a Beer-Lambert law analysis, using the TDDFT transition intensities. Full details of this analysis are given in Section 3.7.7. Using these two approaches, we estimate that the pyridine:amide protomers

are present at between a ~4:1 to 1:1 ratio in the gaseous ion population. An excess of the pyridine protomer is consistent with the general shape of the gaseous absorption spectrum which is resembles the $m/z = 96$ photofragment, and also with the aqueous solution-phase spectrum.

The pyridine:amide protomer ratios following electrospray are intriguing given the fact that the pyridine protomer is calculated to lie considerably lower in energy (by 45 kJ mol^{-1}) than the amide protomer, both in solution and the gas phase. (Relative energies of ~45 kJ mol^{-1} would be expected to give a ratio of 4×10^5:1.) In the other recent studies of the effect of the electrospray process on protomer/deprotomer rations, observations of unexpected isomer ratios following electrospray have been attributed to kinetic bottlenecks that occur during the dynamical electrospray process.[10, 162] However, in these other studies, the molecules investigated displayed one isomer as the lower-energy species in solution, with the second isomer as the lower-energy isomer in the gas phase. The situation in our experiment is different because NA·H$^+$ should exist almost exclusively as the pyridine protomer in solution under mildly acidic conditions, and there would seem no driving force to produce the higher-energy amide protomer on going from solution to the gas phase.

One explanation for the higher than expected quantities of the amide protomer could lie in the known propensity of nicotinamide to form dimers, both in the gas and condensed phase.[192, 193] The unprotonated form of NA has been shown to adopt symmetric amide-amide bound dimer structures. It is useful to consider whether similar dimers could be playing a role in our system. We repeated the measurements presented in this study using pure acetonitrile as the solvent (both with and without an added acid), and also varied the electrospray conditions (drying temperature, source voltages, etc.) but observed remarkably little difference in the ratio of amide:pyridine protomers produced in the gas phase. It is even more surprising that amide protomers are produced in substantial quantities from an aprotic solvent. Ionic dimers have been suggested to play a role in determining the observed protomer and deprotomer ratios in earlier studies of how electrospray influences the observed gas-phase structures.[156] Indeed, such dimers are the key gas-phase species used in the kinetic method for measuring gas-phase thermochemical properties.[194-196] Although

such dimers may not be dominant in bulk solution, the electrospray process enhances their concentration through the desolvation process.

If the dominant pyridine protomer associates with a neutral NA molecule in solution (or during desolvation), it seems likely that the electropositive excess proton will be attracted by the electronegative amide oxygen, producing an asymmetric pyridine-amide bound dimer. Such structures could readily facilitate transfer of the excess proton to the amide functional group, thus enhancing production of the amide protomer. The very recent work of Xia and Attygalle is interesting in this context.[162] They observed an extremely strong influence of the physical source conditions of the electrospray on the ratios of deprotomers of the *p*-hydroxybenzoic acid molecule. Although they failed to directly observe protonated dimers, their findings are consistent with source-induced break-up of preformed dimers. Further consideration of the role of dimers in determining the gas-phase ratios of electrosprayed protomers and deprotomers seems warranted. The results observed for the amide-containing molecule studied here indicate that proton-transferring dimers may play important roles in determining the final protonation sites of electrosprayed protonated peptides.

3.6 Concluding Remarks

The intrinsic photophysics and photochemistry of NA is of current interest as it has received significant attention as a potential sunscreen or cell photoprotector, both in topical skin application and when taken orally.[171-173] Since NA is a common ingredient in many skin creams and other cosmetic products,[197, 198] a fundamental understanding of its intrinsic photostability is important. The gas- and solution-phase absorption spectra of $NA \cdot H^+$ (Figure 3.2a), clearly show that the UV absorption profile is rather weak across the UVA-UVB range (3.1-4.43 eV), only increasing significantly within the UVC region. In line with this, there is relatively low production of photofragments across the important UVA-UVB range indicating that $NA \cdot H^+$ has good photostability across this region. While the intrinsic properties of NA could vary from those of $NA \cdot H^+$, NA could exist as the protonated form upon skin application given the mildly acidic pH of human skin.[199] Overall, the results presented above suggest that although topical of NA is not likely to offer direct UV

photoprotection via a typical sunscreen mechanism,[200] it is entirely safe in terms of its intrinsic properties with respect to sun exposure.

Over recent years, advances in ion trapping techniques, often coupled with cryogenic ion cooling have led to a profusion of elegant IR and UV laser photodissociation spectroscopic studies of electrospray generated, gas-phase molecular ions.[12, 19, 39, 90, 201-204] While IR characterisation is generally the tool of choice for obtaining geometric information on a specific system, such studies can present significant challenges due to issues relating to spectral interpretation.[205] In addition, many of these IR ion spectroscopy experiments have used free-electron lasers to produce the IR photons, which produces challenges in terms of logistics and necessarily time-limited access. UV spectroscopy has been demonstrated to be a viable alternative technique for determining the structures of gaseous ions, and some of these studies have already focused on identifying protonated isomers. For example, Trevitt and co-workers have recently used laser photodissociation spectroscopy to measure the UV spectra of protonated quinolone and isoquinoline, generated from separate, isomerically pure solutions.[206] Jouvet and co-workers have conducted a similar experiment on geometric isomers of protonated aminophenol,[72] although using cryogenic cooling to reduce the internal temperature of the ions. In both sets of experiments, the gas-phase UV spectra were indeed distinctive for different isomers. However, the protonated nicotinamide studied in the current work provides a more challenging test system since any protomers must be distinguished from isomers generated in a single solution.

The UV photofragment action spectra for different fragments of NA·H$^+$ are striking in that they display distinctive spectral profiles. These have been readily assigned as arising from the presence of two chromophores for the NA·H$^+$ ion generated via electrospray. These chromophores are associated with two protomers where the proton is attached to either the pyridine centre or the amide group. As discussed above, there have been a small number of very recent studies that have identified similar isomeric molecules using very advanced custom-built instrumentation or complicated two-photon laser techniques,[72, 206, 207] but this is the first study to illustrate that such structural isomers can be identified via the application of table-top low-resolution UV laser spectroscopy in an adapted commercial mass

spectrometer. The results presented herein show the possible potential of this approach as a new method for detecting protomeric molecules. The technique employed here could offer an alternative to the IM-MS technique for molecular systems with suitable chromophores. Further work is warranted to explore the generality of this approach in other protomeric/deprotomeric systems.

3.7 Supplementary Information

3.7.1 Laser Power Dependence of the Photodepletion of Protonated Nicotinamide.

In order to verify that one-photon processes were occurring under the given experimental conditions (300 ms fragmentation time, 1.0 mJ pulse energy) a power study was undertaken at 260 nm, close to the photodepletion maximum of protonated nicotinamide, Figure 3.7. Photodepletion was found to increase linearly with the pulse energy of the laser, indicating that only one-photon processes were occurring during the experiment.
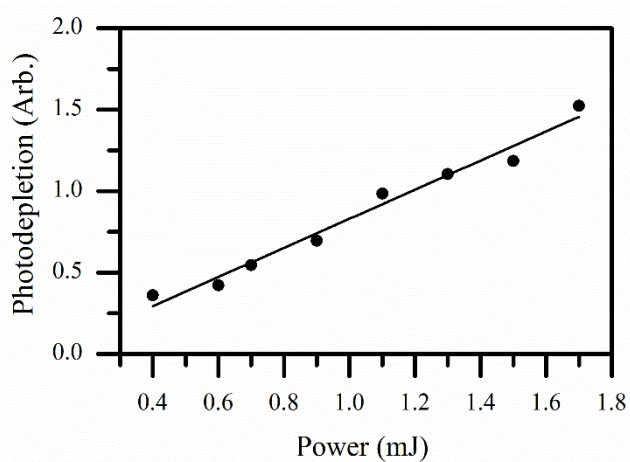
Figure 3.7 Power study comparing the photodepletion of protonated nicotinamide with the average laser pulse energy at 260 nm. The photodepletion shows a linear increase with laser power.

3.7.2 Computational Results: Protonation, Stability and Amide Rotation.

Calculations were conducted as described in Section 3.4. The relative energies of all protonation sites are given in Table 3.2. The relative energies of the aqueous structures of protonated nicotinamide (structures **N1H**, **N8H**, **O9Ha** and **O9Hb**) are given in Table 3.3. A relaxed potential energy scan of the amide group was performed for the **N1H**, **N8H**, **O9Ha** and **O9Hb** structures, in order to calculate the barrier heights for *cis/trans* isomerism. Potential energy scans are given in Figure 3.8, with the corresponding barrier heights given in Table 3.2.

Table 3.2 Relative computed energies of the optimised structural isomers of protonated NA, calculated using the MN12-SX functional with the 6-311+G** basis set.

Structure[a]	Relative Energy (*cis*) / kJ mol^{-1}	Relative Energy (*trans*) / kJ mol^{-1}	Amide Rotation Barrier Height / kJ mol^{-1}
N1H	6.71	0.0	17.43
N8H	111.72	117.44	37.92
O9Ha	53.02	55.52	31.85
O9Hb	44.85	45.37	19.04
C2H	245.70	-	-
C3H	231.24	-	-
C4H	264.98	-	-
C5H	223.16	-	-
C6H	247.51	-	-

a - For atom label definitions, see Figure 3.1.
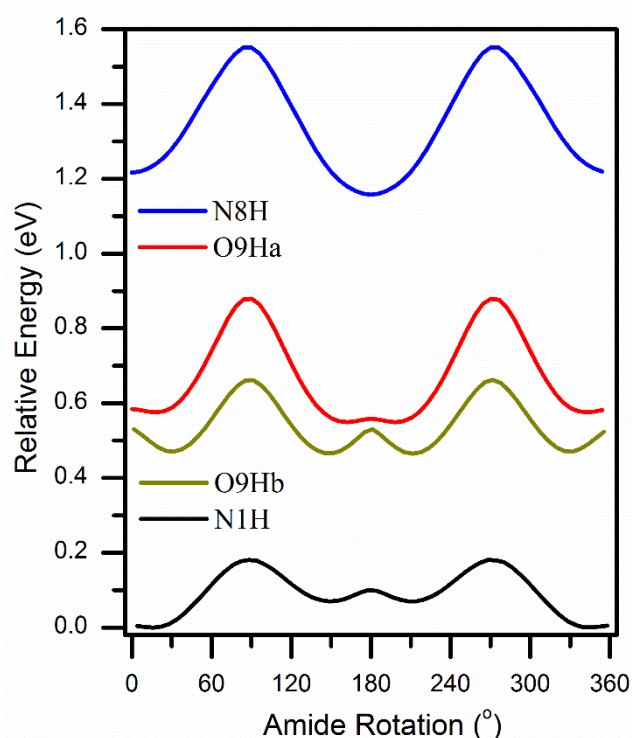
Figure 3.8 Potential energy scans of the rotation of the amide group in nicotinamide, protonated at the pyridine nitrogen (**N1H**), amide nitrogen (**N8H**), amide oxygen with H pointing away from the molecule (**O9Ha**) and amide oxygen with H pointing towards the molecule (**O9Hb**). Structures close to 0º or 360º are *cis*, structures at 180º are *trans*.

Table 3.3 Relative computed energies of the optimised structural isomers of aqueous, protonated NA, calculated using the MN12-SX functional with the 6-311+G** basis set. The solvation was implicitly described using the polariaable continuum model (PCM)

Structure[a]	Relative Energy (*cis*) / kJ mol^{-1}	Relative Energy (*trans*) / kJ mol^{-1}
N1H	1.93	0.0
N8H	90.01	89.96
O9Ha	55.07	54.89
O9Hb	55.46	55.91

a - For atom label definitions, see Figure 3.1.

3.7.3 Collision-Induced Dissociation (CID), Results and Fragmentation.

Low-energy collision induced dissociation (CID) was performed on isolated protonated NA to determine the thermal fragments. Figure 3.9 presents the relative intensities of the protonated NA parent ion, and the corresponding fragment ions as a function of applied CID energy. (The CID energy at which the parent ion intensity decreases to 50% of the total ion intensity, $E_{1/2}$, is 18.6% of the maximum 2.5 V CID energy.)

Figure 3.9 shows that there are three major thermal decay products of protonated NA at m/z = 80, 96 and 106, along with two lower-intensity fragments at m/z = 78 and 124. To establish which of the different possible structures is produced in the CID experiment, structures of potential fragments were optimised using Gaussian 09 and secondary CID experiments were performed. One complication relates to the fact that the excess proton may occupy either the **O9H** or **N8H** position and it may not be possible to definitively determine the distribution of structures that are present in the gas phase using UV spectroscopy. These structures are hence grouped as amide protonated NA; additionally, the **N1H** structure will be referred to as pyridine protonated NA.
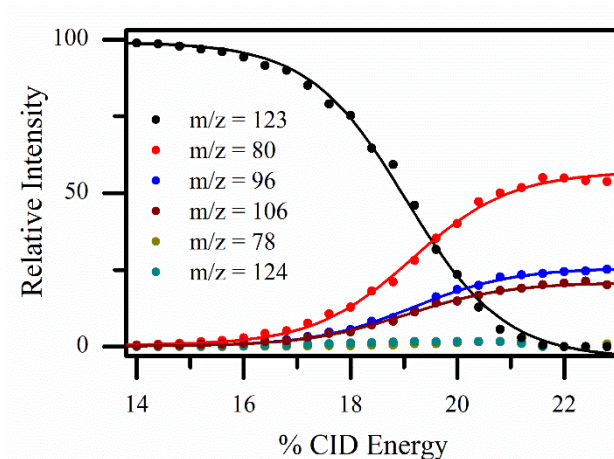
Figure 3.9 % Fragmentation decay curves for protonated nicotinamide upon low energy CID. Onset plots for production of the associated fragment ions are also shown.

The primary CID fragments were isolated within the ion trap and collisionally fragmented (MS3). Secondary CID, Figure 3.10, shows that fragment 106 thermally decays into fragment 78 via the loss of 28 mass units (CO), and that fragment 106 can add 18 mass units (H_2O) within the ion trap to produce fragment 124. This suggests that fragment 106 is either **106a** or **106b** (Section 3.7.2). Additionally, fragment 96 shows a very low conversion into fragment 78 (loss of 18 mass units) upon collisional heating. The addition of 18 mass units to fragment 78 to produce fragment 96 again occurs spontaneously within the ion trap. The high intensity of fragment 96 in the CID experiment suggests that secondary production from fragment 78 (which only appears in trace intensities) is unlikely to be significant, and therefore direct production should dominate. The low efficiency of fragmentation via the loss of water suggests that fragment 96 is primarily produced as a species that is chemically isolated from fragment 78, i.e. **96b** produced from **N1H** (Scheme 3.3). Fragment 80 was only produced directly from protonated nicotinamide and did not thermally fragment.

The overall energy change required to produce each of the CID fragments has been investigated computationally. The overall energy change required to produce a fragment is different from the activation energy of a mechanism, the total change is,

however, indicative of which mechanisms can occur. The production energy of a fragment is estimated as the difference in electronic energy between the fragment and neutral loss with the parent ion. The MN12-SX functional was used to optimise potential fragment structures and neutral loss molecules using the 6-311+G** basis set. The reference energies of protonated NA were taken from the lowest energy structures of pyridine protonated and amide protonated NA (*trans*-**N1H** and *cis*-**O9Hb**, respectively). The production energies are given in Table 3.4. Suspected primary CID fragments are given in Scheme 3.1 and proposed low-intensity CID fragments with $m/z = 78$ and 124 are given in Scheme 3.2.
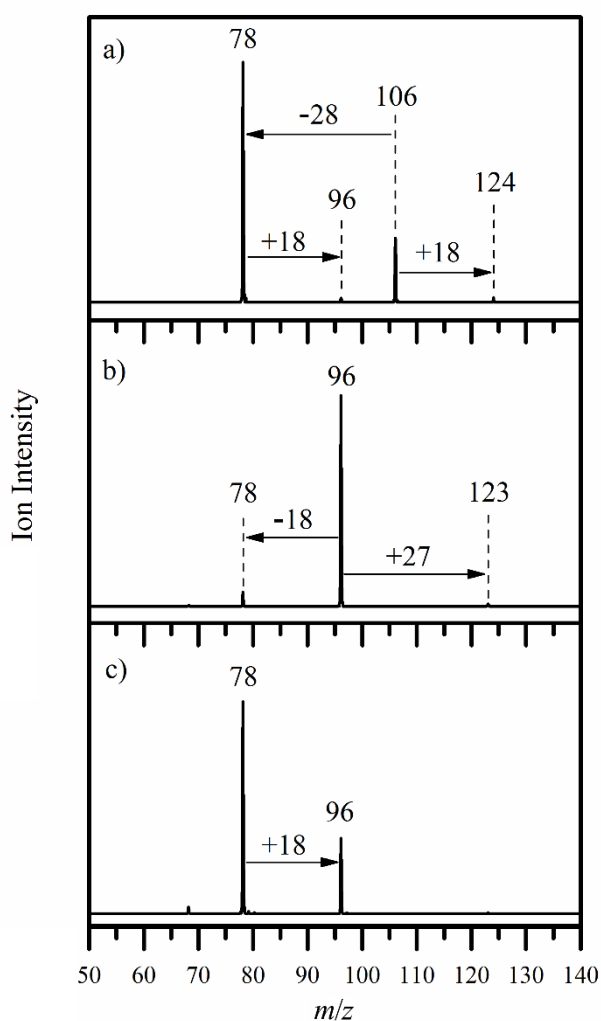
Figure 3.10 Secondary CID (MS3) mass spectra of the collision-induced decay fragments with $m/z =$ a) 106, b) 96 and c) 78. Fragments were isolated following the CID of protonated nicotinamide with 20% of the maximum CID energy. The mass spectra were recorded using CID energies of 22%, 28% and 0% for ions with $m/z =$ 106, 96 and 78, respectively.

Table 3.4 Calculated production energies of the proposed collision-induced dissociation fragments of protonated nicotinamide. Fragment production energies are relative to the structures of the lowest energy amide and pyridine protonated nicotinamide structures dependent on the production route.

Fragment		Initial Structure	Neutral Loss	Production Energy (eV)
106	a	**O9H**	NH_3	2.04
	b	**N1H**	NH_3	4.07
96	a	**O9H**	HCN	3.30
	b	**N1H**	HCN	1.57
80	a	**O9H**	HNCO	2.79
	b	**N1H**	HNCO	0.670
78	a	**O9H**	H_3NCO	4.81
	b	**N1H**	H_3NCO	5.01
124	a	**O9H**	-	0.656
	b	**N1H**	-	0.069

Scheme 3.2 Potential structures for the low-intensity ionic fragments of protonated NA produced during CID.
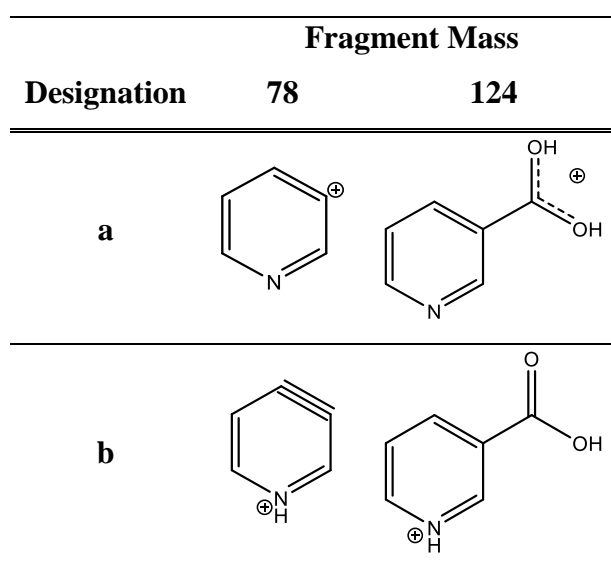
It can be seen that the production of fragment 106 is most favourable as the direct loss of ammonia from the protonated amide side chain. Production of fragment 106 via the loss of a radical or from the **N1H** structure is prohibitively unfavourable, compared with the production of **106a** (Scheme 3.3). Production of fragment 96 is slightly more comparable between **N1H** and **O9H** than fragment 106. However, a difference of more than 1.7 eV favouring production from **N1H** suggests that production from pyridine protonated NA must dominate. Production of fragment **80b** from **N1H** is more favourable than production of **80a** from **O9H** by over 2 eV so is assigned as the major production route (Scheme 3.3).

Fragments 78 and 124 show the most similar production energies from **N1H** and **O9H**. For fragment 78, the lowest direct fragment production is calculated at ~1.96 eV over the production of fragment 96, which may explain why it is only seen in trace quantities. Fragment 124 shows the lowest overall production energies for all fragments, however, this fragment can only be produced by replacing an NH_3 with H_2O in the molecule. As such, the production of fragment 124 must be dependent on the concentration of water within the ion trap as well as the ability of protonated NA to fragment via the loss of NH_3, which is the least significant major fragmentation mechanism. Therefore, it is sensible that fragment 124 only appears as a minor fragment.

The calculated energies of production are strongly indicative that the three major CID fragments can only be produced as dominant fragments if more than one isomer is present in the gas phase. Whilst these calculations cannot estimate the activation energy for production, it can be speculated that the quanta of energy required to induce fragmentation under the experimental conditions is ~2-3 eV.

Chapter 3

3.7.4 Scheme of the CID and Photo-induced Fragments of Protonated Nicotinamide.

Scheme 3.3 Flowchart of proposed CID and photodissociation fragments of protonated nicotinamide. Red outlines indicate the lowest energy amide protonated structures and blue outlines show the lowest energy pyridine protonated structures. Structures are grouped according to their production mechanisms.
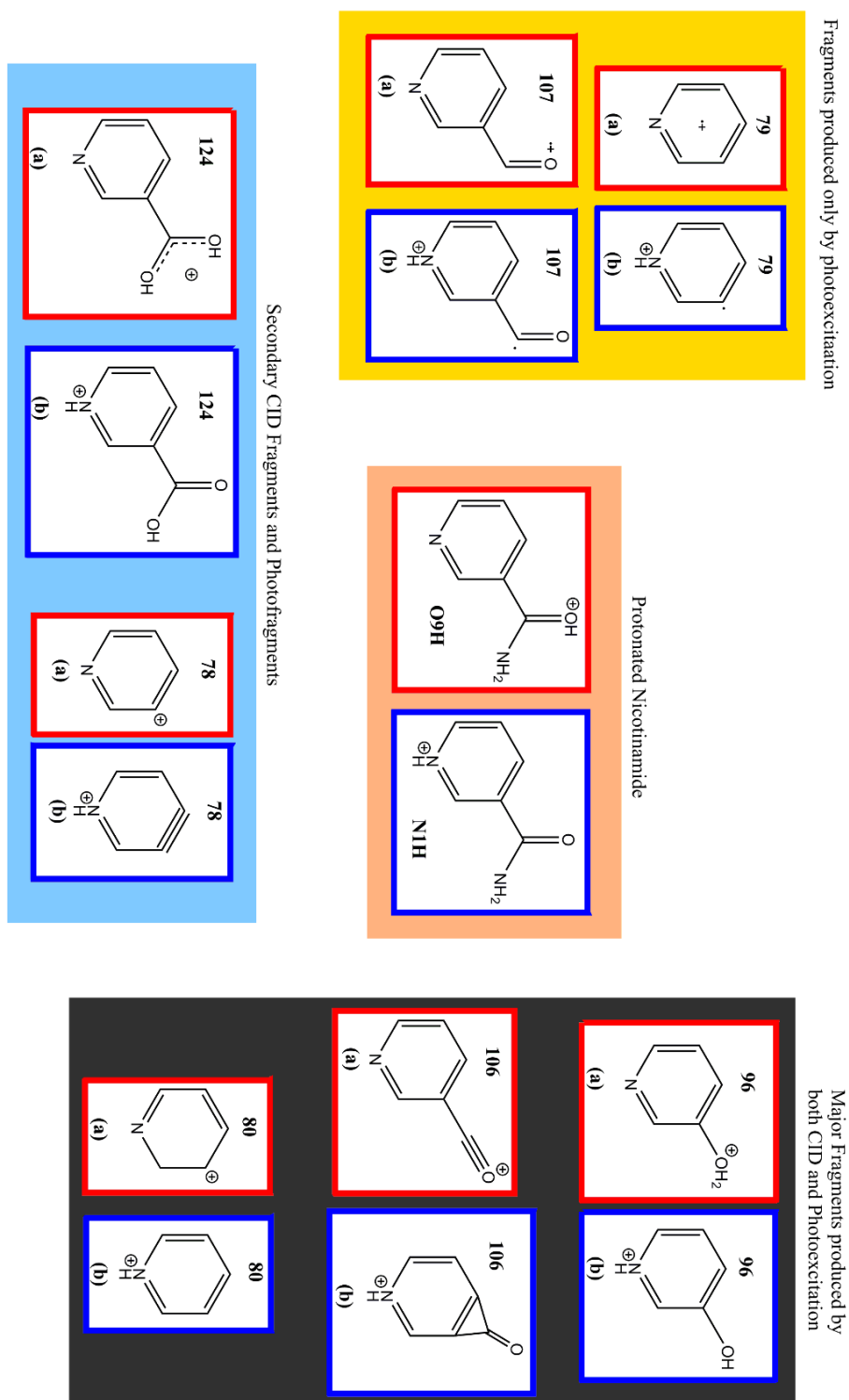
3.7.5 Additional Photofragment Mass Spectra and Action Spectra of minor Photofragments.

3.7.5.1 Additional Photofragment Mass Spectra

Figure 3.11 shows the photofragmentation mass spectra of protonated nicotinamide irradiated at 4.96 and 4.71 eV, these wavelengths are chosen due to them being maxima in the production spectra of fragments 106 and 96, respectively. It can be seen that the relative abundancies of the photofragments (notably $m/z = 80$ and 96) vary significantly with the wavelengths, indicating that the production of these fragments occurs through different absorption bands.
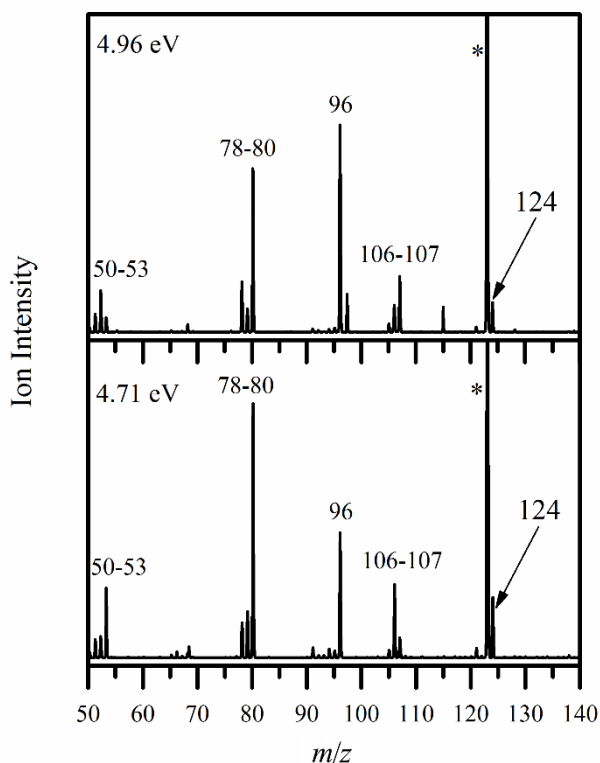
Figure 3.11 Photofragment mass spectra with an excitation photon energy at 4.96 and 4.71 eV. Despite a modest change in photon energies, the ratio between fragments 96 and 106 varies greatly, indicating a different source.* indicates protonated NA ($m/z = 123$).

3.7.5.2 Photofragment Production Spectra of fragments with *m/z* = 78 and 124

Figure 3.12 contains the photofragment production spectra of the low intensity CID fragments with *m/z* = 78 and 124. The photoproduction spectrum of fragment 78, Figure 3.12a, mimics the production spectrum of fragment 96, peaking at 4.92 eV. The similarities between the spectral profiles is strongly indicative of production originating from the pyridine protonated structure. The onset of the production is ~4.0 eV, this is notably larger than the production of intense CID fragments (which are seen below 3.7 eV) reflecting that the thermal production of fragment 78 more unfavourable than the production of intense CID fragments. We note that there is no resolved feature in the production spectrum of 78 relating to secondary fragmentation of fragment 106, seen during secondary fragmentation of fragment 106. An explanation for this is that the secondary reaction of fragment 106 becomes prominent above 5.2 eV, this is a region where the production of fragment 78 is intense, which may mask the additional production.

Fragment 124 has previously been observed in the MS3 CID spectrum of fragment 106, its production was attributed to the addition of water in the ion trap to produce protonated nicotinic acid (*m/z* = 124). The photoproduction spectrum of fragment 124, Figure 3.12b, shows a production onset of ~3.8 eV leading to a production maximum at 4.73 eV before decreasing to zero at 5.8 eV, the spectral profile mimics the production spectrum of fragment 106. Fragment 124 can be assigned as a secondary fragment of 106, produced through the addition of water in the ion trap. Similar to fragment 78, the low production intensity below 4 eV is reminiscent of the low intensity during CID.

It can be concluded that the photoproduction of fragments 78 and 124 occurs in the electronic ground state, following internal conversion from the excited-state surface via a similar process to fragments 106, 96 and 80. These fragments have an onset of production that occurs within the experimental range that is larger than the onset of fragments 80, 96 and 106. The production onset is directly related to the activation energy of production in the electronic ground state and hence explains the low intensity in the CID experiment. In the high-energy spectral region of the experiment,

these fragments resolve the chromophores relating to production from pyridine and amide protonated nicotinamide.
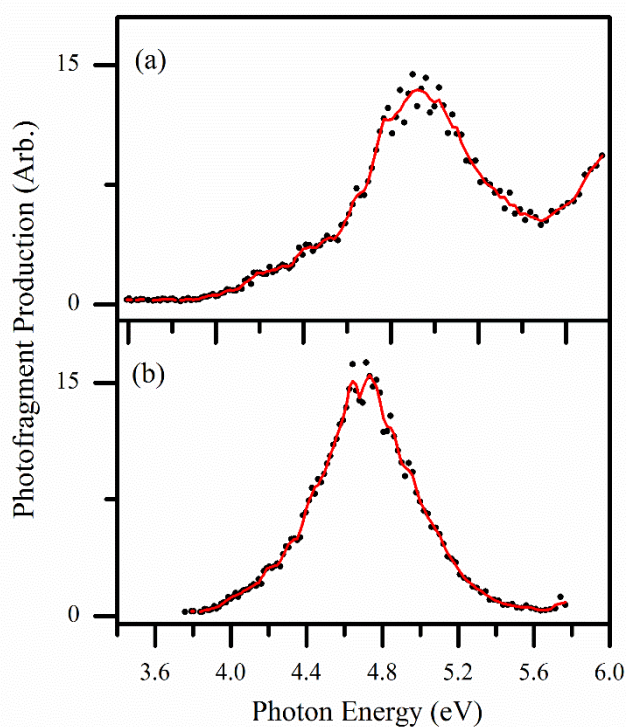
Figure 3.12 Photofragment action spectra of fragments with m/z = a) 78 and b) 124, across the range 3.55 – 5.8 eV. A three-point adjacent average curve is included for each plot.

3.7.5.3 Photofragment Production Spectra of fragments with m/z = 79 and 107

The photoproduction action spectra of fragments 79 and 107 are given in Figure 3.13. Potential structures of fragments 79 and 107 are given in Scheme 3.4 and computational estimations of the production energies are given in Table 3.5. The action spectrum of fragment 79, Figure 3.13a, strongly resembles the production spectrum of fragment 106, with two resolved peaks at 4.20 and 4.75 eV, suggesting a common origin. Fragment 79 is therefore likely to be the radical cation of pyridine (**79a**) produced from amide protonated NA. Interestingly, the production of this fragment from **O9H** is calculated to have an overall production energy of 4.34 eV in the ground state. Since the fragment is produced well below the calculated production energy, we speculate that the pyridine radical cation is therefore produced in a dissociative excited state. The observation of fragment 79 with a similar intensity

86

to fragments 106 and 124 (Figure 3.12), which are produced with similar spectral profiles, suggests that excited state fragmentation is competitive with electronic relaxation. The major difference between the spectral profile of fragment 79 with other amide protonated fragments is the increase in production intensity above 5.4 eV. In this region, the production of fragments 106 and 124 troughs. This change is indicative of a second source of fragment 79.

Fragment 107 is produced via the loss of an NH_2 radical (16 mass units) from protonated NA. The production spectrum, Figure 3.13b, has an onset at 4.26 eV with production increasing to a maximum at 5.10 eV before decreasing to zero by 5.8 eV. Production of **107a** from **N1H** and **107b** from **O9H** has been calculated to be unfavourable by 4.81 and 5.57 eV, respectively, production from **N1H** is therefore likely to dominate. The production maximum is blue-shifted by ~0.25 eV from the photodepletion maximum. This is likely to be due to the production of this species being hindered by the activation energy for this process over the photodepletion maximum of 4.85 eV. The decrease in production to zero from 5.1 to 5.8 eV can be explained by MS3 CID performed on 107 photofragments, as 107 is seen to thermally decay to fragment 79 (Figure 3.14). Above an excitation energy of 5.1 eV, it is likely that the internal energy present in the 107 fragments, following its photoproduction, is sufficient to induce further fragmentation via the loss of CO. This behaviour is reminiscent of fragment 106. The secondary production of fragment 79 may explain the increase in the production spectrum of fragments 79 above 5.2 eV.
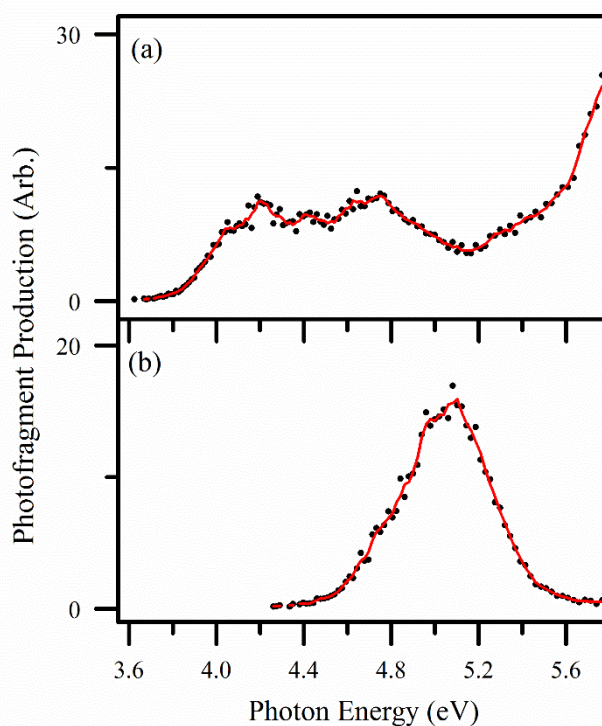
Figure 3.13 Photofragment action spectra of fragments with m/z = a) 79 and b) 107, across the range 3.55 – 5.8 eV. A three-point adjacent average curve is included for each plot.

Scheme 3.4 Schematic structures of the proposed photofragments of protonated NA

	Fragment Mass-to-Charge Ratio	
Designation	79	107
a		
b		
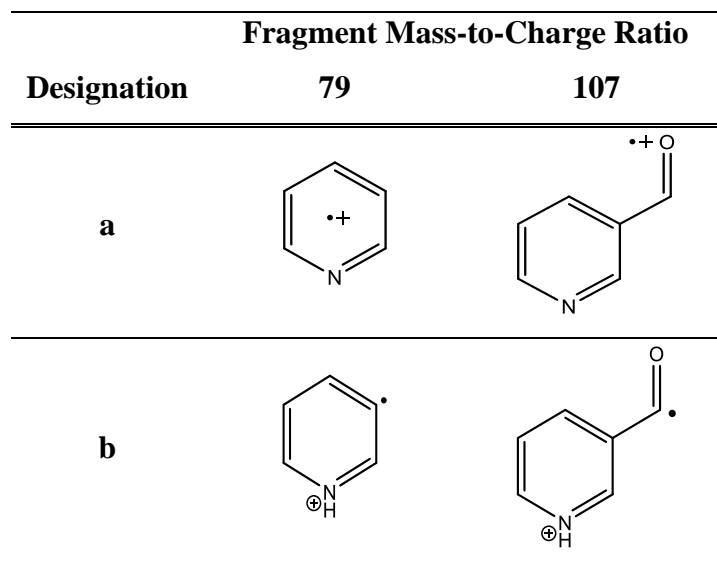
Table 3.5 Calculated production energies of the suspected photodissociation fragments of protonated nicotinamide. Fragment production energies are relative to the structures of the lowest energy amide and pyridine protonated nicotinamide structures dependent on the production route.

Fragment		Initial Structure	Neutral Loss	Production Energy (eV)
79	a	**O9H**	$\cdot OCNH_2$	4.34
	b	**N1H**	$\cdot OCNH_2$	4.60
107	a	**O9H**	$\cdot NH_2$	5.57
	b	**N1H**	$\cdot NH_2$	4.81
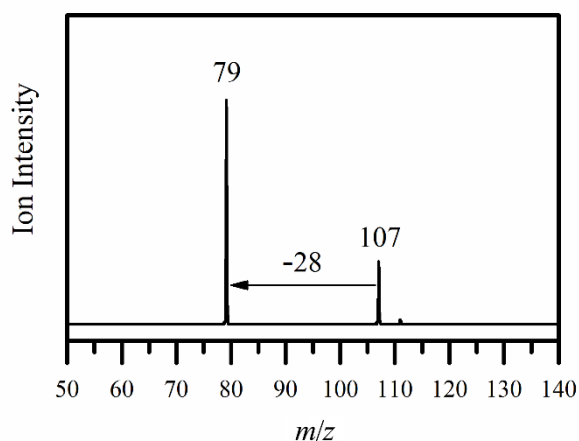
Figure 3.14 Secondary CID (MS3) mass spectrum of the photofragment with $m/z = 107$. Fragment 107 was isolated following the irradiation of protonated nicotinamide at 260 nm. CID was performed on fragment 107 using 16 % of the maximum 2.5 V CID energy.

3.7.5.4 Photofragment Production Spectra of fragments with $m/z = 50, 51, 52$ and 53

Figure 3.15 shows the production spectra of the photofragments with $m/z = 50 - 53$. These fragments are commonly seen as fragment markers for pyridine rings. The structures and fragmentation mechanisms of these fragments are not considered in detail in this work. As with other fragments discussed above, there is a distinction within the photoproduction spectra of fragment production peaking around 4.73 eV ($m/z = 50$ and 53) and 4.96 eV ($m/z = 51$ and 52). This behaviour can be attributed to production of these fragments from either amide or pyridine protonated nicotinamide precursors.
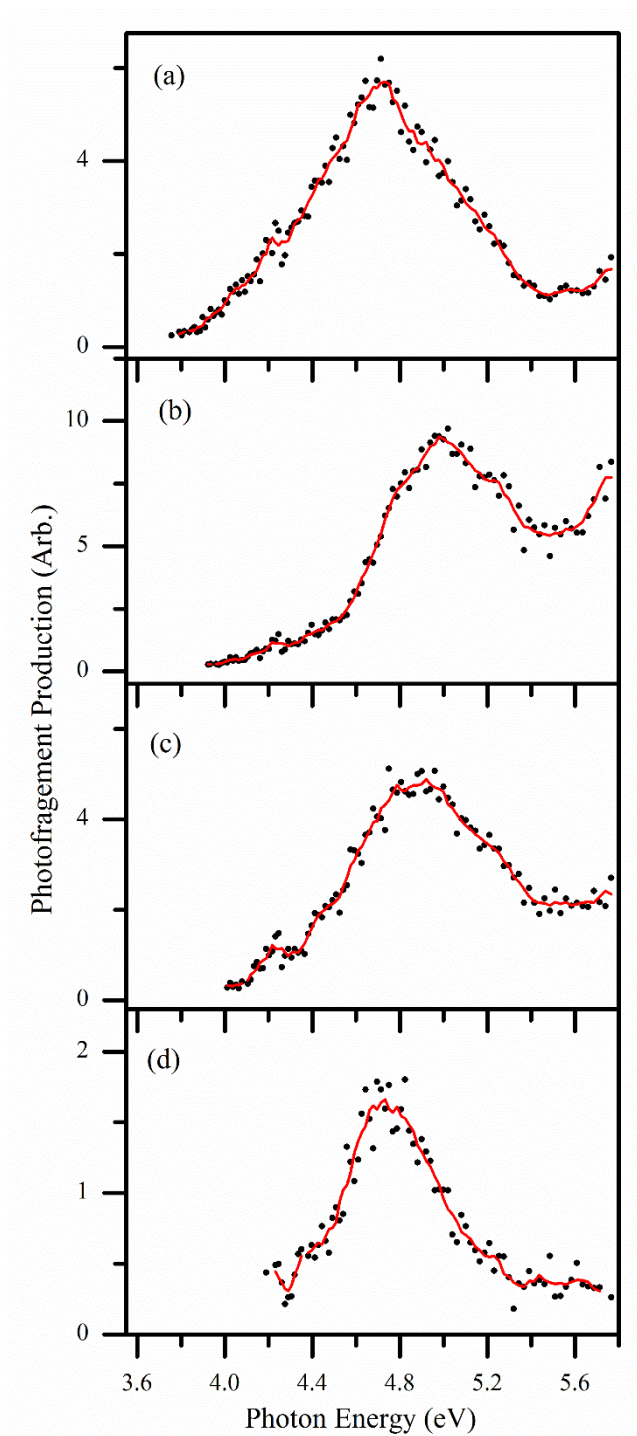
Figure 3.15 Photoproduction spectra of the photofragments of protonated NA with *m/z* = a) 53, b) 52, c) 51 and d) 50, across the range 3.55 – 5.8 eV. A three-point adjacent average curve is included for each plot. Fragments 53 and 50 show an intense production band at ~4.7 eV whereas fragments 52 and 51 peak at 4.9 eV.

3.7.6 TD-DFT Excitation Spectra of the Protonation Site Isomers of Nicotinamide.

Time-dependent density functional theory (TDDFT) has been used to calculate the excitation spectra of protonated nicotinamide. The MN12-SX functional, using the 6-311+G** basis set, produced absorption spectra that qualitatively reproduced the trends in the photoproduction spectra, Figure 3.4. TDDFT consistently overestimated the gaseous excitation energies by 0.5 eV for all of the structures of protonated nicotinamide, the spectra have therefore been offset by 0.5 eV for comparison with experimental results. The average of the TDDFT spectra for the conformational isomers (*cis*/*trans*) of each optimised structural isomer (**N1H**, **O9Ha**, **O9Hb**, **N8H**) is given in Figure 3.16. The energies and oscillator strengths for the calculated electronic transitions are given in Tables 3.6-3.9. When offset by 0.5 eV, the excitation spectra of the **N1H** and **O9Ha** structures most accurately reproduced the gaseous absorption maxima observed in the photoproduction spectra. The nature of the orbitals involved in the strong electronic transitions have been inspected and are given in Tables 3.6-3.9. It can be seen that the only structure to possess distinguishable n → π* transitions from the lone pairs in the amide group is the pyridine protonated structure. The absence of these n → π* transitions for amide protonated nicotinamide is likely to be as a result of the protonation of the carbonyl group.
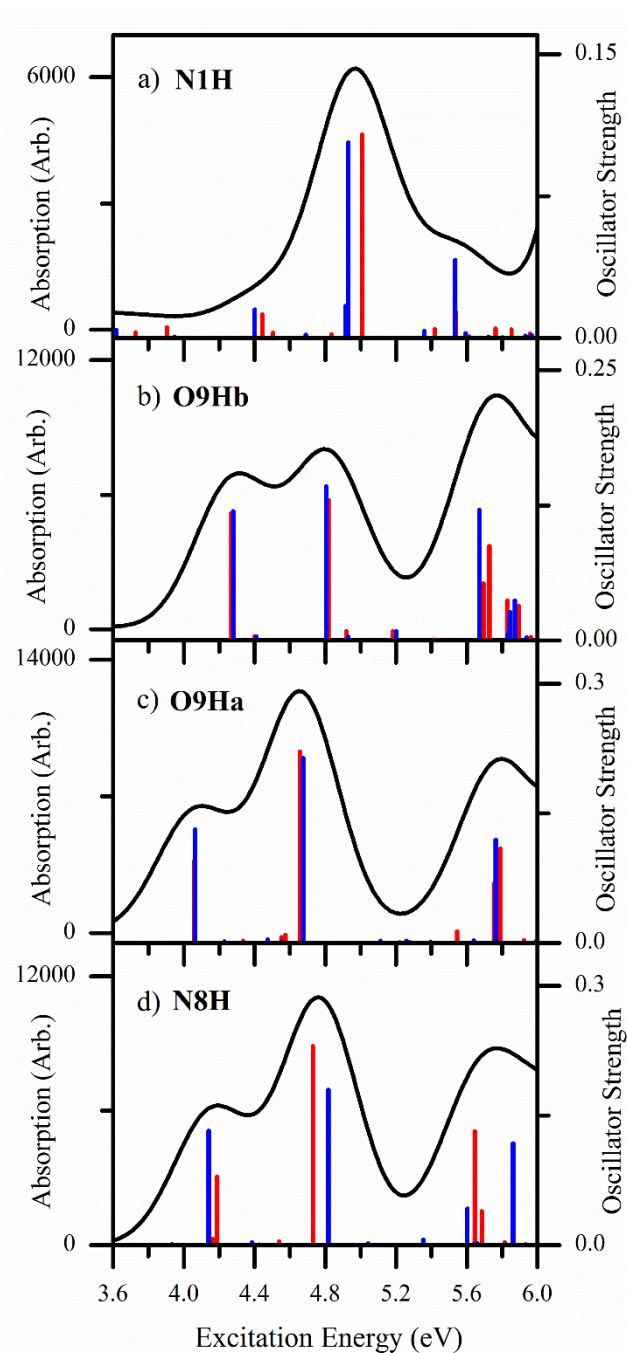
Figure 3.16 Calculated TDDFT excitation spectra of protonated nicotinamide averaged between the *cis* and *trans* structures of: a) **N1H**, b) **O9Ha**, c) **O9Hb** and d) **N8H**, calculated using the MN12-SX functional and shifted by 0.5 eV to lower excitation energies for comparison with the experimental results. The oscillator strengths of individual transitions are given by the vertical bars. The red and blue bars indicate electronic transitions from the *cis* and *trans* structures, respectively. The full line spectrum represents a convolution of the calculated electronic transitions with Gaussian functions (0.25 eV HWHM).

Table 3.6 Calculated transition energies and oscillator strengths of *cis* and *trans* structures of the **N1H** structure from TDDFT calculations with the MN12-SX functional, shifted by 0.5 eV to lower excitation energies for comparison with the experimental results. Only transitions with oscillator strength > 0.005 are listed.

Transition Energy (eV)	Oscillator Strength
cis-**N1H** Amide n → π* Transitions [a]	
3.90	0.0057
4.44	0.0126
cis-**N1H** π → π* Transitions	
5.01	0.1075
5.54	0.0139
cis-**N1H** Amide n → σ* Transitions [a]	
5.76	0.0051
trans-**N1H** Amide n → π* Transitions [a]	
3.38	0.0097
4.40	0.0151
trans-**N1H** Amide n → σ* Transitions [a]	
4.91	0.0169
trans-**N1H** π → π* Transitions	
4.93	0.1034
5.53	0.0413

[a] Transitions originate from orbitals with electron density in the oxygen and nitrogen lone pairs of the nicotinamide

Table 3.7 Calculated transition energies and oscillator strengths of *cis* and *trans* structures of the **O9Hb** structure from TDDFT calculations with the MN12-SX functional, shifted by 0.5 eV to lower excitation energies for comparison with the experimental results. Only transitions with oscillator strength > 0.005 are listed.

Transition Energy (eV)	Oscillator Strength
cis-**O9Hb** π → π* Transitions	
4.27	0.1177
4.82	0.1298
5.73	0.0873
cis-**O9Hb** n → σ* Transitions	
4.92	0.0087
5.83	0.0367
cis-**O9Hb** π → σ * Transitions	
5.18	0.0082
5.69	0.0528
5.90	0.0319
trans-**O9Hb** π → π* Transitions	
4.28	0.1196
4.81	0.1424
5.67	0.1208
trans-**O9Hb** n → σ* Transitions	
5.20	0.0087
5.84	0.0262
5.87	0.0371

Table 3.8 Calculated transition energies and oscillator strengths of *cis* and *trans* structures of the **O9Ha** structure from TDDFT calculations with the MN12-SX functional, shifted by 0.5 eV to lower excitation energies for comparison with the experimental results. Only transitions with oscillator strength > 0.005 are listed.

Transition Energy (eV)	Oscillator Strength
cis-**O9Ha** π → π* Transitions	
4.06	0.0953
4.66	0.2214
5.79	0.1092
cis-**O9Ha** n → π* Transitions	
4.55	0.0066
cis-**O9Ha** π → σ * Transitions	
4.58	0.0094
5.55	0.0133
5.75[a]	0.0688
trans-**O9Ha** π → π* Transitions	
4.06	0.1312
4.67	0.2141
5.76	0.1191

a – Initial orbital is a lone pair on the pyridine nitrogen.

Table 3.9 Calculated transition energies and oscillator strengths of *cis* and *trans* structures of the **N8H** structure from TDDFT calculations with the MN12-SX functional, shifted by 0.5 eV to lower excitation energies for comparison with the experimental results. Only transitions with oscillator strength > 0.005 are listed.

Transition Energy (eV)	Oscillator Strength
cis-**N8H** π → π* Transitions	
4.19	0.0791
4.73	0.2305
5.65	0.1319
cis-**N8H** n → σ* Transitions	
4.16	0.0073
5.69	0.0394
trans- **N8H** π → π* Transitions	
4.14	0.1323
4.82	0.1797
5.60	0.0421
5.86	0.1179
cis-**N8H** n → σ* Transitions	
5.35	0.0064

3.7.7 Estimating the Relative Abundancies of the Gaseous Protomers of Nicotinamide.

Two methods were employed to estimate the abundancies of the gaseous structures of protonated nicotinamide: A simple comparison of the photoproduction of fragments and a Beer-Lambert analysis of the absorption (photodepletion) of gaseous NA using TDDFT. The first method directly compares the production of photofragments that are associated with either the amide or pyridine protonated structures. The percentage of the gaseous population in the amide form is given by Equation 3.3:

$$\% \text{ Amide} = 100 \times \frac{\Sigma PF_{263}}{\Sigma PF_{263} + \Sigma PF_{250}} \tag{3.3}$$

where PF_{263} and PF_{250} are the photofragment production intensities of fragments that peak at 263 nm (4.73 eV, m/z = 50, 53, 79, 106 and 124) and 250 nm (4.96 eV, m/z = 51, 52, 78, 96 and 107), respectively. Fragment 80 is not included due to its involvement in both chromophores. This method compares ΣPF_{263} recorded at 263 nm with ΣPF_{250} recorded at 250 nm, it must therefore be assumed that the peak absorption coefficients of the different structures of protonated NA are similar. The results of the fragment production (Fragment Prod.) comparison are given in Table 3.10.

The second method splits the total absorption of protonated nicotinamide into the sum of its constituent parts, described using the Beer-Lambert law. Absorption coefficients of the amide and pyridine protonated structures of nicotinamide can be approximated using computational (TDDFT) absorption spectra. (We note that there can be considerable uncertainties in these calculated intensities, but is a useful for comparison with the results above.) By taking absorption measurements using two excitation wavelengths (263 and 250 nm), the relative abundancies of the protomers of nicotinamide can be algebraically determined, Equations 3.4 – 3.9:

$$A_{263} = x_{N1}\, \varepsilon_{N1,263} + x_{O9}\, \varepsilon_{O9,263} \tag{3.4}$$

$$A_{250} = x_{N1}\, \varepsilon_{N1,250} + x_{O9}\, \varepsilon_{O9,250} \tag{3.5}$$

$$\frac{1}{A_{263}}\left(x_{N1}\,\varepsilon_{N1,263} + x_{O9}\varepsilon_{O9,263}\right) = \frac{1}{A_{250}}\left(x_{N1}\,\varepsilon_{N1,250} + x_{O9}\varepsilon_{O9,250}\right) \quad (3.6)$$

$$x_{N1}\left(A_{250}\,\varepsilon_{N1,263} - A_{263}\varepsilon_{N1,250}\right) = x_{O9}\left(A_{263}\,\varepsilon_{O9,250} - A_{250}\varepsilon_{O9,263}\right) \quad (3.7)$$

$$\frac{x_{N1}}{x_{O9}} = \frac{A_{263}\,\varepsilon_{O9,250} - A_{250}\varepsilon_{O9,263}}{A_{250}\,\varepsilon_{N1,263} - A_{263}\varepsilon_{N1,250}} \quad (3.8)$$

$$\%\,\text{Amide} = 100 \times \frac{\dfrac{x_{O9}}{x_{N1}}}{1 + \dfrac{x_{O9}}{x_{N1}}} \quad (3.9)$$

where A_n is the gaseous absorption (photodepletion) at wavelength n. x_m is the abundance of ionic species m. $\varepsilon_{m,n}$ is the absorption coefficient of ionic species m at wavelength n. The absorption coefficients of the pyridine and amide protonated structures were taken from the Gaussian-convoluted (0.25 eV HWHM), calculated TDDFT absorption spectra of **N1H** and **O9Ha**, respectively, offset by 0.6 eV. The absorption coefficients of the **N1H** and **O9Ha** structures were taken as an average of the *cis* and *trans* isomers, owing to the similar energies of these conformational isomers (Section 3.7.1). For comparison, absorption coefficients were taken at the experimentally observed maxima (263 and 250 nm) and the computationally observed maxima (259 and 249 nm).

The abundancies of the amide and pyridine protonated structures of NA have been estimated using two datasets: data from the absorption spectrum presented in Figure 3.2a and a study taking longer averages of the absorption at 250 and 263 nm. The second dataset directly compares the gaseous populations of protonated NA upon varying the solvent between water and acetonitrile.

Table 3.10 Calculated percentage abundance of the amide protonated structure of nicotinamide produced via ESI of NA in water or acetonitrile. Data are taken from two datasets: data used in the absorption spectrum of protonated NA and data collected solely at 250 and 263 nm. Two methods are used to determine the abundance of the amide protonated structure: comparison of the photofragment production; and a Beer-Lambert analysis of the absorption using calculated (TDDFT) absorption values at 250 and 263 nm as well as 249 and 259 nm.

Solvent	Absorption Spectrum Data			Fixed Wavelength Data (250, 263 nm)		
	Fragment Prod.	TDDFT ε_{max}		Fragment Prod.	TDDFT ε_{max}	
		Exp. (250, 263 nm)	Comp. (249, 259 nm)		Exp. (250, 263 nm)	Comp. (249, 259 nm)
ACN	-	-	-	42.5	37.9	17.9
Water	46.1	27.2	6.05	45.5	44.1	24.7

Chapter 4

Experiment and theory confirm that UV laser photodissociation spectroscopy can distinguish protomers formed via electrospray

4.1 Preamble

The following work has been published in the journal *Physical Chemistry Chemical Physics*. All data, including experimental and computational, have been collected by me. Data processing routines and the interpretation of the results have also been performed by me. The initial draft of the manuscript was written by me and revised by Caroline Dessent.

Electronic supplementary information (ESI) which was included with the publication is appended to this Chapter as Section 4.7. This includes laser power studies; computational results; solution-phase UV absorption spectra; photofragment mass spectra; and a Gaussian fitting of the experimental photofragment production spectra.

Full Reference to the publication:
"Experiment and theory confirm that UV laser photodissociation spectroscopy can distinguish protomers formed via electrospray”

E. Matthews and C. E. H. Dessent, *Phys. Chem. Chem. Phys.*, 2017, **19**, 17434–17440.

http://dx.doi.org/10.1039/c7cp02817b

4.2 Abstract

The identification of protonation sites in electrosprayed molecules remains a challenge in contemporary physical science. We present the first demonstration that low-resolution, UV laser photodissociation spectroscopy can be applied *in situ* to

identify the protomers of para-aminobenzoic acid (PABA) formed *via* electrospray from a single solution. Electronic absorption spectra are recorded *via* photodepletion and photofragmentation for PABA electrosprayed from solutions of water and acetonitrile. Using this approach, two protomers can be straightforwardly identified, with only the carboxylic acid protomer being produced on electrospray from water while the amine-protonated isomer dominates upon electrospray from acetonitrile. High-level SORCI and MRCI calculations are presented to provide insight into the origin of the distinctive electronic spectra displayed by the protomers. Our results are in excellent agreement with previous PABA studies conducted using established techniques, and demonstrate that UV photodissociation spectroscopy of electrosprayed ions has potential as a new diagnostic tool for identifying protomeric species.

4.3 Introduction

The influence of electrospray ionisation on the structure and properties of gaseous ions has been the subject of much debate in recent years, particularly in relation to the influence of electrospray on the location of protonation and deprotonation sites in the ions formed.[9, 10, 22, 88, 98, 153, 154, 156-158, 162, 165, 166, 208] These studies are driven by the importance of acid–base reactions throughout chemistry and biology, so that correctly identifying the structures of protonation and deprotonation isomers can be crucial to understanding reactive processes. Electrospray ionisation has been successfully employed across analytical chemistry for many years, and is now being increasingly used to probe solution-phase reactions and reactive intermediates for both chemical and biochemical systems.[159, 161, 209, 210] The influence of the electrospray process on the location of protonation and deprotonation sites is therefore of ongoing key chemical interest. Moreover, it is of critical importance to develop innovative experimental methods that can determine the structures of gaseous protomers *in situ* following electrospray ionisation.

Protomer formation in small organic molecules following electrospray has been investigated by a number of mass-spectrometry methods. The effect of varying the electrospray source conditions (*e.g.* the solvent used in electrospray) on protomeric ratios was explicitly investigated in a number of these studies.[4,6] The first such

studies employed collision induced dissociation as a structural tool,[10, 153, 208] and both ion mobility mass spectrometry (IMMS),[88,98,138,158,162,165,169] and infrared multiphoton dissociation (IRMPD) were subsequently employed.[9,88,98,154,157] These studies have led to an emerging view that the electrospray conditions can strongly influence the ratios of protomers or deprotomers obtained following electrospray. This conclusion is in distinct contrast with the more traditional view that molecular ion populations obtained *via* electrospray reflect the solution-phase populations.[9,138,154] Ultimately, this situation means that it is essential to have effective methodologies available that can experimentally identify protomeric species formed in the gas phase *via* electrospray.

In a recent study, we investigated the electronic spectroscopy of the protonated form of the vitamin nicotinamide, generated *via* electrospray.[22] Our UV photodissociation (UVPD) results were consistent with two different protomers of nicotinamide being formed upon electrospray. This result suggested that UVPD spectroscopy could have potential as a new diagnostic spectroscopic tool for identifying protomeric isomers formed from a single solution.[72, 206, 211] UV photodissociation spectroscopy has been used to identify gas-phase isomers previously, but in these cases, different protomers were obtained from isomerically pure solutions as shown in References 72, 206 and 211. Protonated nucleobase tautomers have also been studied by UV action spectroscopy.[45, 212, 213] We note that other isomers have been spectroscopically identified by UV photodissociation. Reference 214 provides a recent example where
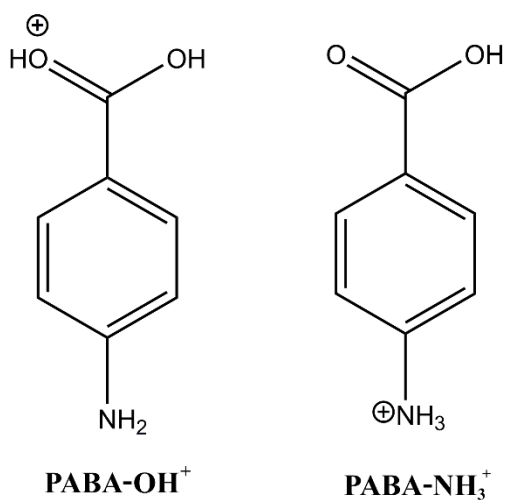
Figure 4.1 Schematic diagram of the **PABA–OH$^+$** and **PABA–NH$_3$$^+$** protomers of PABA·H$^+$, illustrating the lowest energy protonation sites.

Chapter 4

UV action spectroscopy has been used to identify peptide isomers generated *via* electron transfer dissociation. UVPD spectroscopy offers considerable potential as a technique for identifying different protomers as resonant UV absorption is likely to be highly sensitive to the electronic structure of the chromophore.

In this work, we aim to evaluate UVPD for identifying electrosprayed protomers by investigating the prototype molecule, *para*-aminobenzoic acid (PABA). PABA has been extensively studied in both the solution phase and gas phases as a paradigm molecule which possesses two protonation sites (Figure 4.1), namely the carboxylic oxygen (**PABA–OH⁺**) and the amine nitrogen, (**PABA–NH₃⁺**). While the **PABA–OH⁺** protomer is the most stable protomer in the gas-phase, this situation is reversed in the solution phase where **PABA–NH₃⁺** is most stable.[9, 88, 157, 208, 215, 216]

From the previous studies of electrosprayed PABA, it has been established that the gaseous protomers produced depend strongly on the electrospray solvent. Kass and co-workers found that **PABA–OH⁺** was the only gaseous structure when a water/methanol solvent mixture was employed, while both the **PABA–NH₃⁺** and **PABA–OH⁺** protomers were observed when a water/acetonitrile solution was used. [9, 208] These results were subsequently confirmed in an IMMS and IRMPD study.[88] Williams and co-workers were able to demonstrate that the structure of microhydrated PABA·H⁺ moves from the **PABA–OH⁺** isomer to the **PABA–NH₃⁺** structure as the number of solvating water molecules increases.[157] Therefore, in this study, the UVPD spectra of protonated PABA produced from solutions of both water and acetonitrile will be measured, with the expectation that this change in solvent should produce dramatically different gaseous populations of the two possible protomers. This should allow us to firmly establish whether UVPD is able to distinguish such protomeric species, generated from a single solution. High-level SORCI and MRCI calculations are also performed to allow us to confirm the spectroscopic assignments, as well as to provide a basis for understanding any differences in the electronic spectroscopy of different protomers.

Chapter 4

4.4 Methodology

4.4.1 Experimental Methods

The gaseous ion absorption spectra were recorded in vacuo using action spectroscopy. UV photodissociation experiments were conducted in an AmaZon ion-trap mass spectrometer, which was modified for the laser experiments as described in detail elsewhere.[14, 22] UV photons were produced by an Nd:YAG (10 Hz, Surelite) pumped OPO (Horizon) laser, giving ~1 mJ across the range 380–215 nm (3.26–5.77 eV). Scans were conducted using a 1 nm step size. Photofragmentation experiments were run with an ion accumulation time between 20–100 ms with a fragmentation time of 100 ms, ensuring an average of one laser pulse per ion packet. Total absorption is taken as the depletion in ion intensity of mass-selected PABA·H$^+$ ions, following irradiation, according to Equation 4.1:

$$\text{Photodepletion Intensity} = \ln\left(\frac{I_{\text{OFF}}}{I_{\text{ON}}}\right) / P\,\lambda$$

<div align="right">Equation 4.1</div>

where I_{ON} and I_{OFF} are the intensities of the PABA·H$^+$ ion signal with and without irradiation, respectively, P is the tuneable laser power (mJ), and λ the wavelength (nm), following Reference 22. (Section 4.7.1 presents power dependence measurements conducted as part of this work). The photodepletion intensities of mass selected PABA·H$^+$ ions have been averaged at each wavelength across the range 380–215 nm and are plotted against the energy of the excitation photons. The production of photofragments that are associated with the depletion of PABA·H$^+$ ions is calculated using Equation 4.2, where I_{Frag} is the ion intensity of an individual photofragment at a particular wavelength.

$$\text{Photofragment Production} = \left(\frac{I_{\text{Frag}}}{I_{\text{OFF}}}\right) / P\,\lambda$$

<div align="right">Equation 4.1</div>

Solutions of PABA (1×10^{-4} mol L^{-1}) in deionised water or acidified acetonitrile (32 mL acetic acid in 100 mL of MeCN) were introduced to the mass spectrometer through electrospray ionisation (ESI) using a nebulising gas pressure of 10.0 psi, an

injection rate of 300 mL h^{-1}, a drying gas flow rate of 8.0 L min^{-1}, and capillary temperatures of 140 and 200 °C for water and MeCN, respectively. A small volume of acetic acid was added to the MeCN solvent, since this was found to significantly improve the intensity and stability of the electrosprayed PABA·H$^+$ ion signal. Increasing the capillary temperature for MeCN also improved the stability of the ion signal. PABA was purchased from Fisher Scientific Ltd and used without purification. The voltages applied to the ion optics were tuned to maximise the ion signal of PABA·H$^+$ (*m/z* 138) using the automated tuning capabilities of the trapControl (Bruker) software.

4.4.2 Computational Methods

Structures of PABA·H$^+$, protonated at each carbon, nitrogen and oxygen atom, were optimised using the B3LYP/6-311+G(2d,2p) functional and basis set using Gaussian 09.[135, 145, 174, 175, 217, 218] Frequency calculations were performed to ensure that all optimised structures correspond to true energy minima. All optimised structures are given in Section 4.7.2. Time-dependent density functional theory (TDDFT) calculations were performed on the optimised structures of **PABA–NH₃$^+$** and **PABA–OH$^+$**, at the B3LYP/6-311+G(2d,2p) level. The B3LYP optimised structures of **PABA–NH₃$^+$** and **PABA–OH$^+$** were re-optimised at the MP2/6-311+G(2d,2p) level,[219] and these optimised structures were used as starting points in excited state calculations using the quantum chemical package ORCA.[136] Vertical excitation energies were calculated using the SORCI and MRCI methods,[137] with full details of the calculations given in Section 4.7.2. These calculations used a CASSCF(6,6) reference space. Details of the generation and selection of orbitals are also given in Section 4.7.2. All excited-state calculations using ORCA were performed using the aug-cc-pVDZ basis set.[220]

4.5 Results and discussion

4.5.1 Photodepletion absorption spectra of PABA·H$^+$

The UV absorption spectrum of mass-selected PABA·H$^+$, electrosprayed from water, is shown in Figure 4.2a. This spectrum has an absorption onset at 3.3 eV and contains two well-resolved features; a strong band (**I**), observed between 3.4 – 4.1 eV (peaks

Figure 4.2 UV absorption spectra of electrosprayed PABA·H$^+$ ions (*m/z* 138) across the range 3.26 – 5.77 eV (380 – 215 nm), produced from solutions of (a) water and (b) acidified-MeCN. The solid red lines are three-point adjacent averages of the data points.

---

between 3.6–3.8 eV), and a weaker band (**II**) that appears between 4.8–5.4 eV. We note that the "peak" of band **I** appears truncated in the spectrum shown in Figure 4.2a. Power studies conducted at 3.63 eV (Section 4.7.1), show that photodepletion is effectively flat for laser pulse energies >0.6 mJ, indicating that all PABA·H$^+$ ions that spatially overlap with the laser are fragmenting at this excitation energy. Under the experimental conditions (laser pulse energy ~1 mJ), the water-electrosprayed photodepletion spectrum is therefore saturated between 3.55–3.75 eV.

Figure 4.2b displays the corresponding UV absorption spectrum of PABA·H$^+$ formed from electrospray of a solution of acidified MeCN. The difference between this spectrum and the spectrum obtained from water is dramatic. The Figure 4.2b spectrum contains the bands **I** and **II** that were observed in the spectrum of PABA·H$^+$ electrosprayed from water, along with two additional bands; a weak band between 4.5–4.8 eV (**III**) that overlaps with band **II**; and a strong band observed above 5.4 eV which peaks above 5.8 eV (**IV**). We note that fine structure can be seen in bands

II and **III** of Figure 4.2, and this is attributed to vibronic coupling which has been observed in the gaseous electronic absorption spectrum of neutral PABA.[221, 222] The observation of four absorption bands in the spectrum obtained from the MeCN solution, including the previously observed bands **I** and **II**, indicates that there are at least two distinctive species present in the gas phase when the PABA·H$^+$ ion is electrosprayed from MeCN. Since the irradiated ions have been mass-selected, the new species can be unambiguously assigned as a different structural isomer of PABA·H$^+$. The observation of one PABA·H$^+$ protomer when the electospray solvent is protic and two PABA·H$^+$ protomers when the solvent is aprotic is entirely expected from the previous studies reviewed in the introduction.[9, 208] Based on these previous studies, we therefore attribute the UV absorption spectrum obtained by electrospraying from an aqueous solution (Figure 4.2a) as corresponding solely to the **PABA–OH$^+$** protomer, while the spectrum obtained by electrospraying from acetonitrile corresponds to a mixture of the **PABA–OH$^+$** and **PABA–NH$_3^+$** protomers.

Whilst Figure 4.2b clearly shows that two protomers of PABA·H$^+$ are present in the gas phase, the overlap between bands **II** and **III** means that both the **PABA–OH$^+$** and **PABA–NH$_3^+$** isomers are present and cannot be resolved in this spectrum. Photodepletion measures the total absorbance of an ion population and thus combines all of the distinctive photophysical mechanisms that cause ions to fragment. However, it is possible to resolve these separate photoexcitation (and photodecay) channels through inspection of the various photofragmentation channels.[14, 22, 169] Therefore, in the next section, we turn to exploring the photofragmentation behaviour that accompanies excitation of bands **I–IV** in an attempt to resolve the protomeric contributions to each of the absorption bands.

4.5.2 Photofragmentation mass spectra of PABA·H$^+$

Figure 4.3a shows the photofragment mass spectrum of PABA·H$^+$ electrosprayed from an aqueous solution, photoexcited at the absorption maximum of 3.63 eV (peak of band **I**). As discussed above, the structure of the PABA·H$^+$ ion produced under these conditions should be solely **PABA–OH$^+$**. The most prominent fragments in the photofragment mass spectrum (Figure 4.3a) are the *m/z* 120 and 94 fragments. These

Figure 4.3 Photofragment mass spectra of PABA·H$^+$, (a) electrosprayed from an aqueous solution of PABA and excited at 3.63 eV; (b) electrosprayed from a solution of PABA in MeCN and excited at 4.56 eV. * indicates the PABA·H$^+$ ion signal.

fragments have been observed as the primary fragments in previous CID and IRMPD experiments, where they were attributed, respectively, to the loss of water and carbon dioxide from **PABA–OH$^+$**.[9, 208] The production of fragments associated with loss of water and carbon dioxide is entirely consistent with the presence of a protonated carboxylic acid group. Detailed fragmentation mechanisms and production enthalpies of these fragments from the **PABA–OH$^+$** isomer were calculated by Kass.[9] Other prominent photofragments are observed with m/z 65, 77, 92, 93 and 95.

The photofragment mass spectrum of PABA·H$^+$ produced from an electrosprayed solution of MeCN and irradiated at 4.56 eV is given in Figure 4.3b. This spectrum contains all of the photofragments observed in Figure 4.3a, albeit in different ratios, as well as additional prominent fragments with m/z 121 and 139. The m/z 121 fragment is important as it is associated with the loss of NH$_3$, and was observed in the previous CID experiments of Kass and co-workers.[208] The fragment with m/z 139 represents the loss of NH$_3$ followed by the addition of water, which is present within the ion trap, to produce protonated hydroxybenzoic acid. The observation of a

fragment associated with loss of NH$_3$ is strong evidence for the presence of a PABA·H$^+$ protomer that contains a protonated NH$_2$ group. For reference, the photofragment mass spectrum of PABA·H$^+$ electrosprayed from the MeCN solution irradiated at 5.6 eV is given in Figure 4.13 in Section 4.7.4. This spectrum shows that as the photon energy increases, **PABA–NH$_3$$^+$** fragmentation becomes more extensive and favours the production of *m/z* 65. A fragment with *m/z* 65, assigned as C$_5$H$_5$$^+$, was observed as a prominent fragment in a previous IRMPD study of the PABA radical cation and the para-amino benzoyl cation.[21] An additional prominent fragmentation route of **PABA–NH$_3$$^+$** at high photon energies is the loss of a hydrogen radical (*m/z* 137).

4.5.3 Photofragment production spectra of PABA·H$^+$ fragments

Having discussed the identities of the PABA·H$^+$ photofragments, we now turn to exploring the production spectra for the primary photofragments. These spectra are useful as they allow different decay pathways that contribute to the overall photodepletion spectrum to be resolved. For the case where two protomeric species contribute to the overall photodepletion spectrum, inspection of the photofragment action spectra may provide a route for assigning different protomer contributions.

Figure 4.4a shows the production spectrum of the *m/z* 93 photofragment which is produced from PABA·H$^+$ electrosprayed from water. The shape of the spectrum displayed in Figure 4.4a strongly resembles the photodepletion spectrum shown in Figure 4.2a. This observation is unsurprising as the water-electrosprayed PABA·H$^+$ ion is expected to correspond solely to **PABA–OH$^+$**. Bands **I** and **II** appear to display some finer structure that is unresolved for the ambient temperature ions studied here. The photofragment production spectrum also displays two additional weak bands, centred at 4.47 and 5.72 eV, which are indistinguishable from experimental noise in the photodepletion spectrum (Figure 4.4a).

Figure 4.4b presents the summed photofragment production spectra for all of the prominent photofragments that are only observed when PABA is electrosprayed from a MeCN solution, namely *m/z* 121, 137 and 139 (see Figure 4.3b and Figure 4.13). These fragments are primarily associated with the **PABA–NH$_3$$^+$** protomer and

Figure 4.4 Photofragment production spectra of the photofragments with (a) *m/z* 93, from PABA·H⁺ electrosprayed from water; (b) the suim of the fragments with *m/z* 121, 137 and 139, from PABA·H⁺ electrosprayed from MeCN. Fragments are produced following photoexcitation of mass-selected PABA·H⁺ ions, across the range 3.2 – 5.8 eV.

---

therefore resolve the UV spectrum of **PABA–NH₃⁺** with only a minor contamination from **PABA–OH⁺**. Bands **III** and **IV** again display partially resolved sub-structure. Band **IV** is notably weaker in Figure 4.4b when compared to the photodepletion spectrum recorded when electrospraying PABA from MeCN (Figure 4.2b). This can be explained as arising from secondary fragmentation of the primary photofragments between 5.6–5.8 eV. Over this spectral range the photofragments with *m/z* 121 and 139 reduce in intensity, but this reduction is associated with a concomitant increase in the fragment with *m/z* 65, namely $C_5H_5^+$. (Figure 4.13 in Section 4.7.4).

The structure of protonated PABA in aqueous solution was first investigated in 1943 using solution-phase UV absorption spectroscopy, and assigned as **PABA–NH₃⁺**.[216] Following our assignment of the spectrum shown in Figure 4.4b as arising solely from a **PABA–NH₃⁺** protomer, we therefore expect that this spectrum should resemble the aqueous acidic UV-Vis absorption spectrum. For ease of comparison, the solution-phase UV absorption spectra of PABA in both water and MeCN have

been recorded as part of this study, and are included in Section 4.7.3 (Figure 4.12). In both mildly acidic water and MeCN, the absorption onset occurs above 3.8 eV, with three main bands with λ_{max}, of ~4.5, 4.6 and 5.5 eV, strikingly like the spectrum shown in Figure 4.4b which is attributed to **PABA–NH₃⁺**. Indeed, the absence of absorption in the solution-phase spectrum below 3.8 eV suggests that the **PABA–OH⁺** protomer (Gaseous λ_{max} ~ 3.6 eV), is completely absent from the solution phase when the solvent is water or MeCN.

*4.5.4 Calculated excitation spectra of **PABA–OH⁺** and **PABA–NH₃⁺***

Electronic absorption spectra of the **PABA–OH⁺** and **PABA–NH₃⁺** protomers were calculated to determine the nature of the experimental electronic transitions and to test the spectral assignments. Initially, structures of PABA protonated at every carbon, nitrogen and oxygen were calculated using Gaussian 09. The structures were optimised as isolated ions as well as solvated ions with a water or acetonitrile solvent implicitly described using the polarisation continuum model (PCM). Table 4.1 lists the relative energies of the **PABA–OH⁺** and **PABA–NH₃⁺** structures in each local environment. (A complete list of calculated stable gaseous structures and structural energies is given in Section 4.7.2). Table 4.1 shows that in the gas phase, protonation at the carboxylic acid group is more stable than protonation at the amine by 33.7 kJ

Table 4.1 Relative computed energies of the optimised **PABA–OH⁺** and **PABA–NH₃⁺** protomers. Structures were optimised as isolated gaseous ions or as solvated ions, using the PCM method to implicitly describe solvation by water or acetonitrile (MeCN). Energies were calculated using the B3LYP functional with the 6-311+G(2d,2p) basis set.

Solvation Scheme	Relative Electronic Energy / kJ mol⁻¹	
	PABA-OH⁺	**PABA-NH₃⁺**
Gaseous	0.0	33.7
Water	32.9	0.0
MeCN	31.4	0.0

Table 4.2 Experimental and calculated vertical excitation energies (in eV) of the **PABA-OH$^+$** and **PABA-NH$_3^+$** structures of PABA·H$^+$ with the associated oscillator strengths (osc.) given in brackets. Excitation energies are predicted using the multi-reference configuration interaction (MRCI) and spectroscopy oriented CI (SORCI) methods.[a]

Excitation	PABA-OH$^+$			PABA-NH$_3^+$		
	Exp.	SORCI (osc.)	MRCI (osc.)	Exp.	SORCI (osc.)	MRCI (osc.)
S$_1$←S$_0$	3.51	3.73 (0.675)	3.58 (0.625)	4.56	4.72 (0.008)	4.50 (0.070)
S$_2$←S$_0$	4.41	4.45 (0.005)	4.26 (0.000)	5.58	5.84 (0.061)	5.60 (0.279)
S$_3$←S$_0$	4.89	5.09 (0.148)	4.89 (0.164)	-	6.68 (0.811)	6.23 (0.511)
S$_4$←S$_0$	5.67	5.87 (0.018)	5.71 (0.003)	-	6.75 (0.578)	6.30 (0.681)

[a] Details of the calculations are given in Section 4.7.2.

mol^{-1}. Upon solvation (in either water or acetonitrile), the relative energies of these structures swap to favour protonation at the amine, the carboxylic acid protonated structure is less stable by 32.9 and 31.4 kJ mol^{-1} in water and MeCN respectively. These calculations are in good agreement with the previously calculated proton affinities.[9, 208]

The excitation spectra of the two observed protomers of PABA have been calculated using the MRCI and SORCI methods, implemented by the quantum chemistry package ORCA. Table 4.2 lists the calculated and experimental vertical transition energies and transition intensities across the experimental spectral range. The experimental vertical transition energies of **PABA–OH$^+$** and **PABA–NH$_3^+$** were taken from the lowest-energy deconvoluted band components of bands **I**–**IV**. The

Chapter 4

experimental photofragment production spectra (Figure 4.4) have been fitted to Gaussian functions in Section 4.7.5 (Figure 4.14).

Table 4.2 shows that both the SORCI and MRCI computational methods can accurately predict the vertical transitions observed in the experimental spectrum. With **PABA–OH$^+$**, both methods predict excitation to the first excited state (band **I**) to be the most intense transition, with excitations around ~4.9 eV being considerably weaker. Notably, both calculation methods predict the existence of two weak bands around 4.4 and 5.7 eV, and although these bands are not well resolved in the experimental photodepletion spectrum, they are clearly present in the photofragment production spectrum of the *m/z* 93 photofragment (Figure 4.4a). This confirms that the photofragment-resolved peaks are caused by weak electronic transitions and are not artefacts relating to experimental error or multi-photon effects. For **PABA–NH$_3^+$**, the computational transitions confirm that this protomer is not associated with any UV absorption below ~4.5 eV. Both methods additionally show that the absorption cross section of band **III** is significantly weaker than band **IV**, reproducing the trends observed in the photodepletion spectrum (Figure 4.2b). The calculated oscillator strengths suggest that **PABA–OH$^+$** is spectrally brighter than **PABA–NH$_3^+$** across the experimental range, with the MRCI calculations predicting band **I** to be more than twice as bright as band **IV**. This trend is indeed observed in the photodepletion spectra, with the maximum absorption of the **PABA–OH$^+$** protomer occurring with approximately three times the maximum absorption of the **PABA–NH$_3^+$** protomer. When comparing the two computational methods, the MRCI method is more accurate, with a mean absolute error (MAE) across the six transitions of 0.07 eV compared with 0.17 eV for SORCI excitations. The reference space molecular orbitals that were used in the MRCI and SORCI excited-state calculations are given in Section 4.7.2, along with a tabulated list of the orbital transitions that contribute to each excitation. We note that the nature of all of the experimental excitations are π - π*.

TDDFT excitation spectra were calculated for both protomers of PABA·H$^+$, and these results are also presented in Section 4.7.2. TDDFT correctly predicts that the onset of electronic absorption of the **PABA–OH$^+$** structure occurs at lower photon energies than the **PABA–NH$_3^+$** structure. TDDFT also correctly predicts that the

brightest transitions across the studied spectral range are π - π^* in nature. However, while the TDDFT calculations clearly reproduce the key trends of the experimental data, they struggle to accurately reproduce the experimentally observed transition energies.

4.5.5 Quantitative analysis of PABA·H$^+$ structure distributions

The above results sections have shown that electronic transitions within the **PABA–NH$_3^+$** protomer only occur above 4.5 eV, any spectral feature below 4.5 eV must therefore be associated with the **PABA–OH$^+$** protomer. As a result of this, the reduction in intensity of band **I** from the water-electrosprayed to MeCN electrosprayed absorption spectra will be solely indicative of the reduction in abundance of the **PABA–OH$^+$** protomer. By measuring the reduction in photodepletion intensity at the 3.63 eV maximum in Figure 4.2a and b (~42 and ~4, respectively), we estimate that the **PABA–OH$^+$** to **PABA–NH$_3^+$** ratio in the MeCN-electrosprayed spectrum is approximately 1 : 9. This indicates a significant reduction in population of the **PABA–OH$^+$** protomer, which was assigned as the sole protomer in the water-electrosprayed spectrum.

4.6 Concluding remarks

The results presented above demonstrate that UVPD spectroscopy within a laser-interfaced commercial mass spectrometer represents a suitable technique for distinguishing between the protomers of the PABA·H$^+$ system. These measurements were facilitated by the fact that when PABA is protonated at the amine or the carboxylic acid group, the electronic structures of the two resulting protomers are distinctive, and therefore their absorption spectral profiles are also very different. While the overall photodepletion spectrum of PABA·H$^+$ contains contributions from the two protomers, the spectral profiles of the individual protomers are clearly resolved when the photofragmentation production spectra of suitable photofragments (unique to a particular protomer) are inspected. The results we present above are entirely consistent with previous studies of electrosprayed PABA, where electrospray from aqueous solutions has been found to result purely in the

PABA–OH$^+$ protomer, whereas a mixture of **PABA–OH$^+$** and **PABA–NH$_3$$^+$** protomers is produced when the solvent is acetonitrile.[9, 208]

An additional key result to emerge from this work is that the protomer-resolved gas-phase ion spectroscopy demonstrated here provides a basis for identifying dominant protomeric species that are present in solution. Comparison of the protomer resolved gas-phase absorption spectra, with the solution-phase UV spectra have revealed that the amine-protonated species is dominant in bulk solution. This result is in line with past analysis of PABA solutions, and is certainly not a surprising result for this very well-characterised system. However, it does demonstrate that the methodology employed here has potential as an important diagnostic tool for identifying protomeric species present in solutions, *i.e.* the UV spectrum of a given protomer is essentially the same in the gas-phase and in the solution phase (ignoring any solvent shift), thus allowing us to identify a species that is present in solution once the same isomer has been spectroscopically identified in the gas phase.

Given the fact that there are now a growing number of fundamental studies that have clearly established that the protonation or deprotonation sites of electrosprayed ions are solvent-dependent,[9, 10, 88, 98, 153, 154, 156, 208] this factor frequently seems to be ignored when protomeric or deprotomeric molecular systems are investigated following electrospray preparation. The number of such studies has grown significantly over recent years,[209, 223] with a particular focus on biologically (or catalytically) relevant molecular systems. It would seem important that the effects of changing solvent on the spectroscopic or spectrometric results are explored, or better still, that the geometric structure of the protomer (or deprotomer) structure is definitively identified prior to further characterisation. To date, in studies where this has been done it was either achieved using IR spectroscopy or *via* ion mobility mass spectrometry (IMMS).[9, 88, 98, 154, 156-158, 162, 165, 166] Both approaches suffer from some limitations: For IR spectroscopy, free-electron lasers are often used to supply the IR photons, which introduces logistical and access restrictions. Alternatively, when bench-top IR OPO/OPA laser systems are employed, there can be problems relating to insufficient absorption of photons in IRMPD to reach the dissociation threshold which can mean that certain protomeric systems are effectively spectroscopically dark.[9] For IMMS, the calculation of reliable collision cross sections for protomeric

systems can be challenging. [98, 158, 165] The results presented in this work illustrate an alternative *in situ* approach for determining protonation sites in electrospray ions with suitable chromophores, using straightforward instrumentation.

Chapter 4

4.7 Supplementary Information

4.7.1 Laser Power Dependence of the Photodepletion of Protonated para-Aminobenzoic acid and Evidence of Secondary Fragmentation

4.7.1.1 Laser Power Studies

The effect of laser power on the logarithmic depletion in ion signal ($\ln[I_0/I]$) of PABA·H$^+$, electrosprayed from an aqueous solution, has been studied at four photoexcitation energies: 3.63, 3.90, 4.90 and 5.06 eV (342, 318, 253 and 245 nm). These excitation energies span the regions of high absorption in the water-ESI absorption spectrum (Figure 4.2a). Figure 4.5 shows that under the experimental conditions, power ~ 1.0 mJ, photodepletion increases near-linearly at 3.90, 4.90 and 5.06 eV, indicating that the experiment is operating under one-photon conditions. With an excitation photon energy of 3.63 eV, the photodepletion flattens above 0.6 mJ. Under these conditions, it can be assumed that absorption is saturated due to complete fragmentation of all ions that overlap with the laser beam.
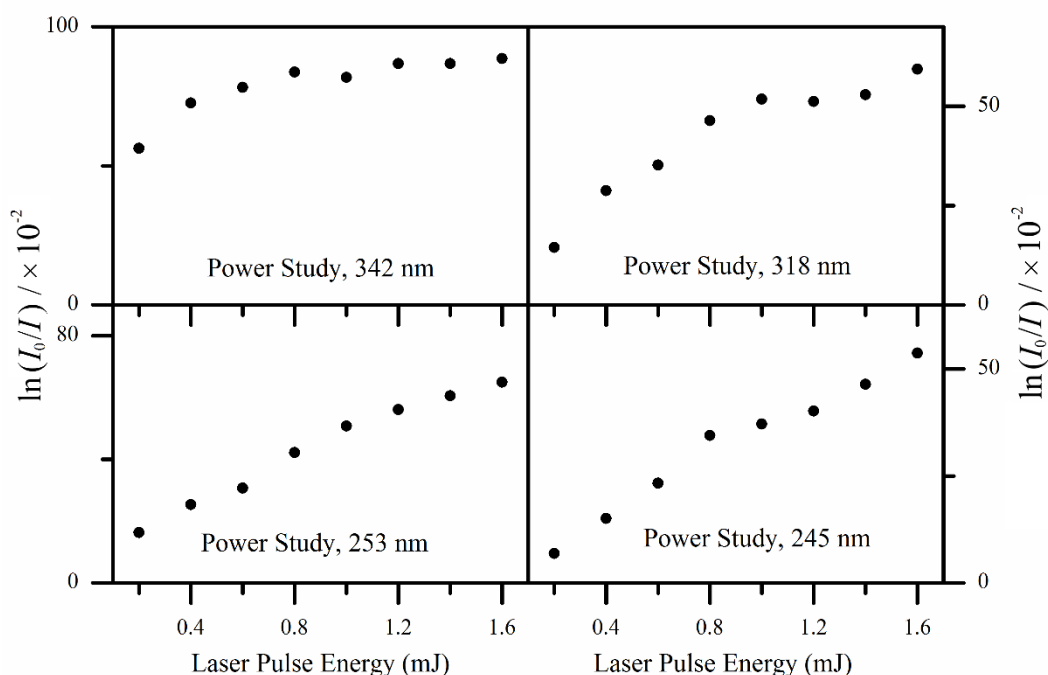
Figure 4.5 Gaseous dependency of the laser power on the photodepletion of PABA·H$^+$ ions with excitation wavelengths of: 342, 318, 253 and 245 nm. PABA·H$^+$ was produced by electrospraying an aqueous solution of PABA.

4.7.1.2 Secondary Fragmentation of Photofragments

Figures 4.6a and 4.6b show the normalised absorption spectra of PABA·H$^+$ electrosprayed from solutions of water and acidified MeCN, respectively. The absorption spectra are represented by photodepletion (given as blue dots) and the sum of all observed photofragments (given as red dots). These spectra are normalised to the absorption value at 4.90 eV (253 nm). Also included is the difference between the photodepletion and photofragment absorption spectra (given as black dots). Figure 4.6a shows that there is a large difference between depletion and fragment production between 3.6-3.8 eV, which we attribute to secondary fragmentation of primary photofragments to low masses which are outside the range of our mass spectrometer (fragments with $m/z < 50$ are not detected in our instrument). Figure 4.6b shows that for the MeCN electrosprayed absorption spectra, secondary fragmentation is significant above 5.4 eV and is a minor process around 3.6 eV.
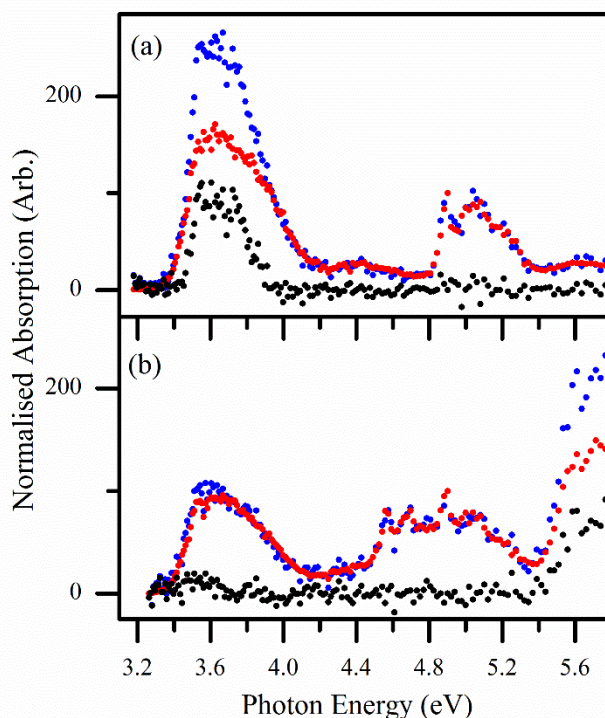
Figure 4.6 Absorption spectra of PABA·H$^+$, electrosprayed from solutions of a) water and b) acidified-MeCN, which are normalised to the absorption value at 4.90 eV (253 nm). Blue dots are photodepletion, red dots are the sum of the observed photofragments and the black dots are the difference between the blue and red dots.

Chapter 4

4.7.2 Computational Results: Protonation, Stability and Excited States

4.7.2.1 Structures and Energies of protonated PABA

Scheme 4.1 Structures and relative electronic energies of the potential structures of protonated PABA calculated using the B3LYP/6-311+G(2d,2p) functional and basis set. Relative energies are given in kJ mol^{-1}.

	Oxygen Protonated	Nitrogen Protonated	Carbon Protonated
Isomer 1	0.0	33.7	51.1
Isomer 2	11.8	75.9	135.7
Isomer 3	20.4		53.6
Isomer 4			48.8
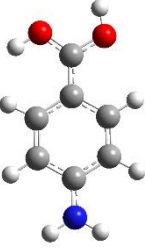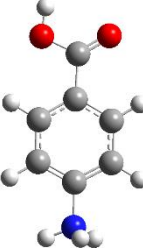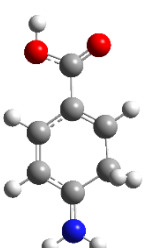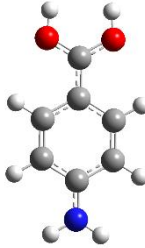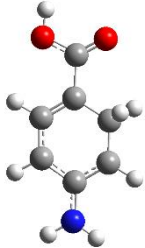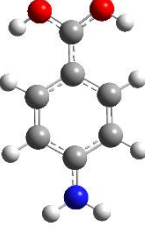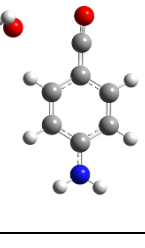
4.7.2.2 Description of the MRCI and SORCI Excited-State Calculations

The excited-state calculations were performed using the MRCI and SORCI modules of the ORCA quantum chemistry package. The B3LYP optimised structures of the lowest energy tautomers of **PABA-OH$^+$** and **PABA-NH$_3^+$** were re-optimised with the MP2/6-311+G(2d,2p) level of theory using Gaussian 09. Frequency calculations were performed on the structures which showed that they were energy minima.

When using ORCA, the aug-cc-pVDZ basis set and its auxiliary basis set (aug-cc-pVDZ/C) were used for all calculations. Natural orbitals were generated using MP2 theory, specifying a relaxed density. The resolution of the identity (RI) approximation was specified when using MP2 theory (RI-MP2) and throughout the CASSCF, SORCI and MRCI calculations. The MP2 natural orbitals were extracted from the generated checkpoint file using the orca_plot utility and were visually assessed. Orbitals which possessed significant electron density above and below the plane of the molecule were classified as π-orbitals, the orbitals were re-ordered such that the π-orbitals would be in the active space of CASSCF calculations. CASSCF(10,9) and CASSCF(8,8) calculations were run for the **PABA-OH$^+$** and **PABA-NH$_3^+$** structures, respectively. A restricted basis set containing six electrons in six orbitals of the CASSCF re-optimised orbitals were used as the active space in the excited-state MRCI and SORCI calculations, the active space was reduced to decrease the computational time. For **PABA-OH$^+$**, an initial MRCI calculation using the B3LYP optimised structure and MP2 natural orbitals was found to most accurately reproduce the experimentally observed absorption transitions. All active space orbitals of **PABA-OH$^+$** and **PABA-NH$_3^+$** are given in Figures 4.7-4.10. The electronic transitions responsible for producing the first four absorption bands in the MRCI and SORCI excitation spectra of **PABA-OH$^+$** and **PABA-NH$_3^+$** are summarised in Tables 4.3 and 4.4, respectively.

Table 4.3 Orbital transitions responsible for the first four absorption bands of **PABA-OH**[+] in the MRCI and SORCI calculations. Percentage contributions were calculated from the weightings predicted for each transition. Orbital transitions which comprise less than 10% of the total absorption are omitted. * indicates a two electron excitation from orbital 35-36.

PABA-OH[+]	MRCI			SORCI		
	Initial Orbital	Final Orbital	Percentage Contribution	Initial Orbital	Final Orbital	Percentage Contribution
$S_1 \leftarrow S_0$	35	36	95.0	35	36	90.2
$S_2 \leftarrow S_0$	35	37	41.4	35	37	23.1
	34	36	57.7	34	36	71.8
$S_3 \leftarrow S_0$	35	37	57.9	35	37	70.5
	34	36	40.6	34	36	21.7
$S_4 \leftarrow S_0$	33	36	93.7	35	38	11.3
				35	36*	41.2
				33	36	39.2

Table 4.4 Orbital transitions responsible for the first four absorption bands of **PABA-NH$_3^+$** in the MRCI and SORCI calculations. Percentage contributions were calculated from the weightings predicted for each transition. Orbital transitions which comprise less than 10% of the total absorption are omitted.

PABA-NH$_3^+$	MRCI			SORCI		
	Initial Orbital	Final Orbital	Percentage Contribution	Initial Orbital	Final Orbital	Percentage Contribution
S$_1$ ← S$_0$	35	37	16.7	35	36	26.1
	34	36	81.5	35	37	21.2
				34	36	30.7
				34	37	17.9
S$_2$ ← S$_0$	35	36	92.0	35	36	40.4
				35	37	19.7
				34	36	25.7
				34	37	14.2
S$_3$ ← S$_0$	35	37	66.7	35	36	30.9
	34	36	13.1	34	37	65.1
	34	37	16.5			
S$_4$ ← S$_0$	34	37	85.1	35	37	55.6
				34	36	42.4
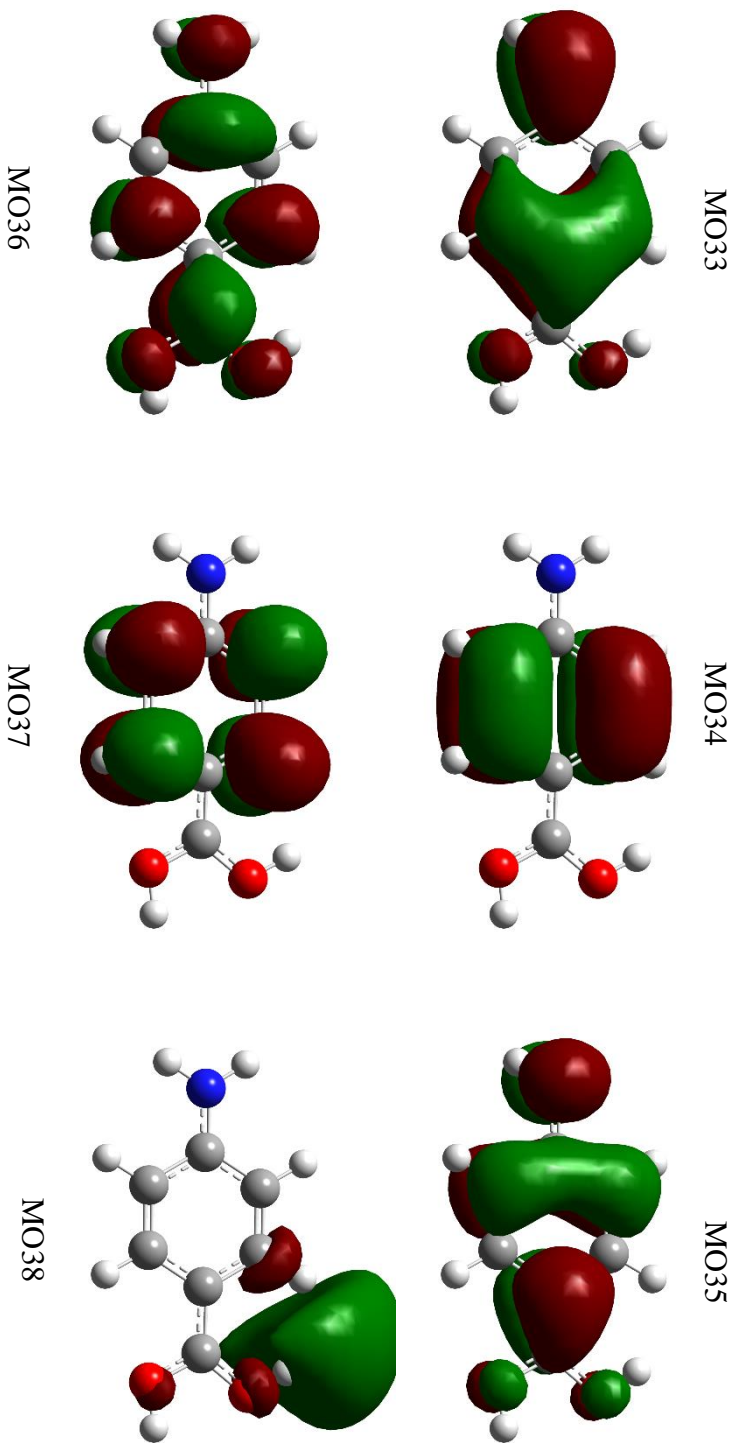
Figure 4.7 Reference space orbitals used within a MRCI calculation to predict the gaseous absorption spectrum of **PABA-OH**$^+$. Details of the calculation are given in the text.
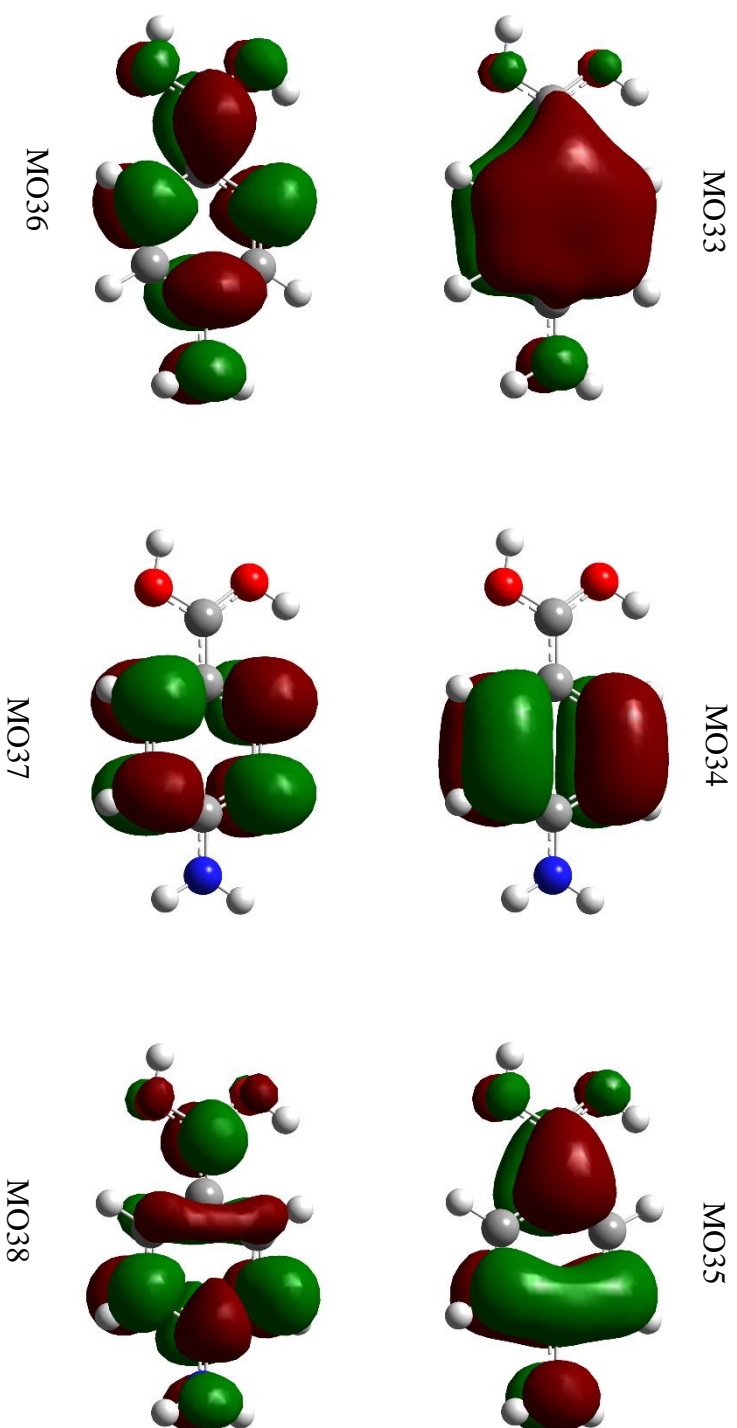
Figure 4.8 Reference space orbitals used within a SORCI calculation to predict the gaseous absorption spectrum of **PABA-OH**+. Details of the calculation are given in the text.
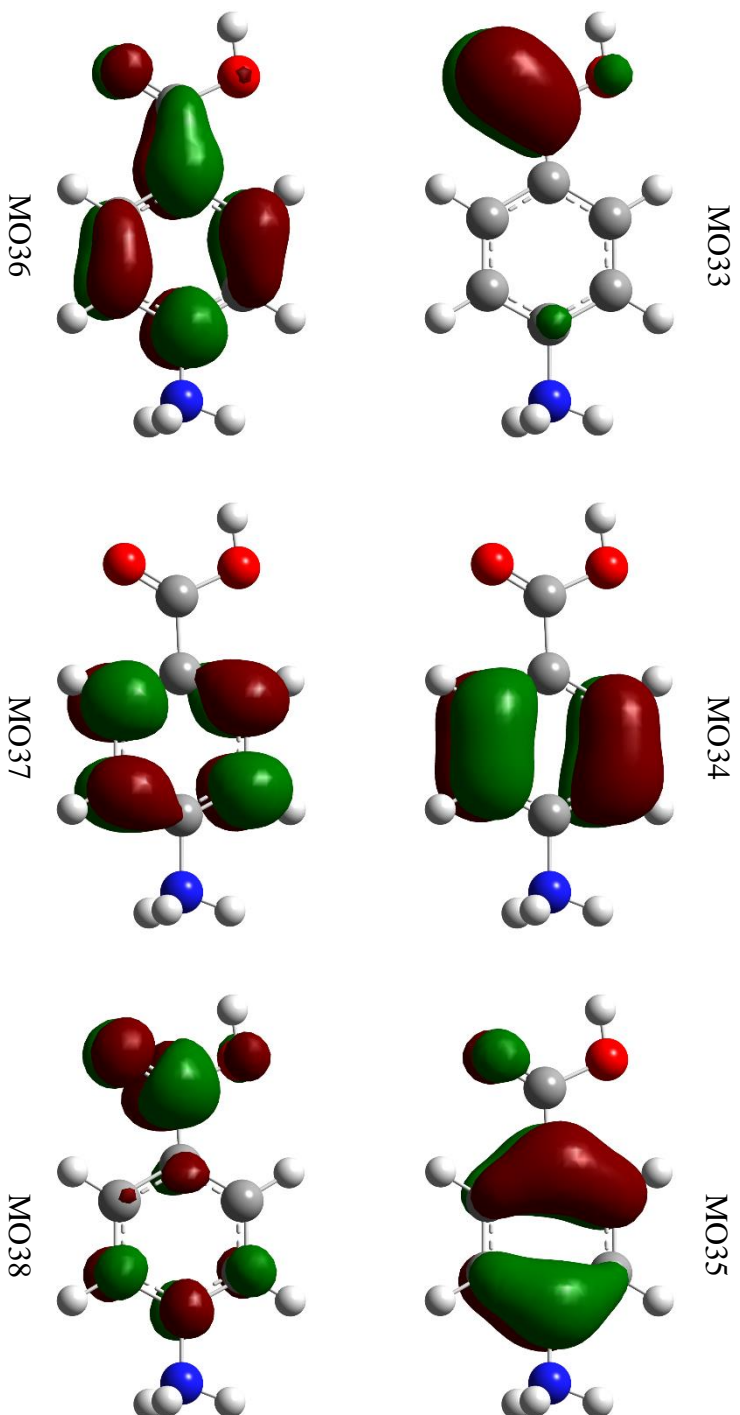
Figure 4.9 Reference space orbitals used within a MRCI calculation to predict the gaseous absorption spectrum of **PABA-NH$_3^+$**. Details of the calculation are given in the text.
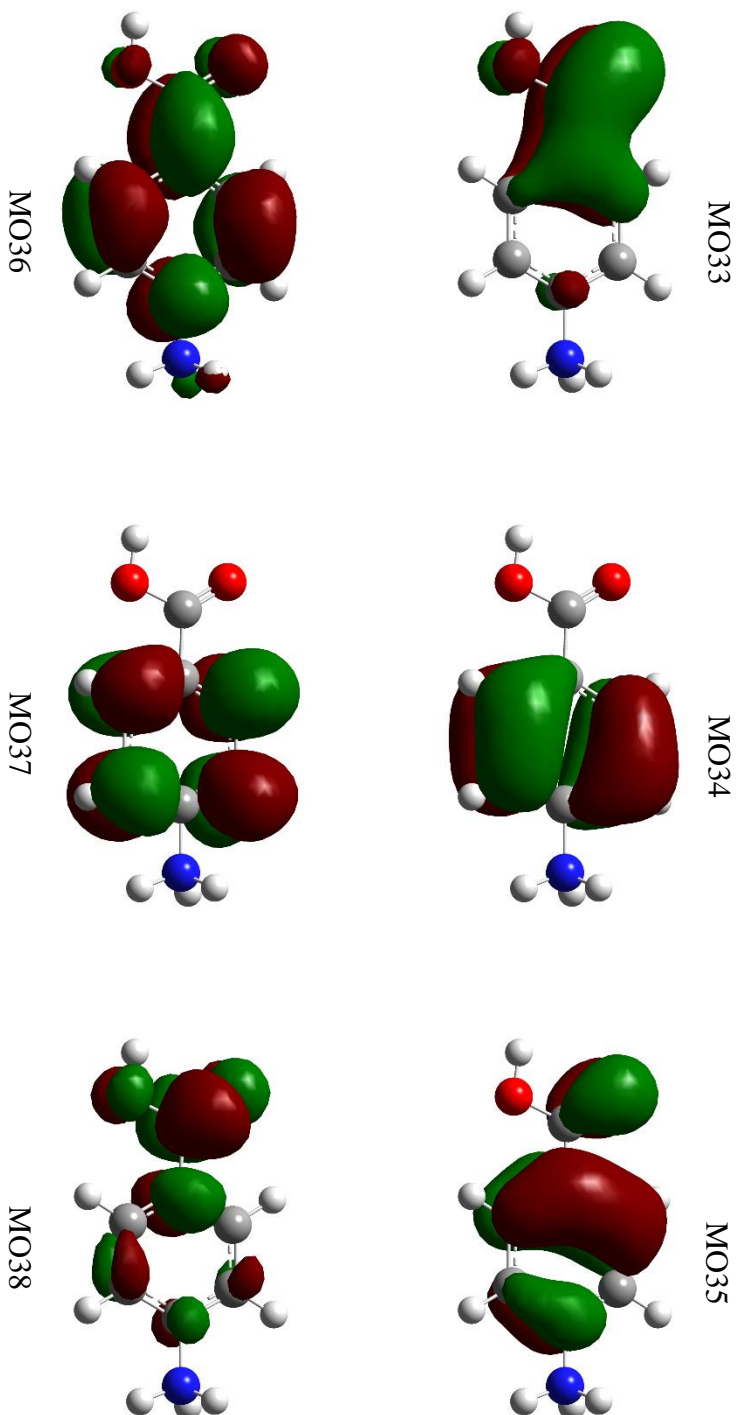
Figure 4.10 Reference space orbitals used within a SORCI calculation to predict the gaseous absorption spectrum of **PABA-NH$_3^+$**. Details of the calculation are given in the text.

4.7.2.3 TDDFT Excited State Calculations

Time-dependent density functional theory (TDDFT) calculations were performed on the B3LYP optimised structures of **PABA-OH$^+$** and **PABA-NH$_3$$^+$** using Gaussian 09. The B3LYP functional and 6-311+G(2d,2p) basis set were used to calculate the first 30 excited states of **PABA-OH$^+$** and **PABA-NH$_3$$^+$**. The resulting TDDFT excitation spectra are presented in Figure 4.11, with the transition energies and oscillator strengths of the individual excitations given in Tables 4.5 and 4.6.
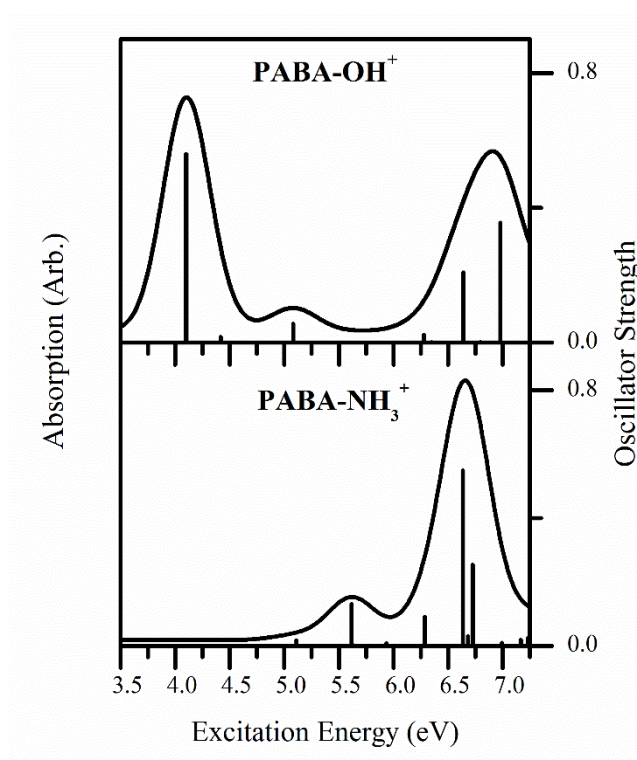
Figure 4.11 TDDFT excitation spectra of PABA protonated at the carboxylic acid (**PABA-OH$^+$**) and amine (**PABA-NH$_3$$^+$**), calculated using the B3LYP functional and 6-311+G(2d,2p) basis set. The oscillator strengths of individual transitions are given by the vertical bars. The full line spectrum represents a convolution of the calculated electronic transitions with Gaussian functions (0.25 eV HWHM).

Table 4.5 Calculated transition energies and oscillator strengths of the **PABA-OH$^+$** structure from TDDFT calculations with the B3LYP functional. Only transitions under 7 eV with oscillator strength > 0.005 are listed.

Transition Energy (eV)	Oscillator Strength
$\pi \rightarrow \pi^*$ Transitions	
4.10	0.5594
4.42	0.0159
5.08	0.0557
6.28	0.0225
6.64	0.2079
6.98	0.3551

Table 4.6 Calculated transition energies and oscillator strengths of the **PABA-NH$_3$$^+$** structure from TDDFT calculations with the B3LYP functional. Only transitions under 7 eV with oscillator strength > 0.005 are listed.

Transition Energy (eV)	Oscillator Strength
$\pi \rightarrow \pi^*$ Transitions	
5.11	0.0168
5.62	0.1302
5.93	0.0070
6.29	0.0909
6.64	0.5490
6.73	0.2534
$\pi \rightarrow \sigma^*$ Transitions	
5.62	0.0052
n (Oxygen Lone Pair) $\rightarrow \sigma^*$ Transitions	
6.68	0.0300
6.99	0.0089

4.7.3 Solution Phase UV Spectra of PABA Under Neutral and Acidic Conditions

The solution-phase absorption spectra of PABA in water and MeCN under neutral and mildly acidic conditions are presented in Figure 4.12. The spectra show that in the pure solvent, neutral PABA absorbs broadly between 4.0-5.0 eV, peaking at 4.45 and 4.33 eV for water and MeCN respectively. PABA also absorbs above 5.3 eV. Upon the addition of HCl, the absorption cross section of the band between 4.0-5.0 eV significantly decreases and the higher energy band shifts to lower energies. The band between 4.0-5.0 eV develops fine structure (most clearly observed in the MeCN spectrum) which peaks at 4.45 and 4.59 eV and 4.48 and 4.60 eV for water and MeCN, respectively. The higher energy band is now resolvable for both solvents, peaking at 5.50 and 5.54 eV for water and MeCN, respectively.

The observed change in the absorption spectra upon the addition of acid is caused by the protonation of PABA. It is notable that even under acidic conditions, no significant absorption is recorded below 4 eV.
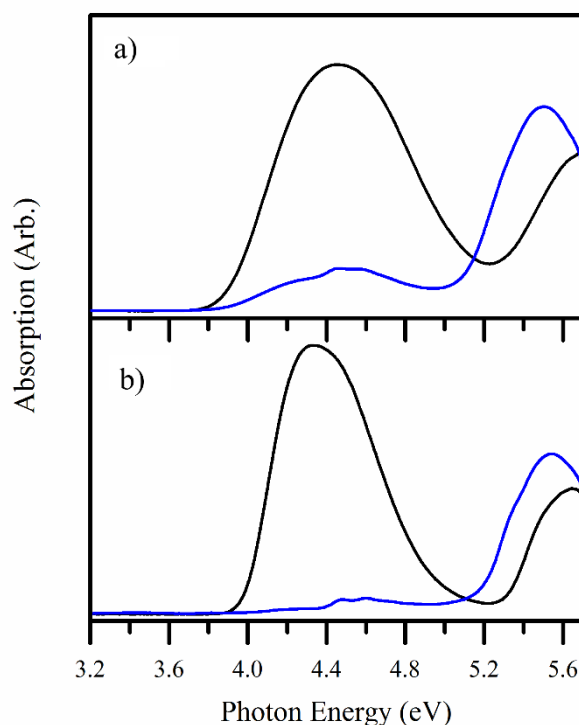
Figure 4.12 Solution phase absorption spectra of PABA ($\sim 2 \times 10^{-4}$ mol dm^{-3}) across the range 3.2-5.65 eV in solutions of: a) water and b) MeCN. Absorption spectra are recorded in the pure solvent (black line) and with 1 drop of 3 M HCl in 3 cm^3 of the PABA solution (blue line).

4.7.4 Additional Photofragment Mass Spectrum

Figure 4.13 shows the photofragment mass spectrum of isolated PABA·H$^+$ irradiated with an excitation photon energy of 5.56 eV (223 nm), PABA·H$^+$ was electrosprayed from a solution of acidified MeCN (producing a mixture of **PABA-NH$_3$$^+$** and **PABA-OH$_3$$^+$**). This photon energy is within band **IV** of the experimental absorption spectra (Figure 4.2b). Figure 4.13 is significantly different from Figure 4.3b where the laser excitation energy is 4.56 eV (272 nm). Figure 4.13 shows that as the photon energy increases, **PABA-NH$_3$$^+$** fragments preferentially into m/z = 137 and 65, with a concomitant reduction in the production of the m/z = 139 and 121 fragments.

Figure 4.13 Photofragment mass spectrum of PABA·H$^+$ electrosprayed from acidified MeCN and irradiated with a photon energy of 5.56 eV (223 nm).

Chapter 4

4.7.5 Gaussian Fitting of the Photofragment Production Spectra

Figure 4.14 shows the Gaussian fitted photoproduction spectra of fragments associated with the **PABA-OH$^+$** (Figure 4.14a) and **PABA-NH$_3$$^+$** (Figure 4.14b) structures of protonated PABA, the data plotted in Figure 4.14 is the same as the data in Figure 4.4. Figure 4.14a can be described well using eight Gaussian functions, which show that bands **I** and **II** can be broken down into two sets of absorption features that peak at 3.51, 3.59 and 3.77 eV and 4.89, 5.06 and 5.26 eV, respectively. The photofragment production spectrum also shows that two weak bands, centred at 4.47 and 5.72 eV, are resolvable. The Gaussian fitting of Figure 4.14b shows that band **III** can be deconvoluted into three separate absorption features which peak at 4.56, 4.67 and 4.84 eV. Band **IV** can be fitted with two Gaussians which peak at 5.56 and 5.84 eV.
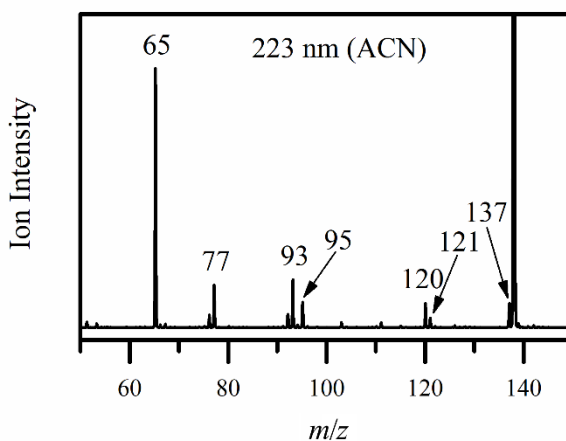
The maximum of the lowest energy Gaussian curve within bands **I** – **IV** is tentatively assigned as the vertical transition energy of that electronic transition. The higher energy Gaussian curve(s) are likely to represent averages of vibronic transitions. However, absolute assignments of the vibronic transitions are not possible in a low-resolution photodissociation experiment.
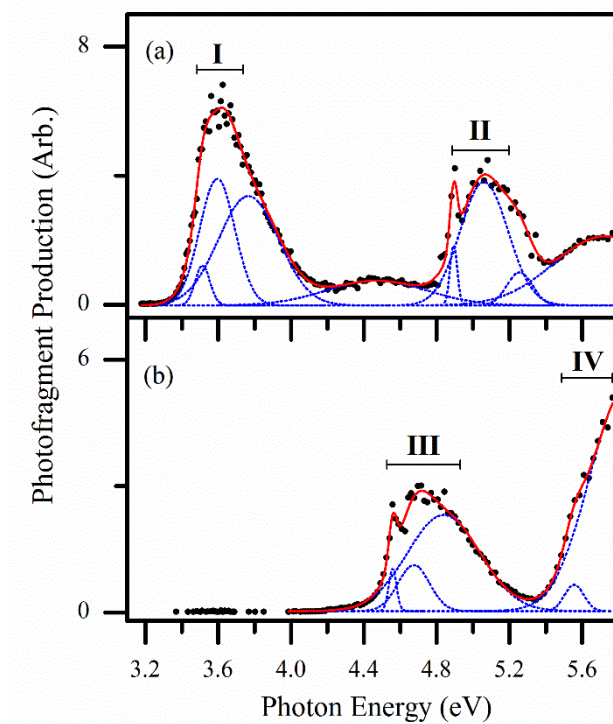
Figure 4.14 Photofragment production spectra of the photofragments with a) *m*/*z* 93, from PABA electrosprayed in water; b) the sum of fragments *m*/*z* 121, 137 and 139, from PABA electrosprayed in MeCN. Fragments are produced following photoexcitation of mass-selected PABA·H$^+$ ions, across the range 3.2 – 5.8 eV. Spectra are fitted with Gaussian functions.

Chapter 5

Evidence for the Impact of Methyl Group Free Rotors on the Stability of Dipole-Bound Excited States in the Flavin Chromophore Anions of Alloxazine and Lumichrome

5.1 Preamble

The following work is currently in preparation to be published. All data were collected, processed and interpreted by me. The initial draft of the manuscript was written by me and has been revised by Caroline Dessent.

Supplementary information is appended to this Chapter as Section 5.7. This includes computational results; solution-phase absorption spectra; electrospray ionisation mass spectra; laser power studies; thermal and photofragment mass spectra; and a photofragment production spectrum.

5.2 Abstract

Lumichrome (LC) is the chromophore of the flavin family of photoactive biomolecules, where key biochemical activity involves interplay between redox (i.e. electron capture) and photophysical events. The relationship between the redox status of the ground and electronic excited states of the cryptochrome group of flavoproteins is not well understood, and demands an improved understanding of the intrinsic photochemistry. Using anion photodissociation spectroscopy, we have measured the intrinsic electronic spectroscopy (564-220 nm) and accompanying photodegradation pathways of the deprotonated anionic form of LC. Experiments were also performed on alloxazine (AL), which is equivalent to LC minus two methyl groups. We find evidence for resonance states which we assign as dipole-bound excited states close to 3.8 eV for both anions, but for AL, this state is sufficiently long-lived to facilitate valence electron capture. Our results suggest that

the presence of methyl group rotors may reduce the lifetime of dipole-bound excited states and hence provide a structural barrier to valence electron capture, and ensuing molecular dissociation.

5.3 Introduction

Flavin cofactors such as flavin mononucleotide (FMN) and flavin adenine dinucleotide (FAD) are amongst the most important photoactive biological molecules.[224] Despite the fact that there have been numerous investigations of the photochemistry and photophysics that underpin flavin photobiology, critical questions remain about the sequence of light and redox events that occur, as well as the role of the protein around the central chromophore.[225]

Previous experimental studies of flavins have fallen into two main groups. The first has focused on characterising the photophysical properties of flavin molecules such as FMN and FAD in aqueous solution, with the goal of better understanding the properties of the chromophore.[226, 227] In contrast, more recent work has centred on studies of the entire flavoprotein, where advanced biochemical and time-resolved techniques are applied to investigate light-induced dynamics of the entire protein. [225, 228] These experimental studies have been complemented by an increasing number of theoretical studies of flavin chromophores.[229-231] However, to date, studies of the electronic properties of isolated (i.e. gas-phase) flavins are sparse.[50, 232] This situation impedes the fundamental understanding of the intrinsic properties, but also seriously hampers theoretical progress due to a lack of important benchmarking data. Furthermore, since the vacuum dielectric constant ($\varepsilon_{vacuum} = 1$) is more similar to the immediate environment of the interior of a protein ($\varepsilon_{protein} = 2\text{-}4$) than for water ($\varepsilon_{water} = 80$),[233] the gas phase is an appropriate medium in which to study intrinsic properties of these key chromophores which typically sit entirely within a pocket of the flavoprotein.

Here, we present the first gas-phase study of the anionic (i.e. deprotonated) form of the smallest flavin chromophore lumichrome (LC), along with the simpler, related
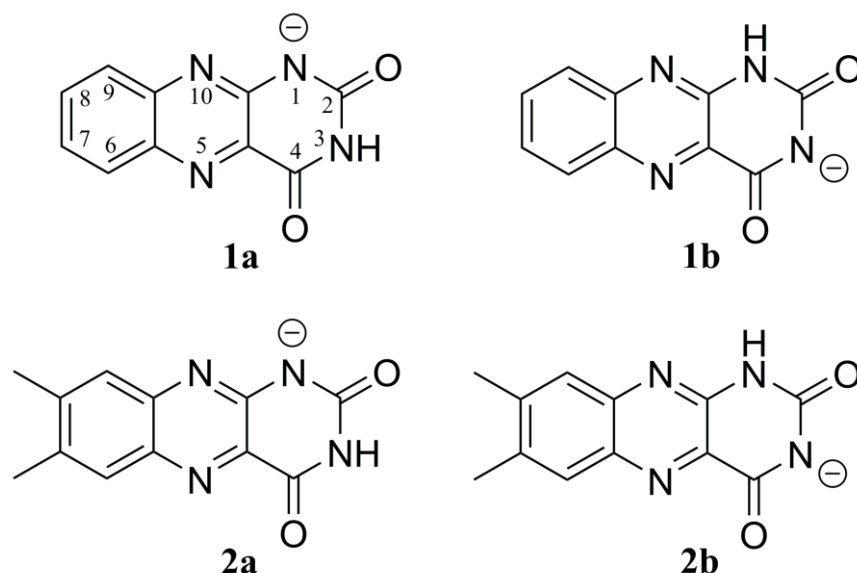
Figure 5.1 Schematic diagram to illustrate the lowest-energy isomers of deprotonated AL (structure **1**) and LC (structure **2**). Atom labels are included on structure **1a**.

chromophore, alloxazine (AL). Solution-phase photochemistry studies have shown that two deprotonated structures of LC exist in basic conditions,[234, 235] these structures are given in Figure 5.1 along with the corresponding structures of deprotonated AL. Our motivation for studying alloxazine is that it is often the subject of theoretical studies due to its modestly simpler structure that lacks the two aromatic methyl groups, and the work we perform here allows us to investigate the extent to which these methyl groups affect the intrinsic electronic properties. Lumichrome is related to the biologically important FMN and FAD by lacking the ribose chain plus phosphate group, and the ribose chain plus adenosine diphosphate, respectively.

In choosing to focus on the simplest flavin chromophore, we adopt a deliberate "bottom up" approach, where we begin by probing the properties of the simplest flavin chromophore, and will then sequentially reintroduce the molecular complexity in future experiments to build towards obtaining a complete understanding of intrinsic flavin chromophore electronic spectroscopy. We employ the general approach of forming the flavin chromophore anions as gas-phase species via electrospray of suitable solutions, and then obtaining the electronic spectrum via laser photodissociation spectroscopy.[19] Indeed, we argue that it is essential to begin a wider study of flavin chromophores by studying the smallest chromophore first, as

Chapter 5

larger flavin chromophores are known to fragment into smaller flavin chromophores following electronic excitation,[232] which offers the potential to seriously hamper the spectral interpretation. A complete knowledge of the properties of the smallest chromophore, will provide a firmer basis for both acquiring and interpreting the experimental data for the larger systems.

5.4 Experimental and computational methods

5.4.1 Experimental Methods

The gaseous photodepletion and photofragment spectra of deprotonated AL and LC, i.e. [AL-H]⁻ and [LC-H]⁻, were recorded *in vacuo* using action spectroscopy in a laser-interfaced mass spectrometer which is described in detail elsewhere.[14, 22, 40] [AL-H]⁻ and [LC-H]⁻ were introduced into the gas phase via electrospray ionisation (ESI) of a solution of AL and LC (1×10^{-5} mol L⁻¹) in methanol; ESI used a capillary voltage of 4250 V, a nebulising gas pressure of 4.0 psi, an injection rate of 300 μL hr⁻¹, a drying gas flow rate of 8.0 L min⁻¹, and a capillary temperature of 180 °C. AL and LC were purchased from Santa Cruz Biotechnology Inc. and used without further purification. Electrospray ionisation readily produces [AL-H]⁻ and [LC-H]⁻ as gas-phase ions, with *m/z* 213 and 241, respectively. (Discussion of the ESI-mass spectrum of AL and LC is included in Section 5.7.3.)

UV photons were produced by an Nd:YAG (10 Hz, Surelite) pumped OPO (Horizon) laser, giving ~1 mJ across the range 400 - 220 nm (3.10 – 5.64 eV) and ~0.5 mJ across the range 564 - 400 nm (2.20 – 3.10 eV). Scans were conducted using 1, 2 and 4 nm step sizes in the wavelength regions of 220 - 292, 292 - 400 and 400 - 564 nm, respectively, so that the average energy difference between the data points is ~0.02 eV across the spectral range. Photofragmentation experiments were run with an ion accumulation time of 20 – 100 ms and a fragmentation time of 100 ms, ensuring an average of one laser pulse per ion packet. Photodepletion and photofragment production intensities were calculated from the photofragment mass spectra as was described in Chapter 2. As was also discussed in Chapter 2, photodissociation data was collected using the multiple reaction monitoring (MRM) method, collecting experimental data for [AL-H]⁻ and [LC-H]⁻ within the same datafiles. Power studies were conducted using excitation wavelengths of 4.77, 4.00

and 2.58 eV (260, 310 and 480 nm, respectively) to test for multiphoton effects. Solution-phase UV absorption spectra of alloxazine and lumichrome (aqueous, pH 11, 1×10^{-4} mol dm^{-3}) were recorded using a Shimadzu 1800 UV spectrophotometer with a 1 cm UV cuvette, using distilled water as a baseline. Sodium hydroxide was used to increase the alkalinity of the solution to pH 11.

5.4.2 Computational Methods

Multiple deprotonated structures of [Al-H]$^-$ and [LC-H]$^-$, were optimised using the PBE0/6-311+G(d,p) functional and basis set, using Gaussian 09.[135, 146, 151, 174, 175, 217, 218] Frequency calculations were performed to ensure that all optimised structures correspond to true energy minima. All structures were also optimised using an implicit water solvent, with frequency calculations to show that the optimised structures were energy minima. Time-dependent density functional theory (TDDFT) calculations were performed on the optimised gaseous structures of the two lowest energy structures of [Al-H]$^-$ and [LC-H]$^-$, at the PBE0/6-311G(d,p) level, extra diffuse functions were removed from the basis set to minimise the amount of sigma character in the predicted transitions. Vertical detachment energies (VDE) and adiabatic detachment energies (ADE) were calculated for the lowest energy structures of [Al-H]$^-$ and [LC-H]$^-$, at the PBE0/6-311+G(d,p) level.

5.5 Experimental and Computational Results

5.5.1 Solution-phase UV of [AL-H]$^-$ and [LC-H]$^-$

Prior to acquiring the gaseous absorption spectra of [AL-H]$^-$ and [LC-H]$^-$, we obtained the aqueous alkaline (pH 11) absorption spectra of AL and LC, this is given in Figure 5.2. The absorption profiles are similar for the two systems, with both showing a region of relatively low absorption in the visible region between 2.6 – 4.2 eV, and a dominant UV band which peaks close to 4.9 eV, followed by the onset of a further band towards the high-energy spectral edge. Similar published spectra have been interpreted as being composed of contributions from two isomeric species of the deprotonated molecules.[235-237] Further discussion on the solution-phase
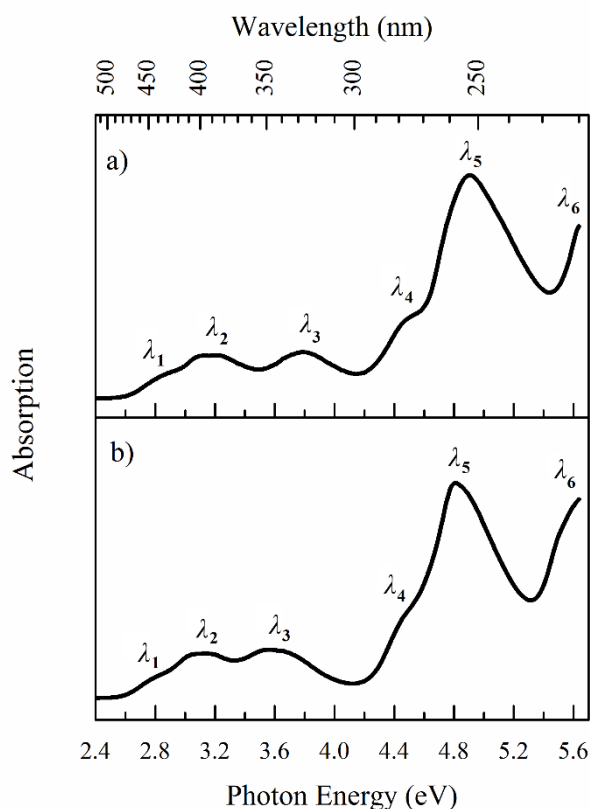
Figure 5.2 Aqueous absorption spectrum (pH 11, 1×10^{-4} mol dm^{-3}) of a) alloxazine and b) lumichrome across the range 2.4 – 5.64 eV (517 – 220 nm). Peak maxima are labelled $\lambda_1 - \lambda_6$ for both alloxazine and lumichrome.

---

absorption spectra of [AL-H]⁻ and [LC-H]⁻ is given in Section 5.7.2. One of the advantages of our gas-phase experiment is that it allows us to distinguish such isomeric species, either via the photodepletion or photofragmentation action spectra that are acquired simultaneously, and hence characterise the photochemistry of individual tautomers.

5.5.2 Gaseous Photodepletion Spectra of AL and LC

Figure 5.3a displays the gaseous absorption spectrum of [AL-H]⁻. Four absorption bands (labelled **I – IV**) are evident, with the absorption onset occurring around 2.3 eV (540 nm). Band **I** is a relatively weak and broad band and is observed in the visible region, centred around 2.8 eV (443 nm). This band decreases in intensity above 2.8 eV and approaches a baseline level by 3.7 eV. An extremely sharp-onset
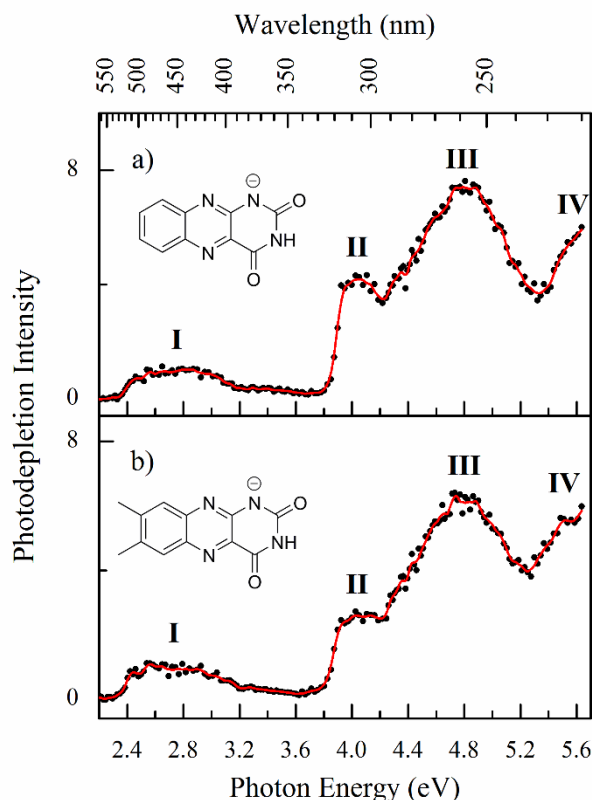
Figure 5.3 Photodepletion spectra of a) [AL-H]⁻ and b) [LC-H]⁻, across the range 2.20 – 5.64 eV (564 – 220 nm). The solid red lines are 5-point adjacent averages of the data points. The inset figures are the lowest-energy calculated structure of a) [AL-H]⁻ and b) [LC-H]⁻.

band (**II**) is observed above 3.8 eV with a maximum at 4.05 eV (306 nm). Band **III** appears as another strong feature between 4.3-5.2 eV with a peak occurring at 4.81 eV (260 nm), while the rising edge of band **IV** is observed above 5.35 eV. An equivalent set of transitions are observed in the photodepletion spectrum of gaseous [LC-H]⁻ (Figure 5.3b), with the λ_{max} of bands **I – IV** appearing at 2.6, 4.03, 4.74, and >5.6 eV respectively. Laser power studies were conducted (Section 5.7.4) to determine the relationship between absorption and laser power within bands **I – III** for [AL-H]⁻ and [LC-H]⁻. Across the spectral range studied, we find that the photodepletion of [AL-H]⁻ and [LC-H]⁻ increases linearly as the laser power increased, showing that multiphoton effects are not significant.

Chapter 5

Comparing the solution-phase and gaseous absorption spectra, both spectra display relatively low intensity absorptions across the visible range, and it seems clear that the dominant UV solution-phase band, is related to the strong Band **III** feature in the gaseous spectrum. However, it is striking that there is no solution-phase band close to 4.0 eV, the location of the sharp-onset feature, Band **II**, in the gaseous spectra. We will return to further discuss the assignment of the absorption spectra below.

5.5.3 Photofragmentation Mass Spectra

We next turn to exploring the photofragment ions that are associated with the excited states that are evident in Figure 5.3. The photofragment mass spectrum of [AL-H]$^-$ following excitation at 4.77 eV (260 nm – Band **III**) is given in Figure 5.4, this shows that [AL-H]$^-$ produces a *m/z* 170 fragment as the dominant fragment which corresponds to the loss of 43 mass units (HNCO) from [AL-H]$^-$. A second, minor fragment with *m/z* 142 is evident, corresponding to loss of HNCO and CO from the parent ion:

$$[AL-H]^- + h\nu \ \rightarrow \quad m/z \ 170 + HNCO$$
$$\rightarrow \quad m/z \ 142 + HNCO + CO$$
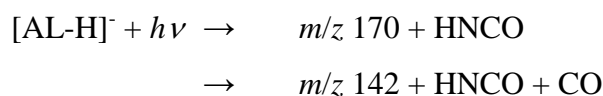
Equations 5.1a and 5.1b

Similarly, when [LC-H]$^-$ is photoexcited at 4.77 eV, the major photofragmentation channels corresponding to loss of 43 and 71 mass units to produce photofragments
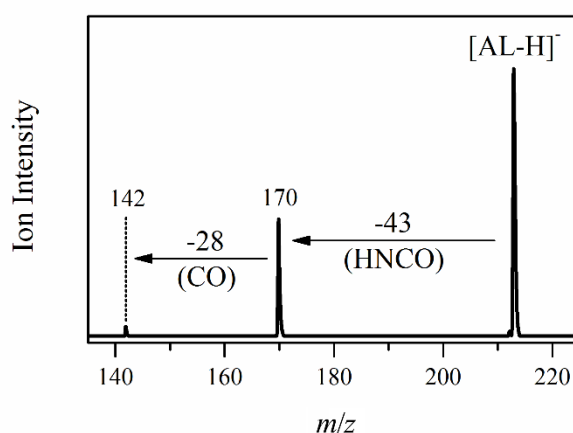
Figure 5.4 Photofragment mass spectra of [AL-H]$^-$ excited at 4.77 eV (260 nm). Assignments of the neutral species lost upon photofragmentation are included.

with m/z 198 and 170, respectively (a photofragment mass spectrum showing this is given in Section 5.7.5):

$$[LC\text{-}H]^- + h\nu \; \rightarrow \qquad m/z \; 198 + HNCO$$

$$\rightarrow \qquad m/z \; 170 + HNCO + CO$$
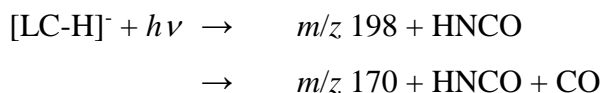
Equations 5.2a and 5.2b

These photofragments appear with similar intensities to the corresponding photofragments of [AL-H]⁻. A number of minor photofragments with m/z 168, 169, 172, 482 and 483 are also observed for [LC-H]⁻, the origin and identities of which are discussed in Section 5.7.5. We note that low-energy collision induced dissociation (CID) of [AL-H]⁻ and [LC-H]⁻ results in fragmentation with loss of HNCO, i.e. thermal excitation versions of Equations 5.1a and 5.2a, mirroring the photofragmentation results where loss of HNCO is the major channel. (CID mass spectra of [AL-H]⁻ and [LC-H]⁻ are given in Section 5.7.5).

5.5.4 Photofragmentation Action Spectra

Photofragment intensities are monitored in our experiment at each scanned wavelength to provide further insight into the nature of the excited states. The action spectrum for production of the major photofragment from [AL-H]⁻ with m/z 170 is displayed in Figure 5.5a, showing that the fragment is produced across the entire spectral range, with the majority of this production occurring within bands **I** – **IV** which are seen in the gaseous absorption spectrum of [AL-H]⁻ (Figure 5.3a). However, band **I** appears more strongly in the photofragment action spectrum, whereas production of the fragment is notably flat across bands **II**-**IV** when compared to the gaseous absorption spectrum. The sharp onset of photofragment production at ~3.8 eV, the onset of band **II** mirrors the photodepletion profile in this region

Figure 5.5b shows the production spectrum of the major m/z 198 photofragment from [LC-H]⁻. This spectrum is somewhat similar to the absorption spectrum of this
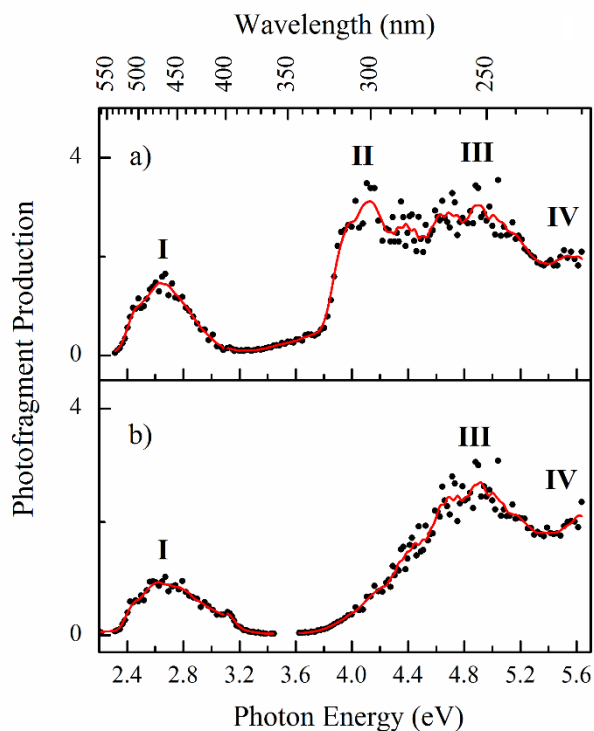
Figure 5.5 Photofragment production spectra of a) the *m/z* 170 photofragment from [AL-H]⁻ and b) the *m/z* 198 photofragment from [LC-H]⁻, across the range 2.20 – 5.64 eV (564 – 220 nm). The solid red lines are 5-point adjacent averages of the data points.

species (Figure 5.3b) but, strikingly, production of *m/z* 198 does not peak across the region of band **II**. In particular, the sharp onset in spectral intensity seen in the absorption spectrum at ~3.8 eV, is completely absent from the spectrum shown in Figure 2b, indicating that the absorption process occurring in band **II** does not result in production of *m/z* 198. For anionic systems, any photodepletion that is not associated with photofragment production is associated with electron-loss processes.

5.5.5 DFT and TDDFT

DFT and TDDFT calculations were performed to allow us to interpret the experimental spectra. The two most stable structures of [AL-H]⁻ (**1a** and **1b**) and [LC-H]⁻ (**2a** and **2b**) involve deprotonation at the same sites. These structures are displayed in Figure 5.1, with the relative energies and selected physical properties of

Chapter 5

Table 5.1: Calculated relative energies and physical properties of structures **1a**, **1b**, **2a** and **2b** of [AL-H]⁻ and [LC-H]⁻ calculated at the PBE0/6-311+G(d,p) level.[a,b] Relative electronic energies, vertical detachment energies, adiabatic detachment energies and dipole moments are shown.

Structure	Relative Energy[b,c] (kJ mol^{-1})	VDE (eV)	ADE (eV)	Dipole Moment (D)	Vertical Dipole Moment[d] (D)
1a	0.0 (0.0)	4.00	3.87	7.8	7.0
1b	21.7 (6.01)	4.64	4.22	12.6	7.6
2a	0.0 (0.0)	3.83	3.71	11.7	9.0
2b	21.2 (5.25)	4.71	-	16.5	16.1

[a] See Figure 5.1 for definitions of the atom labels.
[b] The relative energies are zero-point energy corrected.
[c] Values in parentheses are calculated in water.
[d] The dipole moment of the vertical neutral molecule (*i.e.* neutral with the same geometry as the anion) formed when the excess electron is ionised from the anion.

the anions given in Table 5.1. (The relative zero-point corrected energies of all considered isomers are given in Table 5.2 in Section 5.7.1.) As the relative energies of the other deprotomeric isomers are substantially higher than the **a** and **b** deprotomers, we assume that they are not present in this experiment. Deprotonation at position N1 (**1a** and **2a**) of the alloxazine ring is calculated to be more stable than deprotonation at position N3 (**1b** and **2b**) by 21.7 and 21.2 kJ mol^{-1} for AL and LC respectively. The vertical detachment energies (VDEs) of structures **1a** and **2a** are predicted to be 4.00 and 3.83 eV (310 and 324 nm), respectively, with the corresponding VDEs of structures **1b** and **2b** being significantly higher (4.64 and 4.71 eV, respectively). Both **a** and **b** structures are highly polar, with dipole moments oriented primarily across the long axis of the molecule, indicating that the negative charge largely resides within the fused uracil ring.

Figure 5.6 present the TDDFT excitation spectra of structures **1a** and **1b** of [AL-H]⁻ and **2a** and **2b** of [LC-H]⁻, while the individual transitions that contribute to these spectra are tabulated in Section 5.7.1. Comparing the calculated spectra to the experimental spectra (Figure 5.3), it is evident that the calculated spectra of isomers
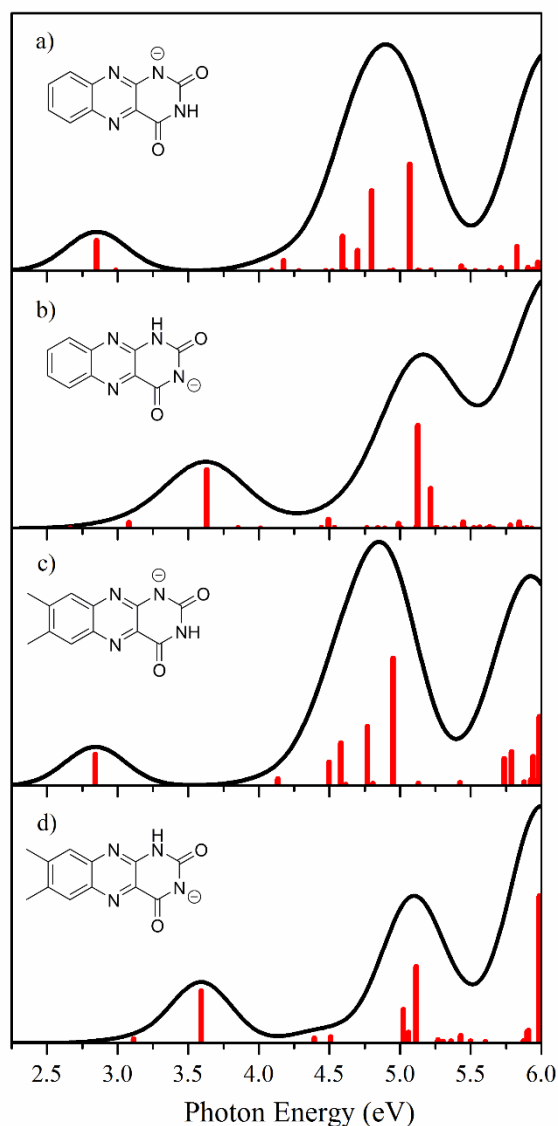
Figure 5.6 Calculated TDDFT excitation spectra of the (a) N1 deprotonated (**1a**) and (b) N3 deprotonated (**1b**) structures of [AL-H]⁻, and the (c) N1 deprotonated (**2a**) and (d) N3 deprotonated (**2b**) structures of [LC-H]⁻. The horizontal red lines are the predicted electronic transitions while the full line spectrum is a convolution of the calculated transitions with Gaussian functions (0.25 eV HWHM). Details of the individual transitions are given in Section 5.7.1. The inset figures correspond to the skeletal form of the relevent structure of [AL-H]⁻ or [LC-H]⁻.

1a and **2a** agree extremely well with the experimental photodepletion spectra of [AL-H]⁻ and [LC-H]⁻ in terms of the agreement between the positions of bands **I** and **III**. In this sense, the TDDFT spectra of structures **1a** and **1b** most accurately reproduce the photofragment production spectrum of *m/z* 198 from [LC-H]⁻. Since the **a**

isomers are calculated to be the lowest energy isomers, this leads to a straightforward assignment of the gas-phase spectra as being associated with the **a** structure deprotomers. This situation is expected for a system where a single isomer has a significantly lower relative energy than the next highest isomer, both in solution and the gas phase, and electrospray occurs in a protic solvent.

5.6 Discussion and Concluding Remarks

We now return to considering the differences between the electronic spectra of [AL-H]⁻ and [LC-H]⁻, and the nature of Band **II**. Although there are modest shifts in the positions of Bands **I** and **III** on going from [AL-H]⁻ to [LC-H]⁻, the most significance difference relates to the observation that the major photofragment (*m/z* 170) from [AL-H]⁻ is produced throughout the regions of bands **I**, **II** and **III**, whereas in [LC-H]⁻, the equivalent photofragment (*m/z* 198) displays no peak in production through the region of band **II**. In particular, whereas the *m/z* 170 photofragment spectral profile closely matches that of the photodepletion profile of [AL-H]⁻ for band **II** in that both display a sharp rising onset after 3.8 eV, such structure is entirely absent from the spectrum of the *m/z* photofragment of [LC-H]⁻. Having calculated the VDEs for [AL-H]⁻ to [LC-H]⁻, as 4.00 and 3.83 eV, respectively, it is now clear that the sharp onsets of the band **II** features correspond to the electron detachment thresholds of the anions. This is turn suggests an explanation of the origin of the band **II** features, as dipole-bound excited states. While dipole-bound states are prominent features of the electronic spectra of some anionic species, these transitions frequently become lower intensity on going from the gas phase to solution, consistent with the absence of a strong band **II** feature in the solution-phase spectra.

It is interesting to note that while the band **II** feature for [AL-H]⁻ (Figure 5.3a) displays a typical "peaked" profile of a dipole-bound excited state, for [LC-H]⁻ (Figure 5.3b), band **II** displays a flatter top. This type of profile has been associated with lower-magnitude dipoles (*i.e.* dipoles that are too small to critically bind an electron to form a stable dipole-bound state).[238] Based on previous experiments, the shapes of the band **II** features would therefore suggest that the vertical dipole moment for [LC-H]⁻, is lower than that for [AL-H]⁻. However, our calculations

(Table 5.1) indicate that the vertical dipole moment of [LC-H]⁻ is in fact modestly larger than that of [AL-H]⁻, so that further factors must be at play.

This leads us to consider what we might expect of the fragmentation channels associated with a dipole-bound state? Typically, such states can either autodetach, or the dipole-bound anion can evolve in a valence anion, which may then subsequently undergo a dissociative process.[239, 240] It is now well acknowledged that the formation of a (meta-)stable dipole-bound state can act as a doorway state that enhances valence anion formation, which may in turn result in molecular dissociation. This leads us to attribute our spectroscopic observations as being consistent with [AL-H]⁻ forming an above-critical threshold dipole-bound state in the region of the VDE, while [LC-H]⁻ forms a sub-critical dipole-bound state. The dipole-bound state for [AL-H]⁻ then acts as a doorway state to a valence state which leads to dissociation with loss of an HNCO neutral unit. In contrast, the sub-critical dipole moment of [LC-H]⁻ results in only electron detachment.

However, the interpretation presented in the above paragraph leads to another question, namely whether it is reasonable that [AL-H]⁻ should be able to form an above critical dipole-bound state, whereas [LC-H]⁻ cannot. Setting aside the values of the vertical dipole moments, the other key difference between alloxazine and lunichrome, is the presence of the two methyl groups in lumichrome. While dipole-bound states are common features of the spectroscopy of even relatively complex molecular anions that have been studied over recent years, few of these studies have compared methylated and non-methylated molecules.[109, 241, 242]

Brauman and co-workers investigated the effects of molecular rotation on the observation of dipole-bound states of anions via photodetachment studies of enolate anions in an ion cyclotron spectrometer over two decades ago.[243] In this seminal work, it was concluded that the binding of the electron by a dipole is very sensitive to the motions of the dipole. Of particular relevance to the current work, were their results for pinacolone enolate, which was found to lack resonances associated with a dipole-bound state, due largely to the presence of internal rotors. From their studies of the series of enolates, they concluded that any molecular rotations can lead to shortening of the lifetime of the dipole-bound state. If the molecule has internal

rotors, the internal and external rotations can couple, thus perturbing the angular momentum of the dipole, so that for molecules such as pinacolone enolate, the dipole-bound state will be very short lived. The deprotonated [LC-H]⁻ versus [AL-H]⁻ systems studied here appear to present a striking example of the effect of methyl rotors on the stability of a dipole-bound excited state for a medium sized biologically relevant anion. As the lifetime of the dipole-bound excited state of [LC-H]⁻ is shortened due to the presence of the internal rotors, there is insufficient time for the dipole-bound state to evolve into a valence state which subsequently dissociated, compared to the timescale for autodetachment.

As discussed in the introductory paragraphs, LC is the key structural component of the flavin family of biomolecules. Their activity as photoreceptors is closely coupled to their redox properties, where a coupled two electron/two proton capture by the LC moiety leads to the reduced form. The results presented here are interesting in this context since they indicate that the presence of the methyl groups which are present in LC compared to AL, may act to prevent single electron capture by LC resulting in dipole-bound state mediated molecular dissociation. It is seductive to speculate that the methyl LC groups fulfil a similar role in biological systems. More generally, these results are the first to probe how internal rotors can affect the photo-induced breakdown that follows the formation of a dipole-bound excited states. Further studies using advance imaging and time resolved techniques are desirable to provide further insight into the nature of electron capture in extended aromatic systems.

Chapter 5

5.7 Supplementary Information

5.7.1 Computational studies of the deprotonation isomers of AL and LC

5.7.1.1 Calculated relative energies of the deprotonation isomers of AL and LC

Deprotonated AL and LC can be formed by removing a hydrogen from either of the two NH sites; however, all possible structures of [AL-H]$^-$ and [LC-H]$^-$ with a single hydrogen on a nitrogen or oxygen atom were used as initial structures. These structures were optimised using the PBE0/6-311++G(d,p) functional and basis set, using Gaussian 09.[135, 146, 151, 174, 175, 217, 218] Frequency calculations were performed to ensure that all optimised structures correspond to true energy minima. All structures were also optimised using an implicit water solvent, with frequency calculations to show that the optimised structures were energy minima. Time-dependent density functional theory (TDDFT) calculations were performed on the optimised gaseous structures of the two lowest energy structures of [Al-H]$^-$ and [LC-H]$^-$ (Figure 5.7), at the PBE0/6-311G(d,p) level. Vertical detachment energies (VDEs) were calculated as the energy difference between the anion and the corresponding neutral, frozen at the anion geometry, while Adiabatic Detachment Energies (ADEs) were calculated as the energy difference between the anion and the fully optimised neutral.

The relative energies of the different deprotonated structures of [Al-H]$^-$ and [LC-H]$^-$, in the gaseous and aqueous phases, are given in Table 5.2. Structures **a** and **b** are the structures formed by deprotonating the neutral AL and LC structures in the N1 and N3 positions, respectively, these structures are the most stable. Structure **a** is calculated to be the most stable structure, both in solution phase and in the gas phase. With a solution phase energy separation of 6.01 and 5.25 kJ mol^{-1} between structures **a** and **b** of [Al-H]$^-$ and [LC-H]$^-$ respectively, the Boltzmann population of structure **b** at 298 K should be 10.7 % and 8.1 % for [Al-H]$^-$ and [LC-H]$^-$, respectively.

Table 5.2 Relative energies (zero-point energy corrected) of the deprotonation isomers of [Al-H]⁻ and [LC-H]⁻. The atom labels refer to Figure 5.1, which is repeated below as Figure 5.7 for ease of reference.

Structure	Protonated	[AL-H]⁻ Rel. Energy / kJ mol⁻¹		[LC-H]⁻ Rel. Energy / kJ mol⁻¹	
		Gaseous	Aqueous	Gaseous	Aqueous
a	N3	0.0	0.0	0.0	0.0
b	N1	21.7	6.01	21.2	5.25
c	CO2	52.0	45.5	51.9	45.1
d	CO4	76.9	64.6	77.0	64.1
e	N5	147.0	97.0	147.2	94.4
f	N10	115.2	60.6	115.6	59.9
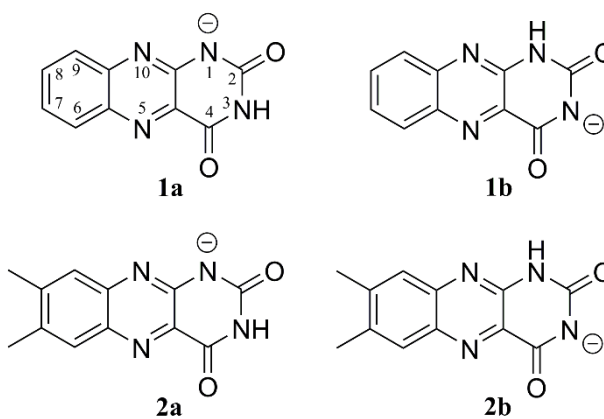
Figure 5.7 Schematic diagram to illustrate the lowest-energy isomers of deprotonated AL and LC. Atom labels used in Table 5.2 are included on structure **1a**.

Chapter 5

5.7.1.2 TDDFT excitation spectra of the deprotonation isomers of AL and LC

TDDFT excitation spectra were calculated for the **a** and **b** isomers of [Al-H]$^-$ and [LC-H]$^-$, as isolated gaseous ions and with an implicit water solvent (simulated using the polarisation continuum model). These gaseous excitation spectra of these deprotonated isomers are presented in Figure 5.6, the orbital transitions which produce the overall excitation spectra are given in Tables 5.3 – 5.6.

Tables 5.3 – 5.6 show that the TDDFT excitation spectra in Figure 5.6 are comprised of $\pi \rightarrow \pi^*$ and $n \rightarrow \pi^*$ transitions, the absorption spectrum of each molecule by the intense $\pi \rightarrow \pi^*$ transitions. The primary molecular orbital transition for the strong excitations (f > 0.02) predicted for protomers **1a** and **2a** are given in Figures 5.8 and 5.9, respectively. The strong orbital transitions of the two molecules, which differ only by methyl groups, are similar which shows that the molecules have similar electronic structures. The result of this is that the excitation spectra of protomers **1a** and **2a** are similar.

Table 5.3 Singlet excitations predicted by TDDFT (PBE0/6-311G(d,p)) calculations for protomer **1a** of [AL-H]$^-$. Transitions <5.6 eV included. MO transitions which contribute more than 20% to the excitation are listed with the transition as well as an assignment of the initial and final orbitals. Oscillator strengths (f) also included.

State	Orbital Transitions	ΔE (eV)	f
S_1	(0.97) 55(π) $\rightarrow$ 56(π*)	2.86	0.1195
S_2	(0.97) 54(n) $\rightarrow$ 56(π*)	2.96	0.0008
S_3	(0.92) 53(n) $\rightarrow$ 56(π*)	3.60	0.0000
S_4	(0.52) 55(π) $\rightarrow$ 57(π*) + (0.42) 52(π) $\rightarrow$ 56(π*)	4.23	0.0444
S_5	(0.85) 51(n) $\rightarrow$ 56(π*)	4.27	0.0002
S_6	(0.85) 49(n) $\rightarrow$ 56(π*)	4.46	0.0000
S_7	(0.90) 54(n) $\rightarrow$ 57(π*)	4.50	0.0001
S_8	(0.80) 50(π) $\rightarrow$ 56(π*)	4.64	0.0337
S_9	(0.38) 55(π) $\rightarrow$ 58(π*) + (0.25) 52(π) $\rightarrow$ 56(π*) + (0.22) 55(π) $\rightarrow$ 57(π*)	4.81	0.2956
S_{10}	(0.47) 55(π) $\rightarrow$ 58(π*) + (0.22) 48(π) $\rightarrow$ 56(π*)	4.87	0.1383
S_{11}	(0.95) 47(n) $\rightarrow$ 56(π*)	5.08	0.0003
S_{12}	(0.87) 53(n) $\rightarrow$ 57(π*)	5.11	0.0001
S_{13}	(0.53) 48(π) $\rightarrow$ 56(π*)	5.14	0.4951
S_{14}	(0.92) 54(n) $\rightarrow$ 58(π*)	5.29	0.0009

Table 5.4 Singlet excitations predicted by TDDFT (PBE0/6-311G(d,p)) calculations for protomer **1b** of [AL-H]⁻. Transitions <5.6 eV included. MO transitions which contribute more than 20% to the excitation are listed with the transition as well as an assignment of the initial and final orbitals. Oscillator strengths (f) also included.

State	Orbital Transitions	ΔE (eV)	f
S_1	(0.97) 54(n) → 56(π*)	2.57	0.0002
S_2	(0.98) 55(π) → 56(π*)	2.98	0.0174
S_3	(0.95) 53(n) → 56(π*)	3.25	0.0000
S_4	(0.94) 52(π) → 56(π*)	3.66	0.2066
S_5	(0.49) 49(n) → 56(π*) + (0.45) 51(n) → 56(π*)	3.83	0.0006
S_6	(0.48) 51(n) → 56(π*) + (0.47) 49(n) → 56(π*)	3.94	0.0006
S_7	(0.94) 54(n) → 57(π*)	4.17	0.0000
S_8	(0.97) 55(π) → 57(π*)	4.36	0.0083
S_9	(0.73) 50(π) → 56(π*) + (0.25) 52(π) → 57(π*)	4.53	0.0148
S_{10}	(0.91) 53(n) → 57(π*)	4.79	0.0003
S_{11}	(0.90) 54(n) → 58(π*)	4.85	0.0002
S_{12}	(0.92) 55(π) → 58(π*)	5.01	0.0083
S_{13}	(0.62) 52(π) → 57(π*)	5.20	0.4455
S_{14}	(0.70) 49(n) → 57(π*) + (0.25) 51(n) → 57(π*)	5.30	0.0000
S_{15}	(0.41) 52(π) → 58(π*) + (0.27) 50(π) → 57(π*) + (0.24) 48(π) → 56(π*)	5.32	0.0842
S_{16}	(0.40) 47(n) → 56(π*) + (0.34) 51(n) → 57(π*)	5.39	0.0000
S_{17}	(0.53) 47(n) → 56(π*) + (0.28) 51(n) → 57(π*)	5.43	0.0000
S_{18}	(0.82) 53(n) → 58(π*)	5.50	0.0002
S_{19}	(0.45) 48(π) → 56(π*) + (0.43) 52(π) → 58(π*)	5.51	0.0343

Table 5.5 Singlet excitations predicted by TDDFT (PBE0/6-311G(d,p)) calculations for protomer **2a** of [LC-H]⁻. Transitions <5.6 eV included. MO transitions which contribute more than 20% to the excitation are listed with the transition as well as an assignment of the initial and final orbitals. Oscillator strengths (f) also included.

State	Orbital Transitions	ΔE (eV)	f
S_1	(0.97) 63(π) $\rightarrow$ 64(π*)	2.85	0.1342
S_2	(0.97) 62(n) $\rightarrow$ 64(π*)	2.99	0.0007
S_3	(0.92) 61(n) $\rightarrow$ 64(π*)	3.62	0.0000
S_4	(0.51) 63(π) $\rightarrow$ 65(π*) + (0.43) 60(π) $\rightarrow$ 64(π*)	4.18	0.0433
S_5	(0.85) 59(n) $\rightarrow$ 64(π*)	4.29	0.0002
S_6	(0.85) 57(n) $\rightarrow$ 64(π*)	4.47	0.0001
S_7	(0.89) 62(n) $\rightarrow$ 66(π*)	4.51	0.0001
S_8	(0.59) 58(π) $\rightarrow$ 64(π*) + (0.24) 60(π) $\rightarrow$ 64(π*)	4.62	0.1360
S_9	(0.30) 58(π) $\rightarrow$ 64(π*) + (0.23) 63(π) $\rightarrow$ 65(π*)	4.77	0.3736
S_{10}	(0.61) 63(π) $\rightarrow$ 66(π*)	4.81	0.0250
S_{11}	(0.50) 56(π) $\rightarrow$ 64(π*)	5.02	0.5776
S_{12}	(0.88) 61(n) $\rightarrow$ 65(π*)	5.10	0.0001
S_{13}	(0.95) 55(n) $\rightarrow$ 64(π*)	5.11	0.0003
S_{14}	(0.99) 63(π) $\rightarrow$ 67(σ*)	5.14	0.0009
S_{15}	(0.92) 62(n) $\rightarrow$ 66(π*)	5.31	0.0009

Table 5.6 Singlet excitations predicted by TDDFT (PBE0/6-311G(d,p)) calculations for protomer **2b** of [LC-H]⁻. Transitions <5.6 eV included. MO transitions which contribute more than 20% to the excitation are listed with the transition as well as an assignment of the initial and final orbitals. Oscillator strengths (f) also included.

State	Orbital Transitions	ΔE (eV)	f
S_1	(0.97) 62(n) → 64(π*)	2.59	0.0002
S_2	(0.98) 63(π) → 64(π*)	3.00	0.0169
S_3	(0.95) 60(n) → 64(π*)	3.27	0.0000
S_4	(0.94) 61(π) → 64(π*)	3.62	0.2408
S_5	(0.49) 57(n) → 64(π*) + (0.44) 59(n) → 64(π*)	3.85	0.0006
S_6	(0.49) 59(n) → 64(π*) + (0.47) 57(n) → 64(π*)	3.96	0.0006
S_7	(0.93) 62(n) → 65(π*)	4.17	0.0000
S_8	(0.96) 63(π) → 65(π*)	4.35	0.0084
S_9	(0.74) 58(π) → 64(π*) + (0.22) 61(π) → 65(π*)	4.47	0.0214
S_{10}	(0.94) 60(n) → 65(π*)	4.79	0.0002
S_{11}	(0.92) 62(n) → 66(π*)	4.87	0.0002
S_{12}	(0.83) 63(π) → 66(π*)	5.02	0.0501
S_{13}	(0.60) 61(π) → 65(π*)	5.13	0.5045
S_{14}	(0.32) 61(π) → 66(π*) + (0.30) 58(π) → 65(π*) + (0.29) 56(π) → 64(π*)	5.24	0.0863
S_{15}	(0.66) 57(n) → 65(π*) + (0.29) 59(n) → 65(π*)	5.30	0.0000
S_{16}	(0.49) 59(n) → 65(π*) + (0.24) 57(n) → 65(π*)	5.39	0.0000
S_{17}	(0.51) 61(π) → 66(π*) + (0.43) 56(π) → 64(π*)	5.42	0.0379
S_{18}	(0.77) 55(n) → 64(π*)	5.44	0.0000
S_{19}	(0.83) 60(n) → 66(π*)	5.52	0.0001
S_{20}	(1.00) 62(n) → 67(σ*)	5.53	0.0002
S_{21}	(0.99) 63(π) → 67(σ*)	5.53	0.0000
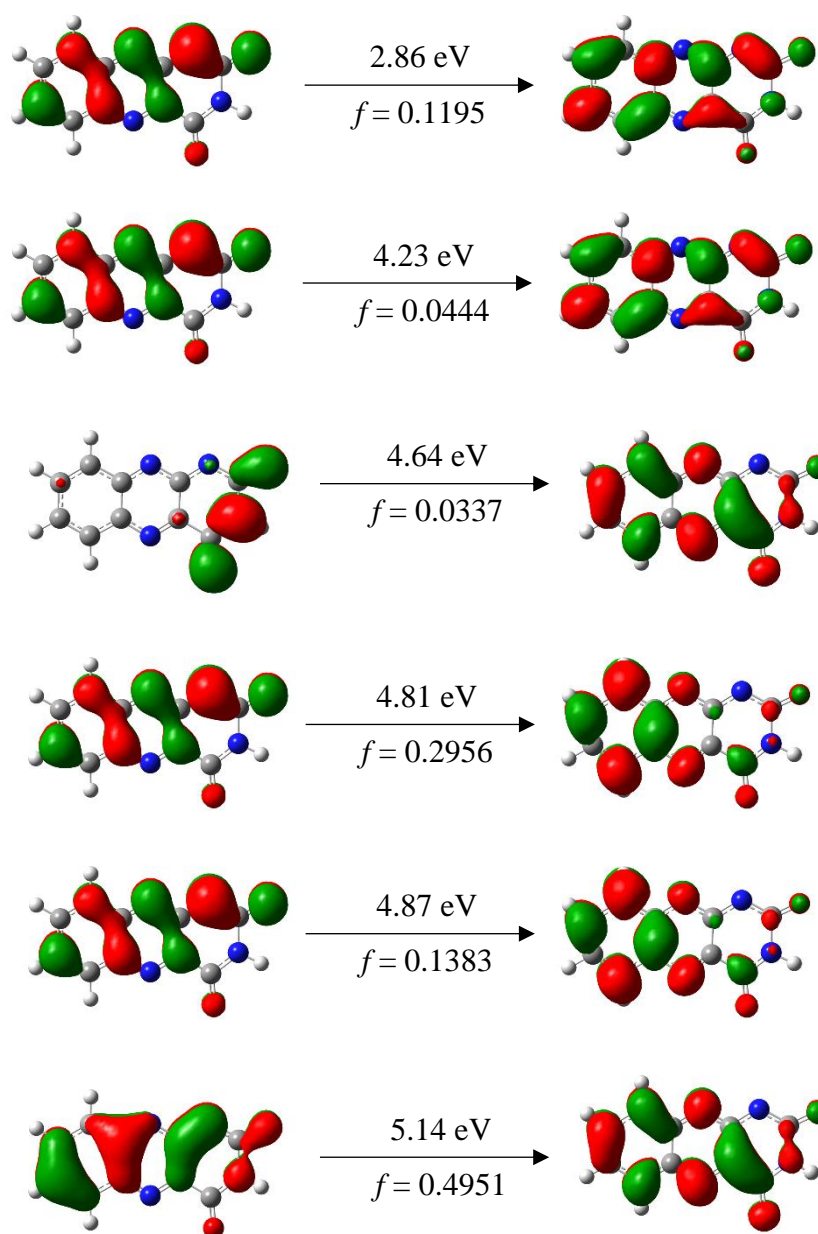
Figure 5.8 Orbital transitions for the strong excitations listed in Table 5.3. The only included orbital transition for each excitation is the transition with the highest contribution to the transition.
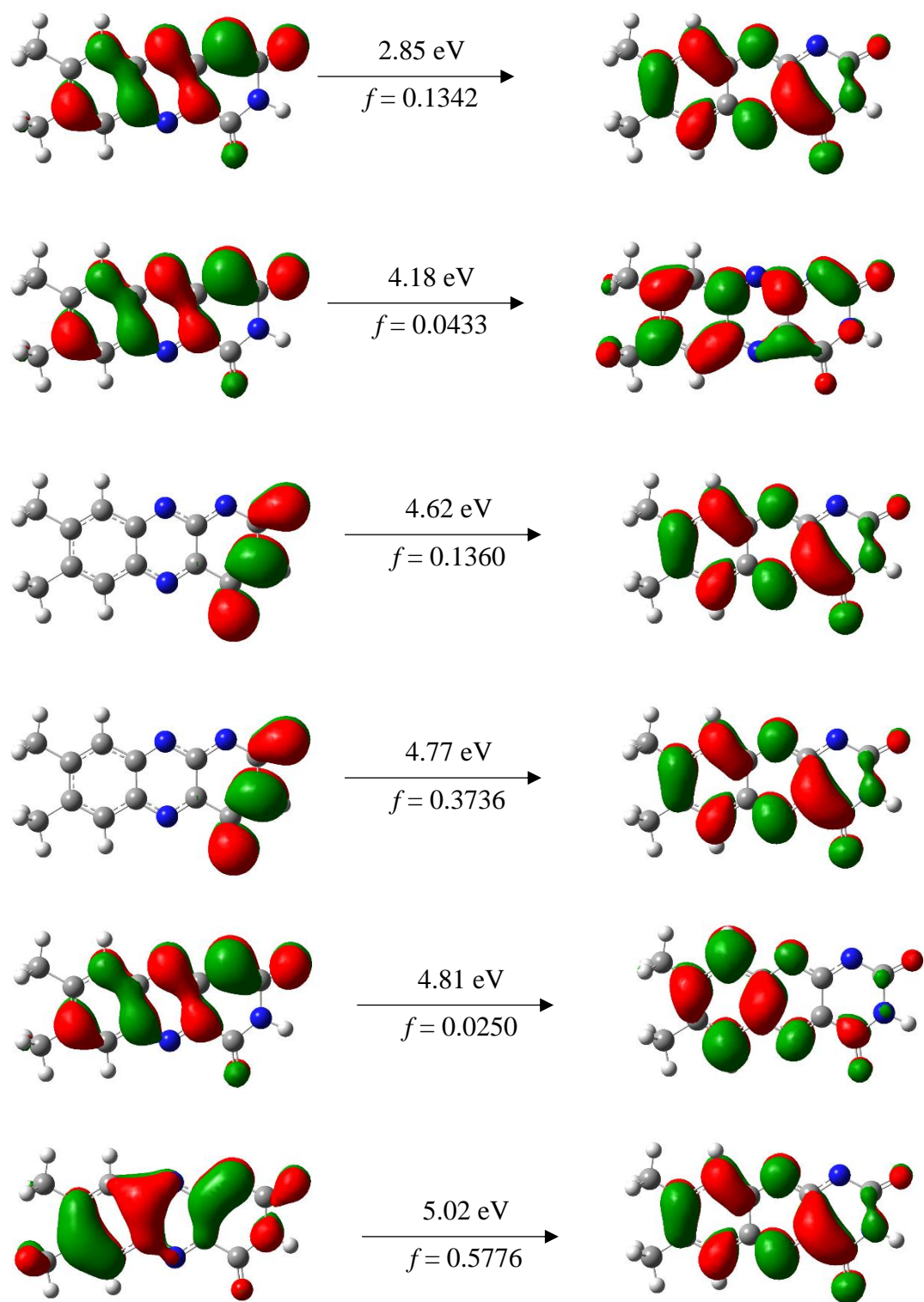
Figure 5.9 Orbital transitions for the strong excitations listed in Table 5.5. The only included orbital transition for each excitation is the transition with the highest contribution to the transition.

Chapter 5

5.7.2 Solution phase absorption spectra of [AL-H]⁻ and [LC-H]⁻

The aqueous absorption spectra of AL and LC under alkaline conditions (pH 11) are given in Figure 5.10. The absorption spectra are similar between the different molecules and show contributions from six absorption bands (3 resolved bands, 2 shoulders and 1 rising edge) across the range 2.4 – 5.64 eV (517 – 220 nm), peak maxima are given in Table 5.7. These spectra match literature spectra for alloxazine and lumichrome under alkaline conditions.[235-237]

In the solution phase, the structures of AL and LC under alkaline conditions has been the subject of some literary dispute. Penzkofer suggests that the neutral LC structure partially tautomerises from an alloxazine to an isoalloxazine ring under mildly basic conditions and that deprotonation occurs with a pKa of approximately 12.5, similar conclusions are reached for AL.[236, 237] This work contradicts an earlier study by Metzler which found that AL and LC deprotonate with pKa = 8.1 and 8.23, respectively.[244] Additionally, Feitelson and Sikorski have both concluded that lumichrome deprotonates with a pKa ~ 8.2 and that, when deprotonated, a mixture of N1 and N3 deprotonated LC (**2a** and **2b**, respectively) is observed.[234, 235] The study by Sikorski provides the most comprehensive analysis of the structure of [LC-H]⁻ through a spectroscopic comparison of LC with its N-methyl derivatives.

The electronic structure calculations present in Section 5.7.1 predict the energy difference between the N1 (**1a**, **2a**) and N3 (**1b**, **2b**) deprotonated structures of [AL-H]⁻ and [LC-H]⁻ to be 6.01 and 5.25 kJ mol⁻¹, respectively, when solvated by an implicit water solvent. Based on these energy differences, the Boltzmann population of the N3 structure at 298 K should be approximately 8 and 11 % for [AL-H]⁻ and [LC-H]⁻ respectively. These computational results agree with the experimental findings of Feitelson and Sikorski.[234, 235] The aqueous absorption spectra of [AL-H]⁻ and [LC-H]⁻, given in Figures 5.10a and 5.10b, respectively, are thus assigned as the absorption spectra of structures **1a** and **2a**, respectively, with a minor contribution from structures **1b** and **2b**, respectively. The absorption spectra of the major and minor isomers of [LC-H]⁻ have been isolated using fluorescence spectroscopy across the region 275 – 500 nm.[234] Structure **2a** has absorption maxima around 400 and 350 nm (λ_2, λ_3), whereas, structure **2b** has absorption maxima at 425 and 340 nm (λ_1, λ_3)

and strongly absorbs below 300 nm (λ_4). Given the structural similarities between AL and LC, the aqueous absorption spectra of structures **1a** and **1b** are likely to be similar to the LC equivalents, i.e. structure **1a** possessing absorption maxima in λ_2 and λ_3 and structure **1b** possessing absorption maxima in λ_1, λ_3 and λ_4.
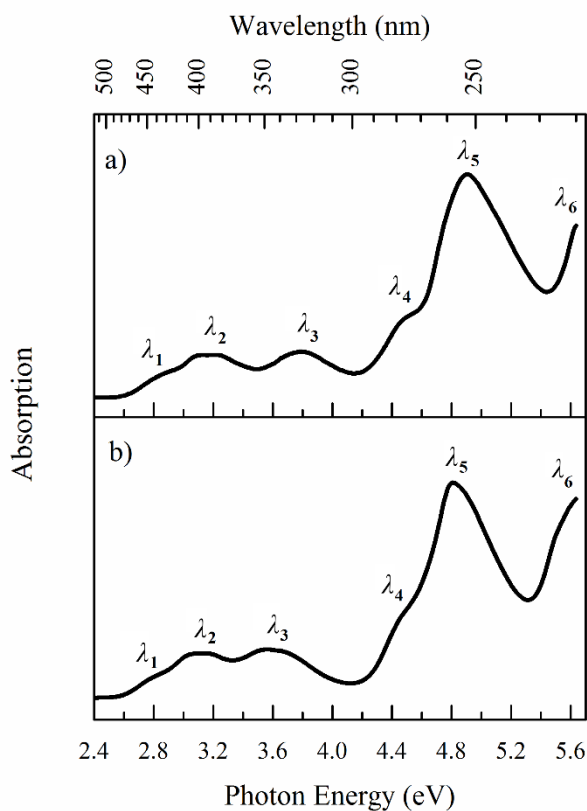
Figure 5.10 Aqueous absorption spectrum of a) [AL-H]⁻ and b) [LC-H]⁻ across the range 2.4 – 5.64 eV (517 – 220 nm). Peak maxima are labelled $\lambda_1 - \lambda_6$ for both [AL-H]⁻ and [LC-H]⁻.

Table 5.7 Solution phase absorption maxima of [AL-H]⁻ and [LC-H]⁻ in water.

Transition	[AL-H]⁻ Absorption Maximum / eV (nm)	[LC-H]⁻ Absorption Maximum / eV (nm)	Origin
λ_1	2.80 (443) *sh*	2.76 (449) *sh*	**1b** (**2b**)
λ_2	3.17 (391)	3.11 (399)	**1a** (**2a**)
λ_3	3.78 (328)	3.56 (348)	**1a**, **1b** (**2a**, **2b**)
λ_4	4.46 (278) *sh*	4.45 (279) *sh*	**1b** (**2b**)
λ_5	4.90 (253)	4.81 (258)	**1a** (**2a**)
λ_6	>5.6	>5.6	

5.7.3 The electrospray ionisation mass spectroscopy of AL and LC

The electrospray ionisation mass spectrum of a mixture of AL and LC, obtained in negative ion mode, is shown in Figure 5.11a. We note that several intense contaminant peaks (*m/z* 255, 283, 297, 311, 325 and 339) are observed alongside the peaks related to [AL-H]⁻ (*m/z* 213) and [LC-H]⁻ (*m/z* 241). The *m/z* 255 and *m/z* 283 peaks are assigned as deprotonated palmitic and stearic acid, which are known contaminants in mass spectrometry.[245] The other peaks have mass differences of 14 *m/z*, indicating that these species are hydrocarbon contaminants which differ by a CH$_2$ group.

A zoomed version of the total ion spectrum, highlighting the mass range where [AL-H]⁻ and [LC-H]⁻ occur, as well as simulated isotope patterns of [AL-H]⁻ and [LC-H]⁻, are presented in Figures 5.11b and 5.11c. Each isotope peak that is simulated is matched by an experimental peak with a similar mass-to-charge ratio, intensity and shape. However, a weak ion is observed with *m/z* 241.6, the identity of this peak is either a contaminant, or the +1 isotope peak of a dianionic [LC-H]⁻ dimer, i.e. [LC-H]⁻·[LC-H]⁻. During laser experiments, the lightest isotope of the [LC-H]⁻ ions was isolated with an isolation width of 1.3 *m/z*. Under these conditions, the weak contaminant with *m/z* 241.6 will be present during laser experiments. If this ion is the +1 isotope peak of a dianion dimer, then the lightest isotope of the dimer will also be present because this ion has the exact same mass-to-charge ratio as [LC-H]⁻.
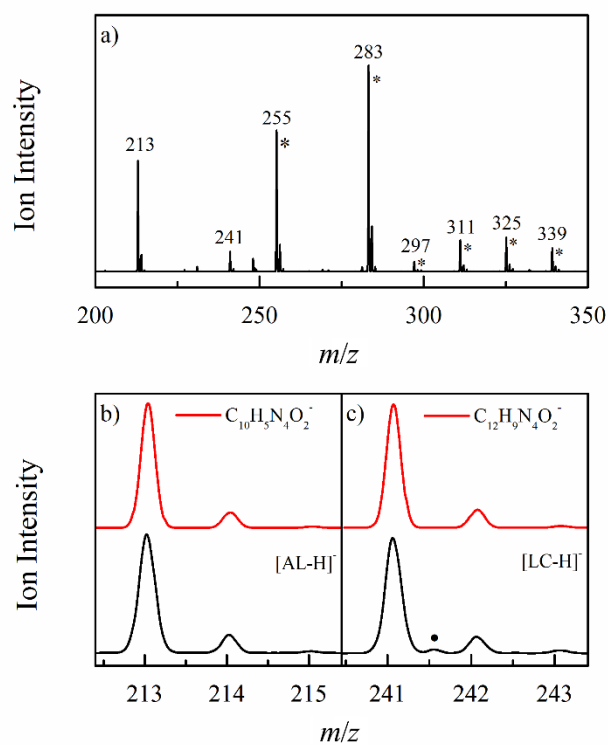
Figure 5.11 a) Total ion mass spectrum of an electrosprayed solution (MeOH) of AL and LC. Expanded spectra of the *m/z* region of b) [AL-H]⁻ and c) [LC-H]⁻ are included. The red lines are simulated isotope patterns for [AL-H]⁻ ($C_{10}H_5N_4O_2^-$) and [LC-H]⁻ ($C_{12}H_9N_4O_2^-$). * indicates a contaminant peak in the total ion spectrum. • indicates an ion with *m/z* 241.6.

Chapter 5

5.7.4 Power studies of the photodepletion cross section of [AL-H]⁻ and [LC-H]⁻

Laser power studies were conducted to determine the relationship between absorption and laser power within bands **I** – **III** for [AL-H]⁻ and [LC-H]⁻. Ion intensities with and without irradiation were collected as the power of the laser was adjusted, the depletion in ion intensity as well as the production intensity of a photofragment were calculated with an excitation energy of 4.77, 4.00 and 2.58 eV (260, 310 and 480 nm). Power studies were repeated a minimum of three times an averaged, the resulting spectra are given in Figures 5.12 and 5.13 for [AL-H]⁻ and [LC-H]⁻, respectively.

Figures 5.12 and 5.13 show that the depletion in ion signal of [AL-H]⁻ or [LC-H]⁻ increases linearly as the laser power increases for all excitation photons tested. This linear relationship shows that single-photon processes will dominate the photodepletion spectrum under the experimental conditions (laser power is ~1 mJ between 220 – 400 nm and ~0.5 mJ between 400 – 564 nm). The production of the photofragment corresponding to the loss of 43 mass units from [AL-H]⁻ or [LC-H]⁻ (*m/z* 170 and 198, respectively) has a different relationship with laser power than depletion. For [AL-H]⁻, production of *m/z* 170 is seen to increase as the laser power increases between 0.5 – 0.7 mJ for all wavelengths tested, above this laser power the production of photofragments is effectively constant; similar behaviour is observed for [LC-H]⁻. The flat photofragment production, despite the increase in parent ion depletion, suggests that the primary photofragment of [AL-H]⁻ and [LC-H]⁻ undergoes secondary photofragmentation at high laser power at all tested wavelengths.
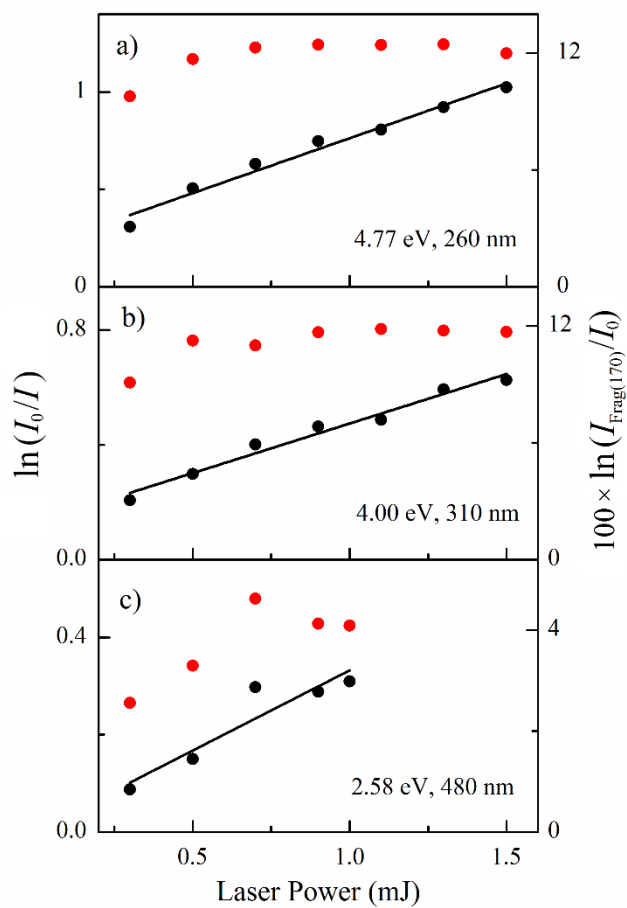
Figure 5.12 Laser power measurements for the photodepletion and photofragment production (*m/z* 170) of [AL-H]⁻, recorded at a) 4.77, b) 4.00, and c) 2.58 eV (260, 310 and 480 nm, respectively).
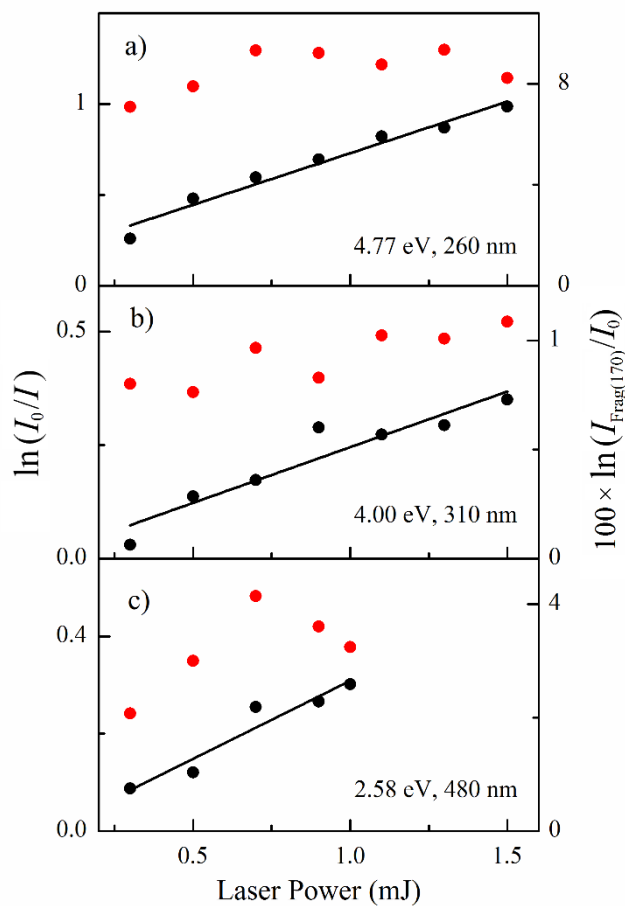
Figure 5.13 Laser power measurements for the photodepletion and photofragment production (*m/z* 198) of [LC-H]⁻, recorded at a) 4.77, b) 4.00, and c) 2.58 eV (260, 310 and 480 nm, respectively).

Chapter 5

5.7.5 The thermal- and photofragmentation of [AL-H]⁻ and [LC-H]⁻

The electronic ground-state fragmentation mechanisms of [AL-H]⁻ and [LC-H]⁻ have been studied using collision induced dissociation (CID), CID mass spectra of [AL-H]⁻ and [LC-H]⁻ are presented in Figure 5.14. [AL-H]⁻ and [LC-H]⁻ are seen to thermally fragment solely by losing 43 mass units (HNCO).

A photofragment mass spectrum of [AL-H]⁻ resulting from excitation at 4.77 eV (260 nm) photons is displayed in Figure 5.15. The most intense photofragment is *m/z* 170 which corresponds to the loss of 43 mass units (HNCO) from [AL-H]⁻, with a second weaker fragment of *m/z* 142 evident. This corresponds to a further loss of CO from the parent ion. The primary photofragment of [AL-H]⁻ is the same as the thermal fragment, showing that it is possible that fragmentation in laser-photodissociation experiments occurs following electronic relaxation to a vibrationally excited electronic ground state.
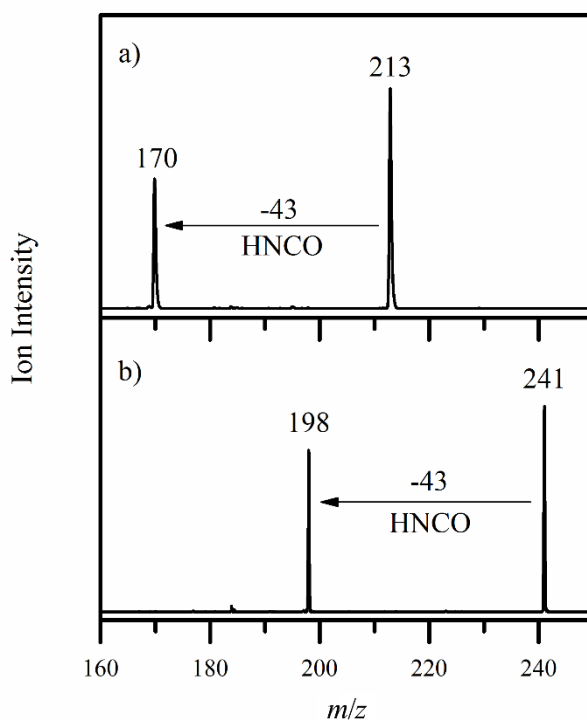
Figure 5.14 CID mass spectra of a) [AL-H]⁻ and b) [LC-H]⁻ fragmented with a fragmentation amplitude of 0.47 V for [AL-H]⁻ and 0.43 V for [LC-H]⁻. Neutral losses required to produce the photofragments are included.
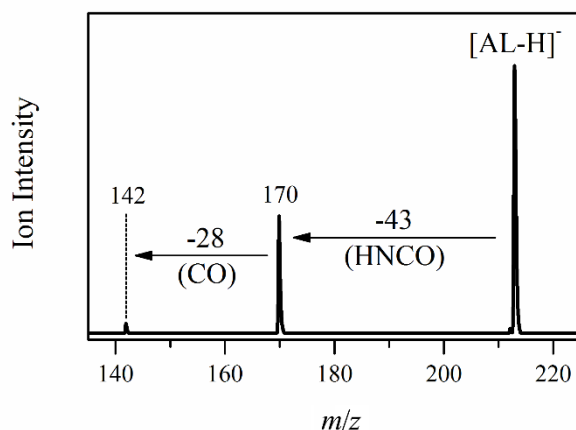
Figure 5.15 Photofragment mass spectra of [AL-H]⁻ excited at 4.77 eV (260 nm). Assignments of the neutral species lost upon photofragmentation are included.

The photofragmentation observed when [LC-H]⁻ is photoexcited at 4.77 eV (Figure 5.16) is primarily the same as for [AL-H]⁻, with the major photofragmentation channels corresponding to loss of 43 and 71 mass units to produce photofragments with m/z 198 and 170, respectively, and these photofragments are seen with similar intensities to the corresponding photofragments of [AL-H]⁻. A number of minor photofragments with m/z 168, 169, 172, 482 and 483 are also observed.

The observation of high mass fragments in the photofragmentation spectrum of [LC-H]⁻ is particularly striking, since an equivalent fragment is not observed in the photofragment mass spectrum of [AL-H]⁻. However, when considering the high mass fragments it is important to remember the low-intensity peak at m/z 241.6 observed in the ESI mass spectrum (Figure 5.11c), this peak could not be separated from [LC-H]⁻ (m/z 241.1) when attempting to isolate [LC-H]⁻ in the ion trap. Given that high mass peaks occur at twice the value of the low-intensity contaminant (m/z 483) and one mass unit below this number, it is reasonable to conclude that the origin of these high mass photofragments is from electron detachment from a dianion with m/z 241.1 and a +1 isotope peak with m/z 241.6. Since the dianionic species occurs with the same mass as [LC-H]⁻, it is possible that the dianion is a dimer of [LC-H]⁻ ions (i.e. [LC-H]⁻·[LC-H]⁻). Inset b in Figure 5.16 compares the high-mass fragments against a simulated isotopic distribution of an electron detached [LC-H]⁻ dimer ($C_{24}H_{18}N_8O_4^{\bullet-}$), a similar isotopic distribution is observed in the experimental and simulated spectra, suggesting a common origin.
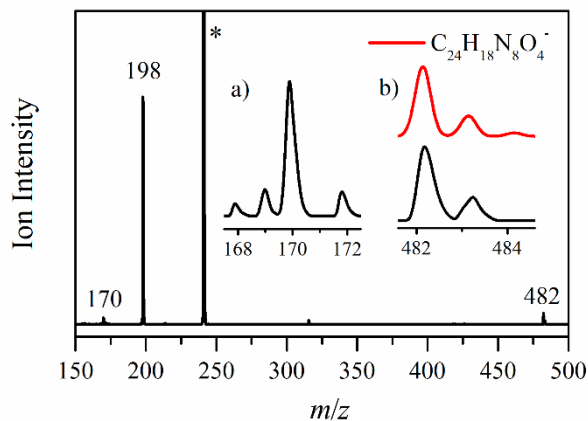
Figure 5.16 Photofragment mass spectra of [LC-H]$^-$ excited at 4.77 eV (260 nm). The insets show an expanded mass spectrum between a) m/z 168 – 172 and b) m/z 482 – 484, including a simulated isotope distribution pattern (red) of [LC-H]$^{\bullet}\cdot$[LC-H]$^-$ ($C_{24}H_{18}N_8O_4$).

Inset a in Figure 5.16 shows a zoomed spectrum between m/z 168 – 172, three low-intensity peaks (m/z 168, 169 and 172) are observed in this region which are not observed in the equivalent region of the photofragment mass spectrum of [AL-H]$^-$. Since the only structural difference between AL and LC is the presence of methyl groups in LC, it is possible that these unique fragments occur following the loss of neutral species involving the two methyl groups. Assignments of all photofragments are included in Table 5.8.

Table 5.8 Assignments of the photofragments of [AL-H]⁻ and [LC-H]⁻.

Alloxazine Fragments		Lumichrome Fragments	
m/*z*	Assignment	*m*/*z*	Assignment
170	[AL-H-HNCO]⁻	198	[LC-H-HNCO]⁻
142	[AL-H-HNCO-CO]⁻	170	[LC-H-HNCO-CO]⁻
		482	[LC-H]·[LC-H]•⁻
		483	[LC-H]·[LC-H]•⁻
		168	[LC-H-HNCO-C_2H_6]⁻
		169	[LC-H-HNCO-C_2H_5]•⁻
		172	[LC-H-HNCO-C_2H_2]⁻

5.7.6 Photofragment action spectrum of the m/z 482 photofragment from [LC-H]⁻

The photofragment production spectrum of *m/z* 482, produced from *m/z* 241, is shown in Figure 5.17. The identity of this fragment has been discussed in Section 5.7.5 and is likely to be a cluster of two [LC-H]⁻ molecules with a single negative charge, originating from a dianionic dimer. The *m/z* 482 production spectrum has an onset of ~3.7 eV, since the fragment is an electron detached photoproduct it is likely that 3.7 eV is the threshold detachment energy of the dianionic species. *m/z* 482 is produced as a trace fragment up to 4.2 eV, whereupon the production increases near-linearly as the photon energy increases. The production spectrum does not peak within band **III**, or indeed in bands **I** and **II**, of the [LC-H]⁻ photodepletion spectrum (Figure 5.3b). This suggests that electron detachment from the dimer occurs by directly absorbing a photon with energy greater than the electron binding energy, rather than auto-detachment from an excited state or via multiphoton ionisation.
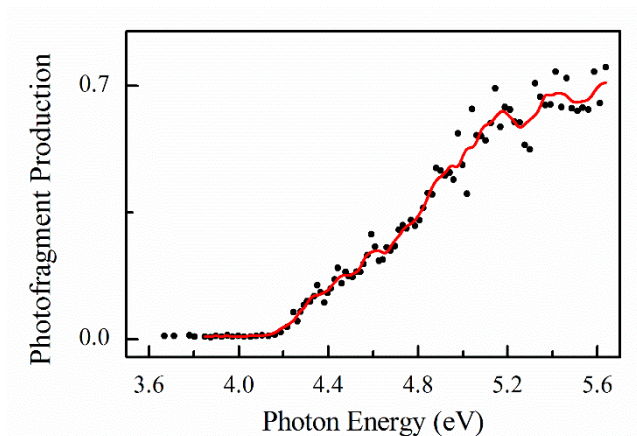
Figure 5.17 Photofragment production spectrum of m/z 482 produced following the mass selection of [LC-H]⁻ (*m/z* 241) across the range 3.6 – 5.6 eV. The solid red line is a five point adjacent-average of the data points.

Chapter 6

UV laser photoactivation of hexachloroplatinate bound to individual nucleobases in vacuo as molecular level probes of a model photopharmaceutical

6.1 Preamble

The following work has been published in the *Physical Chemistry Chemical Physics*. All data, including experimental and computational, have been collected by me. Data processing routines have also been performed by me. The initial draft of the manuscript was written by me and revised by Caroline Dessent, Ananya Sen, Naruo Yoshikawa and Ed Bergström.

Electronic supplementary information (ESI) which was included with the publication is appended to this Chapter as Section 6.7. This includes instrumental details; TDDFT excitation spectra; aqueous absorption spectra; photofragment mass spectra and photofragment production profiles; and calculated fragmentation enthalpies.

Full Reference to the publication:

"UV laser photoactivation of hexachloroplatinate bound to individual nucleobases in vacuo as molecular level probes of a model photopharmaceutical"

E. Matthews, A. Sen, N. Yoshikawa, E. Bergström and C. E. H. Dessent, *Phys. Chem. Chem. Phys.*, 2016, **18**, 15143–15152.

http://dx.doi.org/10.1039/C6CP01676F

Chapter 6

6.2 Abstract

Isolated molecular clusters of adenine, cytosine, thymine and uracil bound to hexachloroplatinate, $PtCl_6^{2-}$, have been studied using laser electronic photodissociation spectroscopy to investigate photoactivation of a platinum complex in the vicinity of a nucleobase. These metal complex–nucleobase clusters represent model systems for identifying the fundamental photochemical processes occurring in photodynamic platinum drug therapies that target DNA. This is the first study to explore the specific role of a strongly photoactive platinum compound in the aggregate complex. Each of the clusters studied displays a broadly similar absorption spectra, with a strong $\lambda_{max} \sim 4.6$ eV absorption band and a subsequent increase in the absorption intensity towards higher spectral-energy. The absorption bands are traced to ligand-to-metal-charge-transfer excitations on the $PtCl_6^{2-}$ moiety within the cluster, and result in $Cl^- \cdot$nucleobase and $PtCl_5^-$ as primary photofragments. These results demonstrate how selective photoexcitation can drive distinctive photodecay channels for a model photo-pharmaceutical. In addition, cluster absorption due to excitation of nucleobase-centred chromophores is observed in the region around 5 eV. For the uracil cluster, photofragments consistent with ultrafast decay of the excited state and vibrational predissociation on the ground-state surface are observed. However, this decay channel becomes successively weaker on going from thymine to cytosine to adenine, due to differential coupling of the excited states to the electron detachment continuum. These effects demonstrate the distinctive photophysical characteristics of the different nucleobases, and are discussed in the context of the recently recorded photoelectron spectra of theses clusters

6.3 Introduction

Photoactive metallodrugs are the subject of intense current investigation as potential chemotherapy treatments.[246] These compounds can frequently act as "prodrugs" which are compounds that have low native toxicity but can be selectively activated in diseased tissue.[247] A number of platinum compounds have been shown to have considerable potential as anti-cancer prodrugs since they become highly cytotoxic upon photoactivation.[248] While the anti-cancer potential of such compounds has been demonstrated through *in vitro* investigations, many questions exist regarding the key

Scheme 6.1 Schematic diagram of the structures of hexachloroplatinate, adenine, cytosine, thymine and uracil.

Hexachloro-platinate   Adenine   Cytosine   Thymine   Uracil
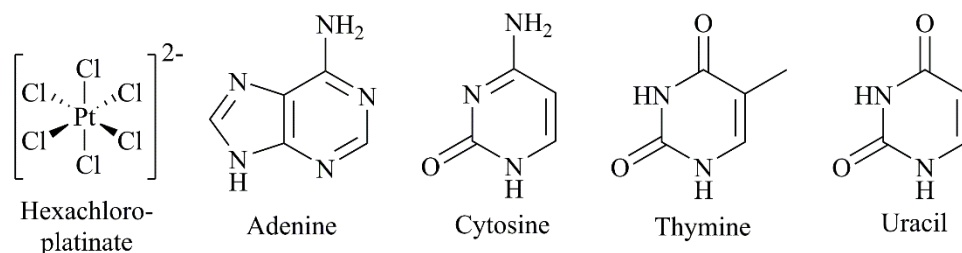
photophysical and photochemical processes that take place in the complex biological medium.[249, 250]

In a recent series of studies, we have used electrospray ionisation to produce nucleobase–platinum complex clusters as isolated gas-phase molecular aggregates.[169, 251, 252] The study of such clusters in the gas phase has considerable potential to contribute to our understanding of the factors that affect metal-compound–nucleobase binding within a well-defined, controlled environment, whilst also allowing the characterisation of the photophysics and photochemistry of the aggregates *via* laser spectroscopy. Our initial work involved $Pt(CN)_4^{2-}$ and $Pt(CN)_6^{2-}$ as simple, model Pt(II/IV) complexes, bound to the DNA nucleobases thymine, cytosine and adenine along with the RNA nucleobase, uracil. The structures of these nucleobases, as well as the structure of the hexachloroplatinate dianions, are given in Scheme 6.1. The $Pt(CN)_4^{2-}$ and $Pt(CN)_6^{2-}$ complexes do not display strong chromophores across the 220–300 nm range studied, hence allowing us to focus in those initial studies on photoexcitation of the nucleobase-centred chromophore. In this work, we investigate aggregates consisting of the same series of nucleobases this time bound to the hexachloroplatinate complex ($PtCl_6^{2-}$), to allow us to study the effect of including a "photoactive" Pt complex within the aggregate cluster, hence moving towards more pharmaceutically relevant model systems.

The intrinsic UV spectroscopy of isolated, gas-phase hexachloroplatinate has been investigated in detail by Weber and co-workers using photodissociation spectroscopy.[23] This study revealed that photoexcitation of $PtCl_6^{2-}$ results in ionic fragmentation of the dianion into $PtCl_5^-$ and Cl^-, with a band profile that peaks at 4.55 eV. $PtCl_4^-$ was also observed as a photofragment through this band, and then as an increasingly intense photofragment to higher excitation energy. It was concluded

that the $PtCl_4^-$ is produced from the initially formed $PtCl_5^-$ due to excess energy residing in the molecule following ionic fragmentation of the initial dianion. Photodetachment (*i.e.* production of $PtCl_6^-$) is also prominent, with excitation of electronic transitions of the dianion leading to resonant enhancement of the photodetachment cross-section superimposed on direct electron detachment above the electron detachment threshold ($\sim$3.75 eV). Wang and Wang have used photoelectron spectroscopy to characterise the electron detachment properties of gas-phase hexachloroplatinate.[253] There have also been several high-level theoretical studies of gaseous $PtCl_6^{2-}$.[254, 255] Therefore, the intrinsic properties of the $PtCl_6^{2-}$ dianion are well established in the gas phase.

The photochemical activity of the $PtCl_6^{2-}$ complex has been very extensively studied in the solution phase as a prototype transition metal complex.[256] While the earliest such measurements were conducted around 200 years ago, there is considerable current work in this field due to the applications of $PtCl_6^{2-}$ in the photoproduction of platinum nanoparticles and in the modification of the surfaces of TiO_2 and CdS to produce tailored photocatalysts.[257-259]

UV light has the potential to effect permanent damage in the structure of DNA, so that the UV photophysics and photochemistry of DNA is of considerable fundamental importance. Since the nucleobase units of DNA are responsible for absorbing UV light, their photophysical properties have been very widely studied. Nucleobases are known to display ultrafast non-radiative decay following UV excitation, which converts the electronic excitation into heat energy which can be dissipated on the ground electronic state. References 260-262 provide reviews of experimental work in this extensive field, while Reference 263 provides a very recent review of associated theoretical studies.

We have recently studied the low-temperature photoelectron spectra of clusters of $PtCl_6^{2-}$ bound to individual nucleobases as a precursor to the current study.[264] Adiabatic electron detachment energies and repulsive Coulomb barriers were obtained, providing us with electron detachment energies to aid the interpretation of the photodissociation spectra presented below. The photoelectron spectra of the $PtCl_6^{2-}\cdot$nucleobase clusters displayed well-resolved, distinct peaks that are

consistent with structures where the $PtCl_6^{2-}$ dianion is largely unperturbed. This is important as it illustrates that the precursor clusters to be studied in this work contain each of the component moieties as intact molecules.

6.4 Experimental and theoretical methods

Experiments were performed using an AmaZon (Bruker Daltonik) ion trap mass spectrometer. Typical instrumental parameters were: nebulising gas pressure of 10.0 psi; injection rate of 250 μL h^{-1}; drying-gas flow rate of 8.0 L min^{-1}; capillary temperature of 100 °C; and ion isolation time of 40 ms. The nucleobase–hexachloroplatinate complexes were prepared by electrospraying solutions of the nucleobase and the dianion (Na$_2$PtCl$_6$ at 1×10^{-4} mol dm^{-3} mixed with droplets of the nucleobase solutions at 1×10^{-2} mol dm^{-3}) in deionised water. (No experiments were conducted for guanine, due to its low solubility in water.) All chemicals were purchased from Sigma Aldrich and used without further purification. Fragment ions with m/z less than ~50 are not detectable in the instrument since low masses fall outside of the mass window of the trap.

Low-energy collision induced dissociation (CID) (also termed resonance excitation) was performed on isolated ions by applying an excitation AC voltage to the end caps of the trap to induce collisions of the trapped anionic complexes with the He buffer gas. We have described these experiments in detail previously,[265, 266] and we refer the reader to these references for further details and a discussion of the limitations of CID experiments for obtaining quantitative information. UV laser photo-fragmentation experiments were conducted in the AmaZon ion-trap mass spectrometer, which was modified for the laser experiments as described in detail in Chapter 2 as well as Section 6.7.1. All experiments were run under one-photon conditions, by ensuring that the photodepletion intensity increases linearly with laser power at several points across the scanned spectral region.

Time-dependent density functional theory (TDDFT) calculations were carried out to aid the interpretation of the experimental spectra. TDDFT have been successfully applied to nucleobases, nucleobase clusters and platinum complexes previously, allowing us to reliably apply these calculations to aid the assignment of electronic

transitions.[267-269] The TDDFT calculations all use the optimized cluster geometries that have been published previously in Reference 264. Gaussian 09 was used for all calculations,[135] employing the M06-2X functional with the split basis set of: 6-311+G(2d,2p) on all first and second row atoms and the def2-TZVPP (from Aldrich *et al.*, triple zeta valence basis set with additional polarisation functions) basis set to describe the platinum valence orbitals with the 60 core electrons represented by the Stuttgart/Dresden electron core pseudopotential, at the Wood–Boring quasi-relativistic level of theory.[147, 174, 175, 270-272] The def2-TZVPP basis set has previously been used successfully to describe the valence electrons of $PtCl_6^{2-}$ in TDDFT calculations.[23]

6.5 Results and discussion

6.5.1 Low-energy collisional activation of the $PtCl_6^{2-}$–nucleobase clusters

The negative ion electrospray mass spectrum (ESI-MS) of a mixed $PtCl_6^{2-}$/thymine solution is displayed in Figure 6.1. While the $PtCl_6^{2-}$ dianion dominates the ESI-MS, peaks resulting from clusters of $PtCl_6^{2-}$ with one and two nucleobases are also clearly visible *i.e.* $PtCl_6^{2-} \cdot T_n$, $n = 1, 2$. The propensity for the solution components to react is evident from the prominent appearance of several other species in the ESI-MS including the deprotonated nucleobase anion $[T–H]^-$, the $T \cdot Cl^-$ cluster, $PtCl_x^-$ ($x = 3–5$) complex ions, and the peaks centred at $\sim m/z = 192, 354$ and 390 mass units which have a chloride ligand of a $PtCl_x$ complex replaced by water or hydroxide. The
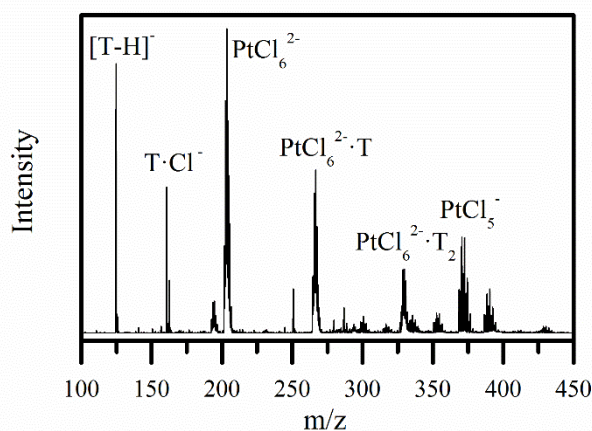
Figure 6.1 Negative ion ESI-MS of a solution of the sodium salt of $PtCl_6^{2-}$ with the nucleobase thymine.

Table 6.1 Low-energy CID results for the $PtCl_6^{2-} \cdot M$, M = A, C, T, U clusters, including $E_{1/2}$ fragmentation energies and CID fragment ions[ab]

Cluster	$E_{1/2}$	Product Ions
$PtCl_6^{2-} \cdot A$	6.42	$PtCl_6^{2-}$, $PtCl_5^-$, $A \cdot Cl^-$, $[A-H]^-$
$PtCl_6^{2-} \cdot C$	6.17	$PtCl_6^{2-}$, $PtCl_5^-$, $C \cdot Cl^-$
$PtCl_6^{2-} \cdot T$	6.50	$PtCl_6^{2-}$, $PtCl_5^-$, $T \cdot Cl^-$
$PtCl_6^{2-} \cdot U$	6.64	$PtCl_6^{2-}$, $PtCl_5^-$, $U \cdot Cl^-$, $[U-H]^-$

a $E_{1/2}$ values are for 50% depletion of the parent cluster.

b Product ions are listed in order of decreasing fragment ion intensity.

rich chemistry evident in the $PtCl_6^{2-}$/thymine mass spectrum contrasts with the much simpler ESI-MS observed for mixtures of thymine with $Pt(CN)_6^{2-}$ and $Pt(CN)_4^{2-}$.[251] Similar mass spectra were observed when solutions of the other nucleobases with $PtCl_6^{2-}$ were electrosprayed.

Low-energy CID was performed for the $PtCl_6^{2-} \cdot M$, M = A, C, T, U clusters, with Table 6.1 summarising the results. Figure 6.2 displays the % fragmentation curves across the collisional activation range. We note that the precursor cluster ions are stable across the low-energy CID range, illustrating that they are stable ground-state molecular clusters and do not undergo metastable decay prior to resonance excitation.[265] The major fragmentation process for each of the $PtCl_6^{2-} \cdot M$ clusters is simple cluster fission, consistent with an initial cluster that is composed of intact $PtCl_6^{2-}$ and nucleobase units:

$$PtCl_6^{2-} \cdot M \quad \rightarrow \quad PtCl_6^{2-} + M$$

Reaction 6.1

In addition, each of the $PtCl_6^{2-} \cdot M$ clusters also fragments *via* a chloride ion transfer reaction:

$$PtCl_6^{2-} \cdot M \quad \rightarrow \quad PtCl_5^- + M \cdot Cl^-$$

Reaction 6.2

This reaction can be viewed as an "ionic fragmentation" reaction of the multiply charged cluster.[265] Reaction 6.2 is most prominent for the $PtCl_6^{2-} \cdot A$ cluster and least
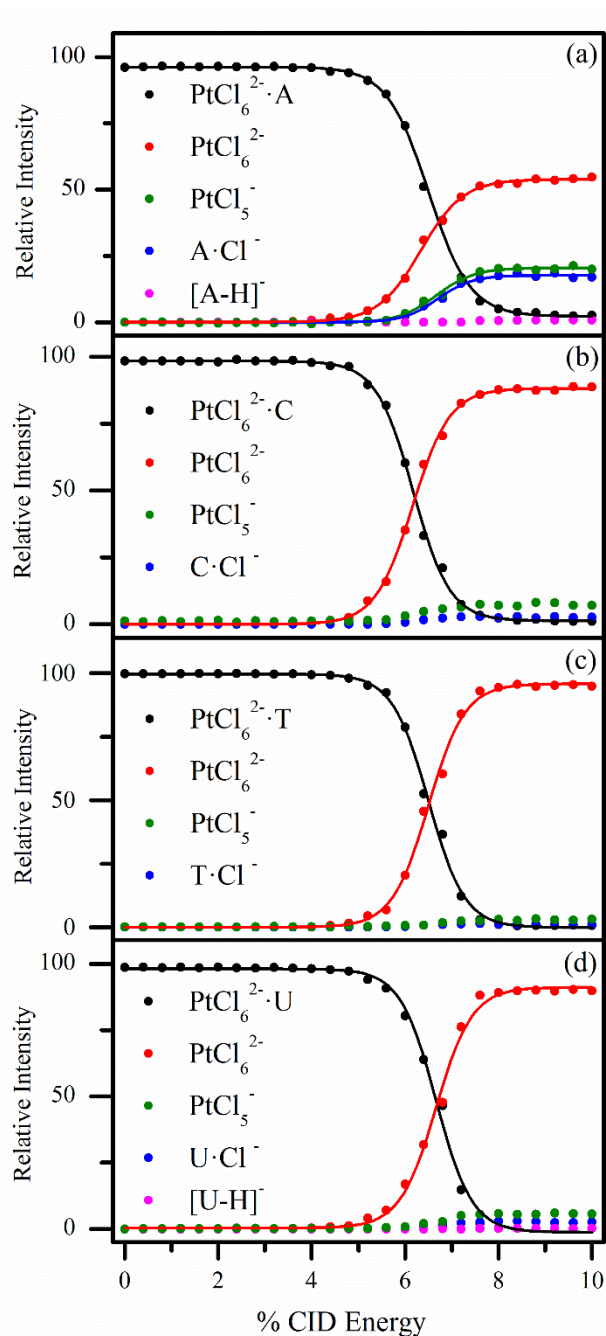
Figure 6.2 % Fragmentation decay curves for (a) $PtCl_6^{2-} \cdot A$, (b) $PtCl_6^{2-} \cdot C$, (c) $PtCl_6^{2-} \cdot T$ and (d) $PtCl_6^{2-} \cdot U$ upon low energy CID. Onset plots for production of the associated fragment ions are also shown. Typical experimental errors (obtained for repeat runs) were $\pm 3\%$.

---

prominent for the $PtCl_6^{2-} \cdot T$ cluster. (The origin of the difference in the fragmentation characteristics may lie in the different structures of systems. Adenine does not contain an electron rich carbonyl whereas $PtCl_6^{2-} \cdot T$ has a carbonyl close to the chloride ligands.) In addition to fragmentation reactions 6.1 and 6.2 the deprotonated nucleobase, *i.e.* $[M–H]^-$, is observed as a very low intensity fragment from $PtCl_6^{2-} \cdot A$

and $PtCl_6^{2-} \cdot U$. Isolation of the $A \cdot Cl^-$ cluster and subsequent CID produced the deprotonated nucleobase as the sole fragment ion,

$$M \cdot Cl^- \quad \rightarrow \quad [M\text{-}H]^- + HCl$$
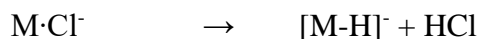
Reaction 6.3

indicating that the deprotonated nucleobase fragments can be formed *via* a two stage process from the $PtCl_6^{2-} \cdot M$ cluster. The low intensity of $[M–H]^-$ as a direct CID product from excitation of the $PtCl_6^{2-} \cdot M$ clusters is intriguing given that $[M–H]^-$ appears so prominently in the ESI-MS. This suggests that $[M–H]^-$ is probably formed *via* solution-phase reactions prior to electrospray.

In summary, the low-energy CID measurements of the $PtCl_6^{2-} \cdot M$ clusters provide further evidence that the clusters are composed of intact $PtCl_6^{2-}$ and nucleobase moieties. The clusters all display similar binding energies (as reflected by the similar $E_{1/2}$ values in Table 6.1), and decay of the clusters on the ground-state potential energy surface results predominantly in formation of $PtCl_6^{2-}$.

6.5.2 Time-dependent density functional theory calculations of the $PtCl_6^{2-}$– nucleobase clusters

Figure 6.3 shows a TDDFT calculated excitation spectrum of the $PtCl_6^{2-} \cdot U$ cluster, with the associated excitation assignments being listed in Table 6.2. The calculated spectrum of $PtCl_6^{2-} \cdot U$ is presented here, with results for the other $PtCl_6^{2-} \cdot M$ clusters (and $PtCl_6^{2-}$) given in Section 6.7.2. TDDFT calculations of uncomplexed $PtCl_6^{2-}$ have been performed previously with the PBE0 functional,[23] producing a calculated UV spectrum with weak and strong bands (**I** and **II**) at 4.74 and 6.19 eV, respectively, both associated with ligand-to-metal charge transfer (LMCT) transitions. Calculations on $PtCl_6^{2-}$ using the M06-2X functional were also conducted as part of this work to allow direct comparison to the cluster calculations, with bands **I** and **II** appearing at 4.59 and 5.98 eV, respectively.

The calculated UV spectrum of $PtCl_6^{2-} \cdot U$ (Figure 6.3) is blue-shifted compared to bare $PtCl_6^{2-}$, with bands **I** and **II** appearing at 4.73 and 6.10 eV. Analysis of the molecular orbitals involved in the bright excitations (oscillator strength >0.005) over
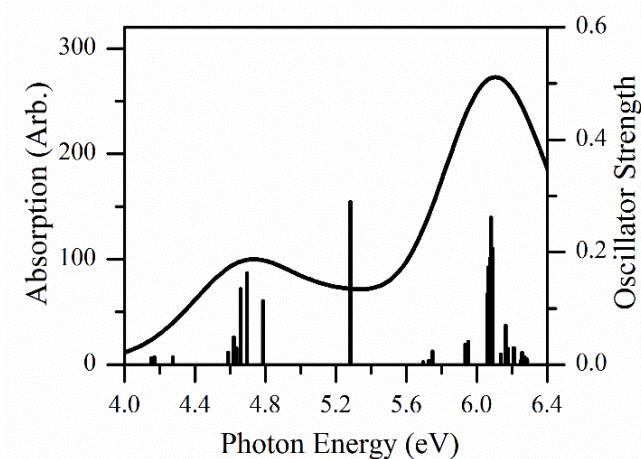
Figure 6.3 Calculated excitation energies of the $PtCl_6^{2-} \cdot U$ from TDDFT calculations with the M06-2X functional. The oscillator strengths of individual transitions are given by the vertical bars. The full line spectrum represents a convolution of the calculated spectrum with a Gaussian function (0.333 eV HWHM).

the experimental range reveals transitions from a ground-state cluster where the MOs either originate from $PtCl_6^{2-}$ orbitals or from orbitals which have electron density primarily in a uracil π orbital but with minor delocalisation to the $PtCl_6^{2-}$ moiety. The corresponding excited states are localised either on $PtCl_6^{2-}$ orbitals or a uracil π^* orbital (Table 6.2). While the $PtCl_6^{2-}$ localised transitions are LMCT in nature (as in uncomplexed $PtCl_6^{2-}$), it is evident that complexation with uracil removes degeneracy from these LMCT transitions in the region 4.1–4.8 eV,[23] and relaxes the selection rules, such that forbidden transitions in uncomplexed $PtCl_6^{2-}$ at 4.6–4.7 eV become allowed. The intense transition at 5.28 eV populates a uracil π^* orbital. This transition occurs close to an experimentally measured and computationally predicted π to π^* transition in gaseous uracil which occurs at ~5.1 eV.[273-275] Gordon and co-workers have performed elegant calculations to probe solvent-induced shifts on the electronic transitions of uracil, and it is evident from these calculations that the gaseous uracil π to π^* transition will shift with sequential solvation.[267]

Similar results were obtained for the other nucleobase clusters (Section 6.7.2). In general, the clustering of the nucleobase to $PtCl_6^{2-}$ blue-shifts the two LMCT bands such that the peak-to-peak separation is unperturbed relative to bare $PtCl_6^{2-}$. This suggests that the nucleobase primarily interacts to stabilise the ground state of $PtCl_6^{2-}$, and inspection of the MOs reveals that the excited state of both LMCT bands is

Table 6.2 Calculated transition energies (4–6 eV) and oscillator strengths of $PtCl_6^{2-} \cdot U$ from TDDFT calculations with the M06-2X functional[a]

Transition Energy (eV)	Oscillator Strength
$PtCl_6^{2-}$ LMCT Transitions	
4.15	0.0116
4.17	0.0142
4.27	0.0135
4.59	0.0216
4.62	0.0492
4.63	0.0300
4.66	0.1352
4.69	0.1632
4.79	0.1142
5.93	0.0367
Uracil π and $PtCl_6^{2-}$ Orbitals $\rightarrow$ Uracil π^* Transitions[b]	
5.28	0.2899
5.75	0.0240

a Only transitions with oscillator strength >0.005 are listed.

b Uracil π orbitals have a minor electronic delocalisation to the $PtCl_6^{2-}$ moiety largely unperturbed by the presence of the nucleobase. Finally, we note that strong nucleobase-centred transitions are seen between 5–5.5 eV for the thymine, cytosine and adenine clusters, analogous to the strong 5.28 eV uracil-centred transition.

6.5.3 Electronic laser photodissociation spectroscopy of the $PtCl_6^{2-}$ – nucleobase clusters

6.5.3.1 Photodepletion spectra of $PtCl_6^{2-} \cdot M$

To explore the $PtCl_6^{2-} \cdot M$ UV photochemistry and photophysics, the complexes were photoexcited from 4.0–5.8 eV (310–215 nm). This region begins around the approximate electron detachment energy for each cluster: $\sim$3.96, 3.98, 4.05 and 4.05 eV for M = A, C, T and U, respectively.[264] (We note that since the clusters studied here are dianionic, the electron detachment threshold is given by the repulsive coulomb barrier height added to the electron affinity.) The gas-phase $PtCl_6^{2-} \cdot M$

photodepletion (absorption) spectra are presented in Figure 6.4. Solution-phase UV-vis spectra are included in Section 6.7.3 for aqueous $PtCl_6^{2-}$, as well as the individual solution-phase nucleobases. These spectra can be used along with the TDDFT calculations to guide the assignment of the gas-phase cluster absorption spectra.[169, 252]

All of the photodepletion spectra display broad, non-Gaussian absorption features over the range 4.2–5.2 eV, peaking between 4.44 and 4.63 eV with a maximum at
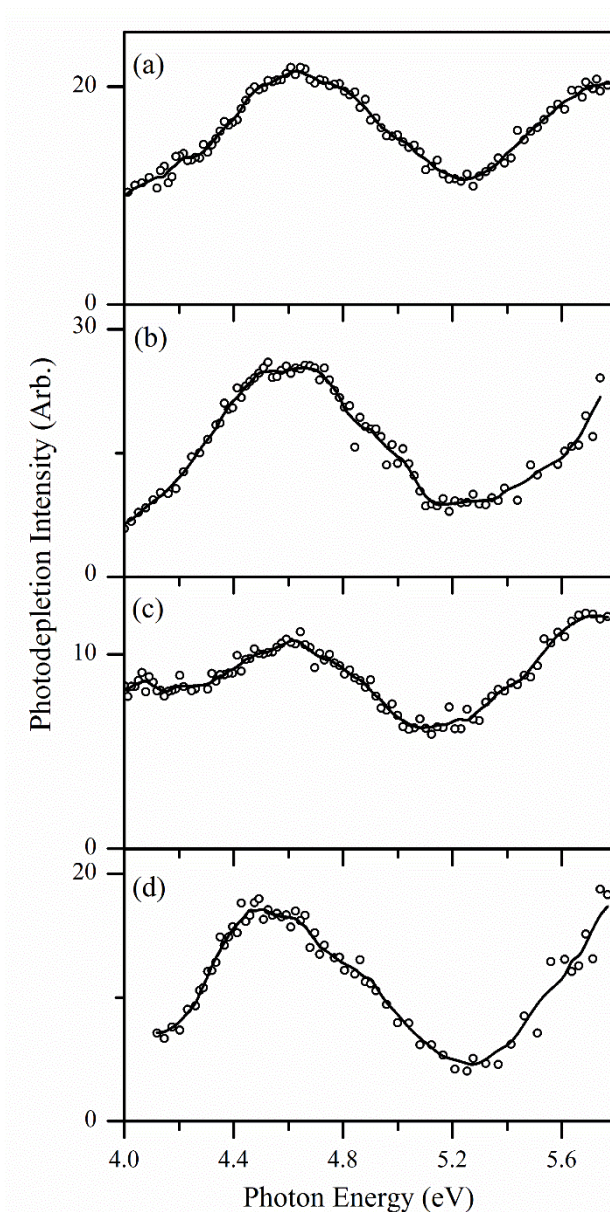
Figure 6.4 Photodepletion (absorption) spectra of (a) $PtCl_6^{2-}\cdot U$, (b) $PtCl_6^{2-}\cdot T$, (c) $PtCl_6^{2-}\cdot C$ and (d) $PtCl_6^{2-}\cdot A$ across the region 4.0–5.8 eV. The solid lines are five-point adjacent averages of the data points.

4.46 eV for adenine; at 4.61 eV for cytosine; between 4.51 and 4.70 eV with a maximum at 4.66 eV for thymine; and at 4.63 eV for uracil. The ~4.6 eV peaks of the $PtCl_6^{2-} \cdot A$ and $PtCl_6^{2-} \cdot T$ spectra are given as ranges due to the flatness of the depletion profiles in these regions. In addition to the ~4.6 eV peak, each spectrum shows an increase in absorption intensity towards higher photon energies. The spectrum of the cytosine complex also displays a weak absorption feature between 4.0 and 4.2 eV which is not observed in the spectra of the other clusters.

The experimental $PtCl_6^{2-} \cdot M$ absorption spectra are in good qualitative agreement with the TDDFT calculated spectra presented in Sections 6.5.2 and 6.7.2, in that they display a broad feature around 4.6 eV, followed by a rising absorption towards 6 eV, both associated with the LMCT transitions on $PtCl_6^{2-}$. In our previous work on the $Pt(CN)_{4,6}^{2-} \cdot$nucleobase clusters,[169, 251, 252] we assigned absorption bands in the 4.7 eV region to nucleobase-centred chromophores, since they have considerably stronger transition intensities than the $Pt(CN)_{4,6}^{2-}$ complexes. However, the solution-phase UV-vis absorption spectra of the uncomplexed $PtCl_6^{2-}$ and the individual nucleobases indicate that $PtCl_6^{2-}$ displays much more intense excitations across the lower-energy spectral region compared to the nucleobases, and the TDDFT calculations support this. Therefore, the $PtCl_6^{2-}$ LMCT excitations will dominate, particularly to lower energies, whereas the nucleobase-centred excitations are stronger around 5.2 eV. The photodepletion peak plateaus, observed for $PtCl_6^{2-} \cdot A$ and $PtCl_6^{2-} \cdot T$ (and $PtCl_6^{2-} \cdot U$ and $PtCl_6^{2-} \cdot C$ to a lesser extent) are likely to arise due to the removal of degeneracy in the LMCT absorption of the nucleobase cluster (it is triply degenerate for bare $PtCl_6^{2-}$).

The weak absorption in the cytosine cluster at 4.1 eV is likely the result of the presence a second geometric isomer of this cluster. Two cluster isomers of $PtCl_6^{2-} \cdot C$ have been observed in the low-temperature photoelectron spectrum of this cluster, with electron detachment energies of 4.04 eV (minor isomer) and 4.25 eV (major isomer).[264] Thus, photodepletion in the low energy region of the spectrum is enhanced due to photodetachment from the minor isomer. (We note that it is also possible that the absorption in this region of the spectrum is due to transitions of a keto tautomer of cytosine that have been observed previously.[6])

6.5.3.2 Photofragment action spectra of $PtCl_6^{2-} \cdot M$

Figure 6.5 presents the photofragment mass spectra of the $PtCl_6^{2-} \cdot M$ clusters recorded at 4.77 eV (270 nm), to illustrate the photochemistry that occurs at this excitation energy. The observed photofragments can be classified into two groups, corresponding either to electron detachment processes of the cluster ($PtCl_6^-$, $[PtCl_5(A–H)]^-$, $PtCl_6^- \cdot A$), or to photoinduced cluster dissociation. This classification is based on identifying $PtCl_6^- \cdot A$ as an unambiguous electron detachment fragment, and other fragments are labelled as electron detachment fragments if they display an action spectrum profile that mirrors that of $PtCl_6^-$. All remaining fragments must then be associated with photoinduced cluster dissociation. When discussing these photoinduced dissociation products, we assume that absorption by either a $PtCl_6^{2-}$ or nucleobase centred-chromophore induces cluster fragmentation following relaxation of the initially populated excited state to a vibrationally excited electronic ground state. This follows either from consideration of the cluster energetics, or from the fact that nucleobase-centred absorptions are known to typically decay on the femtosecond timescale so would not lead to fragmentation in the excited state.[106, 276] Production of the $PtCl_3^-$ photofragment from $PtCl_6^{2-} \cdot A$ has been calculated to be endothermic by >3.5 eV. (Calculated by comparing the difference in the computed SCF energies between $PtCl_6^{2-} \cdot A$ and $PtCl_3^-$, $A \cdot Cl^-$, and two $Cl^{\cdot}$ radicals. All structures and energies were calculated using the method described in Section 6.4. Frequency calculations were performed on the optimised structures to show that they are minima.) Thus, both the internal energy and timescale required to dissociate the excited $[PtCl_6^{2-} \cdot A]^*$ cluster into a nucleobase and three Cl atoms (along with the ionic photofragment) are unlikely to be available in the electronic excited state.

The observation of the CID fragments $PtCl_5^-$ and $M \cdot Cl^-$ for all clusters, $PtCl_6^{2-}$ for all but the adenine cluster and $[M–H]^-$ for all but the cytosine cluster suggests that fragmentation Reactions 6.1 – 6.3 are significant following photoexcitation.
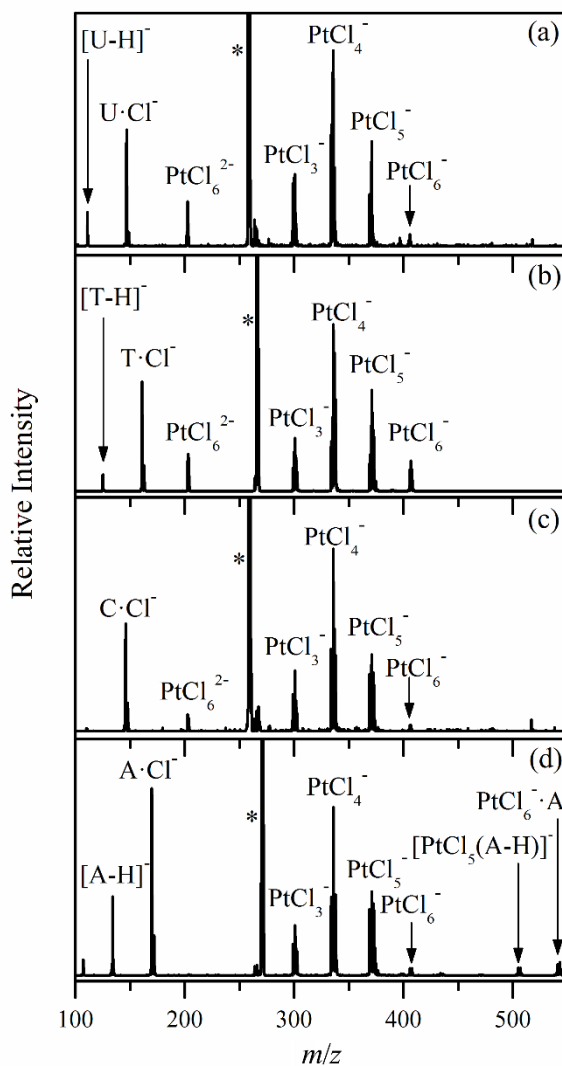
Figure 6.5 Photofragmentation mass spectra (laser on) of the $PtCl_6^{2-} \cdot M$ clusters obtained at 4.77 eV (270 nm) where M = (a) uracil, (b) thymine, (c) cytosine, (d) adenine.[273] The parent peak is denoted by the *.

Production of $PtCl_4^-$ and $PtCl_3^-$ can be attributed to fragmentation of vibrationally excited $PtCl_x^-$ ($x = 4, 5$) species *via* the successive loss of Cl radicals, for example:

$$PtCl_5^{-*} \rightarrow PtCl_4^- + Cl^{\bullet}$$
$$PtCl_4^{-*} \rightarrow PtCl_3^- + Cl^{\bullet}$$
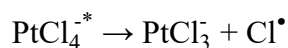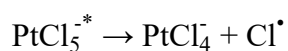
Reactions 6.4a and 6.4b

Chapter 6

The fragmentation mechanism can be assigned as a successive fragmentation process since no fragments were detected that would accompany $PtCl_3^-$ and $PtCl_4^-$ if fragmentation of the parent cluster was direct (*e.g.* Cl_2^-, Cl_3^-, $M \cdot Cl_2^-$, or $M \cdot Cl_3^-$). A mechanism analogous to 6.4a was proposed previously as a pathway to $PtCl_4^-$ in photofragmentation of $PtCl_5^-$.[23] Calculations of the fragmentation reaction energies are included in Section 6.7.5.

(a) Photofragmentation pathways associated with electron detachment. We now return to discussing the photofragment processes that are associated with electron detachment:

$$PtCl_6^{2-}.M + h\nu \rightarrow PtCl_6^-.M + e^-$$
$$PtCl_6^-.M \rightarrow PtCl_6^- + M$$
$$PtCl_6^-.M \rightarrow [PtCl_5(M\text{-}H)]^- + HCl$$
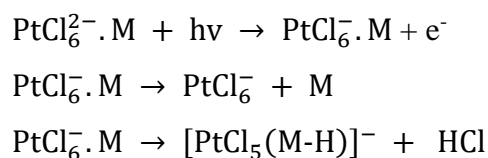
<div align="right">Reactions 6.5a, 6.5b and 6.5c</div>

It is notable that the $PtCl_6^{2-} \cdot A$ cluster produces three prominent electron-detachment fragments ($PtCl_6^-$, $PtCl_6^- \cdot A$ and $[PtCl_5(A–H)]^-$), whereas the other $PtCl_6^{2-} \cdot M$ clusters produce $PtCl_6^-$ as the sole observed electron detachment fragment. (The $[PtCl_5(A–H)]^-$ photofragment is discussed in detail in Section 6.7.4) It is likely that the different fragmentation pathways seen for the $PtCl_6^{2-} \cdot M$ clusters can be traced to the binding energies of the monoanions to the nucleobase within clusters such as $PtCl_6^- \cdot A$ and $[PtCl_5(A–H)]^-$. One possible explanation for this, is the presence of a carbonyl moiety close to the $PtCl_6^-$ binding site for all the nucleobases except adenine (see reference 264 for calculated cluster structures); in the monoanionic clusters, long range carbonyl-chloride repulsion may dominate interactions as the short-range hydrogen bonds weaken from the reduction in excess charge. From the $PtCl_6^{2-} \cdot A$ photofragment mass spectrum (Figure 6.5d) it is evident that the relative intensities of $PtCl_6^-$ and $[PtCl_5(A–H)]^-$ are similar, thus implying that the activation energies for pathways 6.5b and 6.5c are comparable.

Figure 6.6 shows the photoproduction spectra for the summed electron detachment fragments across the range 4.0–5.8 eV. As would be expected, a gradual increase in photodetachment occurs with increasing photon energy for all the $PtCl_6^{2-} \cdot M$ clusters,
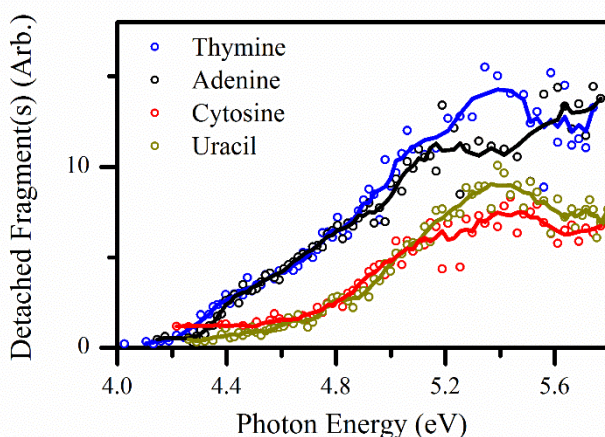
Figure 6.6 Photofragment action spectra of sum of the electron detached fragments ($PtCl_6^-$, $PtCl_6^-\cdot A$ and $[PtCl_5(A–H)]^-$) of the $PtCl_6^{2-}\cdot M$ clusters over the range 4.0–5.8 eV. The solid lines are five point adjacent averages of the data points.

and this corresponds to an increasing number of electronically excited states of the $PtCl_6^-\cdot M$ monoanion. The spectra each have a notable band superimposed on the near-linearly increasing photodetachment cross-section with increasing energy, which peaks between 5.2 and 5.4 eV. This is characteristic of the presence of an excited state, where photoexcitation of this state leads to resonant enhancement of the photodetachment cross-section superimposed on direct electron detachment.[23] It is probable that these excited states are the nucleobase-centred transitions that are expected in this region.

For an electron to become detached from the dianionic $PtCl_6^{2-}\cdot M$ complex, it must have sufficient energy to overcome the repulsive Coulomb barrier (RCB) for electron detachment as well as the electron binding energy. As discussed above, the photoelectron spectra of the $PtCl_6^{2-}\cdot M$ clusters have been measured recently, providing estimates of the detachment thresholds of 3.96–4.05 eV.[264] The onset of electron detached fragments in photodissociation spectroscopy provide alternative measurements of the electron detachment thresholds: inspection of Figure 6.6 provides values of ~4.0–4.2 eV for the clusters, in line with the estimated values from the photoelectron spectra.

(b) Non-electron detachment photofragmentation pathways. The photofragment mass spectra of the $PtCl_6^{2-}\cdot M$ clusters shown in Figure 6.5 illustrate that the

photochemistry of these systems is complex. This can be traced to the fact that each of the components displays chromophore over the spectral region studied, with the $PtCl_6^{2-}$ moiety photodissociating *via* multiple pathways. To simplify the discussion, we therefore focus on two important facets of the photophysics, namely photochemical products that arise following photoexcitation of the nucleobase chromophore and the photochemical production of $Cl^- \cdot M$, which should be produced upon excitation of $PtCl_6^{2-}$ centred-chromophores (see below). Our discussion and grouping together of the numerous photofragments is guided by the action spectra, *i.e.* photofragments that display action spectra with similar profiles are grouped together as they will arise following a common excitation process.

In our recent study of $Pt(CN)_4^{2-} \cdot M$ complexes,[169, 251, 252] the photochemistry and photophysics of the clusters over the region 220–320 nm were dominated by excitation of the nucleobase-centred chromophore with λ_{max} at ~4.7 eV. The resulting nucleobase-localised excited states appear to undergo ultrafast decay, followed by ergodic decay of the electronic ground state cluster. This gives rise to photofragments that are identical to the fragments observed upon low-energy CID of the ground state cluster, both in terms of identity and relative intensity. For the $PtCl_6^{2-} \cdot M$ clusters studied in this work, we would expect to see the respective low-energy CID fragments as photofragments across a similar excitation region. Cluster fission, pathway (1), is the major low-energy CID pathway for each of the $PtCl_6^{2-} \cdot M$ clusters studied here, with $PtCl_6^{2-}$ being an ionic fragment that is uniquely associated with this dissociation pathway. $PtCl_6^{2-}$ is indeed a significant photofragment for $PtCl_6^{2-} \cdot U$ and $PtCl_6^{2-} \cdot T$ (Figure 6.5a and b), but appears with lower intensity for $PtCl_6^{2-} \cdot C$ (Figure 6.5c) and is strikingly absent for $PtCl_6^{2-} \cdot A$ (Figure 6.5d).

Figure 6.7 displays the photofragment action spectra for production of the $PtCl_6^{2-}$, $[M-H]^-$ and $PtCl_5^-$ photofragments across the spectral range. The $PtCl_5^-$ ion was observed in both laser on and laser off measurements. For the cytosine and adenine clusters, the intensity of $PtCl_5^-$ was similar in the laser on and laser of measurements, so that it is not a significant photofragment (*i.e.* it is not a true photofragment in the MS presented in Figure 6.7c and d). For the uracil and thymine clusters, the intensity of $PtCl_5^-$ was adjusted in the photofragment action spectra (Figure 6.5a and b) to remove the background contribution of this ion, so that the plotted spectra are for the

photofragment. For both the $PtCl_6^{2-} \cdot U$ and $PtCl_6^{2-} \cdot T$ complexes (Figure 6.7a and b), $PtCl_6^{2-}$ is produced through a broad band from 4.4–5.4 eV, peaking at ~4.9 eV. The spectral profile of the $PtCl_5^-$ and $[M–H]^-$ ions closely matches that of $PtCl_6^{2-}$,
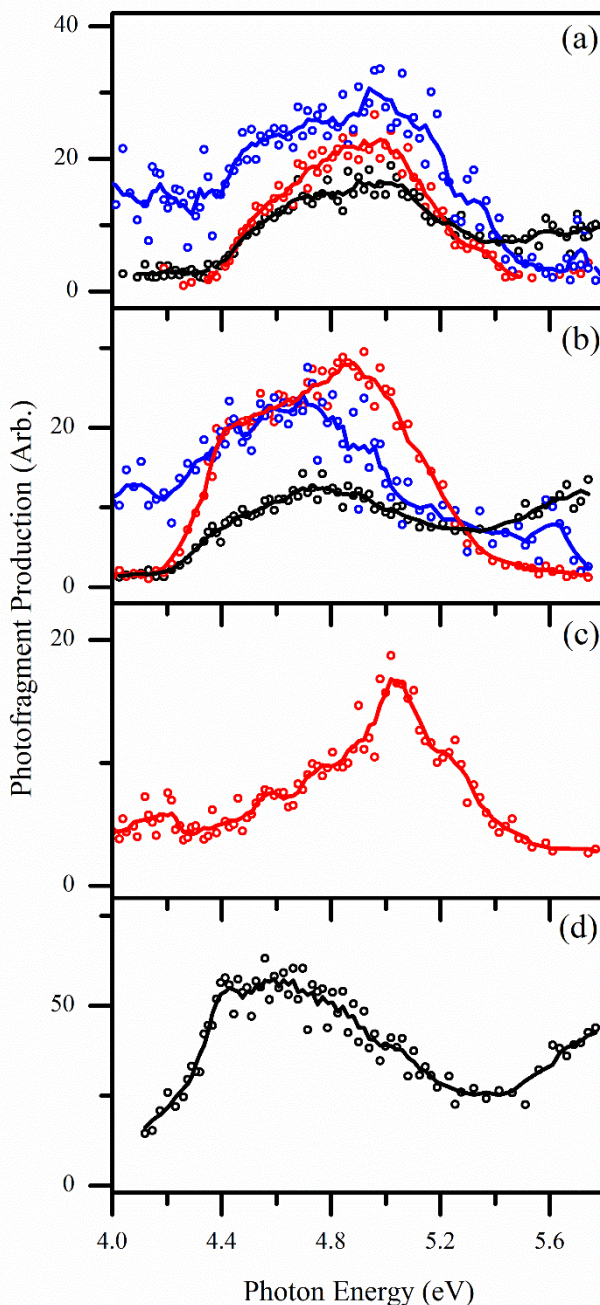
Figure 6.7 Photofragment action spectra of the $PtCl_6^{2-}$ (red circles), $PtCl_5^-$ (blue circles) and $[M–H]^-$ (black circles) photofragments produced from (a) $PtCl_6^{2-} \cdot U$, (b) $PtCl_6^{2-} \cdot T$, (c) $PtCl_6^{2-} \cdot C$ and (d) $PtCl_6^{2-} \cdot A$. Action spectra of $[M–H]^-$ for the cytosine cluster and $PtCl_6^{2-}$ for the adenine cluster are not included due to their low production. $PtCl_5^-$ photoproduction intensities are corrected for trapping impurities. The solid lines are five point adjacent averages of the data points.

indicating that this set of fragments have a common origin that is likely to correspond to ultrafast decay of a nucleobase-centred excited state and subsequent ground-state fragmentation. However, the behaviour of the $PtCl_6^{2-} \cdot C$ and $PtCl_6^{2-} \cdot A$ clusters is distinctive, and warrants further discussion.

For $PtCl_6^{2-} \cdot C$ (Figure 6.7c), only $PtCl_6^{2-}$ is observed (band peaks at ~4.9 eV), and this fragment has a relatively low intensity. No significant production of the accompanying $PtCl_5^-$ or $[M–H]^-$ fragments, which would be expected upon fragmentation of a "hot" ground state cluster, are seen through this band. This is perhaps unsurprising given the low intensity of the $PtCl_6^{2-}$ fragment (which was the dominant fragment obtained upon CID of the ground state cluster), as the $PtCl_5^-$ or $[M–H]^-$ fragments would be produced at even lower intensity than $PtCl_6^{2-}$ (Figure 6.2b) and therefore may be below the detection limit of our experiment. We conclude that the nucleobase-centred deactivation pathway is significantly quenched in $PtCl_6^{2-} \cdot C$, possibly due to competition from electron detachment from the initially-populated excited state.

For $PtCl_6^{2-} \cdot A$, the only photofragment from the $PtCl_6^{2-}$, $[A–H]^-$ and $PtCl_5^-$ set of fragments is $[A–H]^-$. The fact that a $PtCl_6^{2-}$ photofragment is completely absent following photoexcitation of $PtCl_6^{2-} \cdot A$ indicates that ultrafast nucleobase-centred deactivation pathway is not competitive. Instead, it is clear that production of $[A–H]^-$ occurs through a lower-energy band peaked closer to 4.4 eV, and then increases towards higher photon energy. This behaviour would be expected for a photofragment produced by excitation of the LMCT transitions of $PtCl_6^{2-}$ within the cluster. It is also possible that the $[A–H]^-$ photofragment is produced *via* an excited state hydrogen transfer process in adenine.[277] Any accompanying photofragments to $[A–H]^-$ (*e.g.* $PtCl_5^-$) must further fragment into $PtCl_4^-$ or $PtCl_3^-$. The spectra presented in Section 6.7.4 (Figures 6.20 and 6.21) provide evidence for this.

Next we turn to the chloride anion–nucleobase photofragment, $M \cdot Cl^-$. This photofragment is discussed separately as it displays a distinctive photofragment action spectrum to the fragments discussed above. Action spectra for production of $M \cdot Cl^-$ are displayed in Figure 6.8. For all four of the $PtCl_6^{2-} \cdot M$ clusters, the $M \cdot Cl^-$ displays a profile with a maximum intensity close to the low-energy spectral

edge (~4.0 eV) that decreases towards zero by ~5.2 eV, before gradually starting to increase in intensity again towards higher energies. This profile is distinctive amongst the complete set of photofragments. The simplest route for production of $M \cdot Cl^-$ is from ionic fragmentation, *i.e.* Reaction 6.2, through direct photoexcitation of $PtCl_6^{2-}$ within the $PtCl_6^{2-} \cdot M$ cluster. As discussed in the introduction, bare gas-phase $PtCl_6^{2-}$ is known to produce $PtCl_5^-$ with a profile that peaks at ~4.5 eV before
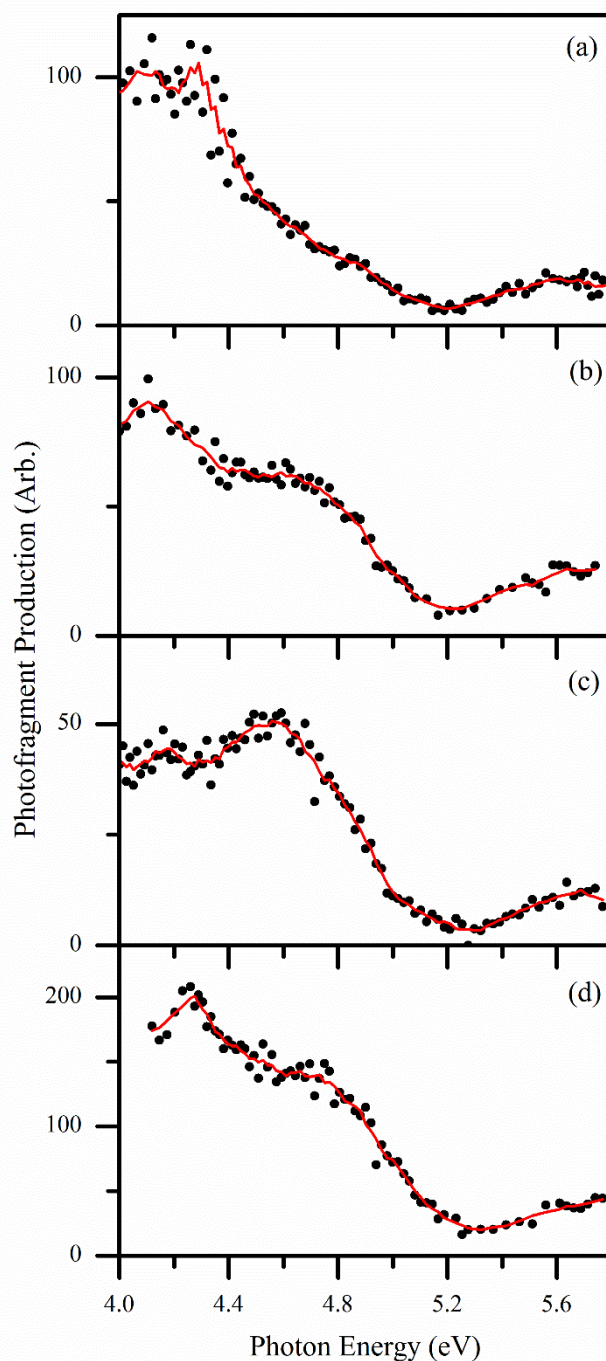
Figure 6.8 Photofragment action spectra of $Cl^- \cdot M$ produced from (a) $PtCl_6^{2-} \cdot U$, (b) $PtCl_6^{2-} \cdot T$, (c) $PtCl_6^{2-} \cdot C$ and (d) $PtCl_6^{2-} \cdot A$. The solid lines are five point adjacent averages of the data points.

tailing down to zero at ~5.0 eV.[23] The $PtCl_5^-$ is thought to arise from photoinduced ionic fragmentation of $PtCl_6^{2-}$.[23] Since photoproduction of $M \cdot Cl^-$ from the $PtCl_6^{2-} \cdot M$ clusters occurs with the same general profile (*i.e.* decreasing towards a low photofragment intensity at ~5.2 eV), we assign the $M \cdot Cl^-$ photofragment as arising from photoinduced ionic fragmentation of the $PtCl_6^{2-}$ within the $PtCl_6^{2-} \cdot M$ cluster. We note that photoproduction of $Cl^- \cdot M$ from the cluster is red-shifted compared to photoproduction of $PtCl_5^-$ from bare $PtCl_6^{2-}$, possibly due to the LMCT transitions of $PtCl_6^{2-}$ in the $PtCl_6^{2-} \cdot M$ cluster being distributed across the range from 4.1–4.8 eV (Section 6.5.2).

Finally, we consider the $PtCl_4^-$ and $PtCl_3^-$ pair of photofragments (spectra are included in Section 6.7.4), which display broadly similar action spectra for all of the clusters, with peaks at ~4.6 and >5.8 eV. From all of the photofragments observed for the $PtCl_6^{2-} \cdot M$ clusters, the spectral profiles of the $PtCl_4^-$ and $PtCl_3^-$ photofragments, most closely resemble the overall profiles of the photodepletion spectra. It is notable that $PtCl_5^-$ is not observed as an accompanying photofragment with the same spectral profile as $M \cdot Cl^-$ from the $PtCl_6^{2-} \cdot M$ clusters. This behaviour is reminiscent of the absence of $PtCl_5^-$ as an accompanying photofragment to $[M–H]^-$ for the $PtCl_6^{2-} \cdot A$ cluster. It is likely that $PtCl_5^-$ is produced as a vibrationally hot ion following LMCT excitation which dissociates with a high cross-section into $PtCl_4^-$ and $PtCl_3^-$. We conclude that the action spectra of $PtCl_4^-$ and $PtCl_3^-$ resemble the photodepletion spectra because these secondary ions are produced whenever $PtCl_5^-$ is formed; the conversion rate is low for nucleobase absorptions but has a near unit probability for LMCT transitions, reflecting the localisation of thermal energy.

6.6 Concluding remarks

We have recently studied the photoelectron spectroscopy of the $PtCl_6^{2-} \cdot M$ clusters, employing 266 nm (4.66 eV) and 193 nm (6.424 eV) as the photodetachment energies.[264] The 266 nm spectrum of the $PtCl_6^{2-} \cdot A$ complex is particularly striking as it displays a very prominent broad featureless band that is indicative of a phenomenom termed "delayed electron detachment" in photodetachment spectroscopy.[278-280] Delayed electron detachment occurs when the photon employed

excites an electronic transition of the system under study, rather than simply detaching an excess electron in a "direct" instantaneous photodetachment process. The delayed electron detachment observed for $PtCl_6^{2-} \cdot A$ in its 4.66 eV photoelectron spectrum indicates that one-photon excitation accesses excited states that are sufficiently long-lived to allow coupling to the electron detachment continuum and subsequent autodetachment. This process appears to have a significant impact on the photochemistry of $PtCl_6^{2-} \cdot A$ at this wavelength, making the action spectra of the photofragments distinctive for this cluster. The detailed photophysics of gas-phase nucleobase molecules is a topic of continuing high-interest, and there have been a number of recent studies exploring how adjacent negative charge modifies the deactivation pathways of adenine. Further characterisation of the detailed excited states and decay pathways available to the $PtCl_6^{2-} \cdot A$ cluster requires time-resolved photodetachment spectroscopy.[8] Such measurements have the potential to provide new insight into the intrinsic nucleobase decay dynamics.

The 266 nm photoelectron spectra of the $PtCl_6^{2-} \cdot T$ and $PtCl_6^{2-} \cdot C$ clusters also display "delayed electron detachment" (strongest for $PtCl_6^{2-} \cdot T$), although for the $PtCl_6^{2-} \cdot U$ cluster, the delayed detachment signal is very small. These observations from the photoelectron spectroscopy study are in line with our general observations of the relative intensities of summed electron detachment photofragments, with electron detachment fragments being more prominent for the $PtCl_6^{2-} \cdot A$ and $PtCl_6^{2-} \cdot T$ clusters. If we compare $PtCl_6^{2-} \cdot A$ and $PtCl_6^{2-} \cdot T$, the fact that $PtCl_6^{2-} \cdot T$ produced $PtCl_6^{2-}$ (formed *via* a cluster fission process) as a significant photofragment indicates that branching between the electron detachment decay pathway and the ultrafast (nucleobase-centred) decay to the hot electronic ground state is more comparable. In $PtCl_6^{2-} \cdot A$, the electron detachment channel dominates strongly. Time-resolved photodetachment spectroscopy is again needed to more fully characterise the novel photophysics observed here.

In previous related work, we have explored the photophysics and photochemistry of clusters composed of nucleobases bound to the $Pt(CN)_4^{2-}$ and $Pt(CN)_6^{2-}$ dianions, *e.g.* $Pt(CN)_4^{2-} \cdot M$.[169, 251, 252] The overall photochemistry of these clusters is simpler than the hexachloroplatinate clusters studied here, since the nucleobase-centred chromophores are considerably stronger than any on

$Pt(CN)_4^{2-}$ and $Pt(CN)_6^{2-}$ over the spectral range covered. Focusing on the $Pt(CN)_4^{2-} \cdot M$ clusters, the laser induced photochemistry fell into two classes dependent on the excitation wavelength. In the region between ~4.4–5.2 eV, excitation of the primarily nucleobase-centred chromophore leads to a photo-induced proton transfer reaction from the nucleobase to the platinum complex, whereas at excitation energies above ~5.2 eV, photodetachment begins to dominate. Both of these photo-induced processes have the capacity to destroy nucleotides (or DNA) that the platinum complexes are bound to, either through the proton-transfer pathways or due to photodetachment releasing destructive free electrons into the vicinity of a nucleobase.[281, 282] For the $PtCl_6^{2-} \cdot M$ clusters studied here, we see similar partitioning into two photochemical regions: a lower energy region (<5.2 eV) where the $PtCl_6^{2-}$ moiety is photolysed, ejecting Cl^- bound to the nucleobase (with potential to initiate a proton-transfer process) and a higher-energy region (>5.2 eV) where electron photodetachment dominates. These experiments demonstrate how selective photoexcitation can drive distinctive photodecay channels for a model photo-pharmaceutical. Such studies provide critical benchmarking data for developing QM/MM methodologies for modelling photoactive metal complex–biomolecule interactions and have the potential to provide a route for facile screening of possible photopharmaceuticlas.

Chapter 6

6.7 Supplementary Information

6.7.1 Instrumental Details and Experimental Description

UV photons for the laser spectroscopy experiments are provided by an Nd:YAG (Powerlite) pumped OPO (Panther Ex), producing ~2 mJ across the range 215-310 nm. A 200 mm UV fused silica focussing lens is used to reduce the beam diameter to ~2 mm when entering the mass spectrometer and is placed such that the focal point occurs within the mass spectrometer.

The mass spectrometer has been modified as follows for performing the laser experiments (Figure 6.9). Two laser windows have been installed in the top flange of the vacuum chamber to provide entrance and exit ports for the laser beam. Two 2 mm holes have been drilled through the ring electrodes, thus allowing the laser beam a path through the centre of the trap. The RF circuit was retuned following the drilling of the holes so that the performance of the mass spectrometer is unaffected by these modifications. The helium pressure within the modified trap is maintained at 5×10^{-6} mbar. A pair of mirrors are situated beneath the ion trap to allow the laser beam to exit the mass spectrometer after passing through the ion trap to assists laser alignment.

All instrument parameters and laser experiments are controlled via the AmaZon software. A typical spectral scan sequence consists of: clear ion trap, accumulate ions in trap (typically 20 – 200 ms), mass selected ion isolation within the trap, fragmentation and mass scan. The MS_n functionality of the mass spectrometer is used to store ions for a variable time period (typically 100 – 500 ms) during the fragmentation window in which they are exposed to the laser. The fragmentation stage is commonly used to study the collision induced dissociation of gaseous ions, in a laser scan the CID amplitude is set at 0 V. A beam shutter (Model SH05, Thorlabs Inc) is used to control the laser beam transmission into the mass spectrometer, and is triggered by the mass spectrometer such that the ion trap is only irradiated during the fragmentation phase of the mass spectrum acquisition.

Chapter 6

The photodepletion intensity of the clusters and the photofragment production have been calculated using Equations 6.1 and 6.2 and are presented as a function of the photon energy.

Photodepletion Intensity $= \ln\left(\frac{I_{OFF}}{I_{ON}}\right)/\lambda \times P$

$$\text{Equation 6.1}$$

Photofragmentation Production $= \left(\frac{I_{Frag}}{I_{OFF}}\right)/\lambda \times P$

$$\text{Equation 6.2}$$

Where I_{ON} and I_{OFF} are the parent peak intensities with laser on and off, I_{Frag} is the fragment intensity with laser on, λ is the excitation wavelength (nm) and P is the laser pulse energy (mJ). As in the CID experiments, peak intensities are averaged over one minute windows. When isolating the $PtCl_6^{2-}\cdot M$ clusters, small quantities of $PtCl_4^-$ and $PtCl_5^-$ were trapped during the isolation procedure. These ions (<1% of parent cluster intensity) were minimised by tuning the isolation parameters of the AmaZon.
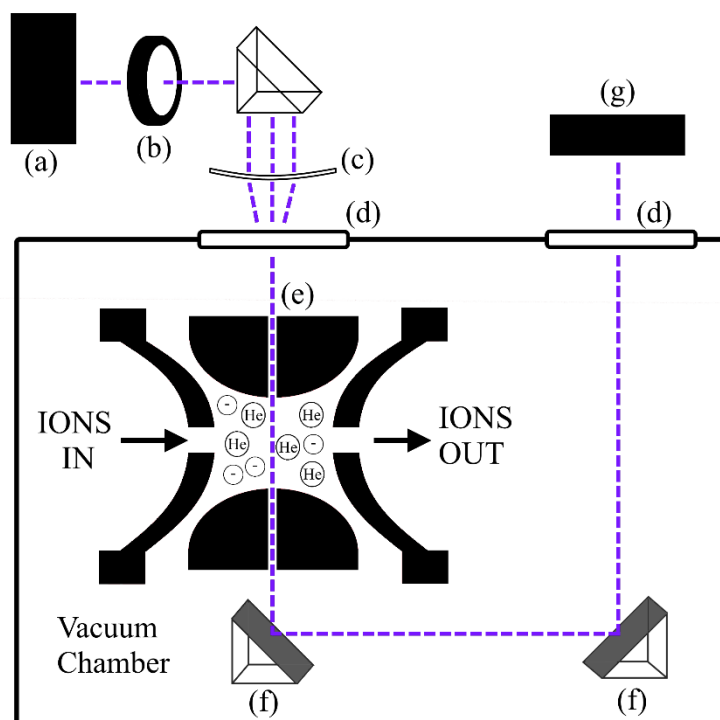
Figure 6.9 Schematic diagram of the experimental apparatus and the modifications to the AmaZon (Bruker Daltonik) mass spectrometer that was used to record the photodissociation spectra of the $PtCl_6^{2-}\cdot M$ (M = uracil, thymine, cytosine and adenine) clusters. Where (a) is an Nd:YAG (Powerlite) pumped OPO (Panther Ex) tuneable laser source; (b) is an optical shutter (Model SH05, Thorlabs Inc); (c) is a 200 mm focal length UVFS lens (LE4467-UV, Thorlabs Inc); (d) is a pair of flange mounted uncoated UVFS windows (WG41050, Thorlabs Inc); (e) is a 2 mm hole drilled through the ring electrode of the ion trap to allow the passage of laser light; (f) is a pair of mirrors; and (g) is a UV-Vis spectrometer (USB2000+ UV-VIS, Ocean Optics Inc).

6.7.2 TDDFT calculations of $PtCl_6^{2-}$ and $PtCl_6^{2-} \cdot M$ where M = A, C, T

6.7.2.1 TDDFT calculations of $PtCl_6^{2-}$
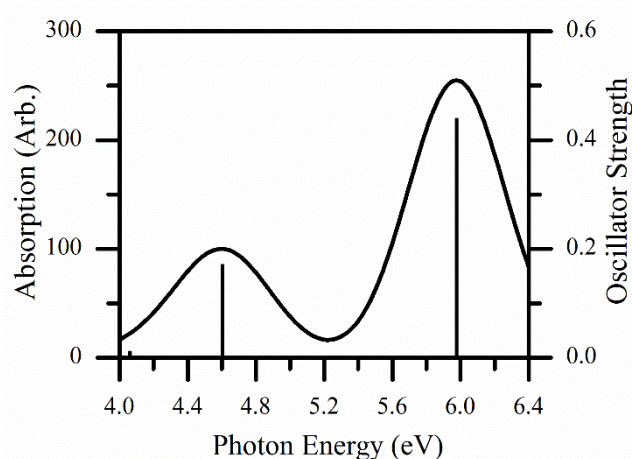
Figure 6.10 Calculated excitation energies of $PtCl_6^{2-}$ from TDDFT calculations with the M06-2X functional. The oscillator strengths of individual transitions are given by the vertical bars. The full line spectrum represents a convolution of the calculated spectrum with a Gaussian function (0.333 eV HWHM).

Table 6.3 Calculated transition energies and oscillator strengths of $PtCl_6^{2-}$ from TDDFT calculations with the M06-2X functional.[a,b]

Transition Energy (eV)	Oscillator Strength
$PtCl_6^{2-}$ LMCT Transitions	
4.06	0.0114
4.59	0.1705
5.98	0.4392

[a] Using a split basis set of: 6-311+G(2d,2p) on all first and second row atoms and the Def2-TZVPP basis set to describe the platinum valence orbitals with the 60 core electrons represented by the Stuttgart/Dresden electron core pseudopotential.

[b] All transitions are triply degenerate.

6.7.2.2 TDDFT calculations of PtCl$_6^{2-}$·T
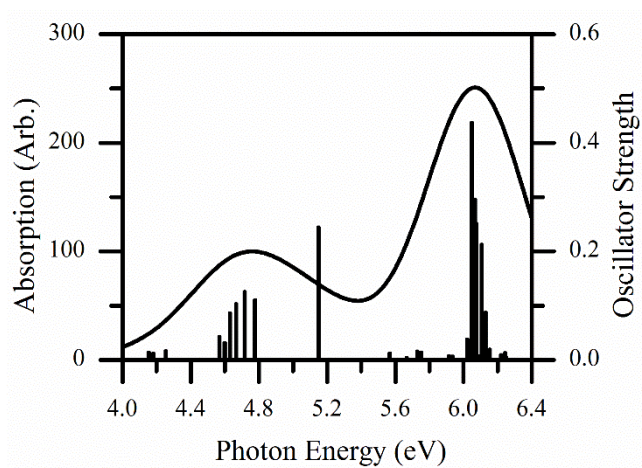
Figure 6.11 Calculated excitation energies of PtCl$_6^{2-}$·T from TDDFT calculations with the M06-2X functional. The oscillator strengths of individual transitions are given by the vertical bars. The full line spectrum represents a convolution of the calculated spectrum with a Gaussian function (0.333 eV HWHM).

Table 6.4 Calculated transition energies and oscillator strengths of $PtCl_6^{2-} \cdot T$ from TDDFT calculations with the M06-2X functional.[a]

Transition Energy (eV)	Oscillator Strength
$PtCl_6^{2-}$ LMCT Transitions	
4.15	0.0143
4.18	0.0123
4.25	0.0171
4.57	0.0439
4.60	0.0316
4.63	0.0866
4.67	0.1040
4.72	0.1264
4.78	0.1110
5.57[b]	0.0131
Thymine π and $PtCl_6^{2-}$ orbitals$\rightarrow$ Thymine π^* Transitions[c]	
5.15	0.2449
5.73	0.0167
5.75	0.0145

[a] Using a split basis set of: 6-311+G(2d,2p) on all first and second row atoms and the Def2-TZVPP basis set to describe the platinum valence orbitals with the 60 core electrons represented by the Stuttgart/Dresden electron core pseudopotential.

[b] Transitions originates primarily from a $PtCl_6^{2-}$ orbital with some delocalisation to the thymine.

[c] Thymine π orbitals have a minor delocalisation across the $PtCl_6^{2-}$ moiety.

6.7.2.3 TDDFT calculations of $PtCl_6^{2-}\cdot C$
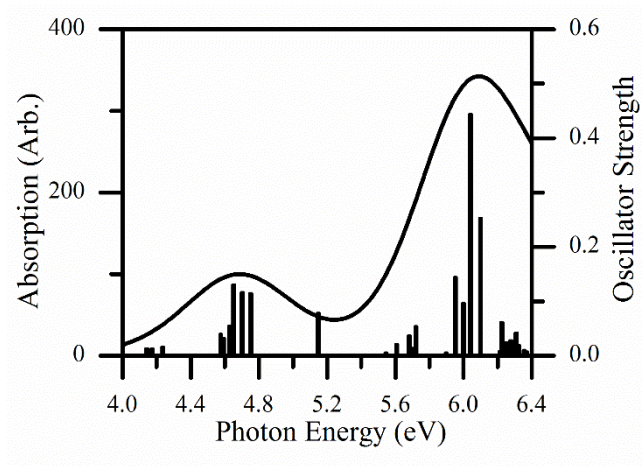
Figure 6.12 Calculated excitation energies of $PtCl_6^{2-}\cdot C$ from TDDFT calculations with the M06-2X functional. The oscillator strengths of individual transitions are given by the vertical bars. The full line spectrum represents a convolution of the calculated spectrum with a Gaussian function (0.333 eV HWHM).

Table 6.5 Calculated transition energies and oscillator strengths of $PtCl_6^{2-} \cdot C$ from TDDFT calculations with the M06-2X functional.[a]

Transition Energy (eV)	Oscillator Strength
$PtCl_6^{2-}$ LMCT Transitions	
4.14	0.0129
4.17	0.0123
4.24	0.0160
4.58	0.0395
4.59	0.0320
4.63	0.0544
4.65	0.1305
4.70	0.1165
4.75	0.1148
5.61[b]	0.0204
5.68[b]	0.0370
5.70[b]	0.0137
Cytosine π and $PtCl_6^{2-}$ orbitals $\rightarrow$ Cytosine π^* Transitions[c]	
5.15	0.0781
5.72	0.0537

[a] Using a split basis set of: 6-311+G(2d,2p) on all first and second row atoms and the Def2-TZVPP basis set to describe the platinum valence orbitals with the 60 core electrons represented by the Stuttgart/Dresden electron core pseudopotential.

[b] A minor contribution to the initial $PtCl_6^{2-}$ orbital by the lone pair of the oxygen on the cytosine.

[c] The initial cytosine orbitals have a minor delocalisation to the $PtCl_6^{2-}$ moiety.

6.7.2.4 TDDFT calculations of PtCl$_6^{2-}$·A
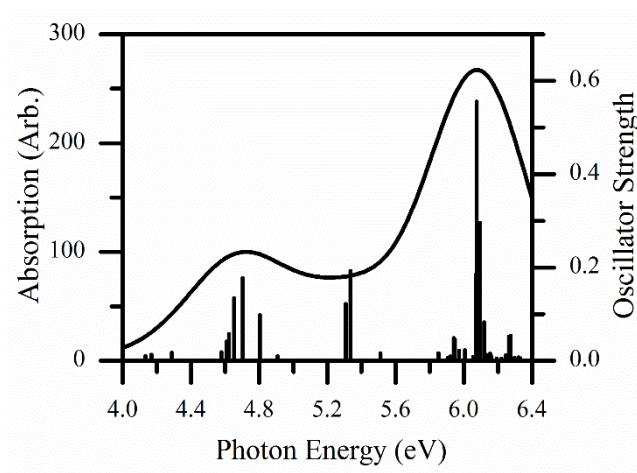
Figure 6.13 Calculated excitation energies of PtCl$_6^{2-}$·A from TDDFT calculations with the M06-2X and functional. The oscillator strengths of individual transitions are given by the vertical bars. The full line spectrum represents a convolution of the calculated spectrum with a Gaussian function (0.333 eV HWHM).

Table 6.6 Calculated transition energies and oscillator strengths of $PtCl_6^{2-} \cdot A$ from TDDFT calculations with the M06-2X functional.[a]

Transition Energy (eV)	Oscillator Strength
$PtCl_6^{2-}$ LMCT Transitions	
4.61	0.0417
4.62	0.0587
4.65	0.1353
4.70	0.1784
4.80	0.0984
Adenine $\pi \rightarrow$ Adenine Rydberg Transition	
4.91	0.0102
$PtCl_6^{2-}$ and Adenine $\pi \rightarrow$ Adenine π^* Transitions[b]	
5.31	0.1227
5.34	0.1937

[a] Using a split basis set of: 6-311+G(2d,2p) on all first and second row atoms and the Def2-TZVPP basis set to describe the platinum valence orbitals with the 60 core electrons represented by the Stuttgart/Dresden electron core pseudopotential.

[b] $PtCl_6^{2-}$ orbitals show delocalisation to the adenine unit.

Chapter 6

6.7.3 Aqueous Absorption Spectra of K_2PCl_6 and the nucleobases U, T, C and A

Solutions of K_2PtCl_6 and the nucleobases were made up in distilled water at a concentration of $\sim 1 \times 10^{-5}$ mol dm^{-3}. UV absorption spectra were recorded using a Shimadzu 1800 UV spectrophotometer with a 1 cm UV cuvette, using distilled water as a baseline. The aqueous absorption spectra were converted to molar absorption coefficients using the Beer-Lambert law. Graphs of excitation energy against molar absorption coefficient for the five aqueous molecules are given in Figure 6.14. The photon energies which gave the maximum absorption (λ_{max}) and the corresponding molar absorption coefficients (ε_{max}) are summarised in Table 6.7. Table 6.7 shows that the maximum absorption of each of the molecules studies occurs between 4.6 – 4.8 eV in distilled water. Aqueous $PtCl_6^{2-}$ has a stronger chromophore than the nucleobases by approximately 2x for adenine, 3x for uracil and thymine, and 8x for cytosine.

Table 6.7 Aqueous absorption maxima and molar absorption coefficients of K_2PtCl_6 and the nucleobases uracil, thymine, cytosine and adenine.

Molecule	λ_{max} / eV	ε_{max} / dm^3 mol^{-1} cm^{-1}
Uracil	4.79	6080
Thymine	4.69	6440
Cytosine	4.63	2180
Adenine	4.76	8520
K_2PtCl_6	4.73	18300
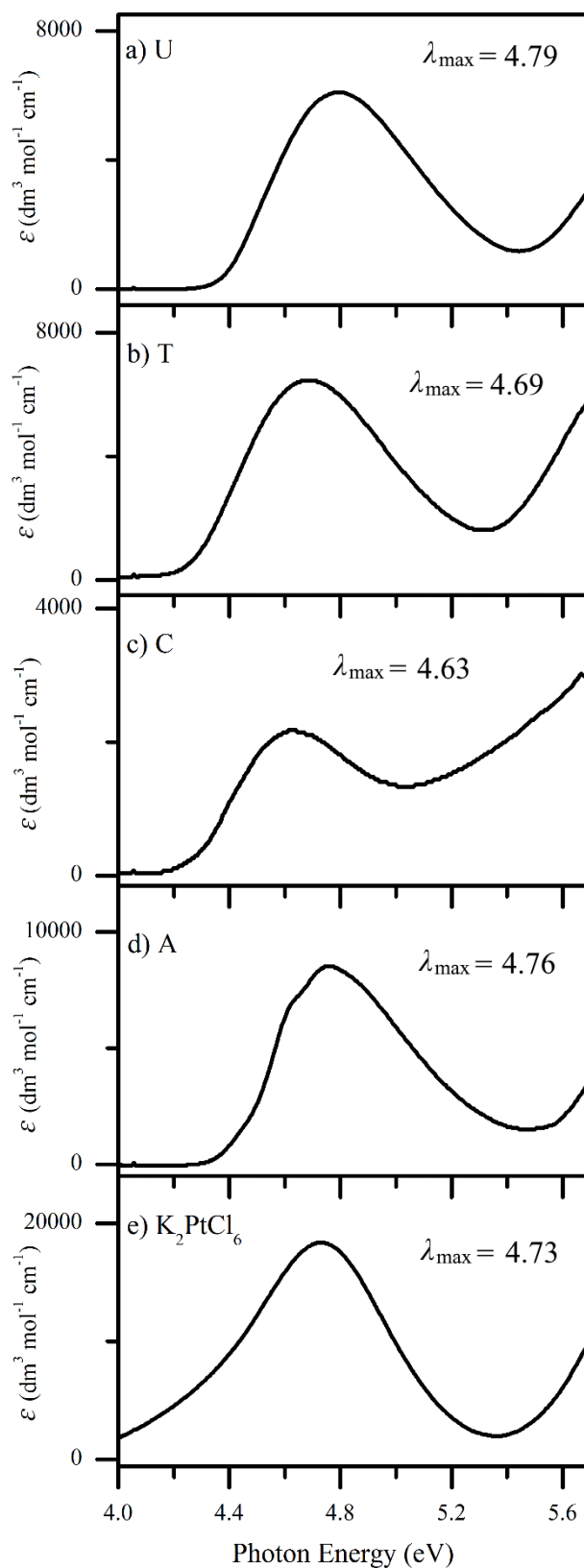
Figure 6.14 Aqueous molar absorption coefficients of: a) Uracil, b) Thymine, c) Cytosine, d) Adenine and e) K_2PtCl_6 across the range 4.0 – 5.7 eV.

6.7.4 Additional Photofragment Mass Spectra and Action Spectra for $PtCl_6^{2-} \cdot M$, M

= U, T, C, A

6.7.4.1 Electron detached fragments of $PtCl_6^{2-} \cdot A$

A series of low intensity fragments are observed in the high mass region of the $PtCl_6^{2-}$
$\cdot A$ photofragment mass spectra, Figure 6.15, consistent with deprotonated adenine
coordinating to the platinum via the loss of HCl. These fragments are only seen as
singly negatively charged species, suggesting that these reactions are only possible
following electron detachment. This behaviour is unique to adenine amongst the
studied nucleobases. Chemical formulae were assigned by comparing the recorded
fragmentation patterns with patterns simulated using the Compass DataAnalysis
(Bruker) software package (an example is given in Figure 6.16).

Collision induced dissociation (CID) was performed on the $PtCl_6^- \cdot A$ and $[PtCl_5(A-H)]^-$ fragments, Figures 6.17 and 6.18, by utilising the MS3 capabilities of the mass
spectrometer. The CID spectra show that $PtCl_6^- \cdot A$ thermally decays into $PtCl_6^-$ and
$[PtCl_5(A-H)]^-$ with a high conversion efficiency, $PtCl_4^-$ is produced as a minor
fragment. $[PtCl_5(A-H)]^-$ thermally dissociates into two lower mass $[PtCl_x(A-nH)]^-$
fragments as well as $PtCl_4^-$ and $PtCl_5^-$. Figures 6.17 and 6.18 shows that there is a
thermal production route for the high mass fragments of $PtCl_6^{2-} \cdot A$ that are seen in
Figure 6.15; $PtCl_6^- \cdot A$ is a primary electron detached fragments, the other high mass
fragments are assigned as secondary electron detached fragments.
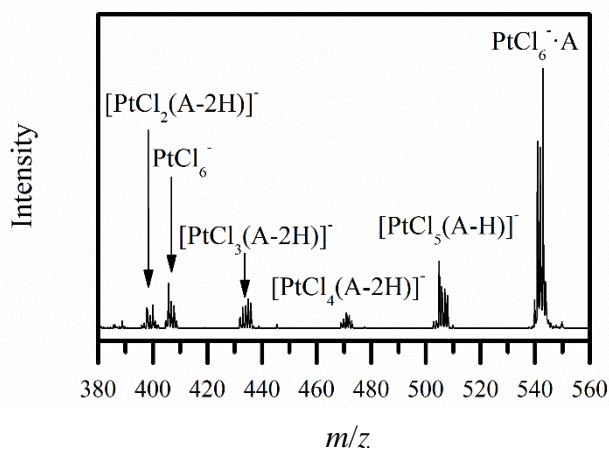
Figure 6.15 Photofragment mass spectrum of $PtCl_6^{2-} \cdot A$ irradiated at 280 nm,
highlighting the electron detached fragments within the high-mass region of the
spectrum.
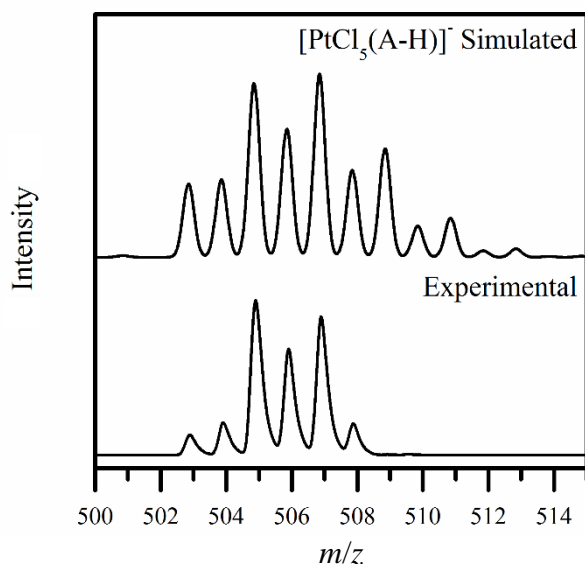
Figure 6.16 A comparison between a simulated isotope pattern of $[PtCl_5(A-H)]^-$ with the corresponding mass spectrum of $PtCl_6^{2-}\cdot A$ irradiated at 280 nm. The simulated patterns were generated using the Compass DataAnalysis (Bruker) software package.
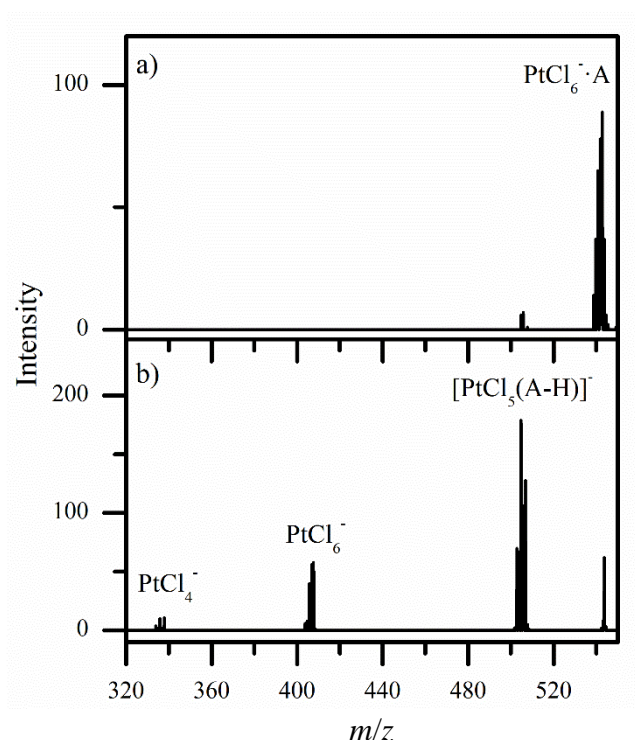
Figure 6.17 Collision-induced dissociation mass spectrum of the $PtCl_6^-\cdot A$ fragment with an excitation voltage of a) 0 V and b) 0.2 V. $PtCl_6^-\cdot A$ was isolated and fragmented, following its photoproduction with an excitation wavelength of 260 nm, using the MS3 capabilities of the mass spectrometer.
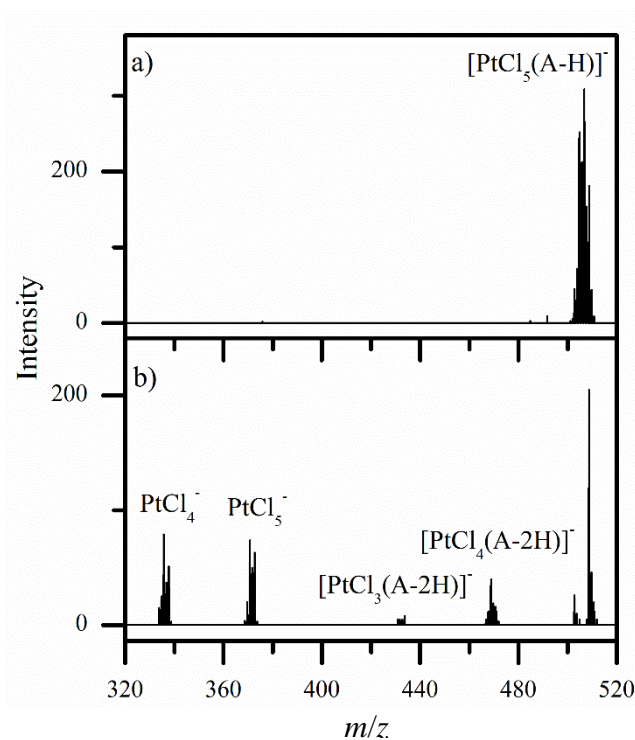
Figure 6.18 Collision-induced dissociation mass spectrum of the [PtCl$_5$(A-H)]$^-$ fragment with an excitation voltage of a) 0 V and b) 0.4 V. [PtCl$_5$(A-H)]$^-$ was isolated and fragmented, following its photoproduction with an excitation wavelength of 260 nm, using the MS3 capabilities of the mass spectrometer.

6.7.4.2 Photofragment Mass Spectra at 215 nm

The photofragment mass spectrum with an excitation wavelength of 215 nm (5.77 eV) is provided, Figure 6.19, to highlight the differences and similarities between the photofragment mass spectrum at 4.77 eV (Figure 4.5). It can be seen that electron detachment is a far more prominent fragmentation channel at 215 nm; production of PtCl$_x^-$ (x=3-5) is comparable between the two wavelengths; PtCl$_6^{2-}$ is quenched at 215 nm; and [M-H]$^-$ is more significant, relative to M·Cl$^-$, at 215nm.
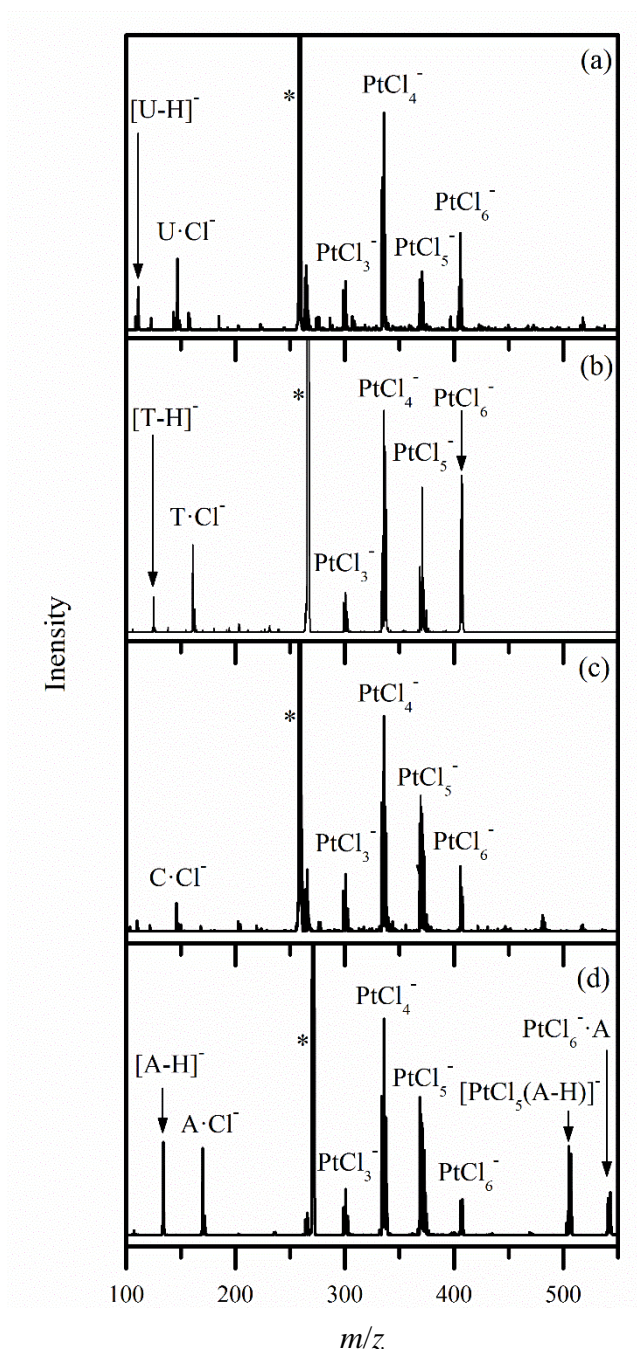
Figure 6.19 Photofragmentation mass spectra (laser on) of the $PtCl_6^{2-}\cdot M$ clusters obtained at 5.77 eV (215 nm) where M = (a) uracil, (b) thymine, (c) cytosine, (d) adenine. The parent peak is denoted by the *.

6.7.4.3 Photoproduction Spectra of PtCl$_4^-$ and PtCl$_3^-$
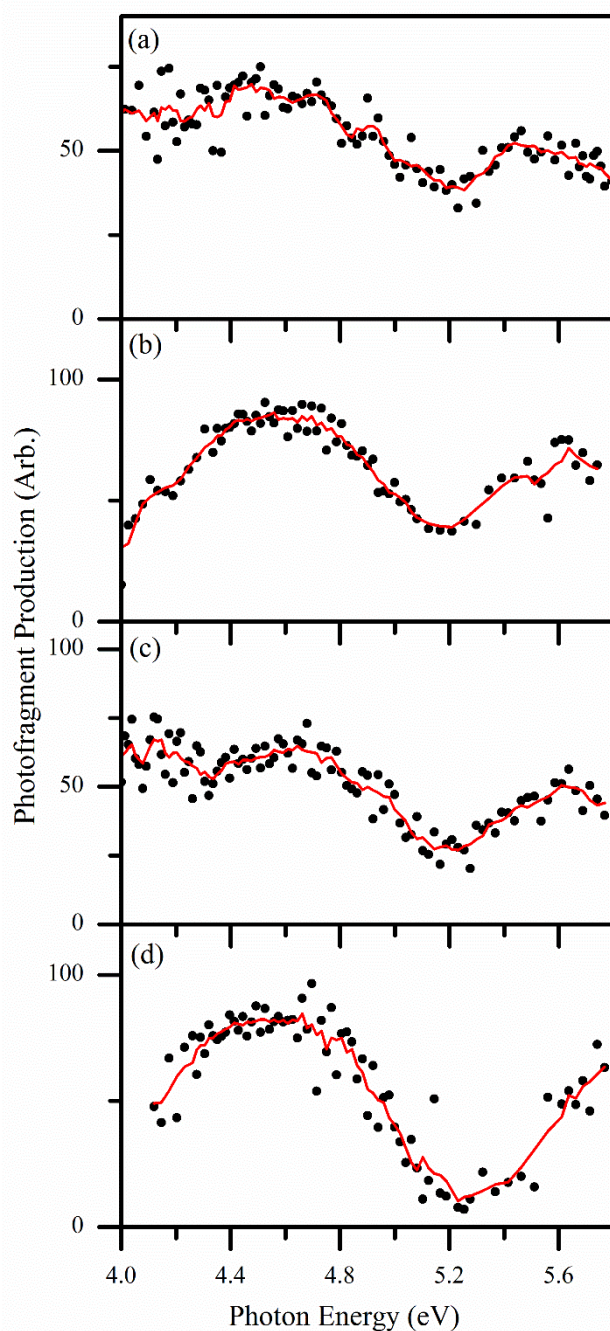
Figure 6.20 Photofragment production spectra of the PtCl$_4^-$ photofragment produced from (a) PtCl$_6^{2-}$·U, (b) PtCl$_6^{2-}$·T, (c) PtCl$_6^{2-}$·C and (d) PtCl$_6^{2-}$·A. The PtCl$_4^-$ photoproduction intensities are corrected for trapping impurities by subtracting the intensity of PtCl$_4^-$ recorded in the corresponding scan without laser.
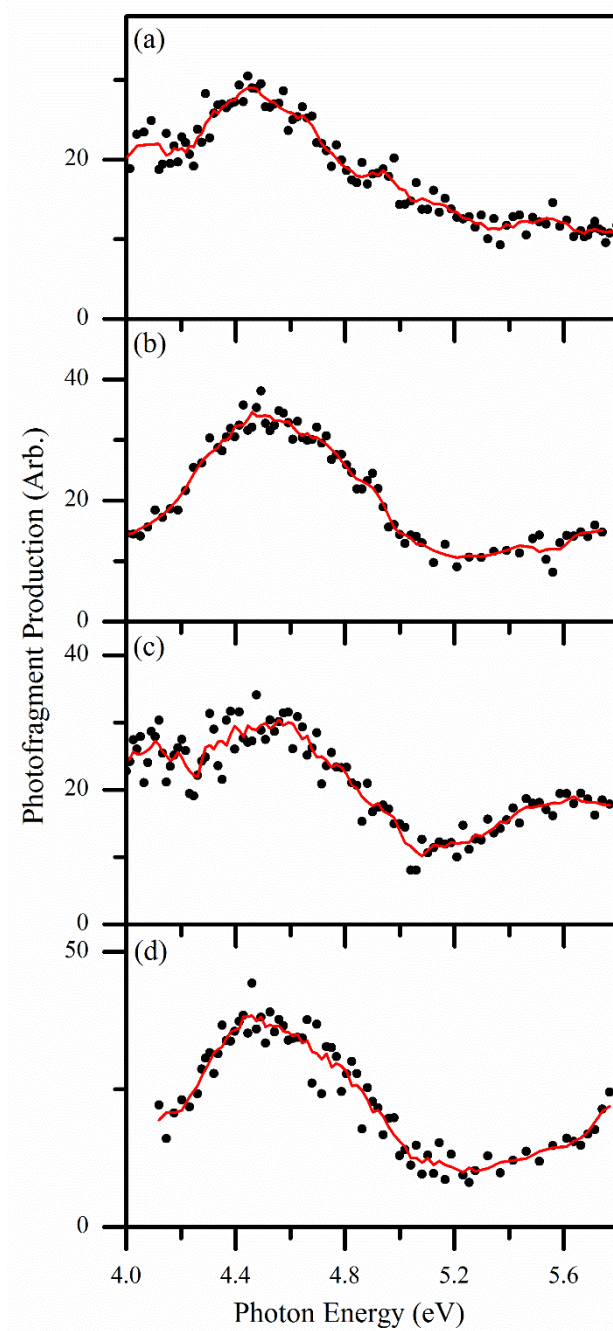
Figure 6.21 Photofragment production spectra of the $PtCl_3^-$ photofragment produced from a) $PtCl_6^{2-} \cdot U$, b) $PtCl_6^{2-} \cdot T$, c) $PtCl_6^{2-} \cdot C$ and d) $PtCl_6^{2-} \cdot A$. These spectra generally match the trends of the $PtCl_4^-$ spectra.

6.7.5 Energetics of Fragmentation Pathways for the $PtCl_6^{2-} \cdot A$ Cluster.

Six fragmentation pathways were selected to describe the production of charged fragments following electronic excitation of the $PtCl_6^{2-} \cdot A$ cluster. The reaction energies were calculated by comparing the difference in the computed SCF energies between products and reactants. All structures and energies were calculated using Gaussian 09 employing the M06-2X functional with the basis sets and electron-core pseudopotential described in Section 6.2. Frequency calculations were performed on the optimised structures to show that they are minima.

Table 6.8 Calculated photofragmentation reaction energies from the $PtCl_6^{2-} \cdot A$ cluster, calculated using Gaussian 09 using the M06-2X functional. Production energies show the total energy change to produce the photofragments from $PtCl_6^{2-} \cdot A$.[a]

Reaction	Parent	Fragments	Reaction Energy (eV)	Production Energy[a] (eV)
1	$PtCl_6^{2-} \cdot A$	$PtCl_6^{2-} + A$	1.35	-
2	$PtCl_6^{2-} \cdot A$	$PtCl_5^- + A \cdot Cl^-$	-0.551	-
3	$PtCl_6^{2-}$	$PtCl_5^- + Cl^-$	-0.726	0.622
4	$A \cdot Cl^-$	$[A-H]^- + HCl$	1.57	1.01
5	$PtCl_5^-$	$PtCl_4^- + Cl^\bullet$	1.72	1.16 (2.73)[b]
6	$PtCl_4^-$	$PtCl_3^- + Cl^\bullet$	2.40	3.56 (5.13)[b]

[a] Production energies represent the sum of the constituent reactions to produce this set of photofragments.
[b] Selected reaction energies also include the production of $[A-H]^-$ and HCl via reaction 4.

Chapter 7

Summary and Outlook

This thesis has presented the results of photodissociation spectroscopy experiments performed on biologically interesting molecular and cluster ions within a commercial mass spectrometer. The purpose of these studies has been to understand the fundamental photophysics of these biomolecules and to determine the fragmentation pathways which are available to these molecules following electronic excitation. These studies also focus on the applicability of laser-interfaced commercial mass spectrometers for performing electronic spectroscopy as well as generating analytical information, such as the distribution of gaseous isomers.

Overall, this thesis has shown that photodissociation within a commercial ion trap can be effectively used to record spectroscopy on gaseous ions, with examples ranging from small protonated organic molecules to dianionic transition metal complex – nucleobase clusters. These studies have resulted in numerous publications for the Dessent research group. The commercial software which enables mass spectra to be recorded and processed has provided an excess of data on individual photofragments. This has been used to determine the nature of the photofragment production mechanisms as well as to record the production of multiple photofragments as a function of the excitation wavelength. Photofragment production spectra are used throughout this thesis to deconvolute the total absorption spectra into the absorption spectra of the species present in the gas phase, and to identify the molecular origin of these deconvoluted absorption spectra. Advancements made in the methods of acquiring photodissociation data throughout this thesis, such as the implementation of the multiple reaction monitoring method and the automation of data collection, have improved the rate and ease at which spectroscopic data are collected.

Section 7.1 will summarise the results from Chapters 3 – 6 and provide insight into additional work that could be carried out to better understand these systems. Section 7.2 will summarise work carried out during my PhD which is not included in this thesis. Section 7.3 will provide an outlook on laser-interfaced commercial mass

spectrometer and will give some interesting improvements and experiments which can be undertaken.

7.1 Summary of Work in this Thesis

7.1.1 Nicotinamide

In Chapter 3, the photochemistry of protonated nicotinamide (NA) is studied using UV photodissociation spectroscopy. This project was initiated to learn more about the properties of nicotinamide adenine dinucleotide (NAD); NAD is a redox-active coenzyme which contains a charged NA moiety in its biologically active form. To better understand the electronic structure and fragmentation pathways of NAD, I first chose to study the isolated nicotinamide chromophore using UV photodissociation. NA, itself, has received interest as a sunscreen molecule. The significance of this NA study, as an individual project, developed into learning whether the UVPD instrument used in this thesis can provide meaningful information about sunscreen molecules; such as recording the efficiency of UV absorption or identifying harmful photofragments.

Aqueous and gaseous electronic absorption spectra show that NA, when protonated, is a poor UVA and UVB absorber but is a strong UVC absorber. Plotting the intensities of individual photofragments as a function of excitation wavelength reveals two distinct production profiles which are not resolved in the total absorption spectrum. Using computational chemistry, all reasonable structures of protonated nicotinamide are geometry optimised and have their excitation spectra simulated using TDDFT. Comparison of the TDDFT spectra with the photofragment production spectra leads to the assignment of both pyridine and amide N-protonated NA being present in the gas phase; NA protonated at the pyridine nitrogen is the major gaseous isomer. The occurrence of two gaseous structural isomers is speculated to be produced from nicotinamide dimers which are known to occur in the solution phase. The direct observation of two NA structural isomers was unexpected, given the simplicity of the NA structure. The presence of isomers complicated the interpretation of the photofragmentation pathways, because not all photofragments could be unambiguously assigned to a certain isomer from its photofragment production spectrum.

To further understand the protonated NA system, it would be useful to perform experiments on the proton-bound dimers of nicotinamide, to establish if these types of ionic clusters are the source of high-energy structural isomers. Additionally, ion mobility prior to UV photodissociation could be used to separate the gaseous isomers of NA, to provide gaseous structural purity when recording the photochemistry of NA. Additionally, now that the gaseous absorption spectrum of NA has been recorded, it may be possible to understand the properties of gaseous NAD, when studied using UV photodissociation.

7.1.2 Para-Aminobenzoic Acid

Chapter 4 is a UV photodissociation study of protonated para-aminobenzoic acid (PABA), this study directly followed the study of NA. The aim of this project was to determine if UV photodissociation was an appropriate technique to distinguish between gaseous isomers and, if so, to develop an experimental methodology for this purpose. PABA was chosen as a test molecule because protonated PABA has a well-known structure change between the solution phase and gas phase; this structure change can be inhibited by controlling the ion source conditions. Despite the body of research surrounding gaseous PABA, it had not been using electronic spectroscopy but instead using CID, IRMPD or IM-MS; this trend is also seen in the wider literature surrounding gaseous protomers.

Protonated PABA was introduced into the gas phase via electrospray from solutions of either water or acidified acetonitrile. When water is the ESI solvent, the electronic absorption spectrum is dominated by two prominent absorption features centred around 3.6 and 5.1 eV. This contrasts to when acetonitrile is used as the ESI solvent, where four prominent absorption features are recorded in the electronic absorption spectrum. These include the two features in the methanol-ESI spectrum and two features centred around 4.7 and 5.7 eV. This result confirms that the distribution of gaseous isomers of protonated PABA is highly influenced by the ESI solvent and that UVPD within a commercial mass spectrometer is a sufficiently sensitive technique to detect changes in gaseous isomer distribution for this molecule. The production of photofragments is recorded alongside the absorption spectrum. Photofragment production spectra of are used to approximate the absorption spectra

of the different protomers. Simulated excitation spectra, using the MRCI and SORCI methods, accurately predict the vertical transition energies and relative oscillator strengths for both protomers of PABA.

Overall, this study has shown that UV photodissociation within a commercial mass spectrometer is able to distinguish between gaseous structural isomers, so long as protonation site reasonably affects the electronic structure of a UV chromophore in the molecule. The ability to record the intensities of many photofragments using commercial software is of great benefit in this study, since the photofragment production spectra were used to isolate the absorption profiles of the protomers. Further studies on PABA as well as related protomeric molecules are useful for understanding more about the process of ESI. Electronic spectroscopy on protomeric ions clustered with solvent molecules is particularly interesting because this may reveal the size of an ESI droplet where the transition between one structure and another takes place. Moreover, the studies on PABA and NA have revealed the importance of considering that a distribution of structural isomers may exist in the gas phase, regardless of the molecule or ion being studied. It is therefore necessary to perform rigorous computational studies to identify low-energy conformational and structural isomers.

7.1.3 Alloxazine and Lumichrome

In Chapter 5, deprotonated alloxazine (AL) and lumichrome (LC) are studied using UV photodissociation spectroscopy. This study was driven by an interest in the biological functions of flavin molecules, these include photochemical reactions and chemical redox. The data presented in Chapter 5 forms part of a larger dataset on deprotonated flavin ions which vary in chemical complexity from the isolated flavin chromophore (AL and LC) to biologically relevant flavin molecules (flavin adenine dinucleotide and flavin monophosphate). Currently, only the data of AL and LC is published; however, the full dataset may eventually be used to identify important photofragments or compare the effect of charge locality on the electronic structure of the flavin chromophore.

Deprotonated AL and LC were studied with UV photodissociation across the range 2.2 – 5.7 eV. This study finds that the gaseous absorption spectra of deprotonated

AL and LC are very similar across this range. The literature surrounding the solution-phase structures of AL and LC is considered, and the solution phase absorption spectra of these molecules under basic conditions are compared with the gaseous absorption spectra, it is found that an additional peak is observed in the gas phase at ~4 eV. The position of this peak coincides with the calculated vertical detachment energies of the lowest energy structures of deprotonated AL and LC, and is thus assigned as an absorption feature related the onset of electron detachment. Tracking the production of the most intense photofragment throughout the absorption region associated with the onset of electron detachment reveals a subtle in behavior for AL and LC. Namely, that deprotonated AL produces a fragment which peaks in this region, indicating the presence of a resonant transition, whereas the fragment from deprotonated LC does not peak in this region. The resonant transition which occurs close to the electron detachment onset of deprotonated AL is assigned as a transition to a dipole-bound excited state, which is able to relax in such a way that a fragment can be produced. However, calculations show that the vertical dipole moment of deprotonated LC is larger than that of AL, this means that deprotonated LC should be more capable of retaining a dipole-bound electron. The absence of a resonantly produced photofragment in this region for LC indicates that if a dipole-bound state is formed, it is unable to relax into a valence-bound state and undergo fragmentation. This is attributed to internal rotors within the LC molecule, which have been previously shown to decrease the lifetime of dipole-bound states in enolate anions.

This study of AL and LC has shown that UV photodissociation studies on gaseous anions is an effective tool to study phenomena related electron detachment. The use of a commercial mass spectrometer was ideal for this project because the commercial software controlling the mass spectrometer enabled the intensities of all photofragments to be tracked; photofragment tracking was critical to the characterisation of the dipole-bound excited-state of AL. This method of photofragment tracking to characterise a dipole-bound excited-state was used in a previously published study of the clusters formed between iodide and the pyrimidine-nucleobases.[239] To further understand the deprotonated AL and LC system, it would be useful to conduct time-resolved photoelectron spectroscopy experiments, to track the evolution of the excited states that are formed in the region surrounding the electron detachment threshold. Such experiments could determine

the rate constants of the dipole-bound excited-states and provide insight into the role of the methyl groups which distinguish AL and LC. Additionally, having studied the photodissociation of these simplest flavin anions, it is sensible to now interpret and contextualise the data that has been collected on functionalised flavins.

7.1.4 Hexachloroplatinate Nucleobase Clusters

In Chapter 6, photodissociation spectroscopy is performed on the clusters formed between hexachloroplatinate ($PtCl_6^{2-}$) and the nucleobases adenine, cytosine, thymine and uracil. This study was initiated to learn about the interactions between a photo-labile transition metal complex and the nucleobases. Additionally, the electronic structure of the hexachloroplatinate dianions, i.e. octahedral geometry with a low-spin d^6-Pt(IV) centre, is also similar to a class of platinum based photopharmaceuticals under research. This study is therefore also relevant to understanding about UV-induced photoactivaton.

The gaseous absorption spectra of the $PtCl_6^{2-}$·nucleobase clusters are broadly similar for each cluster across the range 4 – 5.8 eV, each spectrum has a strong absorption band at ~4.6 eV and a rising edge which peaks above 5.8 eV. These transitions are primarily assigned as ligand-to-metal charge transfer (LMCT) transitions within the $PtCl_6^{2-}$ moiety, this is confirmed with TDDFT calculations. Photofragments mass spectra reveal that the most intense fragments are $PtCl_x^-$ (x = 3-5) and nucleobase chloride. This shows that photoexcitation primarily leads to the dissociation of the $PtCl_6^{2-}$ moiety, and that the nucleobase can effectively capture a chloride anion. Additionally, weak fragments associated with electron detachment and the deprotonation of the nucleobase are also observed. Tracking the intensities of different photofragments across the spectral range reveals differences in the production of photofragments. $PtCl_x^-$ (x = 3-5) fragments are produced in line with the total absorption spectrum, whereas nucleobase chloride is most intense in the low-energy region of the absorption spectrum. This shows that, by selecting the correct excitation wavelength, the gaseous photochemistry of these clusters can be influenced to favour the production of a specific photofragment.

This study has shown that photodissociation spectroscopy is ideal for determining the photochemical fragmentation pathways available to a charged photo-

pharmaceutical as it clusters to a DNA base. Further work in this area could involve increasing the complexity of the nucleobase moiety (e.g. to a nucleoside, nucleotide or oligonucleotide) as well as using a photoactivatable and medically relevant platinum complex.

7.2 Summary of Work Not in Thesis

In addition to the work presented in this thesis, I have worked on other projects which have resulted in papers which I authored. This section will summarise my work studying nucleobase iodide (M·I⁻) clusters as well as my paper on the structure and photochemistry of protonated alloxazine.[239,283]

7.2.1 Nucleobase Iodide Clusters

I initially studied the complex formed between iodide and uracil using photodissociation spectroscopy as part of a collaboration between the Dessent and Neumark groups.[240] These types of clusters can be used to study the destructive effect of low-energy electrons on the DNA nucleobases. In the U·I⁻ cluster, the iodide can be used as a source of a low-energy electron, if the cluster irradiated by a photon with energy greater that the binding energy of the iodide electron, which can be captured and bound by the permanent dipole of the nucleobase in a so-called dipole-bound excited state.

In the collaboration,[240] Neumark used time-resolved photoelectron imaging (TRPEI) to study the evolution of the excited state formed when the U·I⁻ cluster was irradiated. However, the TRPEI instrument could not fully detect or quantify the products that formed following excitation. I studied this system using UV photodissociation and recorded the production of photofragments as a function of excitation wavelength. We discovered that I⁻ and deprotonated uracil ([U-H]⁻) were resonantly produced in spectral regions associated with excitation to a dipole-bound excited state as well as $\pi - \pi^*$ transitions in the uracil. The fragmentation into I⁻ and [U-H]⁻ supported the TRPEI data and showed that the dipole-bound excited state could undergo relaxation to the electronic ground state before the cluster fragmented.

This UV photodissociation study of the U·I⁻ cluster was extended to include all pyrimidine nucleobases (Uracil, Thymine and Cytosine).[239] This revealed that each cluster has a prominent dipole-bound excited state in the vicinity of the vertical detachment energy of the cluster. This absorption feature was observed in photodepletion and photofragment production spectra. Photofragment mass spectra showed that the individual nucleobases had different fragmentation efficiencies, this was discussed in the context of previous time-resolved measurements. Future work on the nucleobase iodide clusters should include the purine nucleobases adenine and guanine. The interaction between guanine and low-energy electrons is especially interesting because guanine is known to be the site of oxidative damage within DNA.

7.2.2 Alloxazine

The gaseous spectroscopy of protonated alloxazine (AL·H⁺) was studied using UV/Vis photodissociation.[283] This work was undertaken to discover the photofragmentation pathways of positively charged flavin ions, as well as to gain insight into the photostability of biological flavin ions.

UV photodissociation was used to fragment gaseous AL·H⁺ across the range 2.34 – 5.64 eV (530 – 220 nm), this was done to record photofragment mass spectra and produce a photodepletion spectrum. The photofragment mass spectra were compared to higher-energy collisional dissociation (HCD) mass spectra. It was concluded that several distinct fragmentation mechanisms were available to AL·H⁺ which lead to different ring-open or ring-closed fragments, the neutral losses required to produce these fragments were discussed. The intensities of all photofragments were plotted as a function of excitation energy, inspection of the spectra revealed that distinct absorption profiles were present in the gaseous experiment, indicating that a distribution of isomers were present in the gas phase. Simulated TDDFT excitation spectra were used assign the gaseous isomers to a dominant N5 protonated structure and a weak O4 protonated structure. The N5 protomer initially fragmented by losing HNCO whereas the O4 protomer initially fragmented by losing HCN.

This study has revealed that the location of a proton influences the ring-opening dynamics within protonated alloxazine and that UV photodissociation is an effective method of distinguishing between gaseous protomers. Now that the fragmentation

mechanisms of the simplest protonated flavin molecule is understood, it would be interesting to expand the study of protonated alloxazine to the functionalised flavins. Such studies could provide insight into photodegradation mechanism within cells.

7.3 Outlook and Future work

The laser-coupled commercial mass spectrometer has been proven, through numerous publications, to be a useful scientific instrument capable of studying photochemistry. The robust design of the mass spectrometer means that it is a reliable tool for producing and analysing gaseous ions. Additionally, the commercial software associated with the mass spectrometer can record the intensities of many photofragments, this makes the instrument suited for analysing photofragmentation pathways. The studies in this thesis have shown that photodissociation spectroscopy should be performed alongside gaseous collisional studies; solution-phase absorption spectra; and quantum chemical calculations. The combination of experimental and computational techniques provides sufficient information to identify gaseous molecules as well as to understand photochemical degradation mechanisms.

This thesis has shown that both organic and inorganic cations and anions can be studied using the laser-coupled mass spectrometer. The studies presented in this thesis are about biologically important molecules. Future photochemistry experiments using the laser-coupled mass spectrometer should also relate to biochemistry because it is important to understand the photochemical mechanisms within cells as well as photodegradation reactions.

7.3.1 Future Experiments and Development

Throughout this thesis, simple molecules and clusters have been studied to gain insights into the photochemistry of complex molecules and clusters. This is seen in studies of nicotinamide, alloxazine and lumichrome, and hexachloroplatinate nucleobase clusters (Chapters 3, 5 and 6 respectively). As has been discussed in Section 7.1, future experiments on the molecules studied in this thesis could have an increased molecular complexity since the fragmentation mechanisms of the simple

molecules are now understood. Such studies would provide a more biologically relevant insight into biological photochemistry.

A method of bridging the gap between solution and gas phase photochemistry is to study ions clustered to solvent molecules.[157] This approach combines the usefulness of mass selection in the gas phase with the biological relevance of the solution phase. Attempts to study gaseous ion-water clusters during my PhD were unsuccessful because of efficient desolvation within the commercial ion source of the mass spectrometer. However, future experiments could attempt to create ion-water clusters within the mass spectrometer by introducing water directly into the vacuum chamber. It may be possible to inject water through the chemical ionisation source of the mass spectrometer, which is situated within the vacuum manifold. Alternatively, water could be introduced directly into the ion trap with the helium buffer gas, or the mass spectrometer could be altered to have a water injection port.

This thesis has shown that gaseous isomers should be considered when studying simple protonated or deprotonated organic molecules. Whilst UV photodissociation spectroscopy is an effective method for distinguishing between gaseous isomers, it cannot physically separate these isomers. Ion mobility spectrometry would be a useful addition to the experimental apparatus since it can separate ions by their size and shape.[162] The ion mobility component could be as a separate instrument, to prescreen samples for multiple structures before studying them with UV photodissociation. Alternatively, ion mobility could be coupled to the existing UV photodissociation instrument, to separate ions by size and shape before photodepletion spectra are recorded, such that the instrument can collect conformer specific absorption spectra.

A focus of this PhD has been to determine gaseous fragmentation mechanisms, which provide information on the unimolecular fragmentation mechanisms available to the biomolecules. Alternative fragmentation mechanisms which involve oxidation can only occur in the solution phase. It is possible to study the production of solution-phase fragments by using mass spectrometry to analyse a solution being irradiated.[284] An interesting way of doing this would be to design an online fragmentation source, where the solution being injected through the electrospray ion source is irradiated.

This type of experiment would complement the gaseous photodissociation spectroscopy experiments.

References

1.   O. P. Ernst, D. T. Lodowski, M. Elstner, P. Hegemann, L. S. Brown and H. Kandori, *Chem. Rev.*, 2014, **114**, 126-163.

2.   R. P. Sinha and D. P. Hader, *Photochem. Photobiol. Sci.*, 2002, **1**, 225-236.

3.   N. J. Farrer, J. A. Woods, L. Salassa, Y. Zhao, K. S. Robinson, G. Clarkson, F. S. Mackay and P. J. Sadler, *Angew. Chem. Int. Ed.*, 2010, **49**, 8905-8908.

4.   J. R. Cannon, M. B. Carnmarata, S. A. Robotham, V. C. Cotham, J. B. Shaw, R. T. Fellers, B. P. Early, P. M. Thomas, N. L. Kelleher and J. S. Brodbelt, *Anal. Chem.*, 2014, **86**, 2185-2192.

5.   T. Baer and R. C. Dunbar, *J. Am. Soc. Mass Spectrom.*, 2010, **21**, 681-693.

6.   E. Nir, M. Müller, L. I. Grace and M. S. de Vries, *Chem. Phys. Lett.*, 2002, **355**, 59-64.

7.   K. Müller-Dethlefs, *J. Electron. Spectrosc. Relat. Phenom.*, 1995, **75**, 35-46.

8.   J. R. R. Verlet, D. A. Horke and A. S. Chatterley, *Phys. Chem. Chem. Phys.*, 2014, **16**, 15043-15052.

9.   J. Schmidt, M. M. Meyer, I. Spector and S. R. Kass, *J. Phys. Chem. A*, 2011, **115**, 7625-7632.

10.   Z. X. Tian, X. B. Wang, L. S. Wang and S. R. Kass, *J. Am. Chem. Soc.*, 2009, **131**, 1174-1181.

11.   J. I. Brauman and K. C. Smyth, *J. Am. Chem. Soc.*, 1969, **91**, 7778-7780.

12.   M. Z. Kamrath, E. Garand, P. A. Jordan, C. M. Leavitt, A. B. Wolk, M. J. Van Stipdonk, S. J. Miller and M. A. Johnson, *J. Am. Chem. Soc.*, 2011, **133**, 6440-6448.

13.   O. V. Boyarkin, S. R. Mercier, A. Kamariotis and T. R. Rizzo, *J. Am. Chem. Soc.*, 2006, **128**, 2816-2817.

14.   E. Matthews, A. Sen, N. Yoshikawa, E. Bergström and C. E. H. Dessent, *Phys. Chem. Chem. Phys.*, 2016, **18**, 15143-15152.

15.   D. Nolting, R. Weinkauf, I. V. Hertel and T. Schultz, *ChemPhysChem*, 2007, **8**, 751-755.

16.   J. P. Reilly, *Mass Spectrom. Rev.*, 2009, **28**, 425-447.

17.   D. M. Wetzel and J. I. Brauman, *Chem. Rev.*, 1987, **87**, 607-622.

18.   R. C. Dunbar, *J. Am. Chem. Soc.*, 1971, **93**, 4354-4358.

References

19. R. Antoine and P. Dugourd, *Phys. Chem. Chem. Phys.*, 2011, **13**, 16494-16509.

20. J. Laskin and J. H. Futrell, *Mass Spectrom. Rev.*, 2005, **24**, 135-167.

21. J. Oomens, D. T. Moore, G. Meijer and G. von Helden, *Phys. Chem. Chem. Phys.*, 2004, **6**, 710-718.

22. E. Matthews and C. E. H. Dessent, *J. Phys. Chem. A*, 2016, **120**, 9209-9216.

23. S. H. Kaufman, J. M. Weber and M. Pernpointner, *J. Chem. Phys.*, 2013, **139**, 194310.

24. M. A. Halim, M. Girod, L. MacAleese, J. Lemoine, R. Antoine and P. Dugourd, *J. Am. Soc. Mass Spectrom.*, 2016, **27**, 1435-1442.

25. N. C. Polfer, *Chem. Soc. Rev.*, 2011, **40**, 2211-2221.

26. L. J. M. Kempkes, J. Martens, G. Berden and J. Oomens, *Int. J. Mass Spectrom.*, 2018, **429**, 90-100.

27. A. F. Cruz-Ortiz, M. Rossa, F. Berthias, M. Berdakin, P. Maitre and G. A. Pino, *J. Phys. Chem. Lett.*, 2017, **8**, 5501-5506.

28. K. S. Lancaster, H. J. An, B. S. Li and C. B. Lebrilla, *Anal. Chem.*, 2006, **78**, 4990-4997.

29. A. J. A. Harvey, A. Sen, N. Yoshikawa and C. E. H. Dessent, *Chem. Phys. Lett.*, 2015, **634**, 216-220.

30. K. C. Smyth, R. T. McIver Jr., J. I. Brauman and R. W. Wallace, *J. Chem. Phys.*, 1971, **54**, 2758-2759.

31. M. Yamashita and J. B. Fenn, *J. Phys. Chem.*, 1984, **88**, 4451-4459.

32. M. Yamashita and J. B. Fenn, *J. Phys. Chem.*, 1984, **88**, 4671-4675.

33. S. Banerjee and S. Mazumdar, *Int. J. Anal. Chem.*, 2012, **2012**, 282574.

34. C. S. Ho, C. W. K. Lam, M. H. M. Chan, R. C. K. Cheung, L. K. Law, L. C. W. Lit, K. F. Ng, M. W. M. Suen and H. L. Tai, *Clin. Biochem. Rev.*, 2003, **24**, 3-12.

35. Y. Inokuchi, T. Ebata and T. R. Rizzo, *J. Phys. Chem. A*, 2015, **119**, 11113-11118.

36. C. T. Wolke, J. A. Fournier, E. Miliordos, S. M. Kathmann, S. S. Xantheas and M. A. Johnson, *J. Chem. Phys.*, 2016, **144**, 074305.

37. F. Rosu, V. Gabelica, E. De Pauw, R. Antoine, M. Broyer and P. Dugourd, *J. Phys. Chem. A*, 2012, **116**, 5383-5391.

References

38.   L. Voronina and T. R. Rizzo, *Phys. Chem. Chem. Phys.*, 2015, **17**, 25828-25836.

39.   N. L. Burke, A. F. DeBlase, J. G. Redwine, J. R. Hopkins, S. A. McLuckey and T. S. Zwier, *J. Am. Chem. Soc.*, 2016, **138**, 2849-2857.

40.   E. Matthews and C. E. H. Dessent, *Phys. Chem. Chem. Phys.*, 2017, **19**, 17434-17440.

41.   C. S. Byskov, J. M. Weber and S. B. Nielsen, *Phys. Chem. Chem. Phys.*, 2015, **17**, 5561-5564.

42.   S. H. Kaufman and J. M. Weber, *J. Phys. Chem. A*, 2014, **118**, 9687-9691.

43.   D. Nolting, C. Marian and R. Weinkauf, *Phys. Chem. Chem. Phys.*, 2004, **6**, 2633-2640.

44.   D. Nolting, T. Schultz, I. V. Hertel and R. Weinkauf, *Phys. Chem. Chem. Phys.*, 2006, **8**, 5247-5254.

45.   C. Marian, D. Nolting and R. Weinkauf, *Phys. Chem. Chem. Phys.*, 2005, **7**, 3306-3316.

46.   S. Grimme and M. Waletzke, *J. Chem. Phys.*, 1999, **111**, 5645-5655.

47.   H. Kang, C. Dedonder-Lardeux, C. Jouvet, G. Grégoire, C. Desfrançois, J. P. Schermann, M. Barat and J. A. Fayeton, *J. Phys. Chem. A*, 2005, **109**, 2417-2420.

48.   H. Kang, C. Jouvet, C. Dedonder-Lardeux, S. Martrenchard, C. Charrière, G. Grégoire, C. Desfrançois, J. P. Schermann, M. Barat and J. A. Fayeton, *J. Chem. Phys.*, 2005, **122**, 084307.

49.   D. Imanbaew, J. Lang, M. F. Gelin, S. Kaufhold, M. G. Pfeffer, S. Rau and C. Riehn, *Angew. Chem. Int. Ed.*, 2017, **56**, 5471-5474.

50.   L. Guyon, T. Tabarin, B. Thuillier, R. Antoine, M. Broyer, V. Boutou, J. P. Wolf and P. Dugourd, *J. Chem. Phys.*, 2008, **128**, 075103.

51.   V. Gabelica, F. Rosu, E. De Pauw, R. Antoine, T. Tabarin, M. Broyer and P. Dugourd, *J. Am. Soc. Mass Spectrom.*, 2007, **18**, 1990-2000.

52.   V. Gabelica, T. Tabarin, R. Antoine, F. Rosu, I. Compagnon, M. Broyer, E. De Pauw and P. Dugourd, *Anal. Chem.*, 2006, **78**, 6564-6572.

53.   B. Bellina, I. Compagnon, L. Joly, F. Albrieux, A. R. Allouche, F. Bertorelle, J. Lemoine, R. Antoine and P. Dugourd, *Int. J. Mass Spectrom.*, 2010, **297**, 36-40.

References

54.   C. Brunet, R. Antoine, J. Lemoine and P. Dugourd, *J. Phys. Chem. Lett.*, 2012, **3**, 698-702.

55.   I. Compagnon, A. R. Allouche, F. Bertorelle, R. Antoine and P. Dugourd, *Phys. Chem. Chem. Phys.*, 2010, **12**, 3399-3403.

56.   Q. Z. Bian, M. W. Forbes, F. O. Talbot and R. A. Jockusch, *Phys. Chem. Chem. Phys.*, 2010, **12**, 2590-2598.

57.   M. W. Forbes and R. A. Jockusch, *J. Am. Soc. Mass Spectrom.*, 2011, **22**, 93-109.

58.   A. M. Nagy, F. O. Talbot, M. F. Czar and R. A. Jockusch, *J. Photochem. Photobiol. A*, 2012, **244**, 47-53.

59.   H. Yao and R. A. Jockusch, *J. Phys. Chem. A*, 2013, **117**, 1351-1359.

60.   M. W. Forbes and R. A. Jockusch, *J. Am. Chem. Soc.*, 2009, **131**, 17038-17039.

61.   M. W. Forbes, A. M. Nagy and R. A. Jockusch, *Int. J. Mass Spectrom.*, 2011, **308**, 155-166.

62.   S. V. Kruppa, F. Bäppler, W. Klopper, S. P. Walg, W. R. Thiel, R. Diller and C. Riehn, *Phys. Chem. Chem. Phys.*, 2017, **19**, 22785-22800.

63.   Y. Nosenko, C. Riehn and W. Klopper, *Chem. Phys. Lett.*, 2016, **659**, 55-60.

64.   E. Bodo, A. Ciavardini, A. Giardini, A. Paladini, S. Piccirillo, F. Rondino and D. Scuderi, *Chem. Phys.*, 2012, **398**, 124-128.

65.   V. Gabelica, F. Rosu, E. De Pauw, J. Lemaire, J. C. Gillet, J. C. Poully, F. Lecomte, G. Grégoire, J. P. Schermann and C. Desfrançois, *J. Am. Chem. Soc.*, 2008, **130**, 1810-1811.

66.   H. Elferink, M. E. Severijnen, J. Martens, R. A. Mensink, G. Berden, J. Oomens, F. P. J. T. Rutjes, A. M. Rijs and T. J. Boltje, *J. Am. Chem. Soc.*, 2018, **140**, 6034-6038.

67.   J. A. Bendo, J. Martens, G. Berden, J. Oomens and T. H. Morton, *Int. J. Mass Spectrom.*, 2018, **429**, 206-211.

68.   L. J. M. Kempkes, G. C. Boles, J. Martens, G. Berden, P. B. Armentrout and J. Oomens, *J. Phys. Chem. A*, 2018, **122**, 2424-2436.

69.   K. I. Öberg, *Chem. Rev.*, 2016, **116**, 9631-9663.

70.   R. Otto, A. von Zastrow, T. Best and R. Wester, *Phys. Chem. Chem. Phys.*, 2013, **15**, 612-618.

References

71.   G. Féraud, C. Dedonder-Lardeux, C. Jouvet and E. Marceca, *J. Phys. Chem. A*, 2016, **120**, 3897-3905.

72.   G. Féraud, N. Esteves-López, C. Dedonder-Lardeux and C. Jouvet, *Phys. Chem. Chem. Phys.*, 2015, **17**, 25755-25760.

73.   M. I. Taccone, G. Féraud, M. Berdakin, C. Dedonder-Lardeux, C. Jouvet and G. A. Pino, *J. Chem. Phys.*, 2015, **143**, 041103.

74.   J. C. Dean, N. L. Burke, J. R. Hopkins, J. G. Redwine, P. V. Ramachandran, S. A. McLuckey and T. S. Zwier, *J. Phys. Chem. A*, 2015, **119**, 1917-1932.

75.   T. K. Roy, V. Kopysov, N. S. Nagornova, T. R. Rizzo, O. V. Boyarkin and R. B. Gerber, *ChemPhysChem*, 2015, **16**, 1374-1378.

76.   N. L. Burke, J. G. Redwine, J. C. Dean, S. A. McLuckey and T. S. Zwier, *Int. J. Mass Spectrom.*, 2015, **378**, 196-205.

77.   C. Seaiby, A. V. Zabuga, A. Svendsen and T. R. Rizzo, *J. Chem. Phys.*, 2016, **144**, 014304.

78.   J. Houmøller, M. Wanko, A. Rubio and S. B. Nielsen, *J. Phys. Chem. A*, 2015, **119**, 11498-11503.

79.   M. B. S. Kirketerp and S. B. Nielsen, *Int. J. Mass Spectrom.*, 2010, **297**, 63-66.

80.   M. H. Stockett, C. Kjær, M. K. Linder, M. R. Detty and S. B. Nielsen, *Photochem. Photobiol. Sci.*, 2017, **16**, 779-784.

81.   F. W. McLafferty, P. F. Bente, R. Kornfeld, S. C. Tsai and I. Howe, *J. Am. Chem. Soc.*, 1973, **95**, 2120-2129.

82.   J. M. Wells and S. A. McLuckey, *Biol. Mass Spectrom.*, 2005, **402**, 148-185.

83.   F. W. McLafferty, *Anal. Chem.*, 1959, **31**, 82-87.

84.   Y. H. Ho and P. Kebarle, *Int. J. Mass Spectrom.*, 1997, **165**, 433-455.

85.   R. Cumeras, E. Figueras, C. E. Davis, J. I. Baumbach and I. Gràcia, *Analyst*, 2015, **140**, 1376-1390.

86.   R. Cumeras, E. Figueras, C. E. Davis, J. I. Baumbach and I. Gràcia, *Analyst*, 2015, **140**, 1391-1410.

87.   C. Masellis, N. Khanal, M. Z. Kamrath, D. E. Clemmer and T. R. Rizzo, *J. Am. Soc. Mass Spectrom.*, 2017, **28**, 2217-2222.

88.   J. Seo, S. Warnke, S. Gewinner, W. Schöllkopf, M. T. Bowers, K. Pagel and G. von Helden, *Phys. Chem. Chem. Phys.*, 2016, **18**, 25474-25482.

References

89.   J. N. Bull, N. J. A. Coughlan and E. J. Bieske, *J. Phys. Chem. A*, 2017, **121**, 6021-6027.

90.   J. S. Brodbelt, *Chem. Soc. Rev.*, 2014, **43**, 2757-2783.

91.   T. Doussineau, R. Antoine, M. Santacreu and P. Dugourd, *J. Phys. Chem. Lett.*, 2012, **3**, 2141-2145.

92.   B. J. Ko and J. S. Brodbelt, *Anal. Chem.*, 2011, **83**, 8192-8200.

93.   J. A. Madsen, T. W. Cullen, M. S. Trent and J. S. Brodbelt, *Anal. Chem.*, 2011, **83**, 5107-5113.

94.   J. S. Brodbelt, *J. Am. Soc. Mass Spectrom.*, 2011, **22**, 197-206.

95.   J. B. Shaw, J. A. Madsen, H. Xu and J. S. Brodbelt, *J. Am. Soc. Mass Spectrom.*, 2012, **23**, 1707-1715.

96.   R. C. Dunbar, J. Oomens, G. Berden, J. K. C. Lau, U. H. Verkerk, A. C. Hopkinson and K. W. M. Siu, *J. Phys. Chem. A*, 2013, **117**, 5335-5343.

97.   P. Nieto, A. Günther, G. Berden, J. Oomens and O. Dopfer, *J. Phys. Chem. A*, 2016, **120**, 8297-8308.

98.   S. Warnke, J. Seo, J. Boschmans, F. Sobott, J. H. Scrivens, C. Bleiholder, M. T. Bowers, S. Gewinner, W. Schöllkopf, K. Pagel and G. von Helden, *J. Am. Chem. Soc.*, 2015, **137**, 4236-4242.

99.   I. Alata, M. Broquier, C. Dedonder-Lardeux, C. Jouvet, M. Kim, W. Y. Sohn, S. S. Kim, H. Kang, M. Schütz, A. Patzer and O. Dopfer, *J. Chem. Phys.*, 2011, **134**, 074307.

100. M. Z. Kamrath, R. A. Relph, T. L. Guasco, C. M. Leavitt and M. A. Johnson, *Int. J. Mass Spectrom.*, 2011, **300**, 91-98.

101. J. D. Rodríguez, M. G. González, L. Rubio-Lago and L. Bañares, *Phys. Chem. Chem. Phys.*, 2014, **16**, 406-413.

102. H. W. Li, Y. Fang, N. M. Kidwell, J. M. Beames and M. I. Lester, *J. Phys. Chem. A*, 2015, **119**, 8328-8337.

103. B. W. Toulson, J. P. Alaniz, J. G. Hill and C. Murray, *Phys. Chem. Chem. Phys.*, 2016, **18**, 11091-11103.

104. E. Nir, C. Plützer, K. Kleinermanns and M. de Vries, *Eur. Phys. J. D*, 2002, **20**, 317-329.

105. E. V. Beletskiy, X. B. Wang and S. R. Kass, *J. Phys. Chem. A*, 2016, **120**, 8309-8316.

References

106.   A. S. Chatterley, C. W. West, V. G. Stavros and J. R. R. Verlet, *Chem. Sci.*, 2014, **5**, 3963-3975.

107.   A. B. Stephansen, S. B. King, Y. Yokoi, Y. Minoshima, W. L. Li, A. Kunin, T. Takayanagi and D. M. Neumark, *J. Chem. Phys.*, 2015, **143**.

108.   X. B. Wang and S. R. Kass, *J. Am. Chem. Soc.*, 2014, **136**, 17332-17336.

109.   J. N. Bull, C. W. West and J. R. R. Verlet, *Chem. Sci.*, 2016, **7**, 5352-5361.

110.   AmaZon Mass Spectrometer User Manual, Bruker Daltonik.

111.   N. R. Daly, *Rev. Sci. Instrum.*, 1960, **31**, 264-267.

112.   M. Dole, L. L. Mack and R. L. Hines, *J. Chem. Phys.*, 1968, **49**, 2240-2249.

113.   H. D. Dewald, *J. Chem. Educ.*, 1999, **76**, 33.

114.   R. B. Cole, *Electrospray and MALDI mass spectrometry : fundamentals, instrumentation, practicalities, and biological applications*, Wiley, Hoboken, N.J., USA, 2010.

115.   L. Konermann, E. Ahadi, A. D. Rodriguez and S. Vahidi, *Anal. Chem.*, 2013, **85**, 2-9.

116.   P. Kebarle and U. H. Verkerk, *Mass Spectrom. Rev.*, 2009, **28**, 898-917.

117.   G. Taylor, *Proc. R. Soc. Lond. A*, 1964, **280**, 383-397.

118.   L. Rayleigh, *Philos. Mag.*, 1882, **14**, 184-186.

119.   N. B. Cech and C. G. Enke, *Mass Spectrom. Rev.*, 2001, **20**, 362-387.

120.   B. A. Thomson and J. V. Iribarne, *J. Chem. Phys.*, 1979, **71**, 4451-4463.

121.   J. V. Iribarne and B. A. Thomson, *J. Chem. Phys.*, 1976, **64**, 2287-2294.

122.   L. L. Mack, P. Kralik, A. Rheude and M. Dole, *J. Chem. Phys.*, 1970, **52**, 4977-4986.

123.   *U.S. Pat.,* 2,939,952, 7 June 1960.

124.   R. E. March and J. F. J. Todd, *Quadrupole ion trap mass spectrometry*, Wiley, Hoboken, N.J., USA, 2005.

125.   É. Mathieu, *J. Math. Pures Appl.*, 1868, **13**, 137-203.

126.   V. I. Baranov, *J. Am. Soc. Mass Spectrom.*, 2003, **14**, 818-824.

127.   M. Barber, D. B. Gordon and M. D. Woods, *Rapid Commun. Mass Spectrom.*, 1990, **4**, 442-446.

128.   A. R. Johnson and E. E. Carlson, *Anal. Chem.*, 2015, **87**, 10668-10678.

129.   M. M. Campbell and O. Runquist, *J. Chem. Educ.*, 1972, **49**, 104-108.

130.   N. N. Dookeran, T. Yalcin and A. G. Harrison, *J. Mass Spectrom.*, 1996, **31**, 500-508.

References

131. G. Grégoire, H. Kang, C. Dedonder-Lardeux, C. Jouvet, C. Desfrançois, D. Onidas, V. Lepere and J. A. Fayeton, *Phys. Chem. Chem. Phys.*, 2006, **8**, 122-128.

132. A. Sen, G. L. Hou, X. B. Wang and C. E. H. Dessent, *J. Phys. Chem. B*, 2015, **119**, 11626-11631.

133. L. S. Wang and X. B. Wang, *J. Phys. Chem. A*, 2000, **104**, 1978-1990.

134. W. Kaiser and C. G. B. Garrett, *Phys. Rev. Lett.*, 1961, **7**, 229-232.

135. Gaussian 09, Revision D.01, M. J. Frisch, G. W. Trucks, H. B. Schlegel, G. E. Scuseria, M. A. Robb, J. R. Cheeseman, G. Scalmani, V. Barone, B. Mennucci, G. A. Petersson, H. Nakatsuji, M. Caricato, X. Li, H. P. Hratchian, A. F. Izmaylov, J. Bloino, G. Zheng, J. L. Sonnenberg, M. Hada, M. Ehara, K. Toyota, R. Fukuda, J. Hasegawa, M. Ishida, T. Nakajima, Y. Honda, O. Kitao, H. Nakai, T. Vreven, J. A. Montgomery Jr., J. E. Peralta, F. Ogliaro, M. J. Bearpark, J. Heyd, E. N. Brothers, K. N. Kudin, V. N. Staroverov, R. Kobayashi, J. Normand, K. Raghavachari, A. P. Rendell, J. C. Burant, S. S. Iyengar, J. Tomasi, M. Cossi, N. Rega, N. J. Millam, M. Klene, J. E. Knox, J. B. Cross, V. Bakken, C. Adamo, J. Jaramillo, R. Gomperts, R. E. Stratmann, O. Yazyev, A. J. Austin, R. Cammi, C. Pomelli, J. W. Ochterski, R. L. Martin, K. Morokuma, V. G. Zakrzewski, G. A. Voth, P. Salvador, J. J. Dannenberg, S. Dapprich, A. D. Daniels, Ö. Farkas, J. B. Foresman, J. V. Ortiz, J. Cioslowski and D. J. Fox, Gaussian, Inc., Wallingford, CT, USA, 2009.

136. F. Neese, *WIREs Comput. Mol. Sci.*, 2012, **2**, 73-78.

137. F. Neese, *J. Chem. Phys.*, 2003, **119**, 9428-9443.

138. E. Schrödinger, *Phys. Rev.*, 1926, **28**, 1049-1070.

139. M. Born and R. Oppenheimer, *Ann. Physik*, 1927, **84**, 457-484.

140. L. H. Thomas, *Proc. Camb. Philos. Soc.*, 1927, **23**, 542-548.

141. E. Fermi, *Rend. Accad. Naz. Lincei*, 1927, **6**, 602-607.

142. P. A. M. Dirac, *Proc. Camb. Philos. Soc.*, 1930, **26**, 376-385.

143. P. Hohenberg and W. Kohn, *Phys. Rev. B*, 1964, **136**, B864-871.

144. W. Kohn and L. J. Sham, *Phys. Rev.*, 1965, **140**, A1133-1138.

145. A. D. Becke, *J. Chem. Phys.*, 1993, **98**, 5648-5652.

146. C. Adamo and V. Barone, *J. Chem. Phys.*, 1999, **110**, 6158-6170.

147. Y. Zhao and D. G. Truhlar, *Theor. Chem. Acc.*, 2008, **120**, 215-241.

References

148. R. Peverati and D. G. Truhlar, *Phys. Chem. Chem. Phys.*, 2012, **14**, 16187-16191.

149. C. T. Lee, W. T. Yang and R. G. Parr, *Phys. Rev. B*, 1988, **37**, 785-789.

150. A. D. Becke, *Phys. Rev. A*, 1988, **38**, 3098-3100.

151. J. P. Perdew, K. Burke and M. Ernzerhof, *Phys. Rev. Lett.*, 1996, **77**, 3865-3868.

152. Y. Zhao, N. E. Schultz and D. G. Truhlar, *J. Chem. Phys.*, 2005, **123**.

153. Z. X. Tian and S. R. Kass, *J. Am. Chem. Soc.*, 2008, **130**, 10842-10843.

154. J. D. Steill and J. Oomens, *J. Am. Chem. Soc.*, 2009, **131**, 13570-13571.

155. M. Almasian, J. Grzetic, J. van Maurik, J. D. Steill, G. Berden, S. Ingemann, W. J. Buma and J. Oomens, *J. Phys. Chem. Lett.*, 2012, **3**, 2259-2263.

156. D. Schröder, M. Buděšínský and J. Roithová, *J. Am. Chem. Soc.*, 2012, **134**, 15897-15905.

157. T. M. Chang, J. S. Prell, E. R. Warrick and E. R. Williams, *J. Am. Chem. Soc.*, 2012, **134**, 15805-15813.

158. J. Boschmans, S. Jacobs, J. P. Williams, M. Palmer, K. Richardson, K. Giles, C. Lapthorn, W. A. Herrebout, F. Lemière and F. Sobott, *Analyst*, 2016, **141**, 4044-4054.

159. A. J. Ingram, C. L. Boeser and R. N. Zare, *Chem. Sci.*, 2016, **7**, 39-55.

160. G. J. Cheng, X. H. Zhang, L. W. Chung, L. P. Xu and Y. D. Wu, *J. Am. Chem. Soc.*, 2015, **137**, 1706-1725.

161. D. Schröder, *Acc. Chem. Res.*, 2012, **45**, 1521-1532.

162. H. X. Xia and A. B. Attygalle, *Anal. Chem.*, 2016, **88**, 6035-6043.

163. A. Largo and C. Barrientos, *J. Phys. Chem.*, 1991, **95**, 9864-9868.

164. K. A. Cox, S. J. Gaskell, M. Morris and A. Whiting, *J. Am. Soc. Mass Spectrom.*, 1996, **7**, 522-531.

165. R. S. Galaverna, G. A. Bataglion, G. Heerdt, G. F. de Sa, R. Daroda, V. S. Cunha, N. H. Morgon and M. N. Eberlin, *Eur. J. Org. Chem.*, 2015, 2189-2196.

166. P. M. Lalli, B. A. Iglesias, H. E. Toma, G. F. de Sa, R. J. Daroda, J. C. Silva, J. E. Szulejko, K. Araki and M. N. Eberlin, *J. Mass Spectrom.*, 2012, **47**, 712-719.

167. F. Lanucara, S. W. Holman, C. J. Gray and C. E. Eyers, *Nat. Chem.*, 2014, **6**, 281-294.

References

168. H. H. G. Jellinek and M. G. Wayne, *J. Phys. Colloid. Chem.*, 1951, **55**, 173-180.

169. A. Sen and C. E. H. Dessent, *J. Phys. Chem. Lett.*, 2014, **5**, 3281-3285.

170. E. Verdin, *Science*, 2015, **350**, 1208-1213.

171. J. Park, G. M. Halliday, D. Surjana and D. L. Damian, *Photochem. Photobiol.*, 2010, **86**, 942-948.

172. A. C. Chen, A. J. Martin, B. Choy, P. Fernández-Peñas, R. A. Dalziell, C. A. McKenzie, R. A. Scolyer, H. M. Dhillon, J. L. Vardy, A. Kricker, G. St George, N. Chinniah, G. M. Halliday and D. L. Damian, *New Engl. J. Med.*, 2015, **373**, 1618-1626.

173. P. Sidaway, *Nat. Rev. Clin. Oncol.*, 2016, **13**, 4-4.

174. R. Krishnan, J. S. Binkley, R. Seeger and J. A. Pople, *J. Chem. Phys.*, 1980, **72**, 650-654.

175. A. D. McLean and G. S. Chandler, *J. Chem. Phys.*, 1980, **72**, 5639-5648.

176. C. E. H. Dessent, J. Kim and M. A. Johnson, *Acc. Chem. Res.*, 1998, **31**, 527-534.

177. R. H. Abu Eittah, M. M. Hamed and A. A. Mohamed, *Int. J. Quantum Chem.*, 1997, **64**, 689-701.

178. E. F. G. Herington, *Discuss. Faraday Soc.*, 1950, **9**, 26-34.

179. C. B. O. Nielsen and K. V. Mikkelsen, *Mol. Phys.*, 2015, **113**, 3253-3263.

180. Y. A. Ranasinghe and G. L. Glish, *J. Am. Soc. Mass Spectrom.*, 1996, **7**, 473-481.

181. P. H. Chen, *J. Org. Chem.*, 1976, **41**, 2973-2976.

182. J. Momigny, H. Wankenne and J. Urbain, *Bull. Class. Sci. Acad. Roy. Belge*, 1965, **51**, 371-387.

183. B. Vogelsanger, R. D. Brown, P. D. Godfrey and A. P. Pierlot, *J. Mol. Spectrosc.*, 1991, **145**, 1-11.

184. R. A. Olsen, L. Liu, N. Ghaderi, A. Johns, M. E. Hatcher and L. J. Mueller, *J. Am. Chem. Soc.*, 2003, **125**, 10125-10132.

185. S. Ullrich, G. Tarczay, X. Tong, C. E. H. Dessent and K. Müller-Dethlefs, *Angew. Chem. Int. Ed.*, 2002, **41**, 166-168.

186. S. Ullrich, G. Tarczay, X. Tong, C. E. H. Dessent and K. Müller-Dethlefs, *Phys. Chem. Chem. Phys.*, 2001, **3**, 5450-5458.

References

187. J. A. Dickinson, M. R. Hockridge, E. G. Robertson and J. P. Simons, *J. Phys. Chem. A*, 1999, **103**, 6938-6949.

188. I. I. Marochkin and O. V. Dorofeeva, *Struct. Chem.*, 2013, **24**, 233-242.

189. A. D. Laurent and D. Jacquemin, *Int. J. Quantum Chem.*, 2013, **113**, 2019-2039.

190. M. Karni and A. Mandelbaum, *Org. Mass Spectrom.*, 1980, **15**, 53-64.

191. K. Levsel, H. M. Schiebel, J. K. Terlouw, K. J. Jobst, M. Elend, A. Preiß, H. Thiele and A. Ingendoh, *J. Mass Spectrom.*, 2007, **42**, 1024-1044.

192. A. Borba, M. Albrecht, A. Gómez-Zavaglia, L. Lapinski, M. J. Nowak, M. A. Suhm and R. Fausto, *Phys. Chem. Chem. Phys.*, 2008, **10**, 7010-7021.

193. R. E. Coffman and D. O. Kildsig, *J. Pharm. Sci.*, 1996, **85**, 848-853.

194. A. Guerrero, T. Baer, A. Chana, J. González and J. Z. Dávalos, *J. Am. Chem. Soc.*, 2013, **135**, 9681-9690.

195. S. A. McLuckey, D. Cameron and R. G. Cooks, *J. Am. Chem. Soc.*, 1981, **103**, 1313-1317.

196. G. Bouchoux, S. Bourcier, V. Blanc and S. Desaphy, *J. Phys. Chem. B*, 2009, **113**, 5549-5562.

197. A. R. Shalita, J. G. Smith, L. C. Parish, M. S. Sofman and D. K. Chalker, *Int. J. Dermatol.*, 1995, **34**, 434-437.

198. J. Wohlrab and D. Kreft, *Skin Pharmacol. Phys.*, 2014, **27**, 311-315.

199. H. Lambers, S. Piessens, A. Bloem, H. Pronk and P. Finkel, *Int. J. Cosmetic Sci.*, 2006, **28**, 359-370.

200. D. R. Sambandan and D. Ratner, *J. Am. Acad. Dermatol.*, 2011, **64**, 748-758.

201. N. S. Nagornova, T. R. Rizzo and O. V. Boyarkin, *J. Am. Chem. Soc.*, 2010, **132**, 4040-4041.

202. K. R. Asmis and D. M. Neumark, *Acc. Chem. Res.*, 2012, **45**, 43-52.

203. D. L. Huang, H. T. Liu, C. G. Ning and L. S. Wang, *J. Phys. Chem. Lett.*, 2015, **6**, 2153-2157.

204. S. M. J. Wellman and R. A. Jockusch, *J. Phys. Chem. A*, 2015, **119**, 6333-6338.

205. A. P. Cismesia, L. S. Bailey, M. R. Bell, L. F. Tesler and N. C. Polfer, *J. Am. Soc. Mass Spectrom.*, 2016, **27**, 757-766.

206. C. S. Hansen, S. J. Blanksby and A. J. Trevitt, *Phys. Chem. Chem. Phys.*, 2015, **17**, 25882-25890.

References

207. M. Broquier, S. Soorkia and G. Grégoire, *Phys. Chem. Chem. Phys.*, 2015, **17**, 25854-25862.

208. Z. X. Tian and S. R. Kass, *Angew. Chem. Int. Ed.*, 2009, **48**, 1321-1323.

209. C. Iacobucci, S. Reale and F. De Angelis, *Angew. Chem. Int. Ed.*, 2016, **55**, 2980-2993.

210. J. Roithová, *Chem. Soc. Rev.*, 2012, **41**, 547-559.

211. G. Féraud, L. Dornenianni, E. Marceca, C. Dedonder-Lardeux and C. Jouvet, *J. Phys. Chem. A*, 2017, **121**, 2580-2587.

212. S. O. Pedersen, K. Støchkel, C. S. Byskov, L. M. Baggesen and S. B. Nielsen, *Phys. Chem. Chem. Phys.*, 2013, **15**, 19748-19752.

213. M. Berdakin, G. Féraud, C. Dedonder-Lardeux, C. Jouvet and G. A. Pino, *Phys. Chem. Chem. Phys.*, 2014, **16**, 10643-10650.

214. H. T. H. Nguyen, C. J. Shaffer, R. Pepin and F. Tureček, *J. Phys. Chem. Lett.*, 2015, **6**, 4722-4727.

215. J. L. Campbell, A. M. C. Yang, L. R. Melo and W. S. Hopkins, *J. Am. Soc. Mass Spectrom.*, 2016, **27**, 1277-1284.

216. W. D. Kumler and L. A. Strait, *J. Am. Chem. Soc.*, 1943, **65**, 2349-2354.

217. T. Clark, J. Chandrasekhar, G. W. Spitznagel and P. V. R. Schleyer, *J. Comput. Chem.*, 1983, **4**, 294-301.

218. M. J. Frisch, J. A. Pople and J. S. Binkley, *J. Chem. Phys.*, 1984, **80**, 3265-3269.

219. M. Head-Gordon, J. A. Pople and M. J. Frisch, *Chem. Phys. Lett.*, 1988, **153**, 503-506.

220. T. H. Dunning, *J. Chem. Phys.*, 1989, **90**, 1007-1023.

221. Y. G. He, C. Y. Wu and W. Kong, *J. Phys. Chem. A*, 2005, **109**, 2809-2815.

222. Y. G. He, C. Y. Wu and W. Kong, *J. Chem. Phys.*, 2004, **121**, 3533-3539.

223. F. Coelho and M. N. Eberlin, *Angew. Chem. Int. Ed.*, 2011, **50**, 5261-5263.

224. Editorial, *Nat. Chem. Biol.*, 2014, **10**, 483-483.

225. K. S. Conrad, C. C. Manahan and B. R. Crane, *Nat. Chem. Biol.*, 2014, **10**, 801-809.

226. P. F. Heelis, *Chem. Soc. Rev.*, 1982, **11**, 15-39.

227. P. Drössler, W. Holzer, A. Penzkofer and P. Hegemann, *Chem. Phys.*, 2002, **282**, 429-439.

References

228. R. Brust, A. Lukacs, A. Haigney, K. Addison, A. Gil, M. Towrie, I. P. Clark, G. M. Greetham, P. J. Tonge and S. R. Meech, *J. Am. Chem. Soc.*, 2013, **135**, 16168-16174.

229. L. Zanetti-Polzi, M. Aschi, I. Daidone and A. Amadei, *Chem. Phys. Lett.*, 2017, **669**, 119-124.

230. X. P. Chang, X. Y. Xie, S. Y. Lin and G. L. Cui, *J. Phys. Chem. A*, 2016, **120**, 6129-6136.

231. A. Udvarhelyi, M. Olivucci and T. Domratcheva, *J. Chem. Theory Comput.*, 2015, **11**, 3878-3894.

232. M. H. Stockett, *Phys. Chem. Chem. Phys.*, 2017, **19**, 25829-25833.

233. T. Simonson and C. L. Brooks, *J. Am. Chem. Soc.*, 1996, **118**, 8452-8458.

234. N. Lasser and J. Feitelson, *Photochem. Photobiol.*, 1977, **25**, 451-456.

235. D. Prukała, E. Sikorska, J. Koput, I. Khmelinskii, J. Karolczak, M. Gierszewski and M. Sikorski, *J. Phys. Chem. A*, 2012, **116**, 7474-7490.

236. A. Penzkofer, *J. Photochem. Photobiol. A*, 2016, **314**, 114-124.

237. A. Tyagi and A. Penzkofer, *Photochem. Photobiol.*, 2011, **87**, 524-533.

238. C. E. H. Dessent, C. G. Bailey and M. A. Johnson, *J. Chem. Phys.*, 1995, **103**, 2006-2015.

239. E. Matthews, R. Cercola, G. Mensa-Bonsu, D. M. Neumark and C. E. H. Dessent, *J. Chem. Phys.*, 2018, **148**, 084304.

240. W. L. Li, A. Kunin, E. Matthews, N. Yoshikawa, C. E. H. Dessent and D. M. Neumark, *J. Chem. Phys.*, 2016, **145**, 044319.

241. S. B. King, A. B. Stephansen, Y. Yokoi, M. A. Yandell, A. Kunin, T. Takayanagi and D. M. Neumark, *J. Chem. Phys.*, 2015, **143**, 024312.

242. S. B. King, M. A. Yandell, A. B. Stephansen and D. M. Neumark, *J. Chem. Phys.*, 2014, **141**, 224310.

243. E. A. Brinkman, S. Berger, J. Marks and J. I. Brauman, *J. Chem. Phys.*, 1993, **99**, 7586-7594.

244. J. Koziol and D. E. Metzler, *Z. Naturforsch. B*, 1972, **27**, 1027-1029.

245. B. O. Keller, J. Suj, A. B. Young and R. M. Whittal, *Anal. Chim. Acta*, 2008, **627**, 71-81.

246. N. A. Smith and P. J. Sadler, *Phil. Trans. R. Soc. A*, 2013, **371**.

References

247.   F. S. Mackay, J. A. Woods, P. Heringová, J. Kašpárková, A. M. Pizarro, S. A. Moggach, S. Parsons, V. Brabec and P. J. Sadler, *P. Natl. Acad. Sci. USA*, 2007, **104**, 20743-20748.

248.   E. Shaili, *Sci. Prog.*, 2014, **97**, 20-40.

249.   M. Fernandez, E. Shaili, A. Gonzalez-Canto, G. Artigas, C. Sanchez, J. A. Woods, P. J. Sadler and V. Marchan, *J. Biol. Inorg. Chem.*, 2014, **19**, S782-S782.

250.   T. Gianferrara, I. Bratsos and E. Alessio, *Dalton Trans.*, 2009, 7588-7598.

251.   A. Sen, T. F. M. Luxford, N. Yoshikawa and C. E. H. Dessent, *Phys. Chem. Chem. Phys.*, 2014, **16**, 15490-15500.

252.   A. Sen and C. E. H. Dessent, *J. Chem. Phys.*, 2014, **141**, 241101.

253.   X. B. Wang and L. S. Wang, *J. Chem. Phys.*, 1999, **111**, 4497-4509.

254.   T. Sommerfeld, S. Feuerbacher, M. Pernpointner and L. S. Cederbaum, *J. Chem. Phys.*, 2003, **118**, 1747-1755.

255.   M. Pernpointner, T. Rapps and L. S. Cederbaum, *J. Chem. Phys.*, 2009, **131**, 044322.

256.   E. M. Glebov, I. P. Pozdnyakov, V. F. Plyusnin and I. Khmelinskii, *J. Photochem. Photobiol. C*, 2015, **24**, 1-15.

257.   M. Sakamoto, M. Fujistuka and T. Majima, *J. Photochem. Photobiol. C*, 2009, **10**, 33-56.

258.   W. Macyk and H. Kisch, *Chem. Eur. J.*, 2001, **7**, 1862-1867.

259.   C. Harris and P. V. Kamat, *ACS Nano*, 2010, **4**, 7321-7330.

260.   C. T. Middleton, K. de La Harpe, C. Su, Y. K. Law, C. E. Crespo-Hernández and B. Kohler, *Ann. Rev. Phys. Chem.*, 2009, **60**, 217-239.

261.   W. J. Schreier, P. Gilch and W. Zinth, *Ann. Rev. Phys. Chem.*, 2015, **66**, 497-519.

262.   K. Kleinermanns, D. Nachtigallová and M. S. de Vries, *Int. Rev. Phys. Chem.*, 2013, **32**, 308-342.

263.   R. Improta, F. Santoro and L. Blancafort, *Chem. Rev.*, 2016, **116**, 3540-3593.

264.   A. Sen, E. M. Matthews, G. L. Hou, X. B. Wang and C. E. H. Dessent, *J. Chem. Phys.*, 2015, **143**, 184307.

265.   W. E. Boxford and C. E. H. Dessent, *Phys. Chem. Chem. Phys.*, 2006, **8**, 5151-5165.

References

266. T. F. M. Luxford, E. M. Milner, N. Yoshikawa, C. Bullivant and C. E. H. Dessent, *Chem. Phys. Lett.*, 2013, **577**, 1-5.

267. A. DeFusco, J. Ivanic, M. W. Schmidt and M. S. Gordon, *J. Phys. Chem. A*, 2011, **115**, 4574-4582.

268. F. Santoro, V. Barone and R. Improta, *J. Comput. Chem.*, 2008, **29**, 957-964.

269. A. Y. Sokolov and H. F. Schaefer, *Dalton Trans.*, 2011, **40**, 7571-7582.

270. F. Weigend and R. Ahlrichs, *Phys. Chem. Chem. Phys.*, 2005, **7**, 3297-3305.

271. F. Weigend, *Phys. Chem. Chem. Phys.*, 2006, **8**, 1057-1065.

272. D. Andrae, U. Häußermann, M. Dolg, H. Stoll and H. Preuß, *Theor. Chim. Acta.*, 1990, **77**, 123-141.

273. L. B. Clark, G. G. Peschel and I. Tinoco, *J. Phys. Chem.*, 1965, **69**, 3615-3618.

274. M. Barbatti, A. J. A. Aquino and H. Lischka, *Phys. Chem. Chem. Phys.*, 2010, **12**, 4959-4967.

275. M. K. Shukla and J. Leszczynski, *J. Comput. Chem.*, 2004, **25**, 768-778.

276. J. C. Marcum, A. Halevi and J. M. Weber, *Phys. Chem. Chem. Phys.*, 2009, **11**, 1740-1751.

277. A. L. Sobolewski and W. G. Domcke, *J. Phys. Chem. A*, 2007, **111**, 11725-11735.

278. E. E. B. Campbell and R. D. Levine, *Ann. Rev. Phys. Chem.*, 2000, **51**, 65-98.

279. H. Häkkinen, B. Yoon, U. Landman, X. Li, H. J. Zhai and L. S. Wang, *J. Phys. Chem. A*, 2003, **107**, 6168-6175.

280. K. Matheis, L. Joly, R. Antoine, F. Lépine, C. Bordas, O. T. Ehrler, A. R. Allouche, M. M. Kappes and P. Dugourd, *J. Am. Chem. Soc.*, 2008, **130**, 15903-15906.

281. J. Simons, *Acc. Chem. Res.*, 2006, **39**, 772-779.

282. Q. H. Bao, Y. F. Chen, Y. Zheng and L. Sanche, *J. Phys. Chem. C*, 2014, **118**, 15516-15524.

283. E. Matthews, R. Cercola and C. E. H, Dessent, *Molecules*, 2018, **23**, 2036.

284. J. N. Bull, E. S. Carrascosa, M. S. Coughlan and E. J. Bieske, *Analyst*, 2017, **142**, 2100-2103.